On wave-mean flow interactions in stratified fluid

Antoine Renaud

Numéro National de Thèse : 2018LYSEN059

THÈSE de DOCTORAT DE L'UNIVERSITÉ DE LYON

opérée par

l'École Normale Supérieure de Lyon

École Doctorale N°52
École Doctorale de Physique et Astrophysique de Lyon (PHAST)
Spécialité de doctorat : Physique

Soutenue publiquement le 08/10/2018, par :

Antoine RENAUD

On wave-mean flow interactions in stratified fluids

De l'interaction entre les ondes et les écoulements moyens dans les fluides stratifiés

---

Devant le jury composé de :

VENAILLE, Antoine	Directeur de recherche	ENS de Lyon, CNRS	Directeur
BOUCHET, Freddy	Directeur de recherche	ENS de Lyon, CNRS	Co-encadrant
LE BARS, Michael	Directeur de recherche	IRPHE, CNRS	Rapporteur
PÉTRÉLIS, François	Directeur de recherche	ENS (LPS), CNRS	Rapporteur
MULLER, Caroline	Chargée de Recherche	ENS (LMD), CNRS	Examinatrice
READ, Peter	Professeur	Université d'Oxford	Examinateur
STAQUET, Chantal	Professeure des universités	LEGI	Examinatrice

Remerciements

Les travaux présentés dans ce manuscrit sont le résultat de quatre années de recherche qui ont débuté par un stage de septembre 2013 à août 2014 co-dirigé par Freddy Bouchet et Antoine Venaille au laboratoire de physique de l'ENS de Lyon. Cette collaboration s'est poursuivie par trois années de doctorat dirigées par Antoine Venaille au sein de ce même laboratoire de septembre 2015 à octobre 2018. Je remercie tous les membres du laboratoire, en particulier son directeur Thierry Dauxois, pour m'avoir chaleureusement accueilli pendant toutes ces années. Merci en particulier à Fatiha Bouchned ainsi qu'à l'ensemble du secrétariat pour leur aide essentielle. Merci également à Cerasela Calugaru et au PSMN sans qui la plupart des calculs numériques présentés dans cette thèse auraient difficilement vu le jour.

Je remercie Michael Le Bars et François Pétrélis d'avoir accepté la tâche fastidieuse d'être les rapporteurs de ma thèse ainsi que Caroline Muller et Chantal Staquet pour l'intérêt qu'elles ont porté à cette thèse. Je remercie également Peter Read qui, en sus, a accepté de faire le déplacement depuis Oxford jusqu'à Lyon pour assister à la soutenance.

Je tiens à témoigner toute ma gratitude à Antoine Venaille et Freddy Bouchet pour m'avoir proposé en 2013 de collaborer avec eux sur un sujet aussi fascinant que la mécanique statistique appliquée aux écoulements géophysiques. J'ai découvert avec plaisir un domaine de recherche qui m'était inconnu. Sous leur direction, j'ai appris énormément, aussi bien sur des aspects techniques que sur une pratique rigoureuse de la recherche scientifique. Leur co-encadrement s'est avéré superbement complémentaire, agréable et efficace. J'ai grandement apprécié nos multiples discussions passionnantes dont l'objet s'est étendu souvent bien au-delà de la science. Pour tout cela, je les en remercie chaleureusement. À Antoine, dont j'ai été le premier doctorant qu'il dirigé, essentiellement seul pendant trois ans, je tire mon chapeau. Les prochains étudiants qui se retrouveront sa direction seront indéniablement entre de très bonnes mains.

Je voudrais exprimer ma reconnaissance à Louis-Philippe Nadeau pour son enseignement de l'utilisation du modèle de circulation générale du MIT, pour sa collaboration concernant les travaux sur l'oscillation quasi-biennale ainsi que pour son soutien amical.

Pour m'avoir aidé à la rédaction de ce manuscrit, à la préparation de ma soutenance, j'adresse mes sincères remerciements à Corentin Herbert, Francesco Ragone, Géraldine Davis, Thibault Lestand, Laurent Chevillard, Nam Phan Van Song, Bertrand Marchand, Romain Graziani et Raphaël Jacquet.

Je voudrais exprimer toute ma reconnaissance envers les amis et les collègues que j'aime tant, qui ont su m'apporter support moral et intellectuel ainsi que leur confiance tout au long de ces années de thèse. Je tiens à témoigner toute ma gratitude à Gabrielle M., Luca G., Pauline H., Hélène B., Tony V., Vincent P., Xavier G., Jérôme T., Samuel P., Jeremy B., Brigitte L., Sylvain D., Laurie M., Jacqueline C., Clémentine R., Lauren O., Thibaud L., Yannick H., Erwan B., Clément P., Clément C., Eric S., ...

Je remercie mes très chers parents, Véronique et Jean-Luc, ainsi que mes frères adorés, Arthur et Maxime, qui m'apportent depuis toujours un soutien inconditionnel.

Je tiens à rendre hommage à Tomàs Tangarife, un collègue passionné et passionnant ainsi qu'un de mes premiers amis sur Lyon, qui nous a quitté subitement au début de ma thèse. Je rend également hommage à ma grand-mère Simone Renaud et mon grand-père Denis Lefèvre qui nous ont quitté pendant ma thèse.

Contents

1. Introduction

1.1 Scientific background

The dynamics of geophysical fluids give rise to many intriguing and complex phenomena. Planetary or stellar flows present large-scale structures evolving at a much slower timescale than the superimposed smaller scales motions. These structures can be stable over a very long period - as reflected by Jovian zonal jets [52], the Jupiter's Great Red Spot which has been swirling since at least the past 400 years [45] (see Fig. 1.1a) or western intensification of mid-latitude oceanic currents such as the Gulf Stream [136]. They can also display slow cyclical behaviours. For instance, the El Niño–southern oscillation (ENSO) generates important modulations of winds and sea surface temperatures over the tropical eastern Pacific Ocean with cycle length ranging from 2 to 7 years [166] (see Fig. 1.1b). Another example is the convection of electrically conducting fluids which can produce pulsating magnetic fields [10] like those observed in the solar magnetic activity [110] or the Earth's magnetic field [102]. **One outstanding question is how these large-scale structures or these long-time signal patterns emerge.**

Microscopic motions generate or largely influence these macroscopic phenomena. By microscopic, we mean any process occurring at scales smaller or faster than the phenomena considered - hereby considered to be macroscopic. A common way to properly distinguish these scales is to use an averaging procedure - say a longitudinal or monthly average - where the mean fields are macroscopic and the fluctuations microscopic.

Among these microscopic-scale processes, waves are of paramount importance. For instance, it is argued that the zonal-mean structure of the jet stream - one of the strongest currents of the Earth's atmosphere - is driven by Rossby waves [157]. Those waves propagate at a planetary scale due to the Earth's rotation.

This thesis focuses on another essential type of waves in geophysical flows: internal gravity waves. Internal gravity waves are rapidly oscillating waves that propagate within stratified environments - ubiquitous in geophysical contexts (see section 2.1). As such, they determine many large-scale oceanic and atmospheric behaviours:

- In the ocean, mixing induced by internal wave breaking is thought to play a key role in the meridional overturning circulation [115].
- In the atmosphere, they contribute to the vertical transfer of zonal momentum and

a. A quasi-stationary pattern

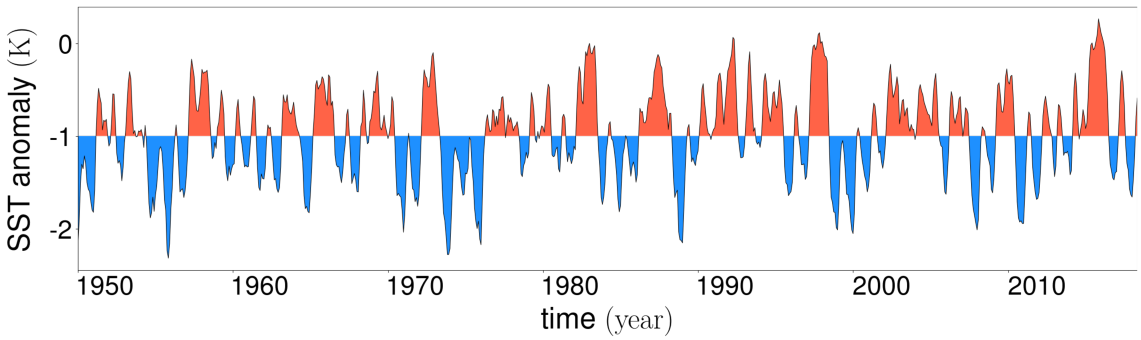

b. A low-frequency chaotic pattern

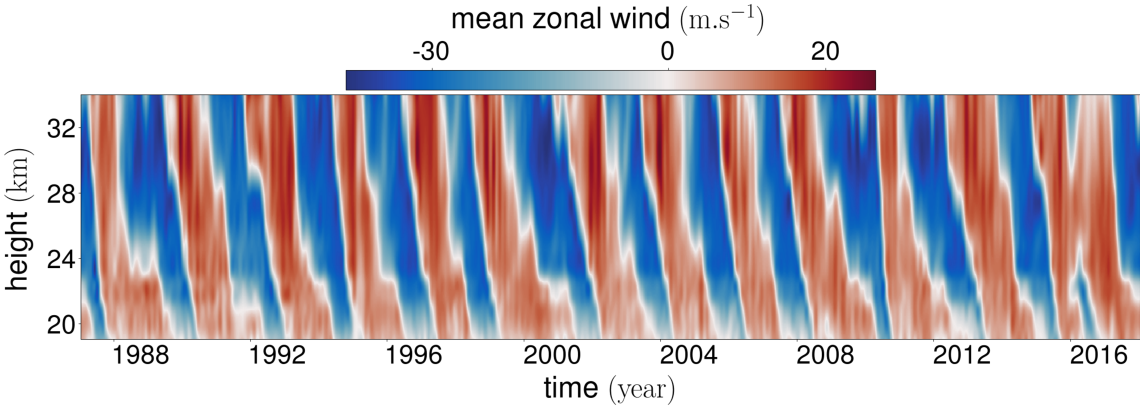

c. A low-frequency quasi-periodic pattern

Figure 1.1: **a. Great Red Spot of Jupiter.** The Great Red Spot is a massive storm, roughly 16 000 km wide – large enough to engulf the Earth. First sighted in 1665 and continuously observed since 1830 [45]. It may draw its energy from the smaller eddies that merge with it. (credit: Nasa). **b. El Niño Southern Oscillation.** Time-series of the sea-surface temperature anomaly averaged over a month and over the area between 5°S-5°N and 170°W-120°W.**c. Quasi-biennial oscillation of equatorial winds in the Earth's lower stratosphere.** Time-height section of the monthly averaged zonal wind measured by radiosonde in the lower stratosphere above Singapore (1.4°N 103.5°E) [112].

thus explain, in part, planetary scale winds [19, 74].

Specifically, when dissipated, internal gravity waves generate flows evolving over timescales that are significantly greater than their oscillation period [30, 147]. This generation of slowly evolving mean flows by damped internal gravity waves is of great interest (see section 2.2 and Chapter 3) and is the cause of a remarkable phenomenon: the quasi-biennial oscillation (QBO) of zonal winds in the lower equatorial stratosphere on Earth (see Fig. 1.1c). The QBO is driven by damped upward-propagating gravity waves generated at the tropopause [7] (see Chapter 4).

The QBO signal has a striking regularity. During the full 65-years time period it has been observed, it showed a quasiperiodic behaviour with periods ranging from 26 to 29 months. In contrast, the ENSO time-series presents a much more erratic signal (see Fig. 1.1b). Similarly, the Earth's magnetic field reversals also present a chaotic structure. **Beyond the question of the emergence of macroscopic features, a second outstanding question is whether their variability can be understood by an intrinsic dynamical variability or through the interaction with the environment.**

For instance, ENSO variability has been linked to chaotic synchronisation to the seasonal cycle [78] while the Earth magnetic field variability has been shown to be an intrinsic feature of the Earth dynamo [26]. On the other hand, the variability of the QBO has been partly explained by a quasi-synchronisation to the seasonal cycle [126]. The QBO received a recent renewed attention with the observation of an unexpected periodicity disruption of the QBO signal in 2016 [118] and the recent discovery of similar wind regimes on Jupiter and Saturn [89, 49]. In particular, the origin of the recent disruptions has been attributed to extra-tropical perturbations. Yet, the mechanism by which these disturbances may affect the stratospheric oscillation has remained elusive. A new look is proposed in Chapter 5.

An immediate approach to studying fluid mechanics phenomena would be to solve directly the primitive dynamical equations of fluids. Yet, in almost all practical problems an analytical resolution is inconceivable. Consequently, a common approach is to resolve these equations numerically. These approaches - referred to as direct numerical simulations - do not rely on an approximation of the equations, which implies that all dynamical scales must be resolved by the numerical model. For the study of the macroscopic features of planetary flows, the use of direct numerical simulations is hopeless. Indeed, such simulations would require a gigantic spatiotemporal grid in order to resolve accurately the macroscopic scales down to the smallest turbulent eddies. Despite the skyrocketing growth of computational power that started in the 80s, it is highly unlikely that such resolutions become attainable in the foreseeable future.

A general and better approach to studying these macroscopic phenomena is to develop reduced models where the essential ingredients of the small and fast scales are captured within a simplified system of equations. The derivation of these reduced models is based on approximations of various complexities:

- Considerations based on symmetries are used to derive amplitude equations capturing the essence of the transition occurring in large-scale flow patterns [47, 121, 51].
- Quasilinear approximations neglecting interactions between different degrees of freedom based on a scale-separation hypothesis have been effective in capturing some large-scale atmospheric features on Earth [3] or some details of the Jovian jets [16].

– Asymptotic expansions take advantage of small or large parameters in the problem (such as the scale separation between the waves and the mean flow among others) to reduce the primitive equations into simpler dynamical models [111]. Together with the quasilinear approach, they have been used extensively for wave-mean flow problems [92, 122, 5, 21, 28]. This thesis builds on this legacy.
– Other techniques consider the full complexity of the interactions between the different scales and numerous degrees of freedom of turbulent flows to use statistical approaches [16, 159]. In particular, the application of statistical mechanics has been successful in describing large-scale quasi-stationary structures such as Jupiter's great red spot [18]. In Chapter 6, we apply the same method to a problem of gravity wave and mean flow interaction.

The study of reduced models is useful for gaining an understanding of the macroscopic patterns and allows for more straightforward investigation of the different parameter regimes [32]. For example, properties inferred from simple models of ENSO have been traced up to quasi-realistic models [33]. However, the mechanisms highlighted in idealised models often fail to be recovered in models with higher complexity [71]. This issue occurred with the observation, in two-level atmospheric models, of a global circulation bifurcation towards regimes with a pro-grade zonal jet at the equator [153]. Nevertheless, the comparison between models of different complexities is an efficient approach to improve our understanding of complex macroscopic dynamics. In fact, the development of a hierarchy of models has been advocated for as a tool to bridge the gap between simple conceptual models and the actual climate system [72, 164]. Idealised models can be confronted with laboratory experiments, sometimes with remarkable success [149, 22, 134]. For a particular instance, Plumb & McEwan, in their now celebrated laboratory experiment [123], successfully reproduced the typical QBO winds reversals. They benefited from the models developed by Lindzen & Holton [92] and Plumb [122] who had identified the minimal ingredients. In addition, modelisation techniques developed to tackle geophysical problems have echoed beyond their primary field of application; such as Lorenz's strange attractor [94, 73] and stochastic resonance [38] among others.

Reduced models are also helpful in improving numerical climate models. Indeed, these models require truncating the dynamics of the smaller and faster scales. However, truncated dynamics fail to properly reproduce many important climate behaviours such as the meridional overturning circulation [125] or the quasi-biennial oscillation [95]. In order to truncate the small-scale dynamics but still keep their resulting effects on larger scales, parametrisations of the subgrid-scale processes are developed. In particular, the skill of climate change predictions hinges critically on the quality of the parametrisations used in climate models [151]. For instance, the development of Gent & McWilliam parametrisation of mesoscale eddy mixing in ocean numerical models [56] resulted in the first non-drifting control simulation in a climate model [55]. In order to develop these parametrisations, a good understanding of the underlying physical mechanisms - supported by the development of reduced models - is of preeminent importance.

1.2 Main objectives

In this thesis, we focus on the interaction between rapidly oscillating waves and slowly evolving mean flows in stratified fluids.

First, we investigate the recently observed periodicity disruption of the QBO on Earth [118] (with analogues on Saturn [48]) and attempt to assess whether **its variability is of external or intrinsic nature**. Revisiting a standard quasilinear asymptotic model, we show the existence of regimes with disrupted periodicity. When the wave amplitude is increased, the idealised model undergoes a series of bifurcations, first from periodic to quasiperiodic oscillations and then, for higher amplitudes, to frequency-locked and eventually chaotic regimes. We also employ the MIT GCM - a widely used general circulation model resolving the primitive equations [96] - to account for the full nonlinear dynamics of the waves. We show that the bifurcations persist in these direct numerical simulations. Although the geometry remains idealised and rotation is ignored, this suggests that reproducing periodicity disruption could be possible using more realistic model configurations.

Based on the phenomenon of critical slowing down associated with the existence of bifurcations [141], we show a possible enhancement of the variability triggered by external perturbation - such as the one observed for the 2016 disruption - in association with an intrinsic dynamical variability . **These first results, presented in Chapter 4**, shed new light on the origin of the QBO variability and is complementary to previous works focusing on the interaction with the extra-tropics [48, 29] or the seasonal cycle [126].

Next, we exploit an analogy between acoustic waves and internal gravity waves to study the generation of boundary flows by internal-waves viscous boundary-layers. The generation of mean flows by dissipated internal gravity waves is analogous to a phenomenon called acoustic streaming [41, 90, 132]. Then, the mean flow generation is supported by high-frequency acoustic waves damped by viscosity. In this context, acoustic viscous boundary layers have been shown to generate strong boundary flows, a phenomenon now referred to as **boundary streaming** [117].

In the case of internal gravity waves, boundaries are essential to their generation in the atmosphere, in the ocean [145, 9] and in experimental studies [123, 60, 147]. However, the role of viscous boundary layers on mean flow generation remains largely unexplored. **We contribute filling this gap by investigating the effect of the internal gravity waves boundary layers on the generation of mean flows.** Using a quasilinear approximation and asymptotic expansions, we show that mean flows are indeed generated within internal-wave viscous boundary-layers. We also demonstrate that the choice of boundary conditions strongly impacts the boundary flows, with a possible application to experimental analogues of QBO [123, 119]. **These results are presented in Chapter 5**.

Finally, we investigate the inviscid interaction between small-scale gravity waves and large-scale mean flow. Here, we extend the definition of inviscid to the absence of any dissipation. At a quasilinear level, the generation of mean flows by the gravity waves requires the presence of dissipative processes - the associated phenomena is called streaming in that case. In an inviscid context, this generation of mean flows is necessarily supported by high nonlinearities concomitant with the breaking of waves. Let us denote

this mean flow generation by inviscid streaming. Addressing precisely the highly nonlinear underlying processes with asymptotic expansion techniques is a very tedious task. **Leaving aside the details of the wave-mean flow interaction dynamics, we consider the simpler problem of the equilibrium outcome of the free evolution of a given initial state - say a pure gravity wave field - and investigate the spontaneous emergence of a large-scale mean flow.**

Ultimately, the fully nonlinear dynamics involves a huge number of degrees of freedom. To address such complexity, the tools of statistical mechanics are particularly powerful. The statistical mechanical approach allows predicting equilibrium macroscopic quantities such as large-scale flow patterns or local flow statistics, without describing the details of the microscopic dynamics, namely the inviscid streaming. Building upon previous applications to the 2D Euler and quasi-geostrophic models [109, 163, 18], we compute the statistical equilibria of the shallow-water model - the simplest model accounting for gravity-waves. In particular, we report the emergence of a large-scale flow in the presence of both system rotation and bottom topography and provide explicit computation for the equilibrium energy partition between the large-scale flow and gravity wave motions. **These results are presented in Chapter 6.**

1.3 Layout

The bulk of this thesis consists of five chapters:

- **Chapter 2** first acquaints the reader with two phenomena central to this thesis: internal gravity waves and wave streaming. Their generic properties are discussed and their importance in geophysical contexts reviewed.
- **Chapter 3** tackles the modelisation of internal gravity wave streaming based upon a two-dimensional zonally periodic geometry, specifically considering upward propagating waves generated from a bottom undulating boundary. After providing a review of the Boussinesq approximation, the wave and mean flow decomposition is defined based on zonal averaging and the coupled wave-mean flow dynamical equations are derived. Then, the quasilinear approximation is introduced. First considering the inviscid propagation of waves, we highlight the impossibility of a secular mean flow growth in this case. Incidentally, we introduce the geometrical optics approximation allowing for the resolution of the inhomogeneous linear problem of the propagation of internal gravity waves within a background shear flow. Next, we incorporate a dissipative process - a linear relaxation of the density variations modelling the atmospheric radiative cooling - and exhibit a steady mean flow growth. Finally, the coupled wave and mean flow dynamics is discussed focusing on the effect of critical layers.
- **Chapter 4** first reviews the quasi-biennial oscillation observation and phenomenology. Then, the standard one-dimensional model is introduced based on the discussion of Chapter 3. The bifurcation from the rest state towards the oscillating solution is addressed. Then, the existence of additional bifurcations towards disrupted periodicity regimes is presented together with an application to the recently observed disruption in the QBO signal. Afterwards, we wrap up about the perspectives of the presented results regarding the inclusion of the planetary rotation in the model.
- **Chapter 5** exploits the analogy with acoustic waves and uses the framework intro-

duced in Chapter 3 to show the emergence of a boundary flow driven by the viscous boundary layers of internal gravity waves.
– **Chapter 6** presents the results of the application of equilibrium statistical mechanics to the inviscid gravity wave and mean flow interaction problem.

In the conclusion, we summarise the main results of the thesis and discuss some perspectives regarding future works. A list of published and submitted scientific publications is provided. The different chapters are accompanied by three appendices providing details on some technical aspects.

2. Internal gravity waves and streaming

In this chapter, we introduce two physical phenomena that will play a central role in this thesis: **internal gravity waves** and **wave streaming**. Internal gravity waves are gravity driven waves - similar to surface waves - but propagating in the interior of stably stratified fluid. Ubiquitous in the geophysical context, these waves play an important role in the large-scale dynamics of the atmosphere and of the ocean as they transport and redistribute momentum and energy. **The momentum transport property of internal gravity waves is the main focus of this PhD thesis. More precisely, we study how momentum is transferred from the gravity wave field to slowly varying large-scale flows.** Momentum is released into the large-scale flow when the gravity waves are dissipated. The underlying processes can be highly nonlinear. **However, important conceptual understanding can be achieved by considering the quasilinear limit**, for which both wave propagation and wave damping are approximated as a linear process. In this regime, the associated acceleration of the mean flow is called streaming. This mechanism is well-known in the acoustics literature where it is referred to as acoustic (or Rayleigh) streaming. However, streaming is not as famous when it comes to internal gravity waves. The importance of internal gravity wave streaming was understood mostly with the discovery of the quasi-biennial oscillation in the 60s.

The purpose of this chapter is to provide a qualitative understanding of internal gravity waves streaming while reviewing the associated literature. Internal gravity waves are discussed in section 2.1 and wave streaming is addressed in section 2.2.

2.1 What are internal gravity waves?

In a fluid with density inhomogeneities, the downward gravitational force tends to bring the heavier fluid below the lighter fluid. At rest, the fluid satisfies the hydrostatic equilibrium associated with a stable density stratification. Then, the isopycnals (surfaces of constant density) are horizontal. Any small perturbation of the isopycnals from the horizontal will induce a buoyancy force opposing this perturbation. This buoyancy force, a combination of the direct gravitational force and pressure forces, is a conservative force acting as a spring resulting in the oscillation of the disturbances of equilibrium stably stratified state. These oscillations are called **internal gravity waves**. The term "internal" generally

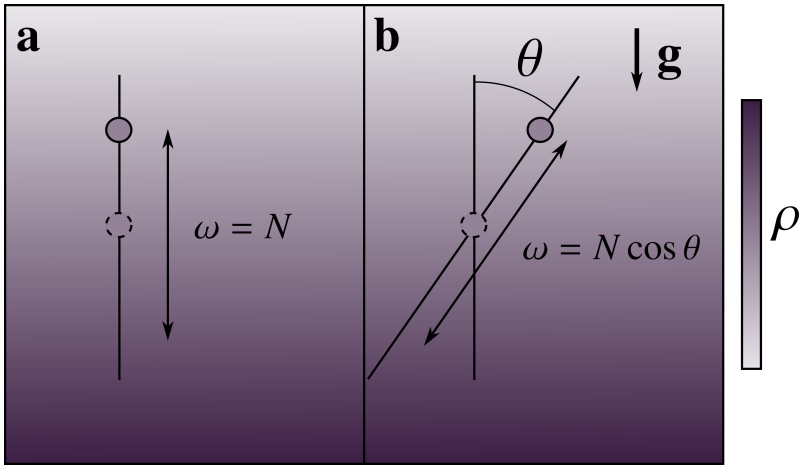

Figure 2.1: **Internal oscillation.** Sketch of a solid particle oscillating vertically (a) or along a slanted axis (b). The colourmap represents the continuous density stratification ρ: the darker the colour, the heavier the fluid. ω is the angular frequency of the oscillations. N is the buoyancy frequency defined in 2.5. $\mathbf{g}$ is the uniform gravitational field pointing downward.

refers to gravity waves propagating into a continuously stratified medium, as opposed to better-known surface-gravity waves associated with discontinuous stratification - such as an air/seawater interface.

In the subsection 2.1.1, we expose the basic mechanism at the origin of the internal gravity oscillations in a continuously stratified fluid. Then, in subsection 2.1.2, we discuss the peculiar propagation properties of internal gravity waves, as observed in laboratory experiments. In subsections 2.1.3 and 2.1.4, we review the importance of these waves in geophysical contexts.

2.1.1 Buoyancy frequency

Let us consider a stably stratified fluid within a uniform gravitational field pointing downward. Let us denote the density field associated with the state of rest $\rho_{\mathrm{bg}}(z)$ with z the upward vertical coordinate. To be stable, ρ_{bg} must be a decreasing function of z. The pressure field $P(z)$ obeys the hydrostatic equilibrium equation

$$\partial_z P(z) = -\rho_{\mathrm{bg}}(z)\, g \tag{2.1}$$

where g is the norm of the uniform gravitational field.

To exhibit the existence of an oscillating behaviour, let us consider an immersed solid particle with infinitesimal volume δV and mass δm such that it is located at a height z at rest. At rest, there is a balance between the gravitational force and the Archimedes force which is the force exerted on the particle by the surrounding hydrostatic pressure such that

$$\frac{\delta m}{\delta V} = \rho_{\mathrm{bg}}(z)\,. \tag{2.2}$$

Now raising or lowering the particle brings it into a lighter or a heavier region. The gravitational and Archimedes force are no longer balanced: their combination tends to

bring the particle back to its stable position z

$$\delta\mathbf{F} = \left(\rho_{\mathrm{bg}}(z+h) - \rho_{\mathrm{bg}}(z)\right)\delta V g\mathbf{e}_z \tag{2.3}$$

where h is the upward displacement to the resting value z.

Considering now the dynamics of the particle, we assume that the resulting motion affects little the surrounding density field such that it remains well-approximated by the background density field ρ_{bg}. Ignoring dissipation and considering small vertical displacement $|h| \ll 1$, the second law of Newton projected on the vertical direction gives at leading order

$$\ddot{h} - \frac{g}{\rho_{\mathrm{bg}}}\frac{\mathrm{d}\rho_{\mathrm{bg}}}{\mathrm{d}z}h = 0. \tag{2.4}$$

We recognise the equation of a harmonic oscillator in which the intrinsic angular frequency

$$N(z) = \sqrt{-\frac{g}{\rho_{\mathrm{bg}}}\frac{\mathrm{d}\rho_{\mathrm{bg}}}{\mathrm{d}z}}, \tag{2.5}$$

is called the **buoyancy frequency**, also known as the Brünt-Vaisälä frequency. In this case, the oscillations are purely vertical and are associated with the angular frequency N (see Fig. 2.1a). In the following, a **linear stratification** refers to stratification with constant buoyancy frequency N, i.e. independent of z.

Let us now constrain the particle to move along a tilted axis whose direction $\mathbf{n}$ makes an angle $-\pi/2 \leq \theta \leq \pi/2$ with the upward direction $\theta = (\widehat{\mathbf{e}_z, \mathbf{n}})$ (see Fig. 2.1b). Then, introducing l the displacement along $\mathbf{n}$ with $l = 0$ the resting position, the associated vertical displacement is $h = l\cos\theta$ and projecting the second law of Newton on the tilted axe gives in the limit of small displacement $|l| \ll 1$

$$\ddot{l} + (N\cos\theta)^2 l = 0. \tag{2.6}$$

Then, the tilted oscillations are associated with the angular frequency

$$\omega = N\cos\theta. \tag{2.7}$$

The particular relation between ω, N and θ in (2.7) carries important consequences leading to remarkable properties of internal gravity waves. Some of these properties are illustrated with experimental observations in the next subsection.

2.1.2 Internal gravity waves propagation

In this subsection, we present some eloquent laboratory observations of internal gravity waves[1]., allowing us to introduce some important properties of these waves.

In the previous subsection, we constrained a solid particle to oscillate along a tilted axis and obtained the oscillation's angular frequency (2.7). We consider here the reversed

[1]Most of the following pictures are borrowed from the PhD thesis [59] and scientific publications of Louis Gostiaux and collaborators, with LG's courtesy. The fluid considered is linearly stratified in salt and the field are acquired using either synthetic strioscopy or particle image velocimetry.

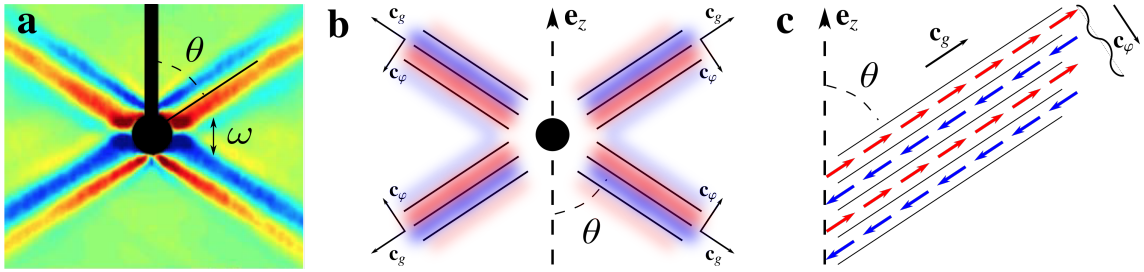

Figure 2.2: **Laboratory generation of internal gravity waves beams. a.** Colour map of a snapshot of the vertical velocity field associated with the internal gravity wave beams generated by a cylinder oscillating vertically at a fixed angular frequency ω in a linearly stratified fluid (borrowed from [59]). **b.** Schematic representation of the four beams observed on panel a, the directions of the group and phase velocities ($\mathbf{c}_g$ and $\mathbf{c}_\varphi$ resp.) associated with each beam are represented. **c.** Detailed scheme of an internal gravity wave beam propagating upward. The coloured arrows represent the direction of the local velocity.

problem with a linearly stratified medium excited at a fixed angular frequency $\omega < N$. Figure 2.2a shows a snapshot of the vertical velocity field associated with the monochromatic excitation of a linearly stratified fluid using a vertically oscillating cylinder. Four internal wave beams radiate away from the source with their direction of propagation making an angle θ with the upward direction satisfying $|\cos\theta| = \omega/N$. This pattern is known as the Saint Andrew's cross of internal gravity waves.

Figure 2.2b is a schematic representation of figure 2.2a in which the directions of the group velocities $\mathbf{c}_g$ and the phase speeds $\mathbf{c}_\varphi$ associated with each beam are represented. Strikingly, the phase speed and the group velocity are orthogonal: $\mathbf{c}_g \cdot \mathbf{c}_\varphi = 0$.

Figure 2.2c shows a detailed schematic of a beam: the velocity field within a beam shares the direction of the group velocity. The Lagrangian motions of the fluid parcels within the wave are therefore constrained to a tilted axis making an angle θ with the upward direction (see Fig. 2.2c). This makes the link with the Lagrangian view described in subsection 2.1.1.

In the experiment described by figure 2.2, the prescribed angular frequency ω of the beams constrains solely the direction of the phase speed $\mathbf{c}_\varphi = (\omega/\mathbf{k}^2)\mathbf{k}$ where $\mathbf{k} = k\mathbf{e}_x - m\mathbf{e}_z$ is the wave vector[2]. The dispersion relation of internal gravity waves thus writes

$$\omega^2 = N^2 \cos^2\theta = \frac{N^2 k^2}{k^2 + m^2}. \tag{2.8}$$

This relation, closely related to the one discussed in the previous subsection (see Eq. (2.7)), is explicitly derived in Chapter 3. There are indeed four solutions for the direction of $\mathbf{k}$ while its modulus is a free parameter. The associated group velocity $\mathbf{c}_g$ writes

$$\mathbf{c}_g = \partial_k \omega \mathbf{e}_x + \partial_m \omega \mathbf{e}_z = \frac{\omega m}{k\mathbf{k}^2}\mathbf{k}^\perp, \tag{2.9}$$

[2]We ignored the third component. Indeed, a wave vector can be brought back to a two-component wave vector by rotating the coordinate system with respect to the upward direction. The negative sign in front of the vertical component is unusual, but we will use this convention all along the thesis as it simplifies greatly some expressions.

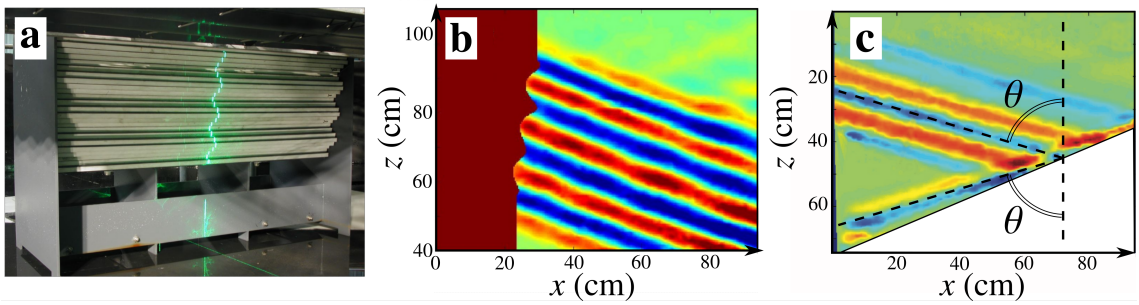

Figure 2.3: **Laboratory generation of internal gravity progressive waves beams. a.** Picture of the generator used to excite a selected internal gravity wave beam with an arbitrary number of wavelengths (borrowed from [59]). **b.** Colourmap of a snapshot of the vertical velocity field associated with the internal gravity wave beam generated by the apparatus showed on the panel **a** within a linearly stratified fluid. **c.** Colourmap of a snapshot of the vertical velocity field associated with the internal gravity wave beam propagating downward being reflected by a tilted boundary (extracted from [61]).

where $\mathbf{k}^{\perp} = m\mathbf{e}_x + k\mathbf{e}_z$. We recover the orthogonality between the phase speed $\mathbf{c}_\varphi$ and the group velocity $\mathbf{c}_g$. Setting the sign of k and m selects one propagation direction among the four possibilities.

The geometry of the cylindrical generator in figure 2.2 is such that the four wave-beams contain less than two wavelengths. Let us now consider an internal gravity beam containing more wavelengths. Figure 2.3a shows a picture of a different generator designed to produce progressive internal gravity beam with a chosen number of wavelengths [60]. Figure 2.3b shows a snapshot of the horizontal velocity component of the generated beam. The generator is set up vertically on the left and the undulated pattern is moving upward at a chosen velocity. The phase speed of the resulting wave beam has to be upward as well. Moreover, the wave beam is necessarily propagating to the right. We are thus left with the downward propagating branch (see Fig. 2.2b). The typical wavelength of the beam is set by the wavelength of the generator projected on the direction orthogonal to the direction of propagation.

The constraint on the angle of propagation is particularly remarkable when considering the reflection of an internal wave beam on a slanted wall. Figure 2.3c shows a snapshot of the vertical velocity field associated with such a reflection observed in laboratory [61]. This highlights the unintuitive reflection rules of internal gravity waves constrained by the dispersion relation (2.8).

An important additional observation is that internal gravity waves are transversal: the direction of the fluid parcels displacement and the phase speed are orthogonal[3] This comes from incompressibility of the flow associated with internal gravity waves, satisfying

$$\nabla \cdot \mathbf{u}' = 0 \tag{2.10}$$

where $\mathbf{u}'$ is the Eulerian velocity field associated with the wave field and $\nabla = (\partial_x, \partial_y, \partial_z)$.

[3]Here, we use the phase speed as reference to differentiate longitudinal waves from transversal waves. Another definition uses the group velocity as reference. With this latter definition, internal gravity waves are longitudinal. This ambiguity stems from the orthogonality of the group velocity and the wave vector.

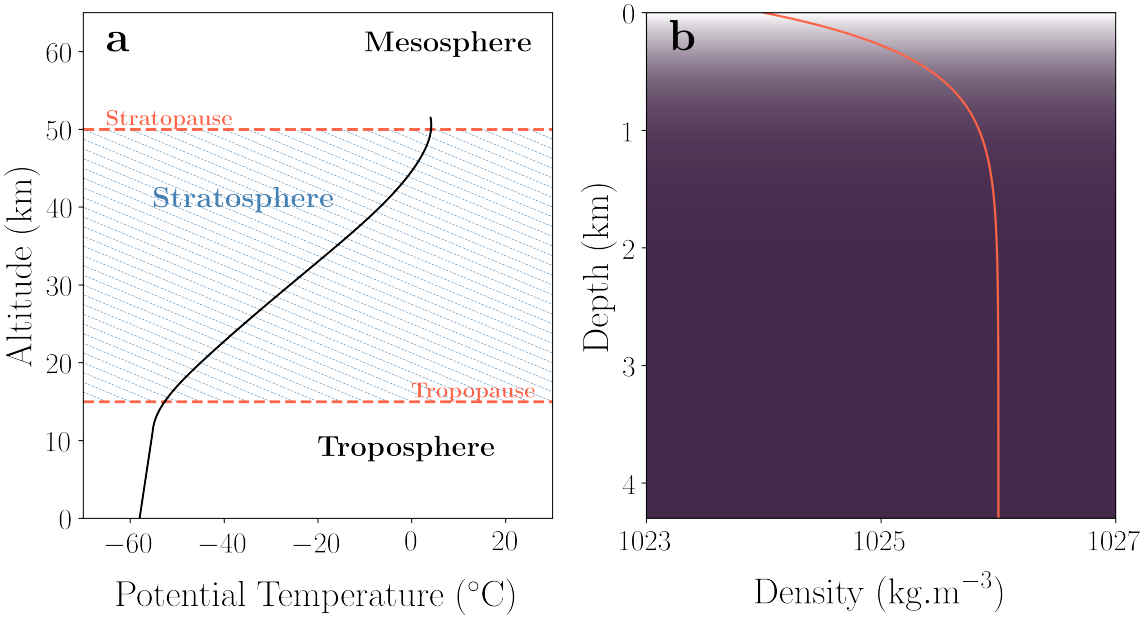

Figure 2.4: **Stratified fluid on Earth. a.** Sketch of the vertical potential temperature profile of the Earth's atmosphere. **b.** Sketch of the vertical density profile of the Earth's oceans

2.1.3 Internal gravity waves in geophysical flows

Internal gravity waves are ubiquitous in geophysical flows. Indeed, geophysical systems present numerous stratified fluid environments supporting the propagation of internal gravity waves.

In the Earth's atmosphere, the potential temperature vertical gradient controls the stability of a fluid parcel (see section 3.1). We show a sketch of the Earth's atmosphere potential temperature vertical profile in figure 2.4a. In the troposphere, i.e. the first 10 to 15 km above the ground, the potential temperature is slightly increasing with altitude resulting in a weakly stable layer where most of the meteorological phenomena, such as cloud convection, occur. Above the tropopause at roughly 15km at the equator (the height varies with the latitude), the potential temperature vertical gradient increases greatly resulting in a much more stable layer called the stratosphere where the internal gravity wave activity is important. The order of magnitude of the buoyancy frequency is typically $N \sim 10^{-2}\text{s}^{-1}$.

The Earth's oceans are stably stratified in density where the temperature and the salt concentration are the stratification agents. A sketch of the mean density vertical profile is shown in figure 2.4b. The density gradient is particularly strong close to the surface where the buoyancy frequency is of the order $N \sim 10^{-2}\text{s}^{-1}$ while in the abyss, the gradient is smaller with a buoyancy frequency of the order $N \sim 10^{-3}\text{s}^{-1}$.

In this PhD thesis, our geophysical applications concern mostly the oceans and the stratosphere, but other geophysical stratified media could be considered: for instance, the solar tachocline is a stably stratified transition layer between the external convective layer of the sun and its inner radiative core where internal gravity waves transport heat and might play a role for the solar dynamo [76]. The existence of a stably stratified layer in the Earth's liquid outer core is also argued [93].

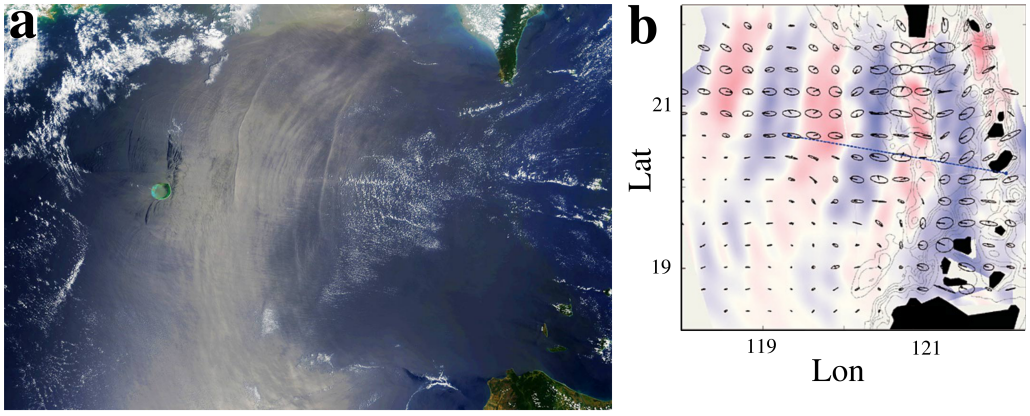

Figure 2.5: **Internal tide. a.** Satellite image of the Luzon Strait, located between Taiwan and the Philippines; internal waves create alternating rough and smooth regions of the ocean that align with the internal waves crests. Sunlight reflects the smooth sections, appearing as white arcs, while the rough sections stay dark. (Credit: NASA/GOA). **b.** Colourmap of the east-west velocity associated with an internal tide obtained in a large scale realistic laboratory experiment modelling the Luzon Strait [107].

In the ocean, internal gravity waves are typically generated by the tides moving water mass above the ocean bathymetry [9]. Figure 2.5 shows a satellite image of a surface signature of such internal tides successfully mimicked in a realistic large-scale experiment. In the stratosphere, internal gravity waves are generated mostly at the level of the tropopause by the turbulent convective motion of the troposphere [150]. They can also be generated by the wind impinging on topography. Then, they are called lee waves or orographic waves [145]. In figure 2.6, we show two remarkable instances of such lee waves in which the internal gravity wave pattern can be seen directly thanks to lenticular clouds formation. Internal gravity waves can also be generated in the wake of strong jets [134, 149].

On rotating planets, gravity waves are coupled with inertial modes leading to mixed inertia-gravity waves [161, 35]. The differential projection of the rotation axis between the equator and the poles leads to the existence of equatorial wave modes which are also coupled with gravity modes leading to mixed Rossby-gravity waves along with Kelvin and Yanai waves [100]. **In this thesis, we do not consider rotation and restrict ourselves to pure gravity waves. Taking into account the effect of rotation is one of the main perspectives of the presented work.**

2.1.4 Nonlinearities, mixing and transport

There has been increasing interest towards internal waves in the international scientific community over the past thirty years in direct relation to the limits currently reached by the resolution of oceanic and atmospheric models. The ocean and the atmosphere form a system with a very wide range of space and time scales in constant interaction. Internal gravity waves are rather at the end of the spectrum, such that the current resolutions of global numerical models fail to capture their dynamics satisfactorily. Yet, it appears that a significant amount of energy and momentum is transported by those waves across oceanic basins and the atmosphere. Consequently, the large-scale dynamics of the oceans and the atmosphere are deeply impacted by the existence of internal gravity waves. This

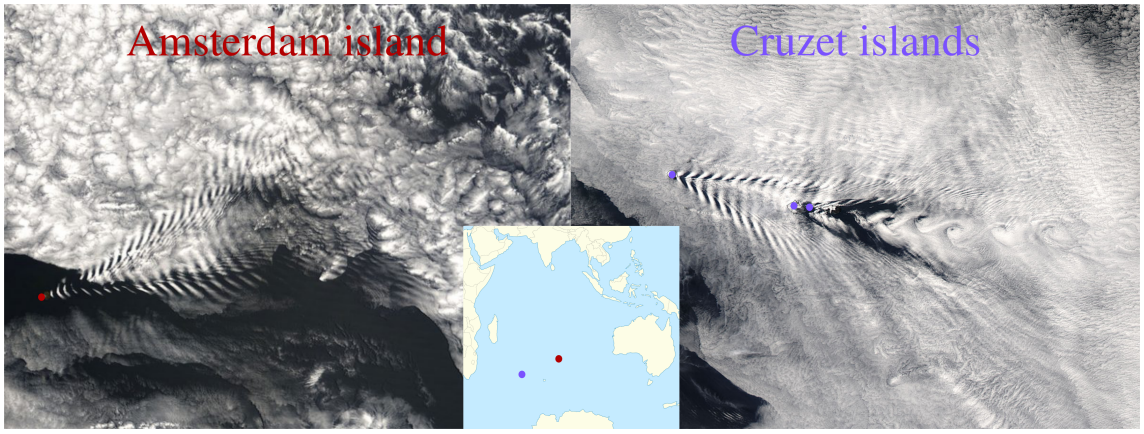

Figure 2.6: **Lee waves.** Picture of lenticular clouds forming a wavy pattern in the lee of the Amsterdam and the Cruzet islands in the Indian Ocean (credit: NASA†)
† Amsterdam: `earthobservatory.nasa.gov/IOTD/view.php?id=6151`
Cruzet: `visibleearth.nasa.gov/view.php?id=72267`

multi-scale interaction is necessarily governed by nonlinearities.

At a linear level, internal gravity waves can extract energy from their sources and propagate away. Linear dissipative processes may damp the waves during their propagation. In most of the geophysical contexts, the molecular viscosities are too small to have a sensible impact regarding the typical scales involved (roughly from 10 to 1000km in the atmosphere [53]). However, the effect of small-scale turbulence is often modelled by an eddy-viscosity several orders of magnitude higher than the molecular value [68, 69]. In the atmosphere, the stratification in potential temperature keeps relaxing to an equilibrium profile maintained by solar radiation. The characteristic timescale of this relaxation is of the order of 10 days which is low enough to impact gravity waves especially when mixed with equatorial modes.

When nonlinearities come into play, instabilities arise leading to the growth of secondary waves and eventually the breaking of the wave [30, 152]. This induces a strong local vertical mixing of the stratification; the vertical density gradients are smoothed out [120, 77]. This mixing impacts many other tracers such as aerosols or biogeochemicals whose vertical diffusion is enhanced [91]. The breaking of waves contributes to the turbulent diffusion and its associated eddy-diffusivity [54]. Likewise, the large-scale flows experience a high vertical eddy-viscosity induced partly by gravity wave breaking. In the ocean, the global contribution to mixing from internal gravity waves is predominant (see [83, 97, 98]). A fine understanding of the nonlinear gravity waves dynamics is therefore crucial to the oceans global energy budget.

Internal gravity waves transport also momentum extracted from the sources which is injected back into the large-scale flows at the breaking or damping locations [155]. This transport plays a major role in the atmospheric dynamics [74]. **The momentum transport property of internal gravity waves is our main interest in this PhD thesis; more precisely how momentum is transferred from the gravity wave field to slowly varying large-scale flows.** In geophysical contexts, the underlying processes can be highly nonlinear. **However, important conceptual understanding can be achieved by considering the quasilinear limit** when the internal gravity wave propagation and the damping processes are linear. In this regime, the associated acceleration of the mean flow

Frame 2.1.1 Internal gravity waves in a nutshell

Internal gravity waves are gravity-driven waves propagating in **stably stratified** fluids characterised by their intrinsic **buoyancy frequency**:

$$N = \sqrt{-\frac{g}{\rho_{\mathrm{bg}}}\frac{\mathrm{d}\rho_{\mathrm{bg}}}{\mathrm{d}z}}, \tag{2.11}$$

where g is the gravitational acceleration and ρ_{bg} is the hydrostatic density.

Monochromatic plane waves properties:

- Dispersion relation:

$$\omega^2 = N^2\cos^2\theta = \frac{N^2k^2}{k^2+m^2} \tag{2.12}$$

- Group velocity orthogonal to phase speed: $\mathbf{c}_g \cdot \mathbf{c}_\varphi = 0$
- Transversal waves: $\mathbf{u}' \cdot \mathbf{c}_\varphi = 0$

In geophysical contexts:

- They are ubiquitous in oceans and atmospheres which are stratified fluids
- They are generated by tides, large-scale flows passing over orography or tropospheric convection.
- They are key contributors to the oceanic mixing.
- They redistribute momentum in the atmosphere.

is called **streaming**.

2.2 What is wave streaming ?

Wave streaming corresponds to the emergence of a slowly evolving mean flow forced by an oscillating wave through nonlinear interactions. By "slowly evolving", we mean that **the timescale of the evolution is much larger than the wave period**. This phenomenon was first discovered and analysed in association with high-frequency acoustic waves damped by viscosity. Two remarkable examples of mean flows induced by acoustic waves are presented in figure 2.7. Such streaming is forced by the action of the Reynolds stress divergence associated with the acoustic waves [90]. The analogous phenomenon of gravity waves streaming was discovered much later with the observation of the quasi-biennial oscillation [75, 122, 5].

In fact, it turns out that the mean flow is little affected by the linear inviscid propagation of waves. The mean flow associated with an inviscid wave packet is located in its vicinity and reversibly vanishes once the wave packet has propagated away. In the geophysical fluid dynamics context, this physical mechanism is related to "non-acceleration" theorems that came up 50 years ago with important contributions from [24, 42, 5] among others. In those cases, dissipative effects are crucial for obtaining an "irreversible" growth of a mean flow. The dissipation may come either from linear or from nonlinear processes (i.e.

viscosity, radiative damping or wave breaking).

It is usual to decompose a flow between a mean flow part and a wave part. In the remaining of the thesis, we will often refer to the mean flow as the large-scale flow. Those flows are indeed associated with typically large space or timescales, or both. A well-known technique to separate the flow into a mean and a fluctuating part is the Eulerian mean decomposition presented in subsection 2.2.1. We also exhibit a mean flow forcing arising from the divergence of a Reynolds stress. Subsection 2.2.2 presents the historical observation of streaming by damped acoustic wave beams. Then, we move to the laboratory observation of streaming induced by a damped internal gravity wave beam in subsection 2.2.3. Subsection 2.2.4 discusses internal gravity wave streaming with zonal symmetry. Finally, in subsection 2.2.5, we will introduce and discuss the importance of critical layers in the geophysical context.

2.2.1 Eulerian wave and mean flow decomposition

A usual and natural way to isolate the part of flow associated with large-scale or long timescale is to average the different fields. We introduce an Eulerian averaging operator denoted by an overline. In practice, it can be either an average over a small length, a short timescale, or an ensemble average. Here, we consider averaging operators which commute with space and time derivatives. We decompose an Eulerian field ϕ into a mean part and a fluctuating part. Such a decomposition is called a Reynolds decomposition; it writes

$$\phi = \overline{\phi} + \phi' \quad \text{with} \quad \overline{\phi'} = 0. \tag{2.13}$$

For instance, ϕ can be a component of the Eulerian velocity field or the density field with $\overline{\phi}$ the mean part and ϕ' the fluctuation. The "Eulerian" denomination is used by the opposition to another approach called "Lagrangian mean" where the fields are averaged following fluid parcels [103]. The Lagrangian mean approach is powerful to investigate the reversible part of the mean flow. However, we are not interested here in the reversible part and focus on the irreversible growth of the mean flow. The Eulerian mean approach appears as a simpler and more natural framework to use in the present study.

The momentum conservation equations of fluids have the following general expression

$$\partial_t \Pi_i + \partial_j \left(\Pi_i u_j \right) = F_i, \tag{2.14}$$

where the index i or j represents the i-th or j-th component of the associated three-dimensional vector using implicit summation rule over repeated indices. $\mathbf{\Pi} = \rho \mathbf{u}$ is the volumic momentum of the fluid with ρ the density field and $\mathbf{u} = (u, v, w)$ the three-dimensional Eulerian velocity field. ∂_j is the derivative with respect to the j-th spatial coordinate. $\mathbf{F}$ is the sum of the volumic forces exerted on the fluid.

Performing the Reynolds decomposition (2.13) to $\mathbf{\Pi}$ and $\mathbf{u}$ and applying the Eulerian average to Eq. (2.14), we obtain an evolution equation for the mean momentum field $\overline{\mathbf{\Pi}}$

$$\partial_t \overline{\Pi}_i + \partial_j \left(\overline{\Pi}_i \overline{u}_j \right) = f_{s,i} + \overline{F}_i \tag{2.15}$$

with

$$f_{s,i} = -\partial_j \overline{\Pi'_i u'_j}. \tag{2.16}$$

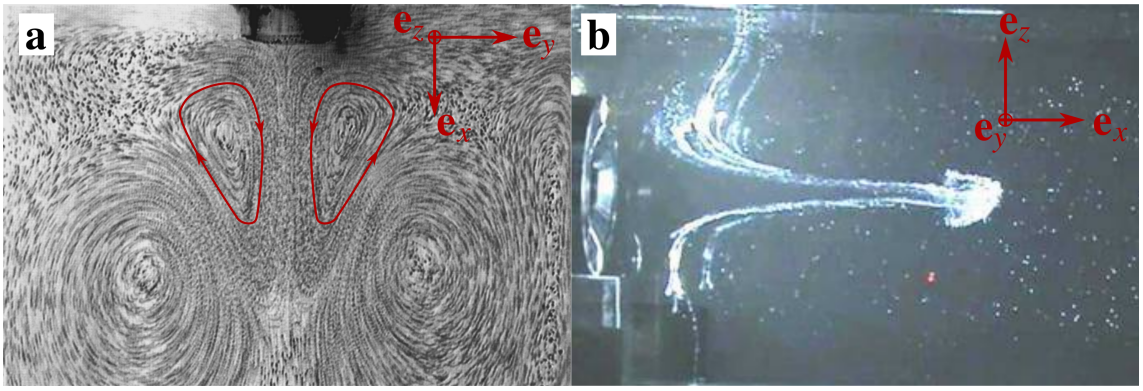

Figure 2.7: **Acoustic streaming.** Visualisation of the streaming or "quartz wind" associated with an ultrasound wave beam. **a.** Extracted from [116]. **b.** Extracted from [15].

Along with the mean forcing $\overline{\mathbf{F}}$, there is an additional forcing $\mathbf{f}_s$ on the right-hand side of (2.15) associated with the fluctuations. It involves the divergence of the Reynolds stress tensor defined by

$$R_{ij} = \overline{\Pi'_i u'_j}. \tag{2.17}$$

R_{ij} is simply the flux along the j-th direction of the i-th component of the fluctuations.

The Reynolds stress tensor is a fundamental concept to the dynamics of large-scale flows. Indeed, in coarse numerical models, the effect of the unresolved scales are often parametrised by using a closed expression for the Reynolds stress tensor [144, 106]. In the next subsections, we investigate the Reynolds stress associated with acoustic wave on a first hand and internal gravity waves on the second hand.

2.2.2 Observation of streaming by a damped acoustic wave beam

Historically, the study of wave streaming started with high-frequency acoustic waves. Acoustic waves are longitudinal waves whose group velocity, wave vector and fluid parcels displacement are collinear within a monochromatic progressive plane wave. Let us consider the case of a small amplitude acoustic wave beam propagating along $\mathbf{e}_x$. We assume that the transversal extent is much larger than the wavelength of the wave such that diffraction can be ignored. The viscosity damps the wave by folding exponentially the beam amplitude along the direction of propagation $\mathbf{e}_x$. Then, the velocity field associated with the wave beam can be expressed in the form

$$\mathbf{u}' = U(y,z)\sin(\omega t - kx)\, e^{-x/(2\Lambda)}\mathbf{e}_x \tag{2.18}$$

where ω is the angular frequency, k is the wave number, U is the transverse envelop of the beam and Λ is the e-folding length due to viscous damping. A similar expression is given in [172].

At the early stage of the mean flow evolution, the mean flow can be ignored against the wave such that the volumic momentum writes $\mathbf{\Pi}' = \rho_0 \mathbf{u}'$ at leading order with ρ_0 the background uniform density. Using the average over a period of the wave $2\pi/\omega$ and injecting the expression of the wave beam (2.18) into (2.16) gives

$$\mathbf{f}_s = \frac{\rho_0}{2\Lambda} U^2(y,z)\, e^{-x/\Lambda}\, \mathbf{e}_x. \tag{2.19}$$

This streaming body force is directed towards the direction of the propagation of the wave beam. The mean flow driven by this force appears clearly in figure 2.7b. The curl of the streaming force projected on the vertical axis $\mathbf{e}_z$ gives

$$(\nabla \times \mathbf{f}_s) \cdot \mathbf{e}_z = -\frac{\rho_0}{2\Lambda} \partial_y \left(U^2 (y,z) \right) e^{-x/\Lambda}. \tag{2.20}$$

Setting the origin of the y-axis at the center of the beam, we have $\partial_y \left(U^2 \right) < 0$ for $y > 0$ and $\partial_y \left(U^2 \right) > 0$ for $y < 0$. As a consequence, a dipolar vorticity structure is generated along with a horizontal jet going in the outward direction from the source. The dipolar structure appears clearly in figure 2.7a (the lower vortical structures are due to the finite geometry of the tank).

Eventually, the streaming body force is balanced by viscous stress leading to a steady mean flow which depends on the geometry of the flow domain [132]. We will not discuss these aspects any further here. Let us move to the case of a damped internal gravity wave beam.

2.2.3 Damped internal gravity wave beams

We now consider an internal gravity wave beam. Following the same idealised discussion as subsection 2.1.2, let us consider the case of a small amplitude internal gravity wave beam with angular frequency ω propagating towards the bottom right direction within a stratified fluid with buoyancy frequency $N > \omega$ (see figure 2.8a). The exact direction of propagation is constrained by the peculiar dispersion relation (see subsection 2.1.2). Ignoring again the diffraction, we model the effect of a viscous damping by an exponential folding of the beam amplitude along the tilted direction of propagation. We introduce the convenient orthonormal basis $(\mathbf{e}_\xi, \mathbf{e}_y, \mathbf{e}_\eta)$ associated with the coordinate (ξ, y, η). This is simply a rotation of the original basis (see figure 2.8a). Then, the velocity field associated with the wave beam writes

$$\mathbf{u}' = U (y,\eta) \sin (\omega t - \kappa \eta) e^{-2\xi/\Lambda} \mathbf{e}_\xi \tag{2.21}$$

where the wave vector writes $\mathbf{k} = \kappa \mathbf{e}_\eta$. A similar expression is provided in [14].

The relevant dynamical equations capturing the internal gravity waves dynamics are the Boussinesq equations (which shall be discussed in more details in the next chapter). In the Boussinesq system, the volumic momentum writes $\mathbf{\Pi}' = \rho_0 \mathbf{u}$ with ρ_0 the background uniform density. Using the average over a period of the wave $2\pi/\omega$ and injecting the expression of the wave beam (2.21) into (2.16) gives

$$\mathbf{f}_s = \frac{\rho_0}{2\Lambda} U^2 (y,\eta) e^{-\xi/\Lambda} \mathbf{e}_\xi. \tag{2.22}$$

This streaming body force, similar to the one associated with an acoustic beam (2.19), is also directed towards the direction of propagation of the wave beam. The component projected on the vertical direction will compete with the buoyancy restoring force by slightly bending the isopycnals and will have little effect on the mean flow. Only the horizontal component matters. Let us consider the curl of the force projected on the vertical axis. Coming back to the variable (x,y,z), we evaluate the result on the plane $z = 0$ (represented in light pink in the figure 2.8). It gives

$$(\nabla \times \mathbf{f}_s) \cdot \mathbf{e}_z|_{z=0} = -\frac{\rho_0}{2\Lambda} \partial_y \left(U^2 (y, x \sin\theta) \right) e^{-x\cos\theta/\Lambda} \cos\theta, \tag{2.23}$$

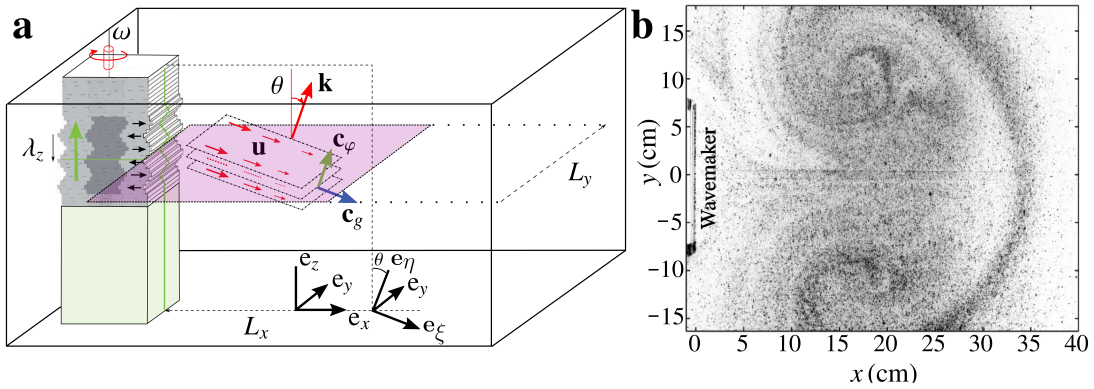

Figure 2.8: Generation of a strong mean vortical flow by an internal wave beam (extracted and transformed from [14]). **a.** Schematic representation of the experimental set up. **b.** Top view of the flow seeded with phosphorescent particles in the horizontal plane emphasised by the pink area in panel a.

where $\theta = (\widehat{\mathbf{e}_\xi, \mathbf{e}_x})$. Setting the origin of the y-axis at the center of the beam, we have again $\partial_y\left(U^2\right) < 0$ for $y > 0$ and $\partial_y\left(U^2\right) > 0$ for $y < 0$. A dipolar vorticity structure is generated associated with a horizontal jet going in the outward direction from the source. An observation of this dipolar structure is provided in figure 2.8b.

For additional references regarding streaming by beam structures of internal gravity waves see [79, 8]. We now move to a case with zonal symmetry.

2.2.4 Internal gravity wave streaming with zonal symmetry

We now consider the particular case of a monochromatic progressive plane internal gravity wave generated at the bottom of a 2D domain, periodic in the horizontal direction. This geometry is useful for comparison against the zonally periodic Earth's equatorial plane[4]. In the remaining of the thesis, the denomination "zonal" will be used when referring to the periodic horizontal direction. The progressive wave propagates upward and is damped by viscosity. The direction of propagation θ is set by the angular frequency $\omega < N$ (see figure 2.9a.). We model again viscous damping by a vertical exponential folding with characteristic damping length scale Λ. Then, the velocity field associated with the wave writes

$$\mathbf{u}' = U_0 \sin\left(\omega t - \kappa\left(x\sin\theta - m\cos\theta\right)\right) e^{-2z/\Lambda}\mathbf{e}_\xi \tag{2.24}$$

where the wave vector writes $\mathbf{k} = \kappa\mathbf{e}_\eta$ and $\theta = (\widehat{\mathbf{e}_\xi, \mathbf{e}_x})$ (see figure 2.9a).

We now consider the average over the zonal period of the wave $2\pi/(\kappa\cos\theta)$. Injecting the expression (2.24) into (2.16) gives

$$\mathbf{f}_s = \frac{\rho_0}{2\Lambda} U_0^2 e^{-z/\Lambda} \sin\theta \mathbf{e}_\xi . \tag{2.25}$$

This streaming body force is directed towards the direction of propagation of the wave beam. The vertical component is balanced by the pressure field such that only the horizontal

[4]Here we mean the plane passing through the equator by opposition to the tangent equatorial beta-plane.

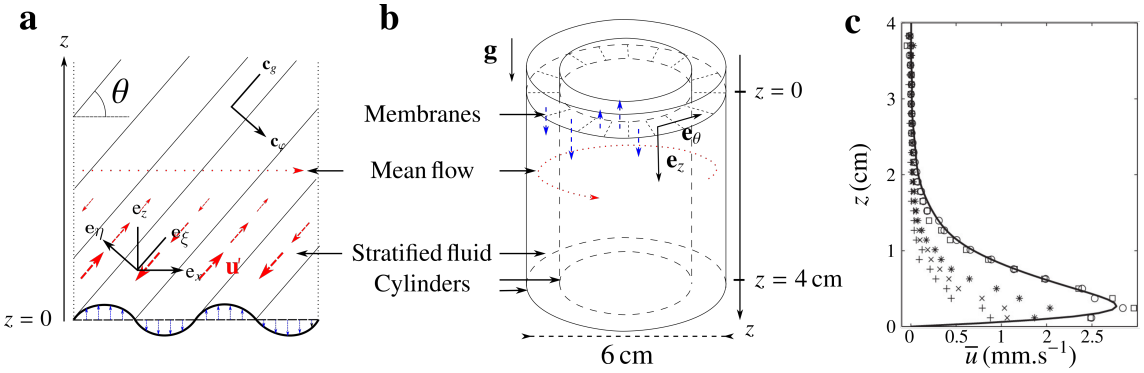

Figure 2.9: **a.** Sketch of a horizontally symmetric internal gravity plane wave propagating upward. **b,c** Horizontally symmetric mean flow generation by a progressive internal wave damped by viscosity and friction (extracted and adapted from [147]) with a schematic representation of the experimental set up (b) and a plot of mean flow vertical profiles taken at different times (c). The solid line corresponds to a theoretical prediction provided by [147].

projection produces a mean zonal flow

$$f_{s,x}(z) = \frac{\rho_0 \sin 2\theta}{4\Lambda} U_0^2 e^{-z/\Lambda}. \tag{2.26}$$

In figure 2.9b, we present the sketch of the experimental set up inspired by the seminal laboratory experiment of Plumb and McEwan [123] and used by [147] to investigate this type of streaming. The horizontal periodicity is achieved by considering an annulus tank of stratified fluid. The gravity wave is generated at the top, travels downward, guided into the periodic orthoradial direction by the lateral walls. The associated observed mean flow is shown in figure 2.9. This qualitatively corresponds to the expected mean flow generated by the zonal acceleration of the form (2.26) along with a no-slip condition at the generation height.

The results presented in this PhD thesis are all obtained in a zonally periodic domain. In Chapter 3, we provide a thorough discussion accompanied by detailed calculations regarding streaming with zonal symmetry.

2.2.5 Streaming in the geophysical context: the importance of critical layers

In the atmosphere and the ocean, the viscosity is small compared to the typical velocities and scales involved; the Reynolds numbers are high. The dissipation of internal gravity wave beams occurs mainly through nonlinear processes. This results in the growth of secondary waves which eventually leads to the breaking or overturning of the waves. These events are at play during the weakly nonlinear propagation of the wave beams within the oceans or the atmosphere. Their breaking can be prematurely provoked by critical reflections on continental shelves [61, 66] or by critical layers [21, 13, 158]. Critical layers are regions of the flow where the flow velocity is close to the horizontal phase speed of the wave[5]. Near critical layers, the direction of propagation of the waves becomes horizontal

[5]Her, we do not think of the horizontal phase speed as the projection of phase speed vector on the horizontal $\omega k/\mathbf{k}^2$ but rather as the scrolling speed of the wave pattern in the horizontal direction ω/k. Those two definitions are very much different.

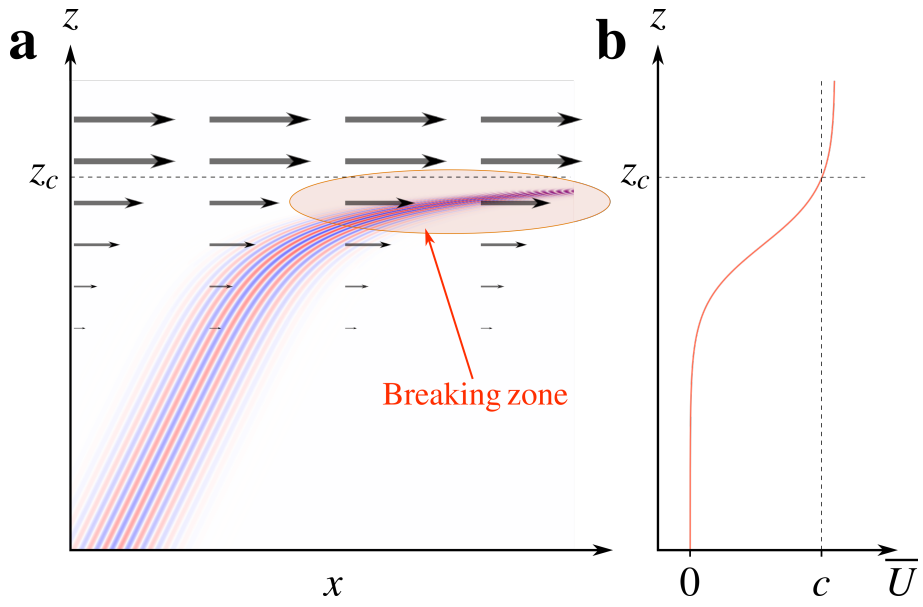

Figure 2.10: Sketch of the effect of a critical layers on a internal gravity wave beam. **a.** Snapshot of the horizontal velocity field associated with the wave beam. **b.** Vertical profile of the background mean flow $\overline{U}(z)$.

(see Fig. 2.10).

The frequency of the beam is Doppler-shifted by the mean flow. The local propagation direction of the wave beam is fixed accordingly through a modified dispersion relation

$$\hat{\omega}^2 = \left(\omega - \overline{U}(z)\,k\right)^2 = N^2 \cos^2\theta(z) \tag{2.27}$$

where $\hat{\omega}$ is the Doppler-shifted frequency and $\overline{U}$ is the background mean flow. It turns out that the direction of propagation of the waves directly controls their stability; the more horizontal the propagation the less stable the wave beam. This linearity criterion is discussed in details in Chapter 3. The flattening of the direction of propagation occurs when the mean flow is directed like the horizontal phase speed of the gravity waves.

In the atmosphere, large parts of the momentum transfer from waves to mean flows occur in critical layers. A striking geophysical phenomenon driven by these momentum transfers is the Earth's quasi-biennial oscillation or QBO. In the equatorial lower stratosphere, the zonal winds oscillate alternately from eastward to westward direction with a period of approximately 28 months. Figure 1.1c shows an *in situ* measurement of these reversals. The descending pattern of the mean zonal flow is characteristic of a phenomenon driven by waves propagating upward and shattering in critical layers. **The dynamics of the QBO will be addressed thoroughly in Chapter 5.**

2.3 Conclusion of Chapter 2

In this chapter, we qualitatively introduced internal gravity waves and wave streaming. The results presented in the remaining of the thesis concerns specifically the streaming generated by internal gravity waves propagating upward in a zonally periodic domain, as discussed in subsection 2.2.4. As we explained in subsection 2.2.5, in geophysical contexts, the streaming is driven by dissipation of internal gravity wave beams associated

Frame 2.2.1 Internal wave streaming in a nutshell

Wave streaming corresponds to the generation of a **slowly evolving mean flow** by the **damping** of **rapidly oscillating waves** propagating in fluids. This phenomenon is captured by the Reynolds averaged momentum equations

$$\partial_t \overline{\mathbf{u}} + (\overline{\mathbf{u}} \cdot \nabla)\, \overline{\mathbf{u}} = \mathbf{f}_s + \overline{\mathbf{F}}, \tag{2.28}$$

where

$$f_{s,i} = -\partial_j \overline{u'_j u'_i} \tag{2.29}$$

is the **streaming body force** corresponding to the **Reynolds stress divergence** of the **wave** velocity field $\mathbf{u}'$. This term arises from the averaging of the convective nonlinear term.

Historically observed in association with **damped acoustic waves**, this phenomenon is also engendered by the **damping of internal gravity waves.**

Internal gravity wave streaming in geophysical contexts:

- The damping of internal gravity waves comes mostly from nonlinear processes.
- The damping and, hence, the streaming is enhanced close to critical layers, where $\overline{u}k \to \omega$.
- The quasi-biennial oscillation of equatorial stratospheric zonal winds is a striking phenomenon powered by internal gravity wave streaming.

with highly nonlinear processes. Investigating wave streaming at a theoretical level using the fully nonlinear Navier-Stokes dynamical equation is tedious and may be even hopeless. However, as seen in subsection 2.2.1, streaming is essentially a matter of momentum conservation such that the details of the dissipation mechanisms do not change the qualitative understanding of the phenomenon.

In Chapter 3, we investigate the streaming in a quasilinear regime where the wave is dissipated by a linear process. It turns out that the highly nonlinear problem posed by critical layers are very well-captured in this framework.

3. Quasilinear streaming

This chapter's goal is to derive the main framework upon which our results regarding the quasi-biennial oscillation and internal wave boundary streaming are built (see Chapters 4 and 5). A detailed treatment of internal wave streaming with zonal symmetry is presented using a quasilinear model. The wave and mean flow decomposition is defined by means of Eulerian averaging. In passing, we resume some standard asymptotic expansion techniques such as the quasilinear approximation and the geometrical optics expansion. The quasilinear approximation amounts to neglect the wave-wave interactions. It allows for a comprehensive discussion of the interaction between the wave and the mean flow. The geometrical optics expansion is a powerful approach for explicitly computing waves propagating within an inhomogeneous medium.

We consider a two-dimensional domain with periodic boundary condition in the horizontal, or zonal direction. Upward-propagating internal gravity waves are generated by an undulating bottom boundary. This configuration, already discussed in subsection 2.2.4, is the bedrock of the results obtained in this chapter and in Chapters 4 and 5.

The following is largely inspired by Vallis' and Bülher's books [21, 161].

Outline of the chapter

In section 3.1, starting from the compressible Navier-Stokes equation, we present two approximations used in the geophysical context leading to the Boussinesq model. Section 3.2 introduces the wave and mean flow decomposition based on a zonal and fast time average along with the quasilinear approximation. In section 3.3, we discuss the inviscid quasilinear problem and show that there is no streaming in this case. We also provide a detailed geometrical optics calculation of a monochromatic progressive plane internal gravity wave propagating within a background shear flow. We accompany the calculations with discussions about the possible effect of nonlinearity and critical layers. In section 3.4, we consider the case of an internal gravity wave dissipated by a simple linear friction damping the density fluctuations. We describe the associated streaming. The mean flow growth close to critical layers is also discussed in details.

3.1 Dynamical framework

The goal of this section is to derive the Boussinesq equations which are the basis of the remaining sections. Considering the inviscid compressible Navier-Stokes equations, we will present two different approximations used in the oceanic and the atmospheric contexts both leading to the simpler Boussinesq equations. The dissipative processes are introduced afterward. Then, the equations are nondimensionalised and the corresponding dimensionless numbers presented.

We consider a two-dimensional domain with a Cartesian metric (the Earth's sphericity is ignored). A uniform gravitational field $\mathbf{g} = -g\mathbf{e}_z$ is considered with $\mathbf{e}_z$ pointing upward. We do not consider any rotation of the system. The inviscid momentum equation writes

$$\mathrm{D}_t\mathbf{u} = -\nabla P - \rho\mathbf{e}_z \tag{3.1}$$

where $\mathbf{u} = (u,w)$ is the two-dimensional velocity field, P is the pressure field and ρ is the density field. The operator $\rho\mathrm{D}_t = \partial_t + \mathbf{u}\cdot\nabla$ is the material derivative and $\nabla = (\partial_x, \partial_z)$ is the gradient operator. The inviscid mass conservation equation writes

$$\partial_t\rho + \nabla\cdot(\rho\mathbf{u}) = 0. \tag{3.2}$$

Finally, the fluid is at a local thermodynamical equilibrium and satisfies an equation of state

$$\rho = \rho\,(P,T) \tag{3.3}$$

where T is the temperature field. To close the system of equations, an additional thermodynamical equation is required. In the inviscid problem, there is no thermal diffusion such that the temperature is passively advected by the flow

$$\mathrm{D}_t T = 0. \tag{3.4}$$

Additional stratification agents can be relevant, such as salinity for the oceanic context or for laboratory experiments. Here, however, we ignore the diffusion of these agents. Their effect is thus concomitant with the temperature[1].

Outline of the section

In subsections 3.1.1 and 3.1.2, we introduce the Boussinesq and the Anelastic approximation to turn the dynamical equations (3.1), (3.2), (3.3) and (3.4) into a simplified set of dynamical equations which will be adequate for the study of the internal gravity waves and their interaction with a large scale flow. In subsection 3.1.3, we introduce the buoyancy frequency and the buoyancy anomaly. In subsection 3.1.4, we introduce the dissipative processes considered in this thesis. In subsection 3.1.5, we precisely defined the domain geometry with the associated boundary conditions. Finally, in subsection 3.1.6, the problem is nondimensionalised, and the corresponding dimensionless numbers are presented.

[1] In the diffusive problem, the difference between the diffusion coefficients of salt and temperature can lead to interesting phenomena such as double diffusion convection[143].

3.1.1 Boussinesq approximation

In the ocean, the dynamical equations are greatly simplified with the Boussinesq approximation. This approximation relies on the typically weak density variations of seawater.

To start with, let us consider the equation of state (3.3) which expresses the density as function of the temperature and pressure

$$\rho\left(T,P\right)=0. \tag{3.5}$$

We now assume weak density fluctuations compared to a reference constant density value ρ_0. A first step consists in linearising the equation of state

$$\rho\approx\rho_0\left(1-\alpha_T\left(T-T_0\right)+\frac{1}{\rho_0 c_s^2}\left(P-P_0\right)\right), \tag{3.6}$$

where α_T is the thermal expansion coefficient and c_s is the phase speed of sound waves.

In the ocean, $\alpha_T\sim\times10^{-4}K^{-1}$, $T-T_0\sim10K$ and $c_s=1500m.s^{-1}$. The typical pressure variation is given by the characteristic hydrostatic pressure $\rho_0 gH$ (with $g\sim10m.s^{-2}$ the gravitational acceleration and $H\sim10km$ the order of magnitude of the Ocean depth). The typical density variation is thus of the order of 5%[2]. This allows assuming $\left|(\rho-\rho_0)/\rho_0\right|\ll1$.

We decompose the density into its uniform reference value ρ_0 and the deviation $\delta\rho\left(\mathbf{x},t\right)$. We also introduce the shifted pressure $\delta p=P-p_0$ with $p_0=P_0-\rho_0 gz$. The fluid's inviscid momentum equation (3.1) writes without approximation

$$\left(\rho_0+\delta\rho\right)\mathrm{D}_t\mathbf{u}=-\nabla\delta p-\delta\rho g\mathbf{e}_z. \tag{3.7}$$

The Boussinesq approximation consists in neglecting the $\delta\rho$ term against ρ_0 in the left-hand side of (3.7). The term $\delta\rho g$ should not be neglected here. It is central to the propagation of internal gravity waves. Then, the inviscid momentum equation writes

$$\mathrm{D}_t\mathbf{u}=-\nabla\Phi+B\mathbf{e}_z, \tag{3.8}$$

where $\Phi=\delta p/\rho_0$ is the pressure potential. $B=-\delta\rho/\rho_0$ is the fluid's buoyancy whose dependence in the thermodynamical variables is approximated by the linearised equation of state

$$B=-\alpha_T\left(T-T_0\right)+\frac{\Phi-gz}{c_s^2}. \tag{3.9}$$

Without approximation, the mass conservation equation (3.2) writes

$$\mathrm{D}_t\delta\rho+\left(\rho_0+\delta\rho\right)\nabla\cdot\mathbf{u}=0. \tag{3.10}$$

In the Boussinesq approximation, the mass conservation (3.2) leads to the incompressibility of the flow at leading order

$$\nabla\cdot\mathbf{u}=0. \tag{3.11}$$

[2]Taking into account the salinity does not change this estimate.

The dynamics of the buoyancy field is associated with the conservation of the thermodynamical fields (3.4). Using the incompressibility of the flow (3.11), we have without further approximation

$$\mathrm{D}_t B = \frac{1}{c_s^2}\mathrm{D}_t\left(\Phi - gz\right). \tag{3.12}$$

The final approximation of the Boussinesq model is to neglect the right-hand side of (3.12) leading to

$$\mathrm{D}_t B = 0. \tag{3.13}$$

The set of equations composed of (3.8), (3.11) and (3.13) forms the inviscid Boussinesq model.

In the atmosphere, the employment of the Boussinesq model is justified by a different approximation called the anelastic approximation.

3.1.2 Anelastic approximation

In contrast to the ocean, the atmosphere density varies significantly on the vertical. The Boussinesq approximation is not applicable in this context. However, the dynamical equations are greatly simplified by the anelastic approximation. This approximation relies on the typically weak local density variations with respect to the height-dependent background density.

Considering the atmosphere as an ideal gas, we introduce an additional thermodynamical variable, the potential temperature

$$\Theta = \frac{p^{c_v/c_p}}{\rho}, \tag{3.14}$$

where c_v and c_p are the constant volume and constant pressure heat capacity of air. It turns out that the potential temperature varies little over the atmosphere's height. Therefore, a relevant reference background state is a state of constant potential temperature Θ_0 with $\partial_z\Theta_0 = 0$.

Let us decompose the density, the pressure and the potential temperature fields into a purely z-dependent background state and a deviation

$$\begin{cases} \rho\left(\mathbf{x},t\right) = \rho_0\left(z\right) + \delta\rho\left(\mathbf{x},t\right) & \text{with } \left|\delta\rho/\rho_0\right| \ll 1 \\ P\left(\mathbf{x},t\right) = p_0\left(z\right) + \delta p\left(\mathbf{x},t\right) & \text{with } \partial_z p_0 = \rho_0 g \text{ and } \left|\delta p/p_0\right| \ll 1 \\ \Theta\left(\mathbf{x},t\right) = \Theta_0 + \delta\Theta\left(\mathbf{x},t\right) & \text{with } \left|\delta\Theta/\Theta_0\right| \ll 1 \text{ and } \Theta_0 = \frac{p_0^{c_v/c_p}(z)}{\rho_0} \end{cases}. \tag{3.15}$$

A relation between the different deviation fields $\delta\rho$, δp and $\delta\Theta$ is provided by the linearisation of Eq. (3.14)

$$\frac{\delta\Theta}{\Theta_0} = \frac{c_v}{c_p}\frac{\delta p}{p_0} - \frac{\delta\rho}{\rho_0}. \tag{3.16}$$

The anelastic approximation consists in neglecting $\delta\rho$ against ρ_0 in the left-hand side of (3.7), however this time $\rho_0(z)$ cannot be absorbed in the pressure field. Introducing the pressure potential $\Phi = \delta p/p_0(z)$, we obtain

$$\mathrm{D}_t\mathbf{u} = -\nabla\Phi - \left(\frac{\delta p}{\rho_0^2}\partial_z\rho_0 + \frac{\delta\rho}{\rho_0}g\right)\mathbf{e}_z. \tag{3.17}$$

Using Eq. (3.16) to replace $\delta\rho$ in (3.17) and using the choice of a constant reference potential temperature leads to the simplified equation

$$\mathrm{D}_t\mathbf{u} = -\nabla\Phi + B\mathbf{e}_z. \tag{3.18}$$

The buoyancy field $B = -g\delta\Theta/\Theta_0$ is now defined by the potential temperature rather than the density.

The anelastic approximation gives a different leading order equation for the mass conservation (3.2)

$$\nabla\cdot(\rho_0(z)\,\mathbf{u}) = 0. \tag{3.19}$$

However, the phenomena considered in this thesis typically involve small variation length scales for the upward velocity w [53]. We thus further neglect $w\partial_z\rho_0$ against $\rho_0\partial_z w$ and recover the incompressibility condition of the Boussinesq model

$$\nabla\cdot\mathbf{u} = 0. \tag{3.20}$$

The equation for B is directly related to the Lagrangian conservation of the potential temperature

$$\mathrm{D}_t B = 0. \tag{3.21}$$

The set of equations (3.18), (3.20) and (3.21) forms the inviscid Boussinesq model in the atmospheric context, this time with a buoyancy defined in terms of the potential temperature.

3.1.3 Buoyancy frequency

Let us consider the background buoyancy field B_{bg} associated with the stratification in density for the ocean or potential temperature for the stratosphere (see figures 2.4). The background buoyancy is an increasing function of z. The local buoyancy frequency, previously introduced in Eq. (2.5), writes

$$N^2(z) = \partial_z B_{bg}(z)\,, \tag{3.22}$$

where N is positive. We now introduce the buoyancy anomaly

$$b = B - B_{bg}, \tag{3.23}$$

and the associated pressure potential anomaly

$$\phi = \Phi + \int_0^z B_{bg}. \tag{3.24}$$

The momentum equation (3.18) and the buoyancy equation (3.21) can be rewritten in terms of b

$$\begin{cases} \mathrm{D}_t \mathbf{u} & = -\nabla\phi + b\mathbf{e}_z \\ \mathrm{D}_t b + N^2 w & = 0 \end{cases}. \tag{3.25}$$

In general, the buoyancy frequency varies on the vertical. For instance, the buoyancy gradients are about ten times greater in the thermocline of the oceans than in the abyss. As a consequence, internal gravity waves travelling upward from the abyss can destabilise and break once they encounter the thermocline. As mentioned in subsection 2.2.5, the background flow also influences the propagation properties of internal gravity waves. **In this thesis, we focus on the effects of the background flow rather than the vertically varying stratification. For sake of simplicity, we thus consider the buoyancy frequency N to be a constant in the remaining of the thesis.**

3.1.4 Dissipative processes: viscosity and radiative cooling

As explained in section 3.2, dissipative processes are crucial to streaming which requires the damping of waves. In this thesis, we consider two dissipative processes.

First, we take into account the viscous effect associated with the diffusion of momentum. The momentum equation in (3.25) is modified accordingly

$$\mathrm{D}_t \mathbf{u} = -\nabla\phi + b\mathbf{e}_z + \nu\Delta\mathbf{u}, \tag{3.26}$$

where ν is the kinematic viscosity and $\Delta = \partial_x^2 + \partial_z^2$ is the Laplacian operator. To account for turbulent diffusion, the typical viscosities considered in this thesis can be several orders of magnitude higher than the molecular value of air or seawater. Viscosity has an important role for the dynamics of both the wave and the mean flow and is discussed in details in chapters 4 and 5.

We consider an additional linear dissipative process restoring the linear background stratification at a rate γ which is thought to be a model for the radiative cooling of the stratosphere (see discussion in section 2.2). The buoyancy equation in (3.25) now writes

$$\mathrm{D}_t b + N^2 w = -\gamma b. \tag{3.27}$$

To be consistent, an eddy-diffusivity should be considered for the temperature field together with the eddy-viscosity. In the atmosphere, the radiative cooling is dominant. In the ocean or in laboratory, however, the mixing is important. Nevertheless, for sake of simplicity, buoyancy diffusion is ignored in the remaining.

3.1.5 Domain geometry and boundary conditions

The domain $\mathcal{D}$ is Cartesian and two-dimensional. We consider periodic boundary condition in the zonal x-direction with length L. The term "zonal" refers here to the eastward or westward direction on Earth which is periodic with $L = 40\,000\,\mathrm{km}$ at the equator. A solid boundary is considered at the bottom of the domain located at

$$z = h_b(x,t), \tag{3.28}$$

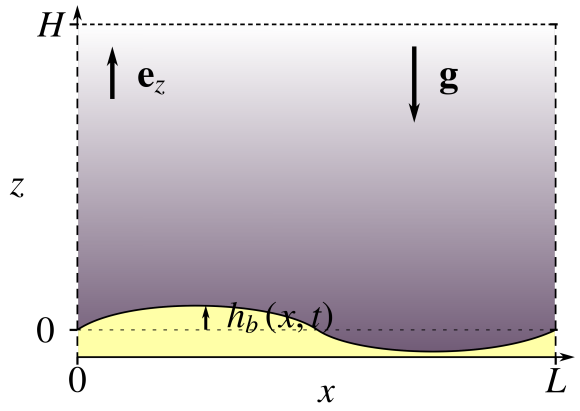

Figure 3.1: Sketch of the two-dimensional periodic domain with a bottom oscillating boundary with equation $z = h_b(x,t)$.

with $\int_0^L h_b(x,t)\mathrm{d}x = 0$ (see 3.1). This boundary mimics the tropopause height variations (see Fig. 4.3) or the membrane displacements in experimental setups [122, 119, 147] (see Fig. 2.9b). A local normal vector of the boundary is given by $\nabla(z - h_b(x,t))$. Let us note $\mathbf{u}_b = (u_b, w_b)$ the velocity of a point located at $(x, z = h_b)$ moving with the boundary. By differentiating Eq. (3.28) following a point moving with the boundary, we obtain the following property for $\mathbf{u}_b$

$$w_b = \partial_t h_b + u_b \partial_x h_b. \tag{3.29}$$

In the inviscid case, the impermeability condition states that the velocity $\mathbf{u}_b$ of a point moving with the boundary and the velocity $\mathbf{u}|_{z=h_b}$ of the same point but moving with the fluid must have the same projection on the local normal direction to the boundary. Using the property (3.29), it gives

$$\left(\mathbf{u}|_{z=h_b} - \mathbf{u}_b\right) \cdot \nabla(z - h_b) = 0 \quad \Longrightarrow \quad \mathrm{D}_t(z - h_b)|_{z=h_b} = 0. \tag{3.30}$$

In the viscous case, we consider a no-slip condition stating that the velocity of the fluid relative to the boundary must be zero. It simply writes

$$\mathbf{u}|_{z=h_b} = \mathbf{u}_b, \tag{3.31}$$

where $\mathbf{u}_b$ is the boundaries' velocity. When considering the viscous case, we always consider that the boundary's motion is purely vertical with $u_b = 0$ such that $w_b = \partial_t h_b$. Then, the no-slip boundary condition adds the following constraint

$$u|_{z=h_b} = 0. \tag{3.32}$$

This no-slip boundary condition is relevant for the experimental setup shown in figure 2.9b. However, it is debatable in application to the tropopause. Nevertheless, a no-slip condition is often considered in idealised model of the stratosphere coupled to an undulating tropopause [75, 122, 126, 28]. For some instances, free-slip condition will be considered and discussed in Chapter 5 and in appendix B.

We consider the domain to be semi-infinite without upper boundary such that the internal gravity waves propagating upward will never be reflected. However, for the numerical resolutions of the dynamical equations, we consider an upper flat boundary at $z = H$. Then, we consider an impermeability condition in the inviscid scenario, with $w|_{z=H} = 0$, and an additional free-slip condition in the viscous scenario, with $\partial_z u|_{z=H} = 0$.

3.1.6 Nondimensionalised Equations and dimensionless numbers

Here, we nondimensionalise the Boussinesq dynamical equations (3.26), (3.27) and (3.20) and introduce the associated dimensionless numbers. To nondimensionalise the equations, reference length and time scales are required. In this PhD thesis, we use the scales of the wave as references.

Let us introduce Ω and K the characteristic angular frequency and zonal wave number of the wave field, respectively. We consider Ω^{-1} and K^{-1} for the reference space and time scale. This choice is arbitrary here but will turn out useful to compute asymptotic expressions for the wave field. We construct the characteristic velocity, buoyancy and pressure field using combinations of K and Ω leading to the associated dimensionality. We thus consider $U = \Omega K^{-1}$ as reference velocity, $\Omega^2 K^{-1}$ as reference buoyancy anomaly and $\Omega^2 K^{-2}$ as reference pressure potential.

The resulting nondimensionalised dynamical equations write

$$\begin{cases} \mathrm{D}_t \mathbf{u} & = -\nabla\phi + b\mathbf{e}_z + \mathrm{Re}^{-1}\Delta\mathbf{u} \\ \mathrm{D}_t b + \mathrm{Fr}^{-2} w & = -\Gamma b \\ \nabla\cdot\mathbf{u} & = 0 \end{cases}, \tag{3.33}$$

where

$$\mathrm{Re} = \frac{\Omega}{\nu K^2} = \frac{U}{\nu K}, \tag{3.34}$$

is the wave Reynolds number,

$$\mathrm{Fr} = \frac{\Omega}{N} = \frac{UK}{N} \tag{3.35}$$

is the wave Froude number and $\Gamma = \gamma\Omega^{-1}$ will be referred to as the nondimensionalised cooling rate. These definitions of the Reynolds and Froude numbers are more natural in the context of lee wave generation, where U is the characteristic velocity of the background flow passing over a static topographic undulation with characteristic wave number K. However, in this context, the correct definition of the Froude number is still in debate [101]. We consider K^{-1} as reference bottom undulation, such that the boundary conditions (3.30) and (3.31) keep the same expression in nondimensionalised form.

A summary of the Boussinesq equations is provided in frame 3.1.1.

3.2 Wave and mean flow decomposition and quasilinear dynamics

In this section, following Bühler's book [21], we define a mean flow based on zonal and fast-time averaging. After deriving the coupled wave and mean flow coupled dynamical equations, we introduce the quasilinear approximation: the dynamical equations for the wave part of the flow is linearised. This framework will be the starting point for most of the analytical results and discussions regarding wave streaming.

Frame 3.1.1 The nondimensionalised Boussinesq model

The Boussinesq model is at the foundation of the results presented in the remaining of Chapter 3 and in chapters 4 and 5. The considered geometry consists in a two-dimensional zonally periodic domain with an undulating bottom boundary. We provide here a summary of the main equations in the nondimensionalised form. The terms in red are ignored when considering the inviscid problem.

- Dynamical equation

$$\begin{cases} \text{Momentum equation} & \mathrm{D}_t\mathbf{u} = -\nabla\phi + b\mathbf{e}_z + \mathrm{Re}^{-1}\Delta\mathbf{u} & (3.36a) \\ \text{Buoyancy equation} & \mathrm{D}_t b + \mathrm{Fr}^{-2} w = -\Gamma b & (3.36b) \\ \text{Mass conservation} & \nabla\cdot\mathbf{u} = 0 & (3.36c) \end{cases}$$

- Boundary conditions

$$\text{With } z = h_b(x,t), \begin{cases} \text{Impermeability condition} & D_t\left(z - h_b\right) = 0 & (3.37a) \\ \text{No-slip condition} & u = 0 & (3.37b) \end{cases}$$

- Dimensionless numbers

$$\begin{cases} \text{Froude number} & \mathrm{Fr} = \Omega/N & (3.38a) \\ \text{Wave Reynolds number} & \mathrm{Re} = \Omega/(\nu K^2) & (3.38b) \\ \text{Nondimensionalised cooling rate} & \Gamma = \gamma/\Omega & (3.38c) \end{cases}$$

3.2.1 Zonally periodic wave and mean flow decomposition

Taking advantage of zonal periodicity, we decompose the Eulerian fields into mean and fluctuation parts using a zonal average combined with a fast time average

$$\overline{\phi}\left(z,t\right) = \frac{1}{(2\pi)^2}\int_{t-\pi}^{t+\pi} \mathrm{d}t' \int_0^{2\pi} \mathrm{d}x\, \phi\left(x,z,t'\right) \quad \text{and} \quad \phi'\left(x,z,t\right) = \phi\left(x,z,t\right) - \overline{\phi}\left(z,t\right), \tag{3.39}$$

where $\phi\left(x,z,t\right)$ can be any field, $\overline{\phi}$ is the mean part and ϕ' the fluctuation. We define the mean flow as the part of the flow characterised by the mean fields $\left(\overline{u},\overline{w},\overline{b},\overline{p}\right)$ and the wave as the part of the flow characterised by the associated fluctuations $\left(u',w',b',\phi'\right)$.

When considering isolated progressive waves, the zonal and fast time averages are concomitant. However, it will be useful when we will consider more than one progressive wave in chapters 4 and 5.

3.2.2 Joint Dynamical Equations

In this subsection, we derive the nonlinear coupled dynamical equation for the mean flow and the wave.

Mean Flow Equations

Horizontally averaging the continuity equation (3.36c) gives $\partial_z\overline{w} = 0$. Integrating this gives a z-independent vertical velocity $\overline{w}(t)$. In 2D model of the equatorial plan, it can be

prescribed to account for tropical upwelling [126]. In this thesis, we ignore any global upward or downward motion of the flow and simply consider $\overline{w} = 0$.

The averaging of the vertical projection of the momentum equation (3.36a) gives the hydrostatic equation for the mean pressure

$$\partial_z \overline{\phi} = \overline{b} - \partial_z \overline{w'^2}. \tag{3.40}$$

The vertical projection of the Reynolds stress divergence $\partial_z \overline{w'^2}$ plays a marginal role as it simply results in a second order change in the hydrostatic pressure.

The averaging of the horizontal projection of the momentum equation (3.36a) gives the mean flow evolution equation

$$\partial_t \overline{u} = -\partial_z \overline{u'w'} + \mathrm{Re}^{-1} \partial_z^2 \overline{u}\,. \tag{3.41}$$

The mean flow evolution depends on the vertical divergence of the Reynolds stress component $\overline{u'w'}$ which will be also referred to as upward momentum flux. **The mean flow equation (3.41) will be at the core of the discussion all along this PhD thesis.**

The averaging of the buoyancy equation (3.36b) gives the evolution equation for the mean buoyancy

$$\partial_t \overline{b} = -\partial_z \overline{w'b'} - \Gamma \overline{b}. \tag{3.42}$$

The mean buoyancy evolution depends on the vertical divergence of the mean wave upward buoyancy flux $\overline{b'w'}$. However, this equation have little interest in the context of this thesis (see subsection 3.2.5).

Wave Equations

By subtracting the mean flow equations to the dynamical equations in (3.36), we obtain the wave evolution equations

$$\begin{cases} \overline{\mathrm{D}}_t u' + w' \partial_z \overline{u} & = -\partial_x \phi' + \mathrm{Re}^{-1} \Delta u' + \mathcal{B}\left(\mathbf{u}', u'\right) & \text{(3.43a)} \\ \overline{\mathrm{D}}_t w' & = -\partial_z \phi' + b' + \mathrm{Re}^{-1} \Delta w' + \mathcal{B}\left(\mathbf{u}', w'\right) & \text{(3.43b)} \\ \overline{\mathrm{D}}_t b' + \left(\mathrm{Fr}^{-2} + \partial_z \overline{b}\right) w' & = -\Gamma b' + \mathcal{B}\left(\mathbf{u}', b'\right) & \text{(3.43c)} \\ \partial_x u' + \partial_z w' & = 0, & \text{(3.43d)} \end{cases}$$

where

$$\overline{\mathrm{D}}_t = \partial_t + \overline{u} \partial_x \tag{3.44}$$

is the mean material derivative and $\mathcal{B}$ is a differential bilinear form which for any couple of vector and scalar fields $(\mathbf{a}, b)$ returns $(\overline{\mathbf{a} \cdot \nabla b} - \mathbf{a} \cdot \nabla b)$.

As the mean pressure does not interfere with the dynamics of the other fields, the mean hydrostatic equation (3.40) will be ignored in the remaining.

3.2.3 Quasilinear dynamics

Here, we present the quasilinear approximation. The mean flow equations are kept in their exact form. To solve these equations, we need to know the upward momentum flux $\overline{u_\prime w'}$ and buoyancy flux $\overline{b'w'}$ on the right-hand side of Eqs. (3.41) and (3.42). This is achieved

in principle by solving the fully nonlinear equations for the fluctuation (3.43). In practice, however, their numerical resolution is costly in computational resources. Indeed, the smallest scale to resolve is typically much smaller than the domain considered, leading to a huge number of numerical grid points. An approach to overcome this issue is to parametrise the buoyancy and momentum flux using turbulent diffusivities. Another possibility is to strongly truncate the dynamics using turbulent closures *inter alia*.

For the study of wave streaming, in our case, a relevant truncation is to ignore the wave-wave interactions by neglecting the bilinear terms in the fluctuations equations (3.43).In the coupled dynamics of the wave and the mean flow, the only nonlinearities kept are thus the mean upward momentum flux $\overline{u'w'}$ and the mean upward buoyancy flux $\overline{b'w'}$ in the mean flow equations (3.41) and (3.42). This approach is therefore called quasilinear. The linearised evolution equations for the waves writes

$$\begin{cases} \overline{\mathrm{D}}_t u' + w' \partial_z \overline{u} & = -\partial_x \phi' + \mathrm{Re}^{-1} \Delta u' & \text{(3.45a)} \\ \overline{\mathrm{D}}_t w' & = -\partial_z \phi' + b' + \mathrm{Re}^{-1} \Delta w' & \text{(3.45b)} \\ \overline{\mathrm{D}}_t b' + \left(\mathrm{Fr}^{-2} + \partial_z \overline{b}\right) w' & = -\Gamma b' & \text{(3.45c)} \\ \partial_x u' + \partial_z w' & = 0. & \text{(3.45d)} \end{cases}$$

3.2.4 Quasilinear boundary conditions

Here we discuss only the specific boundary conditions introduced in subsection 3.1.5. Let us first notice that the zonal averaging is not well-defined close to the bottom undulated boundary as the zonal average passes by the outside of the fluid's domain. This issue is overcome by considering the more opportune Lagrangian mean [103, 21] rather than the Eulerian mean. However, the quasilinear regime requires the bottom undulation generating the waves to be small compared to the vertical variation of the fields such that the boundary condition can be expressed by the first order terms of a Taylor expansion in z on an asymptotically flat bottom boundary. At leading order in the wave amplitude, the impermeability boundary condition (3.37a) gives

$$w'|_{z=0} = \partial_t h_b + \overline{u}|_{z=0} \partial_x h_b. \tag{3.46}$$

In the viscous case, the average and the deviation of the additional no-slip condition (3.37a) give at leading order a bottom boundary condition for the mean flow and an additional condition for the wave field

$$\begin{cases} \overline{u}|_{z=0} & = 0 \\ \left(u' + h_b \partial_z \overline{u}\right)|_{z=0} & = 0 \end{cases}. \tag{3.47}$$

3.2.5 Mean buoyancy

Here, we show that, in the quasilinear regime, the mean buoyancy remains bounded by the square of the wave amplitude.

Let us first assume that $|\mathrm{Fr}^2 \partial_z \overline{b}| \ll 1$. We multiply the buoyancy equation (3.45c) by the wave buoyancy b' and take the average of the result. Then, the mean upward buoyancy flux writes

$$\overline{b'w'} = -\mathrm{Fr}^2 \left(\partial_t \frac{\overline{b'^2}}{2} + \Gamma \overline{b'^2} \right). \tag{3.48}$$

Frame 3.2.1 The coupled wave and mean flow quasilinear model

Here, we summarise the coupled wave and mean flow equation simplified by the quasilinear approximation. This approximation amounts to neglect the wave-wave interactions. The terms in red are ignored when considering the inviscid problem. To simplify the notation, we introduced the mean material derivative $\overline{\mathrm{D}}_t = \partial_t + \overline{u}\partial_x$.

- Mean flow equations

$$\partial_t \overline{u} = -\partial_z \overline{u'w'} + \mathrm{Re}^{-1}\partial_z^2 \overline{u} \tag{3.50}$$

- Linearised wave equations

$$\begin{cases} \overline{\mathrm{D}}_t \mathbf{u}' + w'\partial_z \overline{u}\,\mathbf{e}_x & = -\nabla\phi\, p' + b'\mathbf{e}_z + \mathrm{Re}^{-1}\Delta u' & (3.51a) \\ \overline{\mathrm{D}}_t b' + \mathrm{Fr}^{-2} w' & = -\Gamma b' & (3.51b) \\ \nabla\cdot\mathbf{u}' & = 0 & (3.51c) \end{cases}$$

- Boundary condition

$$\begin{cases} \text{Impermeability} & \left(w' - \overline{\mathrm{D}}_t h_b\right)|_{z=0} = 0 & (3.52a) \\ \text{No-slip wave} & \left(u' + h_b\partial_z\overline{u}\right)|_{z=0} = 0 & (3.52b) \\ \text{No-slip mean} & \overline{u}|_{z=0} = 0 & (3.52c) \end{cases}$$

And injecting (3.48) into the mean buoyancy equation (3.42) leads to

$$\partial_t\left(\overline{b} - \mathrm{Fr}^2\partial_z\frac{\overline{b'^2}}{2}\right) = -\Gamma\left(\overline{b} - \mathrm{Fr}^2\partial_z\overline{b'^2}\right). \tag{3.49}$$

Starting from $\overline{b}(z,t=0)=0$, Eq. (3.49) ensures that $\overline{b}$ remains in the order of $\mathrm{Fr}^2\partial_z\overline{b'^2}$. This is also true in the inviscid case. This means that the mean buoyancy scales with the square of the wave amplitude at all time. Also, the Froude is at most equal to 1. Thus, the approximation $|\mathrm{Fr}^2\partial_z\overline{b}| \ll 1$ is indeed satisfied.

In the fully nonlinear regime, the wave can overturn and induce local mixing of the background linear stratification. In the atmosphere, those changes are cancelled out by radiative cooling. In the oceanic context, the stratification is not maintained by radiation but supported by planetary-scale meridional overturning circulations. The mixing induced by internal gravity waves is a key ingredient in maintaining the mean oceanic stratification [115]. These aspects are not discussed any further in this thesis and **the mean buoyancy and its dynamics are ignored in the remaining.**

3.3 Inviscid waves and reversible mean flow generation

In this section, we consider the inviscid dynamics. In subsection 3.3.1, we first show that, in this context, the mean flow generated with the wave field is transient such that the wave-induced flow reversibly vanishes once the waves have propagated away. An

additional goal of this section is to provide a detailed calculation of the wave field. In subsection 3.3.2, we solve the linear wave equations (3.50) in the absence of a mean flow, recovering the properties of internal gravity waves discussed in section 2.1. We also provide a discussion about the stability of the wave with respect to the nonlinear equations. In subsection 3.3.3, we move to the propagation within a sheared mean flow and provide a detailed treatment of the geometrical optics regime. In subsection 3.3.4, we take a close look on critical layers.

3.3.1 Weak induced mean flow response

This subsection is largely inspired by Oliver Bühler's book [21] where additional details can be found. Let us first introduce the relative vorticity $\zeta' = \nabla^\perp \cdot \mathbf{u}'$ with $\nabla^\perp = (\partial_z, -\partial_x)$ the curl operator.

Computing $\overline{b'\nabla^\perp \cdot (3.51a) + \zeta'(3.51b)}$ and using (3.48) and (3.51c) leads to

$$\partial_z \overline{u'w'} = -\partial_t \left(\mathrm{Fr}^2 \overline{b'\zeta'} \right) + \partial_t \left(\mathrm{Fr}^4 \frac{\overline{b'^2}}{2} \right) \partial_z^2 \overline{u}. \tag{3.53}$$

We inject Eq. (3.53) into (3.50). Starting from an arbitrary initial mean flow $\overline{u}(z, t=0) = U(z)$ along with a rest state for the wave, we introduce the induced mean flow $\delta\overline{u} = \overline{u} - U$. Assuming that $\delta\overline{u}$ scales as the square of the wave amplitude, we integrate the result in time. It leads to

$$\delta\overline{u} = \mathrm{Fr}^2 \overline{b'\zeta'} - \mathrm{Fr}^4 \frac{\overline{b'^2}}{2} \partial_z^2 U. \tag{3.54}$$

In figure 3.2, we show a sketch of a wavepacket travelling upward for $U = 0$. The induced mean flow $\delta\overline{u}$ (also represented in the figure) is circumscribed to the vicinity of the wavepacket and is following it has it travels upward. From Eq. (3.54), we see that there is no steady acceleration of the mean flow and that $\delta\overline{u}$ scales as the square of the wave amplitude at all times. This shows the necessity of wave damping for streaming.

We come back to the effect of dissipation in section 3.4. But first, we investigate the structure and properties of inviscid waves. In the remaining of the inviscid discussion of this section, we ignore the induced flow $\delta\overline{u}$.

3.3.2 Homogeneous internal gravity waves

In this section, we solve the inviscid linear equations (3.51) in the absence of background mean flow $\overline{u} = 0$. Then, the equations are homogeneous. This allows describing internal waves properties and structure in the simplest possible context. The following results will help the discussion regarding the inhomogeneous problem discussed in subsections 3.3.3 and 3.3.4.

The incompressibility of the flow (3.51c) allows us to introduce the wave sreamfunction ψ' such that

$$\mathbf{u}' = \nabla^\perp \psi' = (-\partial_z \psi', \partial_x \psi'). \tag{3.55}$$

Then, Eq. (3.51c) is automatically fulfilled. Now computing $\partial_t \left(\nabla^\perp \cdot (3.51a) \right) - \partial_x (3.51b)$ leads to the homogeneous internal gravity wave propagation equation for ψ'

$$\partial_t^2 \Delta \psi' + \mathrm{Fr}^{-2} \partial_x^2 \psi' = 0. \tag{3.56}$$

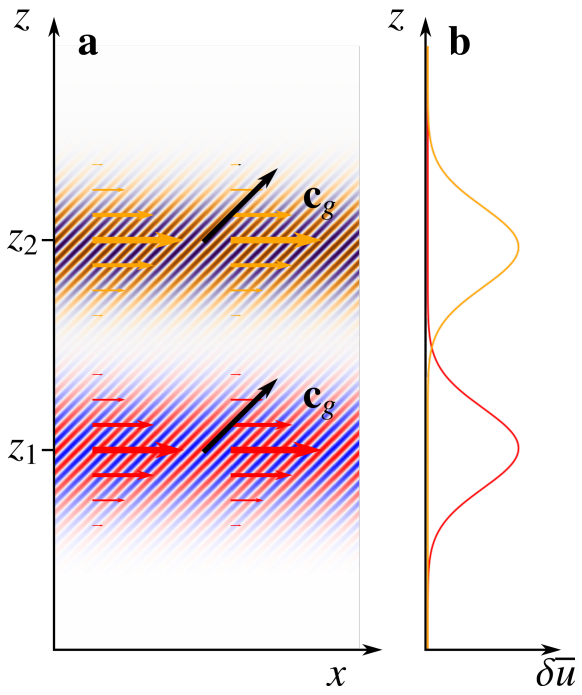

Figure 3.2: Sketch of zonally periodic wavepacket travelling upward (**a**) along with the induced mean flow (**b**). Two different colourmaps and line's colours are used to differentiate two different snapshots of the wavepacket taken at $t = t_1$ and $t = t2$ with $z_2 = z_1 + c_{g,z}(t_2 - t_1)$. This sketch is inspired from Oliver Bühler's book [21] and Bruce Sutherland's paper [154].

Monochromatic Plane Waves

A standard first step to investigate linear waves is to consider monochromatic plane waves. Indeed, any solution of the linear equation can be decomposed on a monochromatic plane wave basis. Then, let us consider a monochromatic plane wave where the angular frequency $\omega = 1$ and the zonal wave number $k = 1$ are prescribed by the bottom boundary

$$h_b(x,t) = \varepsilon \mathbb{R}\mathrm{e}\left[e^{i(t-x)}\right]. \tag{3.57}$$

The parameter ε introduced here controls the amplitude of the wave.

We thus look for solution of (3.56) of the form

$$\psi'(t,x,z) = \mathbb{R}\mathrm{e}\left[\tilde{\psi} e^{i(t-x+mz)}\right]. \tag{3.58}$$

where $-m$ is the vertical wave number[3]. By injecting (3.58) in (3.56), we obtain the dimensionless version of the dispersion relation of internal gravity waves (2.8) discussed in section 2.1.2

$$m^2 = \mathrm{Fr}^{-2} - 1. \tag{3.59}$$

Froude numbers greater than one lead to evanescent solutions with pure imaginary vertical wave number. **In this thesis, we restrain the discussion to propagative solutions with**

[3]The minus sign is not standard here. It will be used all along this thesis as it will lighten the different following expressions.

Fr < 1. In the nondimensionalised form, the group velocity derived in (2.9) writes

$$\mathbf{c}_g = \mathrm{Fr}^2 m \mathbf{k}^\perp, \tag{3.60}$$

with $\mathbf{k}^\perp = (m, 1)$.

The vertical wave number m is obtained by solving Eq. (3.59) with the constraint of positive upward group velocity (3.60) such that only the upward propagating solution is considered. It gives

$$m = \sqrt{\mathrm{Fr}^{-2} - 1} > 0. \tag{3.61}$$

Then, the wave structure is computed by injecting the monochromatic plane wave ansatz (3.58) into the equations (3.55) and (3.51b)

$$(u', w', b', \phi') = \mathbb{R}\mathrm{e}\left[\left(\tilde{u}, \tilde{w}, \tilde{b}, \tilde{p}\right) e^{i(t-x+mz)}\right], \tag{3.62}$$

with

$$\left(\tilde{u}, \tilde{w}, \tilde{b}, \tilde{p}\right) = \left(-im, -i, \mathrm{Fr}^{-2}, -im\right) \tilde{\psi}. \tag{3.63}$$

Boundary conditions matching

We now determine the value of $\tilde{\psi}$ using the impermeability condition (3.52a). Injecting the wave structure (3.62) into (3.52a) and using (3.63) gives

$$\tilde{\psi} = -\varepsilon. \tag{3.64}$$

A relevant and useful approximation: Hydrostatic Limit

In the limit $\mathrm{Fr} \ll 1$, the vertical wave number becomes very large with

$$m = \mathrm{Fr}^{-1} + o\left(\mathrm{Fr}^{-1}\right). \tag{3.65}$$

Then, the propagation of the wave becomes quasi-horizontal and the wave vector becomes quasi-vertical with $|c_{g,z}/c_{g,x}| = |1/m| = \mathrm{Fr}$. The wave reaches a hydrostatic regime. Indeed, using the wave structure (3.63), we have $|\partial_t w'/b'| \sim \mathrm{Fr}^2$. The linearised vertical projection of the momentum equation (3.51a) reduces to the hydrostatic balance with

$$\phi'_z = b'. \tag{3.66}$$

In the ocean and the stratosphere, the internal wave activity is much stronger for angular frequencies much lower than the typical buoyancy frequency (see figure 3.3). The associated Froude numbers are thus typically small. This makes the hydrostatic approximation relevant to the linear description of waves. However, nonlinear processes like the overturning of isopycnals by wave breaking are typically non-hydrostatic processes.

Overturning criterion

Here, we introduce a simple criterion on the wave amplitude ε and the Froude number Fr to the validity of the quasilinear regime. Additional criterion should be considered but this simple one will be useful when investigating the critical layers.

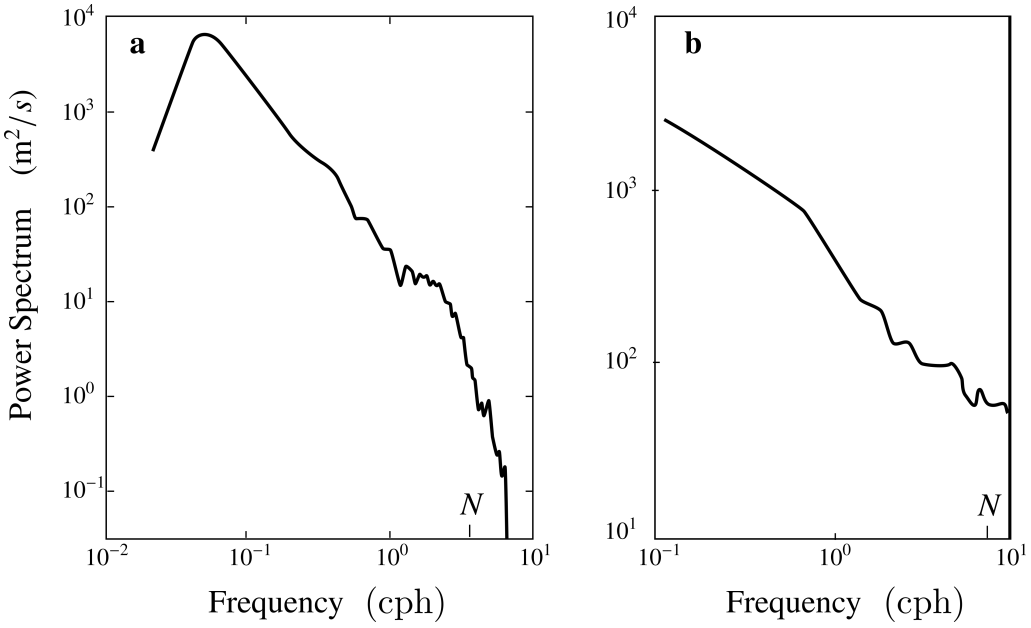

Figure 3.3: Frequency power spectra of internal gravity waves measured in the ocean (**a**) and the lower stratosphere (**b**) (adapted from [23] and [50] respectively). The frequencies are given in cycle per hour ($1\text{cph} = 3 \times 10^{-4}\text{s}^{-1}$) We reported the typical values of the buoyancy frequency N.

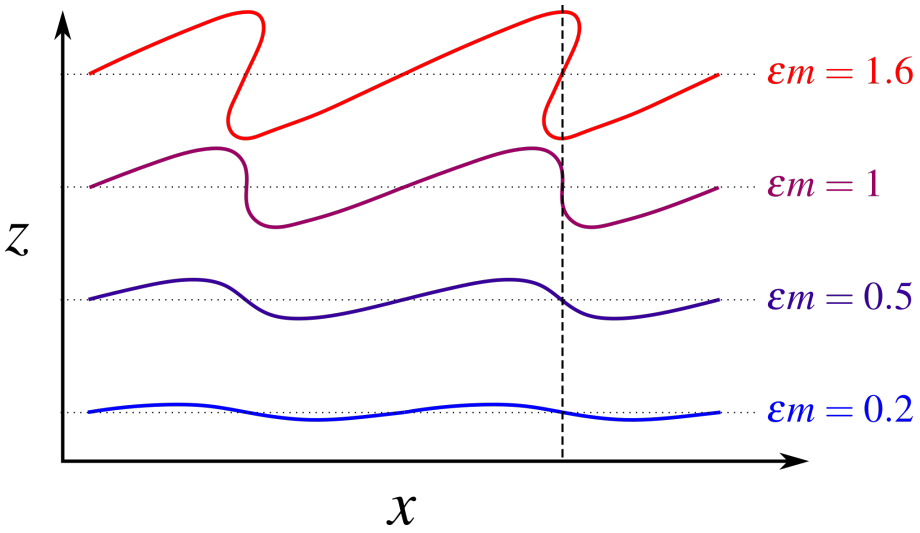

Figure 3.4: Sketch of isopycnals for different value of εm. ε is the amplitude of the fluid parcels' vertical displacement associated with the internal gravity waves. m is the vertical wave number.

Considering the total buoyancy associated with the background linear stratification and the buoyancy anomaly due to the internal wave, the isopycnals are the iso-buoyancy lines satisfying the equation

$$\mathrm{Fr}^{-2} z + b'(x,z,t) = \mathrm{Fr}^{-2} z_0 \tag{3.67}$$

where z_0 is height of the isopycnal at rest. Using Eqs. (3.64), (3.62) and (3.63), the isopycnals equation (3.67) writes

$$z - \varepsilon \cos(t - x + mz) = z_0. \tag{3.68}$$

Sketches of the isopycnals characterised by Eq. (3.68) are shown in figure 3.4 for different values of ε for a fixed m value. We expect the overturn to occur when the gradient of the isopycnal points downward. This happens when its vertical projection becomes negative

$$\partial_z (z - \varepsilon \cos(t - x + mz) - z_0) = 1 - \varepsilon m \cos(t - x + mz). \tag{3.69}$$

From (3.69), we see that if $\varepsilon m > 1$, then there is a local overturning of the isopycnals. This illustrated in figure 3.4. Using Eq. (3.61), this gives us the following stability criterion for ε and Fr

$$\varepsilon \sqrt{Fr^{-2} - 1} < 1. \tag{3.70}$$

3.3.3 Inhomogeneous propagation within sheared background flow

In this section, we solve the inhomogeneous linear problem of the propagation of internal gravity waves within a stationary sheared background mean flow. The formalism developed here for the inviscid case will be useful before extending it to the dissipative case. Additional details regarding the calculations presented here can be found in Vallis' and Bülher's books [161, 21] and the paper of Muraschko and collaborators [111].

We consider now the equations (3.51) with $\overline{u} = U(z)$. The associated Richardson number is assumed large enough everywhere, $\mathrm{Ri} = N^2 / (\partial_z U)^2 \gg 1$, such the mean flow remains stable. We obtain the following inhomogeneous wave propagation equations. Let us introduce again the streamfunction ψ' introduced in Eq. (3.55), and compute $\overline{\mathrm{D}}_t \nabla^\perp \cdot$ (3.51a) $- \partial_x$(3.51b). This leads to the inhomogeneous internal gravity wave propagation equation for ψ'

$$\overline{\mathrm{D}}_t^2 \Delta \psi' - \left(\partial_z^2 U\right) \overline{\mathrm{D}}_t \partial_x \psi' + \mathrm{Fr}^2 \partial_x^2 \psi' = 0. \tag{3.71}$$

Monochromatic Plane Wave

Let us look for a solution of the form of a monochromatic plane wave where the angular frequency $\omega = 1$ and the horizontal wave number $k = 1$ are prescribed by the bottom boundary. Keeping the z-dependence, we look for a solution of (3.71) of the form

$$\psi'(t,x,z) = \mathbb{R}\mathrm{e}\left[\tilde{\Psi}(z)\, e^{i(t-x)}\right]. \tag{3.72}$$

We introduce the local Doppler-shifted angular frequency

$$\hat{\omega}(z) = 1 - U(z) \tag{3.73}$$

and assume that the mean flow satisfies $0 < \hat{\omega}^2 < \mathrm{Fr}^{-2}$ everywhere. Injecting (3.72) into (3.71) leads to Taylor-Goldstein equation

$$\partial_z^2 \tilde{\Psi} + \left(m^2(z) + \frac{\partial_z^2 U(z)}{1 - U(z)} \right) \tilde{\Psi} = 0, \tag{3.74}$$

where $m(z)$ is the local vertical wave number satisfying

$$m(z) = \sqrt{\frac{1}{(1 - U(z))^2 \mathrm{Fr}^2} - 1}. \tag{3.75}$$

Weak inhomogeneity and geometrical optics regime

Let us assume that the background flow, $U(z)$ varies little over a typical vertical wavelength of the wave. In this case, the solution of Eq. (3.74) can be well-approximated by the first term of a geometrical optics asymptotic series also known as the Wentzel-Kramers-Brillouin (WKB) approximation.

We introduce for the purpose the ansatz

$$\tilde{\Psi}(z) = \tilde{\psi}(z) \exp\left\{ i \int_0^z m(z') \, \mathrm{d}z' \right\}, \tag{3.76}$$

where $\tilde{\psi}$ is the local wave amplitude which varies slowly along the variation of the propagation medium. After injecting (3.76) into (3.74), the WKB approximation amounts to neglect the z-derivative of a slowly varying field against a multiplication by the vertical wave number. We are left with simple amplitude equation

$$\partial_z \left(m \tilde{\psi}^2 \right) = 0. \tag{3.77}$$

The integration is straightforward

$$\tilde{\psi}(z) = \sqrt{\frac{m(0)}{m(z)}} \tilde{\psi}(0) \tag{3.78}$$

where $\tilde{\psi}(0)$ is determined by the boundary condition (3.52a)

$$\tilde{\psi}(0) = -(1 - U(0)) \varepsilon. \tag{3.79}$$

The local wave structure is computed by injecting (3.72) along with (3.76) into (3.55) and (3.51b). With the WKB approximation, we obtain at leading order

$$(u', w', b', \phi') = \mathbb{R}\mathrm{e}\left[\left(\tilde{u}, \tilde{w}, \tilde{b}, \tilde{p} \right) e^{i(t-x)} \right] \tag{3.80}$$

with

$$\left(\tilde{u}, \tilde{w}, \tilde{b}, \tilde{p} \right) = \left(-im, -i, \hat{\omega}^{-1} \mathrm{Fr}^{-2}, -i\hat{\omega} m \right) \tilde{\psi} \exp\left\{ i \int_0^z m(z') \, \mathrm{d}z' \right\}. \tag{3.81}$$

We recover the structure of the homogeneous case (3.62) by setting $U = 0$.

The stability criterion obtained for the homogeneous case in Eq. (3.70) needs to be updated to the inhomogeneous problem. After some algebra, we obtain

$$\varepsilon\sqrt{m(z)\,m(0)}\frac{1-U(0)}{1-U(z)}<1. \tag{3.82}$$

The upward momentum flux can be computed using $\overline{u'w'}=\mathbb{R}\mathrm{e}[\tilde{u}\tilde{w}^*]/2$. It gives

$$\overline{u'w'}(z)=\frac{m}{2}|\tilde{\psi}|^2=\frac{\varepsilon^2 m(0)\,(1-U(0))^2}{2}. \tag{3.83}$$

We recover the result $\partial_z\overline{u'w'}=0$ for a steady wave obtained in Eq. (3.53).

3.3.4 Critical layers

So far we restricted ourselves to background flows satisfying $0<\hat{\omega}^2(z)<\mathrm{Fr}^{-2}$. The mean flow is thus constrained in the range $1-\mathrm{Fr}^{-1}<U(z)<1$. The lower bound is almost always satisfied in the oceanic or atmospheric contexts as the Froude number is small most of the time. However, the mean flow often approaches or oversteps the upper bound. The region of the flow where the mean flow approaches 1 is called a critical layer. First studied by [13], these critical layers are important to wave streaming (see subsection 2.2.5). Here, we describe the effect of critical layers on the wave field at the inviscid level and take a close look at the stability criterion.

Let us consider background mean flow which increases from $U(z=0)=0$ at the bottom and crosses the value 1 at a given critical height z_c with

$$1-U(z)\underset{z\to z_c}{\sim}\delta U\,(z_c-z) \tag{3.84}$$

where $\delta U>0$ is the local mean flow shear at the level of the critical height. Then, the Doppler shifted angular frequency goes towards zero $\hat{\omega}(z\to z_c)=0$ and the local vertical wave number defined in (3.75) diverges close to the critical height

$$m(z)\underset{z\to z_c}{\sim}\frac{1}{\mathrm{Fr}\delta U}(z_c-z)^{-1}. \tag{3.85}$$

This means that the wave becomes hydrostatic close to the critical height. A direct consequence is that the group velocity introduced in (3.60) becomes more and more horizontal

$$\begin{cases} c_{g,x}(z) & \underset{z\to z_c}{\sim} 1 & \text{(3.86a)}\\ c_{g,z}(z) & \underset{z\to z_c}{\sim} \mathrm{Fr}\delta U^2(z_c-z)^2. & \text{(3.86b)}\end{cases}$$

If we consider an unsteady wave, the upward propagation of fronts or envelops is controlled by the upward group velocity. Then, an infinite time is required for a wavefront or a wavepacket to reach the critical height. Indeed, let us consider the evolution for the vertical position $z_f(t)$ of a front or an amplitude maximum of a wave packet

$$\frac{\mathrm{d}}{\mathrm{d}t}z_f=c_{g,z}(z_f)\underset{z_f\to z_c}{\sim}\mathrm{Fr}\delta U^2(z_c-z_f)^2. \tag{3.87}$$

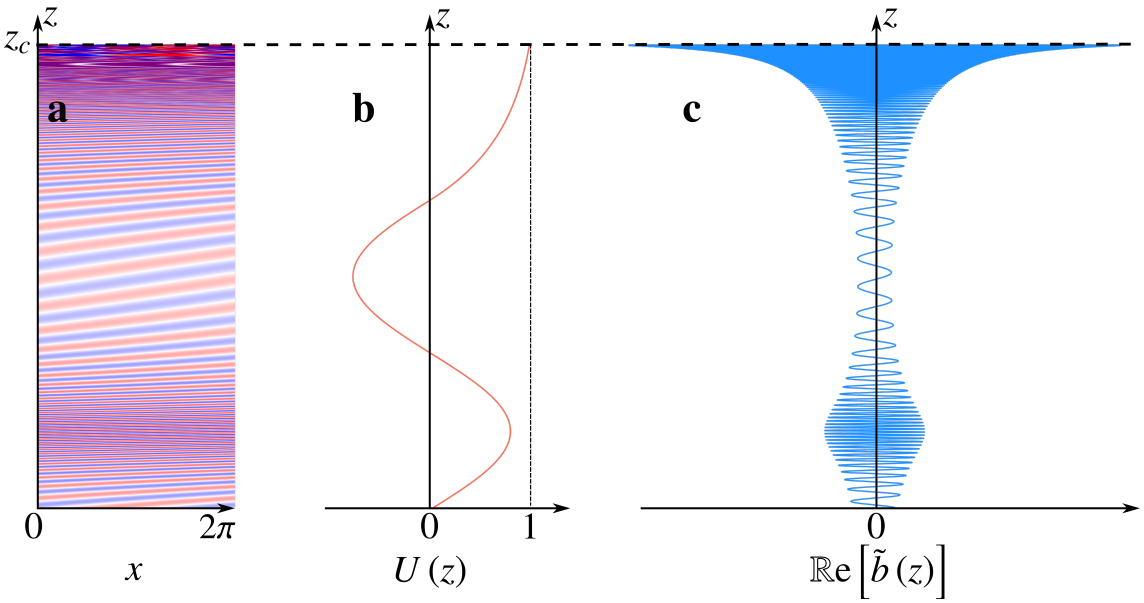

Figure 3.5: A snapshot of buoyancy anomaly b' is shown on panel **a** using a colourmap. It has been computed using the geometrical optics approximation (see Eq. (3.80)) associated with a background flow $U(z)$ plotted in panel **b** with $\mathrm{Fr} = 0.1$. A vertical profile of the buoyancy anomaly is plotted on panel **c**.

Integrating in time Eq. (3.87) leads to the asymptotic results

$$z_c - z_f(t) \underset{t\to\infty}{\sim} \frac{1}{\mathrm{Fr}\delta U^2}\frac{1}{t}. \tag{3.88}$$

The steady wave solution considered in previous subsections ignored the propagation of the front. Later, we will consider mean flows slowly evolving in time such that the steady wave approximation breaks in the presence of critical layers, independently of any other relevant criteria.

Nevertheless, let us continue with the steady solution. The validity of static WKB approximation is not altered near the critical height as the local wave number is diverging. Then, the stability criterion (3.82) breaks close to the critical height

$$\varepsilon\sqrt{m(z)\,m(0)}\frac{1-U(0)}{1-U(z)} \underset{z\to z_c}{\sim} \varepsilon\mathrm{Fr}^{-1}\left(1-\mathrm{Fr}^2\right)^{1/4}\delta U^{-3/2}\left|z_c - z\right|^{-3/2}. \tag{3.89}$$

In the presence of critical layers, the quasilinear regime is not valid. In figure 3.5, we show the inviscid solution computed for an arbitrary background flow $U(z)$ with a critical layer ($U(z_c) = 1$) within the geometrical optics regime. We represent the buoyancy anomaly b' computed in Eq. (3.80) in order to visualise the region of the flow where the stability criterion (3.82) is less satisfied. Indeed, the wave approaches the overturning threshold where the amplitude of the buoyancy anomaly is large (see Eq. (3.67) and figure 3.4).

In the case of an inviscid dynamics, we have seen that there is no streaming, i.e. no irreversible growth of a mean flow. Nevertheless, in the presence of critical layers, the dissipative processes, however weak they are, will act through nonlinearities. We propose to call the associated mean-flow growth an anomalous streaming by analogy with the anomalous diffusion in turbulence. It turns out that this anomalous streaming

governed by nonlinearities is fairly modelled by the quasilinear model with vanishingly small dissipation.

In the next section, we look at the effect of the linear buoyancy friction which damps the waves and consequently drives a secular mean flow growth.

3.4 Wave streaming with radiative damping

In this section, we investigate the effect of a linear buoyancy friction to the wave and for the dynamics of the mean flow. For the sake of simplicity, the effect of viscosity will be discussed later in chapters 4 and 5. The dynamics of the mean flow is drastically different from the inviscid case discussed above. A mean flow is accelerated steadily by the divergence of the upward momentum flux of the damped waves.

In subsection 3.4.1, we investigate the homogeneous case, with no background flow. After showing that the mean flow grows secularly, in subsection 3.4.2, we compute the wave field in the geometrical optics regime for an arbitrary frozen-in-time mean flow. We discuss the effect of the radiative damping on the critical layers in subsection 3.4.3.

3.4.1 Homogeneous damped propagation and secular mean flow growth

We solve the equations (3.51) with $\overline{u} = 0$ and $\mathrm{Re} = \infty$. The radiative damping modeled by the term $-\Gamma b'$ on the right-hand side of Eq. (3.51b) is the only dissipative process considered here.

Injecting (3.55) and computing $(\partial_t + \Gamma)\nabla^\perp \cdot (3.51a) + \partial_x (3.51b)$ leads to the following simplified propagation equation.

$$(\partial_t + \Gamma)\, \partial_t \Delta \psi' + \mathrm{Fr}^{-2} \partial_x^2 \psi' = 0. \tag{3.90}$$

Monochromatic Plane Waves

Let us look for a solution of the form of a monochromatic plane wave where the angular frequency $\omega = 1$ and the zonal wave number $k = 1$ are prescribed by the bottom boundary (3.57). Injecting the ansatz (3.58) into (3.90), we obtain the dispersion relation for internal gravity waves damped by radiative cooling

$$m^2 = \frac{1}{\mathrm{Fr}^2 (1 - i\Gamma)} - 1. \tag{3.91}$$

The vertical wave number $-m$ is necessary a complex number. We look for upward propagating waves such that the solution of (3.91) is the complex root with positive imaginary part. Let us decompose m into its real and imaginary part

$$m = m_r + i \frac{1}{2\Lambda_\Gamma}, \tag{3.92}$$

where $m_r \in \mathbb{R}$ is associated with the vertical oscillation and $\Lambda_\Gamma \in \mathbb{R}_+$ is the e-folding length of the wave. Taking the imaginary part of the dispersion relation (3.91), we obtain the relation

$$\frac{m_r}{\Lambda_\Gamma} = \frac{\Gamma}{\mathrm{Fr}^2 (1 + \Gamma^2)}. \tag{3.93}$$

Then, m_r and Λ_γ must share the same sign such that $m_r \in \mathbb{R}_+$.

In the limit of weak damping $\Gamma \ll 1$, we have

$$\begin{cases} m_r & = m_0 + o(\Gamma) \quad (3.94a) \\ \Lambda_\Gamma & = m_0 \mathrm{Fr}^2/\Gamma + o(\Gamma), \quad (3.94b) \end{cases}$$

where m_0 is the inviscid vertical wave number given in (3.61). The e-folding length Λ_Γ diverges as the linear friction coefficient Γ vanishes.

By injecting the plane wave ansatz in (3.55), (3.52a) and (3.51b), we obtain the structure of the plane wave which has the same expression as in the inviscid case (3.63) but with the complex vertical number m defined by (3.91) and (3.92).

Consequences for the Mean Flow

Here, we show that the damping of the internal gravity wave by radiative cooling is now associated with a steady mean flow growth. The mean upward momentum gives

$$\overline{u'w'}(z) = \frac{1}{2}\mathbb{R}\mathrm{e}\left[\tilde{u}\tilde{w}^*\right] e^{-z/\Lambda_\Gamma} = \frac{m_r \varepsilon^2}{2} e^{-z/\Lambda_\Gamma}. \quad (3.95)$$

Injecting (3.95) into to the mean flow evolution equation (3.50) leads to

$$\partial_t \overline{u} = \frac{m_r \varepsilon^2}{2\Lambda_\Gamma} e^{-z/\Lambda_\Gamma}. \quad (3.96)$$

Let us rescale the height and the time by introducing $Z = z/\Lambda_\Gamma$ and $T = t/\mathcal{T}$ with

$$\mathcal{T} = \frac{2\Lambda_\Gamma}{m_r \varepsilon^2} = \frac{2\mathrm{Fr}^2(1+\Gamma)}{\Gamma \varepsilon^2}. \quad (3.97)$$

where we used (3.93). Then, the mean flow evolution equation writes in the compact form

$$\partial_T \overline{u}(Z,T) = e^{-Z}. \quad (3.98)$$

Starting from rest, the mean flow increases linearly with time

$$\overline{u}(Z,T) = e^{-Z} T. \quad (3.99)$$

This shows existence of a secular mean flow growth called wave streaming associated with the radiative damping of a steady wave beam. This observation is actually generic: it extends to any arbitrary dissipative processes [123, 90].

The resulting mean flow $\overline{u}$ in (3.99) has been obtained assuming that the mean flow can be neglected in the wave equations (3.51). Due to the linear growth, this hypothesis breaks down when $\overline{u}$ becomes of order one. This happens after a time of the order of the characteristic timescale $\mathcal{T}$. Then, the mean flow needs to be taken into account in the wave equation leading us to the inhomogeneous problem.

3.4.2 Coupled wave and mean flow evolution

The secular mean flow growth established in Eq. (3.99) invites us to consider the effect of the mean flow on the wave. The mean flow evolution and the wave evolution needs to be treated together as the wave-mean flow coupling is strong. The goal of this subsection, is to solve the set of coupled equations (3.50) and (3.51). As a start, we will ignore the effect of viscosity on the wave field. We will come back to this process in Chapter 5.

Timescale separation

To simplify the problem, we assume that there is a large timescale separation between the wave and the mean flow such that the wave field sees the mean flow as frozen in time with $\overline{u}(z,t) = \overline{u}(z)$ in Eq. (3.51).

We introduced a characteristic timescale $\mathcal{T}$ for the mean flow evolution in Eq. (3.97). The characteristic vertical length of the mean flow is given by the damping length scale of the wave Λ_Γ introduced in Eq. (3.92). The relevant characteristic timescale to compare against $\mathcal{T}$ is the time it takes for a wavefront to propagate to a height Λ_Γ

$$\tau_p = \frac{\Lambda_\Gamma}{C_{g,z}} = \frac{\Lambda_\Gamma}{\mathrm{Fr}^2 m_r}, \tag{3.100}$$

where $c_{g,z}$ is the vertical group velocity of the inviscid wave defined in (3.60) where the vertical number has been replaced by the oscillatory component m_r of the complex vertical number introduced in (3.92). We have

$$\frac{\tau_p}{\mathcal{T}} = \frac{\varepsilon^2}{2\mathrm{Fr}^2}. \tag{3.101}$$

Then, assuming a timescale separation comes down to assume $\varepsilon \ll \mathrm{Fr}$.

However, as we inferred in the previous section, in the presence of critical layers this assumption necessarily breaks (see Eq. (3.88)). **Nevertheless, we will assume a time scale separation between the wave and the mean flow dynamics in the following. The wave will be computed as the steady response to a frozen in time mean flow.** This approximation greatly simplifies the analytical resolution of the couple wave and mean flow dynamics.

Propagation equation

We now consider the wave equations (3.51) with a frozen in time mean flow $\overline{u}(z,t) = \overline{u}(z)$ and ignore viscosity such that the radiative damping is the only dissipative process damping the wave.

Considering the streaming function ψ' introduced in Eq. (3.55) and computing $(\overline{\mathrm{D}}_t + \Gamma)\nabla^\perp(3.51\mathrm{a}) + \partial_x(3.51\mathrm{b})$ leads to the following simplified propagation equation

$$\left(\overline{D}_t + \Gamma\right)\overline{D}_t \Delta\psi' - \partial_z^2 \overline{u}\left(\overline{D}_t + \Gamma\right)\partial_x \psi' + \mathrm{Fr}^{-2}\partial_x^2 \psi' = 0. \tag{3.102}$$

where $\overline{D}_t = \partial_t + \overline{u}\partial_x$ is the mean material derivative.

Monochromatic plane waves and geometrical optics regime

Looking for a solution of the form of Eq. (3.72), we obtain the Taylor-Goldstein equation (3.74) where the local vertical wave number $m(z)$ satisfies now the damped dispersion relation

$$m^2(z) = \frac{1}{\mathrm{Fr}^2\left((1-\overline{u}(z))^2 - i\Gamma(1-\overline{u}(z))\right)} - 1. \tag{3.103}$$

We decompose m into its real and imaginary part

$$m(z) = m_r(z) + i\frac{1}{2\Lambda_\Gamma(z)}. \tag{3.104}$$

Vertical length scale separation and geometrical optics regime

In order to use the WKB approximation, we assume that there is a vertical scale separation between the wave field and the mean flow. The characteristic vertical length of variation of the mean flow is given by the e-folding length Λ_Γ of the wave field introduced in (3.92).

We now assume the damping to be weak with $m_r\Lambda_\Gamma \gg 1$ such that vertical variations of the wave is dominated by m_r. We fall directly in the right scaling for the WKB approximation to be valid as Λ_Γ will be the characteristic vertical variation length of the mean flow. In the limit $\Gamma \ll 1$ we have

$$m_r\Lambda_\Gamma = \frac{1-\mathrm{Fr}^2}{\Gamma} + o\left(\Gamma^{-1}\right). \tag{3.105}$$

In this PhD thesis, the Froude numbers considered are not typically close to one. The condition $m_r\Lambda_\Gamma \gg 1$ is thus directly fulfilled by the condition $\Gamma \ll 1$.

This approximation also breaks in the presence of critical layers. Indeed, if $1-\overline{u} \ll \Gamma$, then from Eq. (3.103), we have $m \approx (1+i)/\sqrt{2\mathrm{Fr}^2\Gamma(1-\overline{u})}$ such that $m_r\Lambda_\Gamma \approx 1/2$.

However, it turns out that the WKB approximation works well even if the scale separation is not very well satisfied.

Geometrical optics regime

Using the WKB approximation (3.76) with (3.106) we have

$$\tilde{\Psi}(z) = \tilde{\psi}(0)\sqrt{\frac{m(0)}{m(z)}}\exp\left\{i\int_0^z m(z')\,\mathrm{d}z'\right\}. \tag{3.106}$$

with $\tilde{\psi}(0)$ given by the boundary condition (3.79) and the local vertical wave number $m(z)$ is now given by (3.103) and (3.104)

Considering the ansatz (3.72), **the momentum flux divergence** is given by the following formula

$$\partial_z\overline{u'w'} = \frac{1}{2}\mathbb{I}\mathrm{m}\left[\tilde{\Psi}^*\partial_z^2\tilde{\Psi}\right]. \tag{3.107}$$

Injecting the ansatz (3.76) into (3.107), in the WKB approximation $\partial_z^2\tilde{\Psi}$ is dominated by $-m^2\tilde{\Psi}$. Then, using (3.106), the momentum flux divergence associated with the WKB solution writes

$$\partial_z\overline{u'w'} = -\frac{1}{2}\mathbb{I}\mathrm{m}\left[m^2(z)\right]|\tilde{\psi}(0)|^2\left|\frac{m(0)}{m(z)}\right|\exp\left\{-\int_0^z\frac{\mathrm{d}z'}{\Lambda_\Gamma(z')}\right\}. \tag{3.108}$$

3.4.3 Mean flow response

Injecting (3.108) into the non-viscous mean flow evolution equation (3.50) leads to a closed one-dimensional non-linear integrodifferential equation.

To greatly simplify the resulting equation, let us consider the hydrostatic and weak dissipation limits with $\Gamma \ll 1-\overline{u} \ll \mathrm{Fr}^{-1}$. In this regime, the momentum flux divergence (3.108) writes

$$\partial_z\overline{u'w'}(z) = -\frac{\varepsilon^2\Gamma\mathrm{Fr}^{-2}\left(1-\overline{u}(0,t)\right)}{2\left(1-\overline{u}(z,t)\right)^2}\exp\left\{-\Gamma\mathrm{Fr}^{-1}\int_0^z\frac{\mathrm{d}z'}{\left(1-\overline{u}(z',t)\right)^2}\right\}. \tag{3.109}$$

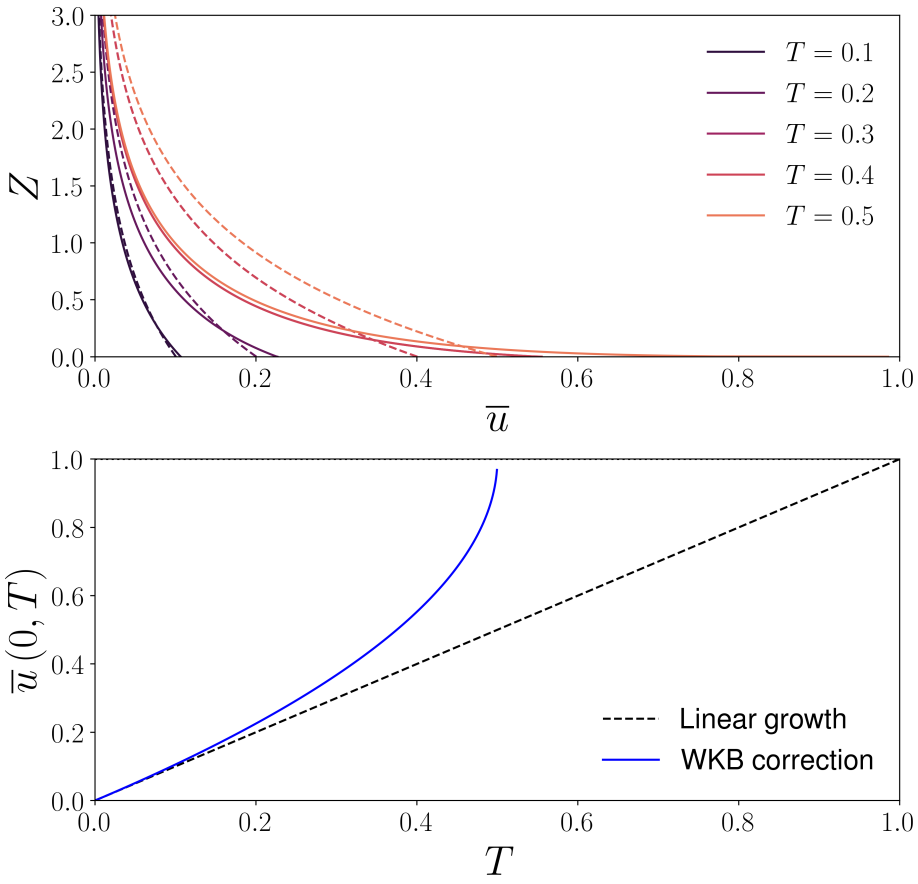

Figure 3.6: **top**. Vertical mean flow profiles $\overline{u}(Z,T)$ with $T \in \{0.1, 0.2, 0.3, 0.4, 0.5\}$. The homogeneous calculation (3.99) is represented in dashed lines while the inhomogeneous WKB solution (3.111) is represented in solid lines. **bottom**. Bottom value of the mean flow $\overline{u}(0,T)$. The homogeneous calculation is represented by a dashed black line while the inhomogeneous WKB solution is represented by a solid blue line. The upper horizontal dotted black line represents the critical value $\overline{u} = 1$.

Then, the mean flow evolution equation (3.50) writes

$$\partial_t \overline{u}(z,t) = \frac{\varepsilon^2 \Gamma \mathrm{Fr}^{-2}(1-\overline{u}(0,t))}{2(1-\overline{u}(z,t))^2} \exp\left\{-\Gamma \mathrm{Fr}^{-1} \int_0^z \frac{\mathrm{d}z'}{(1-\overline{u}(z',t))^2}\right\}. \tag{3.110}$$

Introducing the rescaled space-time variables $Z = z\Gamma\mathrm{Fr}^{-1}$ and $T = t\varepsilon^2\Gamma\mathrm{Fr}^{-2}/2$, Eq. (3.110) writes in the simple form

$$\partial_T \overline{u}(Z,T) = \frac{1-\overline{u}(0,T)}{(1-\overline{u}(Z,T))^2} \exp\left\{-\int_0^Z \frac{\mathrm{d}Z'}{(1-\overline{u}(Z',T))^2}\right\}. \tag{3.111}$$

This equation can directly be solved for the bottom value leading to

$$\overline{u}(0,T) = 1 - \sqrt{1-2T}. \tag{3.112}$$

The bottom mean flow evolution is represented in Fig. 3.6 against the linear growth obtained in the homogeneous case in Eq. (3.99). Taking into account the effect of the mean flow in the wave field computation amplifies the mean flow growth.

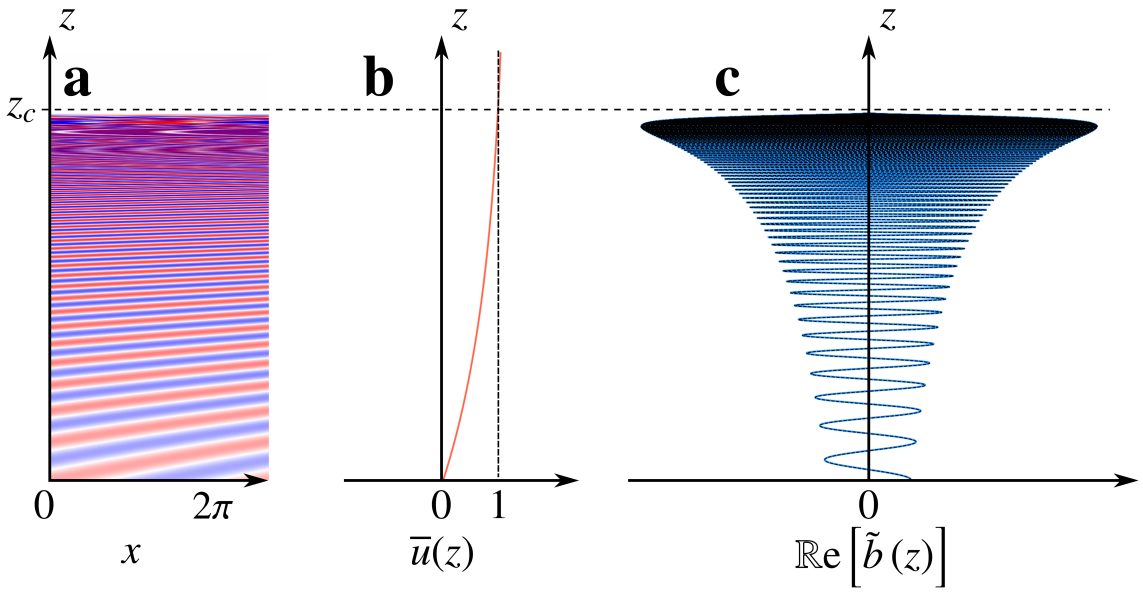

Figure 3.7: A snapshot of buoyancy anomaly b' of the damped wave field is shown on panel **a**. It has been computed using the geometrical optics approximation associated with a background flow $U(z)$ plotted in panel **b** for $\mathrm{Fr} = 0.1$ and $\Gamma = 0.0001$. A vertical profile of the buoyancy anomaly is plotted on panel **c** in blue line.

Critical Layers

Considering the same set up as in subsection 3.3.4 with a background mean flow increasing from $U(z=0)=0$ at the bottom and crossing the value 1 at a given critical height z_c with

$$1 - U(z) \underset{z\to z_c}{\sim} \delta U\,(z_c - z) \tag{3.113}$$

where $\delta U > 0$ is the mean flow shear at the level of the critical height. The local vertical wave number defined in (3.103) diverges close to the critical height

$$m(z) \underset{z\to z_c}{\sim} \frac{1+i}{\sqrt{2\mathrm{Fr}^2\Gamma\delta U}}\,|z_c - z|^{-1/2}. \tag{3.114}$$

Then,

$$\Lambda_\Gamma(z) \underset{z\to z_c}{\sim} \sqrt{\frac{\mathrm{Fr}^2\Gamma\delta U}{2}}\,|z_c - z|^{1/2}. \tag{3.115}$$

Consequently, the integral $\int_0^{z_c} \mathrm{d}z'/\Lambda_\Gamma(z')$ is convergent and the momentum flux divergence (3.108) gives

$$\partial_z\overline{u'w'}(z) \underset{z\to z_c}{\sim} -\frac{|\tilde{\psi}(0)|^2\,|m(0)|}{\mathrm{Fr}^2\Gamma\delta U}\exp\left\{-\int_0^{z_c}\frac{\mathrm{d}z'}{\Lambda_\Gamma(z')}\right\}|z_c - z|^{-1/2}. \tag{3.116}$$

There is a singularity in the streaming body force which is diverging at the level of the critical layer.

This divergence is associated with the instability of the wave which can be easily emphasised using Eqs. (3.82) and (3.114). A way to account for the extra damping due to

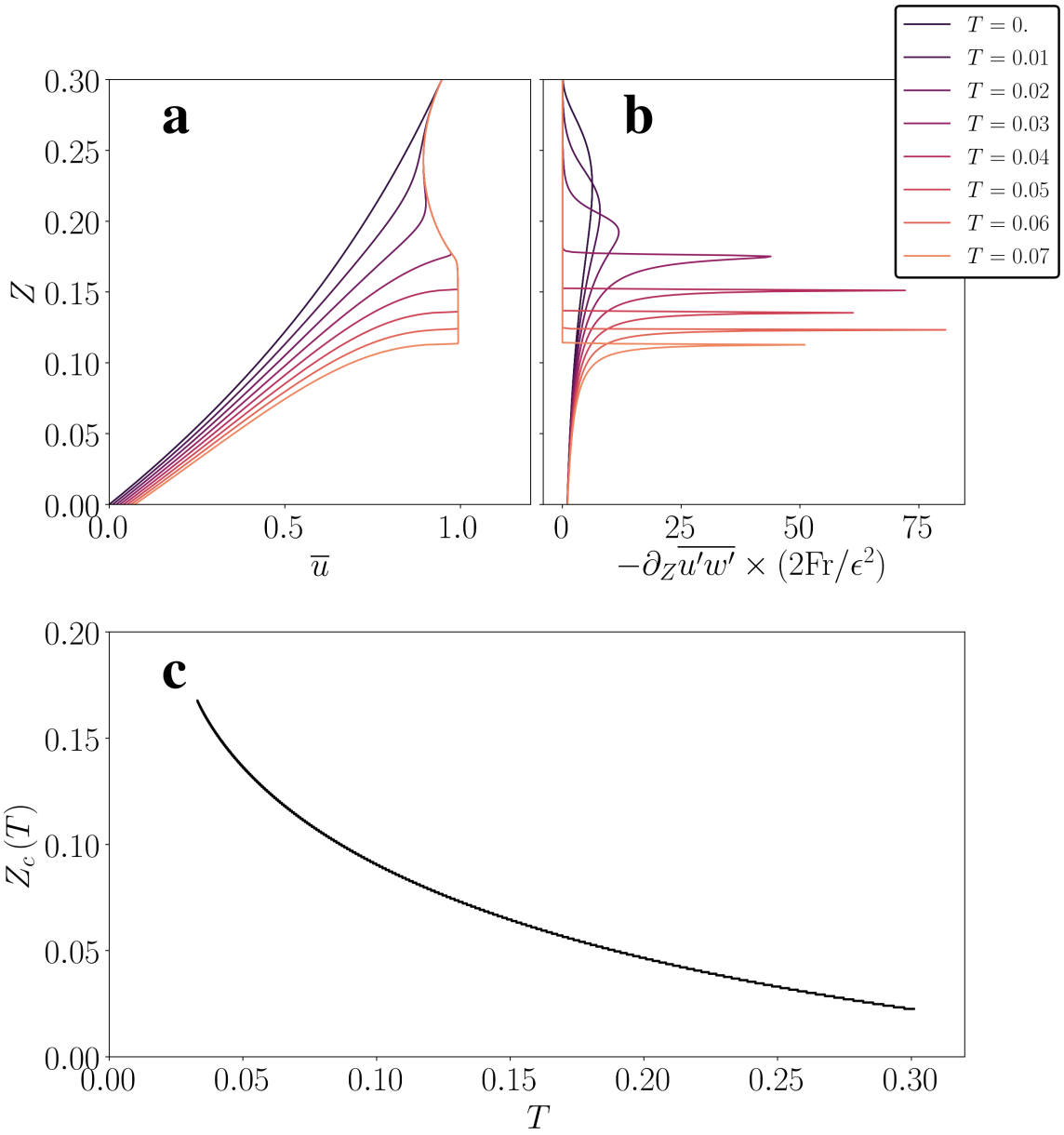

Figure 3.8: **Mean flow evolution close to critical layers. a.** Vertical mean flow profiles $\overline{u}(Z,T)$ computed by integrating (3.111) numerically starting from an initial mean flow profile approaching the critical value 1. **b.** Streaming body force (from the right-hand side of (3.111)). The vertical profiles are associated with the mean flow profiles represented in panel a. **c.** Lowest critical height as a function of time, $Z_c(T)$.

nonlinear instability is to have an exponential folding going towards zero at the critical height z_c. This is easily achieved by taking limit $\Gamma \ll 1-\overline{u}$ which amounts to perform the limit of weak damping before considering the limit $z \to z_c$. In practice, Γ is indeed small such that this limit is actually valid apart in a very close vicinity of z_c.

For sake of simplicity, let us consider the hydrostatic limit $1-\overline{u} \ll \mathrm{Fr}^{-1}$ in addition. Then, we have at leading order

$$m(z) = \frac{1}{\mathrm{Fr}\,(1-\overline{u}(z))} + i\frac{\Gamma}{2\mathrm{Fr}\,(1-\overline{u}(z))^2}. \tag{3.117}$$

The WKB expression obtained in this regime is shown in figure 3.7c. It turns out that there is a very good numerical agreement with the solution without the weak damping approximation, even close to the critical layer. Indeed, a very fine vertical grid would be required to capture the divergence obtained in Eq. (3.116).

The mean flow evolution in the presence of critical layers is thus well-captured by Eq. (3.111). We integrate this equation numerically starting from an initial mean flow profile approaching the critical value 1. The resulting mean flow profiles are shown in figure 3.8a and the associated streaming body force profiles are represented in figure 3.8b. We see that the streaming force creates a critical layer. Then, the mean flow reaches the value 1 with a quasi horizontal asymptote. Then, the streaming force causes the descent of the critical layer. The lowest critical height of the mean flow profile Z_c is decreasing with time. We represented the temporal evolution of $Z_c(T)$ in figure 3.8c.

This descent of the mean flow is a characteristic [92] of waves shattering on their critical layers. With this in mind and looking at the descending pattern of the observation of quasi-biennial oscillation shown in figure 1.1c, wave-driven nature of the phenomenon is clearer now.

3.5 Conclusion of Chapter 3

In this rather technical chapter, we detailed the general framework and computational techniques useful to the next two chapters. After introducing the Boussinesq dynamical equations, we defined the mean flow with the help of zonal symmetry. Considering the quasilinear dynamics together with a geometrical optics approximation, we derived explicitly the internal gravity wave field. We exhibited that in the absence of dissipation, internal waves fail to force an irreversible flow. However, we also showed that the wave is necessarily unstable in the vicinity of critical layers which suggest anomalous dissipation effects and a concomitant anomalous streaming. With the addition of linear friction in the buoyancy equation, we derived the resulting streaming force and computed the associated mean flow growth. We exhibited an enhanced acceleration close to critical layers in association with a downward propagation of the critical level. In this analysis, we ignored the effect of viscous diffusion and looked at the effect of a single upward propagating monochromatic progressive wave. In the next chapter, we investigate the combination of two waves propagating upward but with opposite zonal direction while taking into account viscous diffusion at the level of the mean flow. This configuration represents a standard model for the quasi-biennial oscillation.

4. The quasi-biennial oscillation

In the Earth's lower equatorial stratosphere, zonal winds blow alternately eastward and westward with a period of approximately 28 months. These low-frequency reversals known as the **quasi-biennial oscillation (QBO)** [7] present analogues in other planetary atmospheres [89, 34], laboratory experiments [123, 119] and numerical simulations [168, 135, 28]. During most of the 65 years time period it has been observed, the QBO showed a rather robust periodicity (see Fig. 4.1). The consensus explanation for this periodic behaviour is based on the wave-mean flow interaction theory [5] and goes back to the 70s when the key role of damped gravity waves have been identified [92, 75, 122]. Based on the pioneering work of Holton & Lindzen [92, 75], Plumb derived a simple one-dimensional model of the QBO [122], where two contra-propagating internal gravity waves are damped by radiative cooling. This model has been successful in reproducing the salient periodic feature of the QBO. Yet, the QBO signal is not absolutely periodic. A reversals cycle length ranges from 26 to 29 months. These frequency variations have been associated in part with erratic synchronisations to the seasonal cycle [129, 126]. However, the possibility of an intrinsic origin of the QBO variability has not been addressed. During the northern hemisphere $2015-2016$ winter, an unexpected disruption of its periodic structure has been observed [118, 114, 37] along with other intriguing disruptions in Saturn's analogous reversals [48]. The origin of these disruptions has been attributed to extra-tropical perturbations [29, 48]. However, the mechanism by which these disturbances may affect the stratospheric oscillation has remained elusive. These observed disruptions together with the recent updates in the observational data of Saturn's QBO analogue [64] triggered a renewed scientific interest in the quasi-biennial oscillation and its reduced models [128, 70].

While idealised models have been successful in explaining the emergence of periodic solutions, the observations suggest the possibility of other regimes with enhanced variability. A natural starting point is to revisit these simplified models and explore a wider range of parameters. In this chapter, we argue that periodicity disruptions are already present in the standard 1D models [75, 122] and can be triggered by changes in external wave forcing. We unveil a surprisingly rich landscape of bifurcations which suggests an important intrinsic variability of the quasi-biennial oscillation dynamics. Based on these results, we propose an interpretation for the recently observed disruption of the Earth's

QBO.

Outline of the chapter

In section 4.1, we review the observations and the accepted phenomenology. A good introduction to the quasi-biennial oscillation can be found in Vallis' book (second edition) [161] or in the review of Baldwin and collaborators [7] for more details and references. In section 4.2, we present the standard 1D model developed by Plumb in 1977 [122] and re-explore the spontaneous emergence of the oscillating flow. In section 4.3, we present the computation of the extended bifurcation diagram of the standard 1D model presenting additional regimes with disrupted periodicity. These results are also tested against fully nonlinear simulations of a forced stratified fluid.

4.1 Phenomenology of the quasi-biennial oscillation

The quasi-biennial oscillation, **hereafter "QBO"**, denotes the oscillation of the zonal mean winds at the equator within the lower stratosphere, at altitudes of roughly 20 to 40 kilometres and latitudes between 15°N and 15°S. These winds blow at velocities of 15 to 35 metres per second (about 54 to 126 kilometres per hour). Strikingly, these winds oscillate alternatively between easterlies and westerlies with a period of roughly two years (about 28 to 29 months) hence the term "quasi-biennial". The oscillation has a downward phase propagation.

4.1.1 Observations

The first observation of a strong zonal wind in the equatorial stratosphere was made during the Krakatoa eruption in 1883 with the westward advection of the massive dust clouds which followed [162]. Westerly equatorial stratospheric winds were first observed in 1908 from balloons launched from tropical regions in Africa [11]. The reversals and the downward phase propagation have been observed 50 year later. In 1960, the QBO was discovered independently by R.J. Reed [130] and R.A. Ebdon [39] both from radiosonde measurement which started in 1953. Since then, the data acquisition has continued, revealing a striking regularity in the reversals. Figure 4.1 shows the time-height section of measurements starting from 1953 until today. This figure has been borrowed from the website of the free university of Berlin[1]. The most emblematic feature of the QBO signal is the downward phase propagation (red arrow). This downward phase propagation is the hallmark of the wave-driven nature of the phenomenon.

This phenomenon is all the more remarkable that it has also been measured on other planetary equatorial stratospheres. A quasi-quadrennial (in terms of terrestrial years) oscillation of the temperature anomalies in the Jovian equatorial stratosphere has been discovered in 1991 [89]. Figure 4.2a, shows the temperature anomalies in Jupiter's equatorial stratosphere at different heights (in pressure coordinate) and latitudes (extracted from [27]). A similar oscillation has been discovered in Saturn's equatorial atmosphere in 2008 [49]. Figure 4.2b, shows vertical mean zonal wind profile inferred from Cassini's measurement using the thermal wind balance [64] revealing a period close to 15 terrestrial

[1] `http://www.geo.fu-berlin.de/en/met/ag/strat/produkte/qbo/`, the figure is updated every month

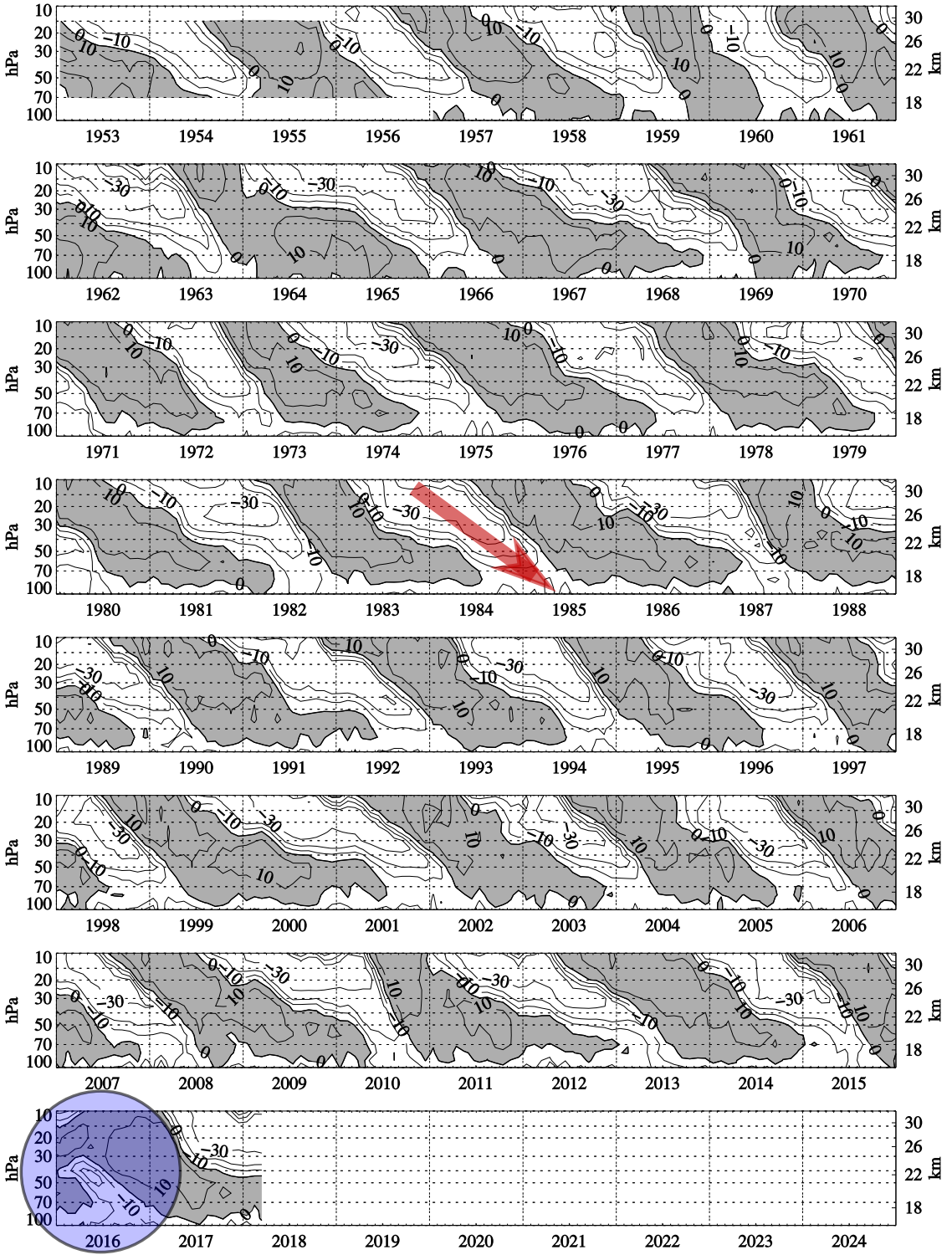

Figure 4.1: **Time-height section of monthly mean zonal winds** (m/s) at equatorial stations: Canton Island, 3°S 172°W (Jan 1953 - Aug 1967), Gan-Maledive Islands, 1°S 73°E (Sep 1967 - Dec 1975) and Singapore, 1°N 104°E (since Jan 1976). Isopleths are at $10m/s$ intervals; westerlies are shaded. This figure is borrowed from the institute for meteorology of the free university of Berlin [112]. The red arrow emphasises the downward phase propagation while blue circle highlights the recent periodicity disruption.

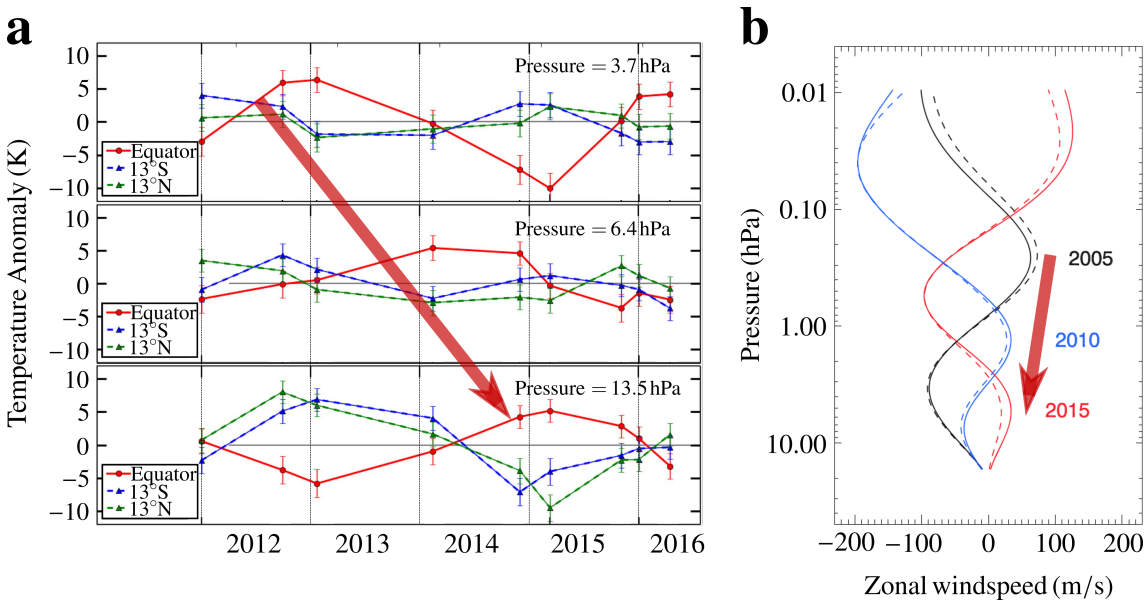

Figure 4.2: **QBO-like oscillations on Jupiter and Saturn. a.** Plots of temperature anomaly signals measured at different heights and latitudes in Jupiter's stratosphere (extracted from [27]). **b.** Plots of vertical mean zonal wind profiles of Saturn's equatorial stratosphere inferred from Cassini's temperature measurements using the thermal wind equations (borrowed from [64]).

years. Both Jupiter's and Saturn's observations present the salient feature of a downward phase propagation similar to the one shown in figure 4.2. Observations further suggest that this phenomenon may also occur in Venus' atmosphere [137]. As such, these wind reversals may be a common feature of almost all planetary atmospheres [128]. In addition, similar oscillations may also occur in the stratified stellar interior [81, 135].

4.1.2 Phenomenology

The general consensus is that the QBO is due to gravity waves streaming, as suggested by the pioneering article of Richard Lindzen and James Holton [92]. The mechanism at the origin of the QBO is illustrated in Fig. 4.3. A broad spectrum of vertically propagating gravity waves is emitted from the lower atmosphere. The momentum flux induced by the wave damping, breaking and overturning generates the zonal mean flow at the origin of the QBO. Wave breaking occurs mostly in critical layers (see sections 2.2 and 3.4). As a consequence, the vertical profile of the driving force exerted by the wave on the mean zonal flow depends on the vertical profile of the mean zonal flow itself. This two-way feedback is responsible for the downward phase propagation of the QBO, as discussed in section 3.4 (see Fig. 3.8).

A variety of waves contribute to the QBO, from large-scale and low-frequency equatorial waves to a large spectrum of internal gravity waves. On Earth, observations suggest a dominant contribution from the equatorial waves. These waves have first been discovered by Matsuno in 1966 within a rotating shallow-water framework [100] but have quickly been extended to models with continuous stratification, with applications to the quasi-biennial oscillations [75]. The eastward acceleration of the zonal flow is due mainly to Kelvin waves [165, 44] while the westward acceleration is due essentially to Rossby-gravity waves

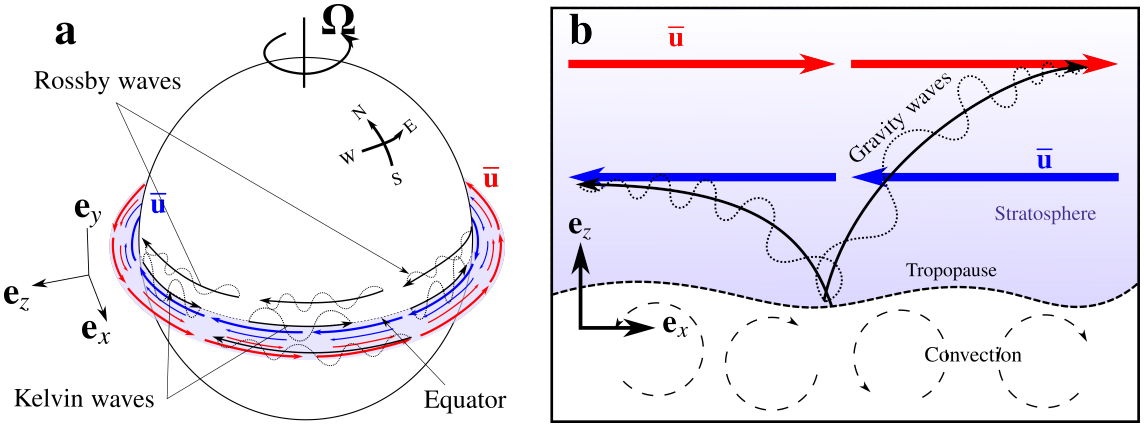

Figure 4.3: **Sketch of the QBO mechanism a.** Planetary view of the propagation of Rossby-gravity waves and Kelvin waves equatorial propagation. The vertical profile of the QBO is sketched at the equator. **b.** Sketch of the equatorial plane representing the upward propagation of gravity waves affected by the sheared mean zonal wind.

[19] (see Fig. 4.3a). The zonal phase speeds of these equatorial waves are what sets the amplitude of the QBO signal (see Fig. 3.8 on page 59). On the other hand, the rate of downward propagation is related to their amplitude. The measured amplitude of these equatorial waves is not sufficient to explain the observed downward propagation [36]. Moreover, the upwelling occurring in the tropical atmosphere reduces the downward phase propagation by roughly 1 km per month [104]. Consequently, the required amplitude of the waves is even greater. The momentum flux provided by the equatorial waves must be supplied by a broad spectrum of small-scale gravity waves generated by turbulent convection occurring in the troposphere (see Fig. 4.3b.). In the stratosphere, damping occurs due to wave breaking and radiative processes acting to maintain the stratification. The typical time-scale of these radiative processes is of the order of 20 days is comparable to the typical period of observed tropical waves (see e.g. Fig. 1 of [80]).

The wind pattern associated with the QBO is confined at the equator, where the Coriolis parameter f (i.e. the Earth rotation projected on the local vertical axis) vanishes. This is explained in part by the fact that the equatorial waves generating the mean flow are themselves trapped in the equatorial region [100, 31]. Another possible explanation is the balance of the low-frequency wave forcing (with a period close to 2 years) with the Coriolis torque due to the meridional circulation at higher latitudes. More details concerning this second explanation are provided in [7]. Two-dimensional models of the QBO, focusing on the equatorial plane, ignore most of the effect of rotation but reproduce qualitatively well the phenomena. However, capturing the meridional extent of the QBO signal requires a 3D model with a meridional increase of the Coriolis parameter. **In this thesis, we restrict our selves to the two-dimensional problem and leave the 3D and rotational effects to future work.** Nevertheless, we provide some perspectives regarding rotation and 3D effects in subsection 4.3.3

Another very important process which controls the QBO is momentum diffusion. At the planetary scale, momentum diffusion is mostly the result of small-scale turbulent processes. Part of the turbulence actually comes from the breaking of gravity waves themselves. In the stratosphere, estimates of the associated eddy diffusivity present huge uncertainties

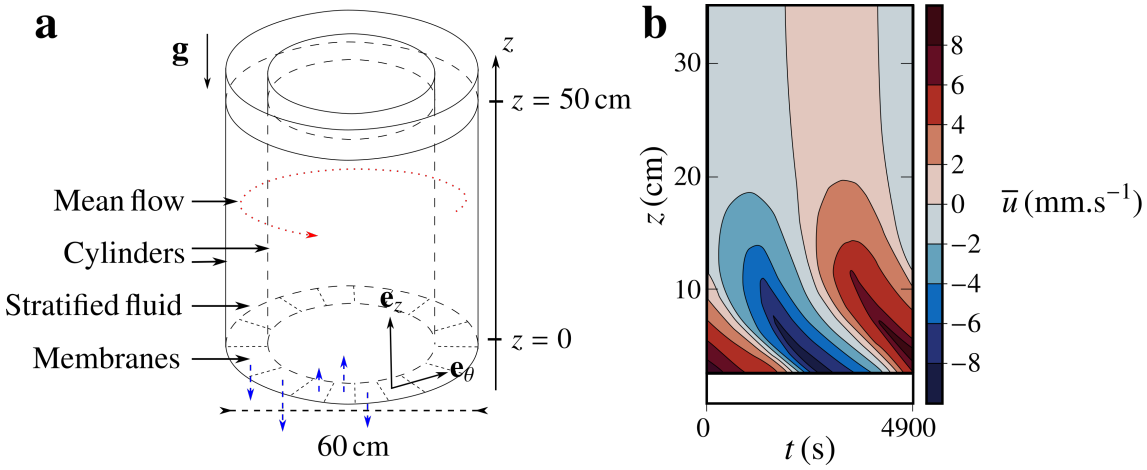

Figure 4.4: **Plumb and McEwan experiment: A laboratory analogue of the QBO. a.** Sketch of the experimental apparatus. **b.** Time-height section of the azimuthally averaged measured azimuthal flow (borrowed and adapted from [123]).

[67]. Yet, as we shall see, the balance between gravity wave streaming and (eddy) viscous stresses is important to the reversals of the zonal wind. The details of this mechanism are better understood through the use of conceptual models.

4.1.3 Laboratory analogue

The theory for the QBO discussed in the previous subsection, first developed by Lindzen and Holton in 1968 [92], then refined by Plumb [122], has been successfully tested with the celebrated laboratory experiment conducted in 1978 by Plumb and McEwan [123]. They identified the salient ingredients for the spontaneous emergence of low-frequency flow reversals, namely (i) a horizontally periodic geometry (ii) two damped upward propagating gravity waves travelling towards opposite periodic directions. They designed a tank formed of two concentric cylinders with the azimuthal direction being the analogue of the Earth's zonal direction. The tank is filled with stably stratified fluid (salted water) and a standing wave is generated at the bottom using flexible membranes and pistons. This forces counter-propagating internal gravity waves in the fluid. These waves are damped by the viscosity and by the lateral walls' friction instead of radiative effects predominant in the atmosphere. A sketch of the experimental apparatus is provided in figure 4.4a.

By increasing the wave amplitude, Plumb and McEwan reported the occurrence of an instability resulting in the emergence of a slowly varying and oscillating azimuthal mean flow. The mean flow eventually reaches a limit cycle whose pattern, shown in figure 4.4b, is in strikingly good qualitative agreement with the atmospheric observation shown in figure 4.1. The experimental study of mean flow reversals driven by gravity waves is still an active field of research interest. The Plumb and McEwan experiment has been reproduced by Otobe and collaborators in 1998 [119] with further analyses. The apparatus shown in figure 2.9a is currently used at LPS (ENS, Paris) to study the details of the QBO bifurcation [146]. Moreover, an attempt to reproduce similar mean flow reversals driven by convectively forced waves is under investigation at IRPHE (Marseilles) [85].

4.1.4 Periodicity disruptions

During the year 2016, the QBO presented a significant deviation from its quasiperiodic behaviour documented since 1953 [118]. An easterly jet formed roughly midway of the usual bottom westerly phase (see blue circle in Fig. 4.1). Moreover, this jet appeared at a lower altitude than previously observed. The analysis of the momentum fluxes suggests that an exceptionally strong extra-tropical Rossby wave coming from the northern hemisphere triggered the sudden westward acceleration of 2016 [29]. On Saturn, a similar disruption has been explained by an extra-tropical event [48].

The influence of the external environment on the QBO variability is undeniable. However, how the QBO reacts to external perturbations may hinge on the intrinsic properties of its dynamics. For instance, the variations in the timing of each reversals has been attributed to the erratic synchronisation of the QBO phases to the seasonal cycle [129]. Rajendran and collaborators studied a simple model of the QBO accounting for the annual cycle signature in the tropical upwelling [126]. They revealed that the synchronisation regime depends greatly on the wave forcing amplitude which controls the intrinsic period of the reversals. Similar results applied to the El Niño southern oscillation have been obtained using simple models [78] and traced up to quasi-realistic models [33].

This has been a strong incentive for us to revisit the standard one-dimensional model of the QBO in order to understand what controls its variability. After first presenting the model in section 4.2, we unveil many unsuspected regimes with altered periodicity in section 4.3. Based on these results we propose a novel interpretation of the 2016 disruption.

4.2 An idealised 1D model

Here, we present the one-dimensional model, first derived by Plumb in 1977 [122], capturing the basic dynamics of the QBO. We start from the 2D and zonally periodic configuration already introduced in Chapter 3. Many notations and results of Chapter 3 are used in this section.

4.2.1 Model derivation and periodic flow reversals

Following [122], we consider the propagation of two monochromatic plane waves propagating upward with opposite zonal direction. These waves are deflected differently by the mean zonal flow depending on their zonal direction of propagation. To simplify the discussion, we assume that the waves are damped solely by radiative cooling; viscosity is ignored in the wave equations (3.51). The effects of viscous damping will be discussed in section 4.3 and Chapter 5.

Considering a frozen-in-time sheared mean flow, the two waves are computed separately using the static geometrical optics expression (3.72), (3.103) and (3.106) obtained in Chapter 3. For an arbitrary background flow shown in figure 4.5b, a color-plot of the associated wave field is shown in figure 4.5b. The color-plots associated with the two separate parts of the wave field are shown in figures 4.5a and c.

Let us rewrite the mean flow equation introduced in (3.50)

$$\partial_t \overline{u} - \frac{1}{\mathrm{Re}} \partial_z^2 \overline{u} = -\partial_z \overline{u' w'}. \tag{4.1}$$

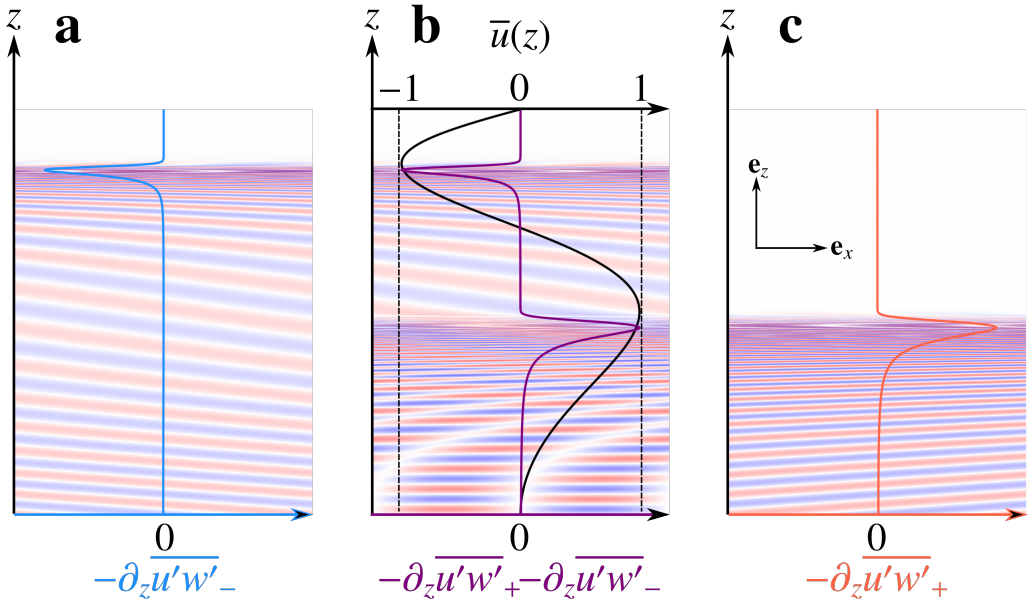

Figure 4.5: **Idealised configuration.** The colour-plot of the wave field associated with a standing wave excitation is shown in panel **b** while the colour-plot of the wave fields associated with each individual components are shown in panels **a** and **c** separately. These wave fields are computed using the static geometrical optics approximation developed in Chapter 3 using the mean flow profile $\overline{u}(z)$ plotted in panel **b** with a black line. Following the same decomposition, the streaming body force is shown in panel **b** with a purple line while the individual contribution coming from each waves are shown in panel **a** and **c** with blue and orange lines respectively.

The upward momentum flux divergence associated with the wave field can be decomposed into two terms associated with each progressive component individually

$$\partial_z\overline{u'w'} = \partial_z\overline{u'w'}_+ + \partial_z\overline{u'w'}_-, \tag{4.2}$$

where the indices $+$ and $-$ refer to the horizontal direction of propagation (see Fig. 4.5). Cross terms vanish thank to the combination of the horizontal and fast time average (see eq. (3.39)). Using the static geometrical optics approximation, and considering the limit $\Gamma \ll 1-\overline{u} \ll \mathrm{Fr}^{-1}$, the expression of $\partial_z\overline{u'w'}_+$ is given by Eq. (3.109) that we reproduce here for clarity

$$\partial_z\overline{u'w'}_+(z) = -\frac{\varepsilon^2}{2\mathrm{Fr}^2}\frac{1-\overline{u}(0,t)}{(1-\overline{u}(z,t))^2}\exp\left\{-\frac{\Gamma}{\mathrm{Fr}}\int_0^z \frac{\mathrm{d}z'}{(1-\overline{u}(z',t))}\right\}. \tag{4.3}$$

Assuming also $\Gamma \ll 1+\overline{u} \ll \mathrm{Fr}^{-1}$, the expression for $\partial_z\overline{u'w'}_-$ is simply the opposite of Eq. (4.3), with $1-\overline{u}$ replaced everywhere by $1+\overline{u}$. The vertical profiles of $-\partial_z\overline{u'w'}_+$, $-\partial_z\overline{u'w'}_-$ and their sum are represented in figures 4.5a, c and b respectively.

The viscous contribution to the damping of the wave is ignored. However, viscosity is an essential ingredient of the mean flow equation, as it acts on the curvature of the velocity profile. Computation of the mean flow requires one more boundary condition than in the inviscid case. Here, we consider a no-slip bottom boundary condition (3.52c). The

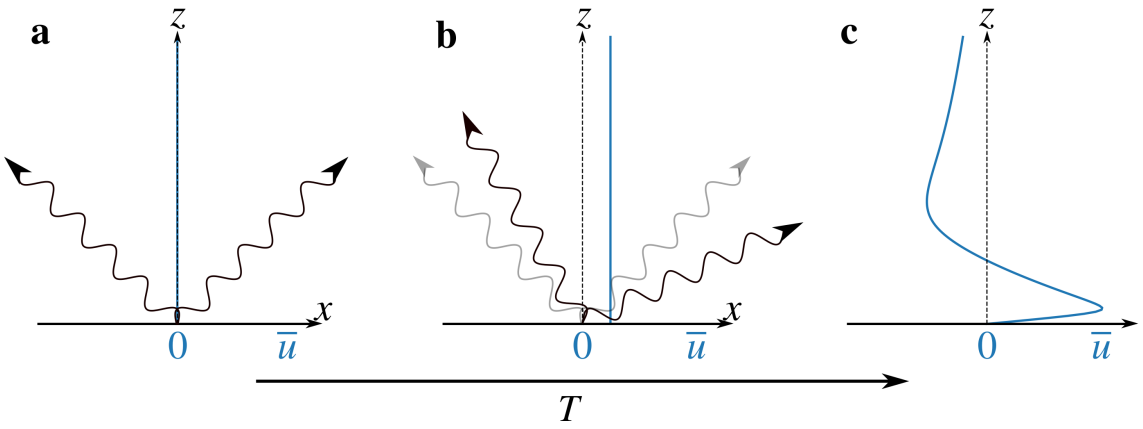

Figure 4.6: **Instability of the rest state.** The two counter-propagating component of the wave are represented with undulated arrows, the mean flow vertical profiles are represented by blue lines. When there is no mean flow (panel **a**), the streaming forces associated with the two waves are cancelling each other out by symmetry. With a small homogeneous positive mean flow (panel **b**), the wave propagating rightward is slightly bent towards the ground while the other one is slightly bent upward. The symmetry is broken and one wave is forcing the mean flow lower than the other. As the result, an inhomogeneous vertical mode grows (panel **c**). Unless this growth is compensated by a sufficiently high viscosity, the rest state is unstable.

evolution equation (3.50) becomes

$$\partial_t \overline{u} - \frac{1}{\mathrm{Re}}\partial_z^2 \overline{u} = \frac{\varepsilon^2 \Gamma}{2\mathrm{Fr}^2} \sum_{j=1}^{2} \frac{(-1)^j}{1-(-1)^j \overline{u}} \exp\left\{ -\Gamma \mathrm{Fr}^{-1} \int_0^z \frac{\mathrm{d}z'}{1-(-1)^j \overline{u}} \right\}. \tag{4.4}$$

Following Vallis' book [161], Eqs. (17.64) and (17.65), we introduce the characteristic length and time

$$\Lambda_\Gamma = \frac{\mathrm{Fr}}{\Gamma} \quad , \quad \mathcal{T} = \frac{2\mathrm{Fr}^2}{\varepsilon^2 \Gamma}. \tag{4.5}$$

Using the rescaled space and time variables $Z = z/\Lambda_\Gamma$ and $T = t/\mathcal{T}$, Eq. (4.4) is rewritten in the nondimensionalised form

$$\partial_T \overline{u} - \frac{1}{\widetilde{F}}\partial_Z^2 \overline{u} = \sum_{j=1}^{2} \frac{(-1)^j}{\left(1-(-1)^j \overline{u}\right)^2} \exp\left\{ -\int_0^Z \frac{\mathrm{d}Z'}{\left(1-(-1)^j \overline{u}\right)^2} \right\}, \tag{4.6}$$

with

$$\widetilde{F} = \frac{\varepsilon^2 \mathrm{Re}}{2\Gamma}. \tag{4.7}$$

The dimensionless QBO equation (4.6), is a nonlinear integrodifferential equation controlling the evolution of the mean flow $\overline{u}$. The only parameter left, $\widetilde{F}$, measures the relative strength of the wave forcing to the viscous stress. We solve this equation numerically using a centered second-order finite difference method in Z and a second-order Adams-Bashforth

Frame 4.2.1 Standard 1D model of the Quasi-Biennial Oscillation

Two upward propagating internal gravity waves with opposite zonal phase speed, damped by radiative cooling force a mean zonal flow. The mean flow evolution equation reduces to a one-dimensional integrodifferential equation which has been first proposed by Plumb [122]. In nondimensionalised form, it writes

$$\partial_T \overline{u} - \frac{1}{\widetilde{F}} \partial_Z^2 \overline{u} = -\partial_Z \left(e^{-\int_0^Z \frac{\mathrm{d}Z'}{(1-\overline{u})^2}} - e^{-\int_0^Z \frac{\mathrm{d}Z'}{(1+\overline{u})^2}} \right). \tag{4.8}$$

A single parameter $\widetilde{F} = \mathcal{F}_0 \Lambda/(c\nu)$, measuring the relative amplitude of the wave forcing with respect to the mean viscous stress, controls the stationary solution. $\mathcal{F}_0 = ((u'w')|_{z=0})_{\text{r.m.s.}}$ is the bottom momentum flux amplitude of the wave, $\Lambda = c^2 k/(N\gamma)$ is homogeneous damping length scale associated with radiative cooling γ, c and k are the zonal phase speed and wave number of the waves, N is the buoyancy frequency and ν is the eddy-viscosity. The characteristic length, time and mean flow scales used to nondimensionalised the equation are Λ, $\mathcal{T} = c\Lambda/\mathcal{F}_0$ and c respectively.

A no-slip bottom boundary condition is used

$$\overline{u}|_{Z=0} = 0, \tag{4.9}$$

although the use of a free-slip condition may also be justified.
The derivation of this model relies upon **five important hypotheses**:

- Quasilinear approximation (wave-wave interaction neglected)
- Static geometrical optics approximation
- Hydrostatic approximation
- Weak damping approximation
- Viscous damping of the wave ignored

scheme in T. A solid wall is added at the upper boundary with a free-slip condition. The details of the numerical resolution are provided in appendix A. A summary of the model is provided in frame 4.2.1.

For small values of wave forcing, the rest state, $\overline{u} = 0$, is a stable fixed point of Eq. (4.6). However, as the forcing is increased, this fixed point becomes unstable. We notice that no fixed point exists in the inviscid limit [122]. Figure 4.6 illustrates the wave-mean flow mechanism underlying this instability. Above a given forcing threshold, the mean flow $\overline{u}$ is attracted towards a limit cycle whose time-height section is shown in figure 4.7a. The essential features of the observed QBO are reproduced (see Fig. 4.1): the reversals and the downward phase propagation.

Figure 4.7b shows the vertical profile of the mean flow at different stages of the QBO limit cycle, equally spaced in time. The mechanism at the origin of the reversals appears clearly. Starting with the profile b-01, we are in a configuration similar to the one shown in figure 4.5. The streaming coming from the wave propagating rightward, dominant at

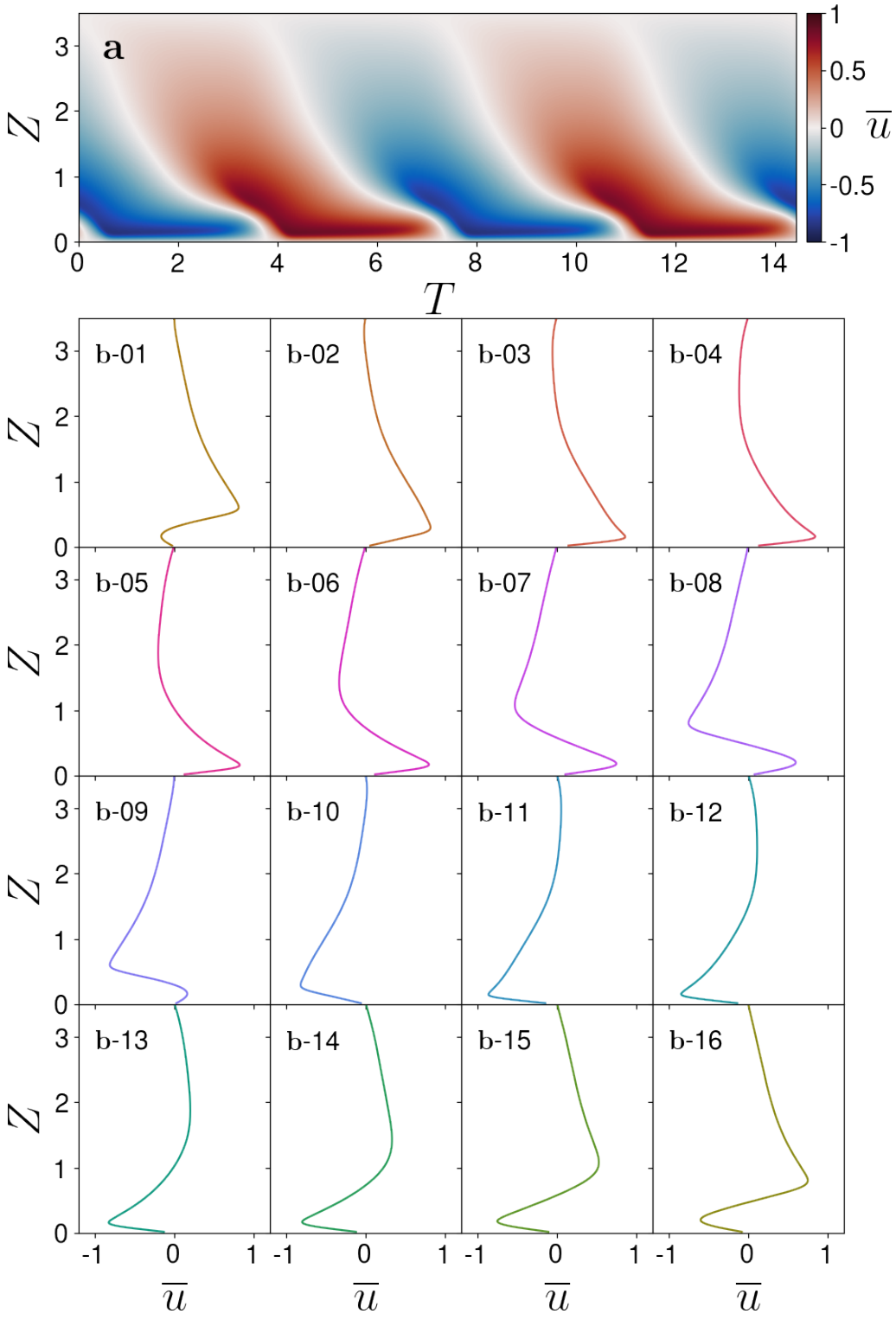

Figure 4.7: **1D model. a.** Time height section of the mean flow $\overline{u}$ limit cycle obtained by solving numerically Eq. (4.6) with $\widetilde{F} = 10$, $N_z = 200$, $Z_{max} = 3.5$ and $\delta T = 0.003$ (see appendix A). The period of the reversals is $T_{\text{qbo}} \approx 7.2$. **b**-01 to **b**-16. Vertical profile of the mean flow $\overline{u}(Z, T_i)$ shown at different time of the limit cycle with $T_i = i \times T_{QBO}/16$ for panel **b**-i.

lower heights, is forcing the mean flow towards the critical value $+1$. Then, from b-02 to b-07, the rightward forcing is balanced by the viscous stress due to the positive shear at the bottom. Meanwhile, the wave propagating leftward is forcing the mean flow towards the critical value -1 at a greater height. In b-08, the negative shear created by the combined effect of the rightward and leftward forcing is strong enough for the associated viscous stresses to come into play. Then, the rightward forcing is counterbalanced by the viscous stress associated with both the positive shear at the bottom and the negative shear above it. This is how the reversal is triggered. Then, the profile b-09 is the symmetric of b-01 and the same scenario begins in the reversed direction.

4.2.2 The QBO bifurcation

In subsection 4.2.1, we introduced the standard 1D model reproducing the salient features of the QBO signal. The stationary solution of the model is controlled by a single parameter $\widetilde{F}$. If this parameter is low enough (corresponding to the small wave forcing), the rest state is stable and there is no reversal. By increasing $\widetilde{F}$ sufficiently, we obtained a limit cycle, corresponding to periodic flow reversals. The bifurcation associated with the transition from the rest state towards the oscillating state has been studied in details by Yoden and Holton in 1988 [171].

The 1D model they considered is identical to the one summarised in frame 4.2.1 (page 70). Performing a numerical linear stability analysis of the rest state, they obtained a critical value $\widetilde{F}_c \approx 4.25$ associated with a Hopf bifurcation. This means that at the critical value $\widetilde{F}_c$, a pair of complex-conjugate eigenvalues of the problem linearised about the rest state crosses the imaginary axis - moving from negative to positive real part. We built a bifurcation diagram by directly computing the stationary solutions of the fully nonlinear problem for different values of $\widetilde{F}$. Figure 4.8a shows the peak-to-peak amplitude of the signal as a function of the parameter $\widetilde{F}$ while 4.8b shows the period of the signal. At the transition, the period of the obtained signal is well-defined and corresponds to the linear stability computation of Yoden and Holton with $T_{\mathrm{qbo},c} \approx 11$.

In the considered 1D model, a no-slip boundary condition is used for the mean flow at the bottom. This choice is actually considered in most of the literature treating similar 1D models. We show that changing the boundary condition significantly impact the nature of the bifurcation. This effect had to our knowledge been overlooked in previous studies. In appendix B, we present a study of the QBO bifurcation when a free-slip condition is considered for the mean flow instead of the no-slip condition (4.9) with

$$\partial_Z \overline{u}|_{Z=0}. \tag{4.10}$$

It turns out that the linear stability analysis is solvable analytically in this case. We explicitly compute the critical value $\widetilde{F}_c = j_{0,1}^2/16 \approx 0.36$ where $j_{0,1}$ is the first non-zero root of the zeroth order Bessel function of the first kind. A direct computation of the bifurcation diagram is shown in figures 4.8c and d, confirming the analytical prediction of $\widetilde{F}_c$ in the free-slip case.

There is an order of magnitude difference between the critical values obtained in the free-slip and the no-slip case. Moreover, the bifurcation is no longer a Hopf bifurcation as the period of the stationary signal diverges close to the transition (see Fig. 4.8d). These results demonstrate that the choice of the boundary condition should not be overlooked. In

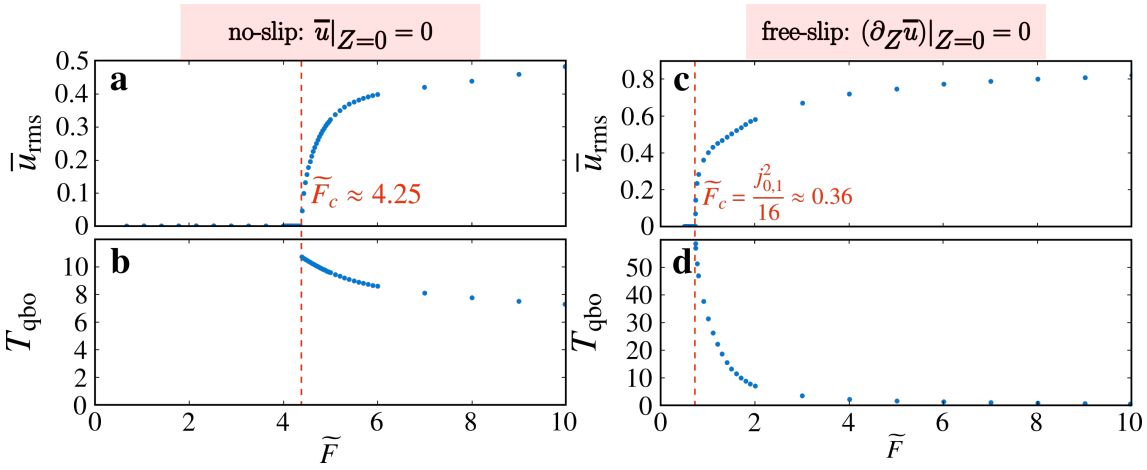

Figure 4.8: **Bifurcation from rest state to limit cycle. a.** Peak-to-peak amplitudes of the stationary solutions of the fully nonlinear 1D model (summarised in frame 4.2.1 page 70) as a function of $\widetilde{F}$. **b.** Periods of the stationary solutions (if applicable). The prediction of Yoden & Holton [75] has been emphasised by a vertical dashed orange line. **c** and d. Same as a and b but with a free-slip bottom boundary condition of the mean flow instead of no-slip. The analytical prediction is emphasised by a vertical dashed orange line.

Chapter 5, we will show that the choice for the bottom boundary condition impacts the so-far ignored viscous boundary layers of the waves which in turns affect the bifurcations in the QBO model.

In the remaining of this chapter, we consider the no-slip boundary condition only and chase new transitions by increasing the forcing parameter $\widetilde{F}$ beyond the first Hopf bifurcation.

4.3 Quasiperiodic route to chaos in models of the QBO

In the previous section, we reviewed the periodic solution of a standard 1D model of the QBO and revisited the first bifurcation from a stable rest state towards a periodic limit cycle. Numerous physical systems present such bifurcation from steady regimes (here the rest state) towards periodic nonlinear solutions. Many of them present additional bifurcations when a forcing parameter is further increased with a transition from the periodic limit cycle to quasiperiodic solutions along with frequency locked regimes for certain ranges of the parameter. Eventually, these systems reach chaotic states with the concomitant sensibility to initial condition. These sequence of bifurcations, known as the quasiperiodic route to chaos, have been observed through the study of the onset of fluid turbulence in simple geometries.

In this chapter, we show the existence of a quasiperiodic route to chaos in the standard 1D model of the QBO (see subsection 4.3.2). First, we begin, in subsection 4.3.1, by a brief review of the quasiperiodic route to chaos in the context of fluid mechanics illustrated with an observation made in Rayleigh-Bénard convection.

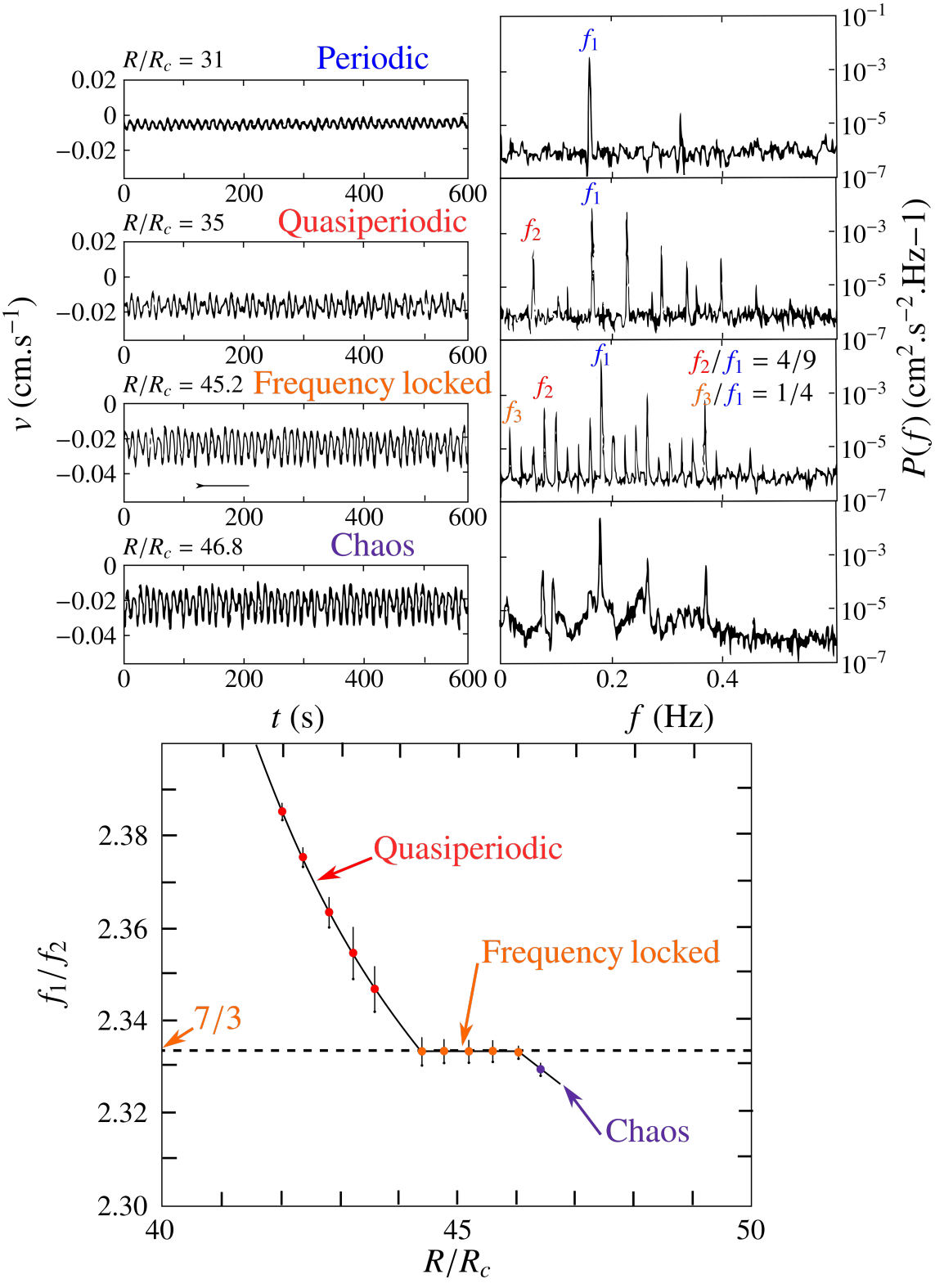

Figure 4.9: **Quasiperiodic route to chaos in Rayleigh-Bénard convection** (Borrowed and adapted from [58, 156]) The upper-left panels show measured velocity signal for different Rayleigh numbers while the upper-right panels show the associated power-spectrum highlighting the different regimes. The lower panel shows the ratio of two primary frequencies of the signal as a function of the Rayleigh number. The rational number associated with the frequency locked regimes is different between the upper and lower panels due to a non-reproducibility reported by [58].

4.3.1 Quasiperiodic route to chaos in fluid mechanics

Since the seminal work of Reynolds [131], the onset of turbulence in fluids has thoroughly been studied. A few numbers of scenarios have been observed when increasing the forcing on flows - often reflected by the Reynolds number - within various geometries. Steady laminar solutions prevail at low forcing. At higher forcing, the flow may transition towards stationary solution breaking the spatial symmetry of the original state, or to periodic limit cycles breaking time translation symmetry of the original state. By even further increasing the forcing, the flow undergoes additional bifurcation bringing more and more complexity. A chaotic regime is reached when the Lyapunov characteristic exponents of the dynamics - characterising the rate of separation of infinitesimally close trajectories - are positives.

One of these scenarios is the quasiperiodic route to chaos with first insights from Landau & Lifshitz followed by a complete characterisation by Ruelle, Takens & Newhouse [113]: starting from a nonlinear periodic solution, the system undergoes a sequence of bifurcations adding a new frequency to the initial periodic motion. When there are two frequencies with an irrational ratio, the flow pattern is then described as quasiperiodic. When there are more than two frequencies, Ruelle, Takens & Newhouse showed that the flow is then chaotic in general. Sometimes, the paired-ratios of the different frequencies of the system become rational for an extended range of the forcing parameter such that the motion recovers a periodic structure. Such regimes - referred to as frequency locked - are often embedded within quasiperiodic or chaotic states.

The quasiperiodic route to chaos - although not the unique one - has been observed in many configurations from Taylor-Couette flows [105], channel flows [65] or Rayleigh-Bénard convection [57]. Figure 4.9 shows a quasiperiodic to chaos observed in Rayleigh-Bénard convection by Gollub & Benson [58] for increasing Rayleigh numbers R [2]. We see the emergence of additional frequencies as the Rayleigh number is increased. For some range of the Rayleigh number, the ratio of frequency peaks is locked into a rational number.

In next subsection, we report a similar quasiperiodic route to chaos in the standard 1D model of the QBO. In this model the zonal flow $\overline{u}$ is forced by the gravity wave streaming whose amplitude is controlled by the parameter $\widetilde{F}$ playing a similar role to the Rayleigh number here.

4.3.2 Periodicity disruption of a model QBO (*submitted publication*)

Here, we further explore the bifurcation diagram of the standard 1D model of the QBO summarised in frame 4.2.1 (page 70). We already described the emergence of a periodic orbit. We now show that this model presents a quasiperiodic route to chaos with the emergence of quasiperiodicity, frequency locking and eventually chaos. In the context of the solar tachocline with a similar 1D quasilinear-model, Kim & McGregor have offered the first glimpse into those regimes [81]. However, their pioneering observation was sparse, and they did not build any bifurcation diagram. Here we fill this gap.

In figure 4.10, we present five well-chosen regimes of the idealised 1D model of the QBO associated with four increasing values of the forcing parameter $\widetilde{F}$. The left panels

[2] The Rayleigh number compares the transport of heat coming from the convection to the transport coming from the diffusion. In the context of Rayleigh-Bénard convection, increasing the Rayleigh number amounts to increase the Reynolds number.

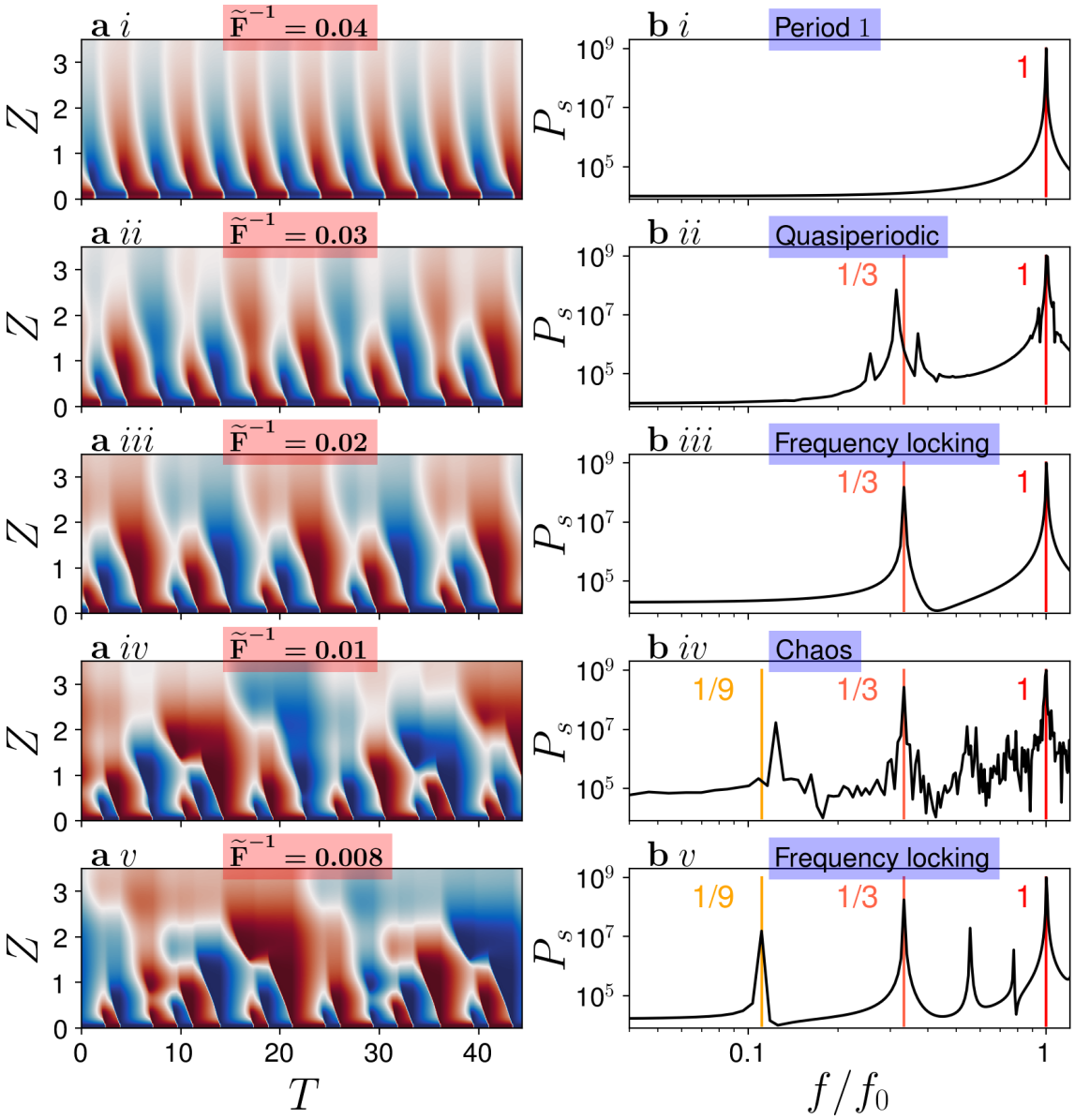

Figure 4.10: **Secondary bifurcations of the 1D QBO-model. a.** Time-height sections of the stationary mean flows $\overline{u}(Z,T)$ of the 1D QBO-model for $\widetilde{F}^{-1} = 0.04$ (*i*), 0.03 (*ii*), 0.02 (*iii*), 0.01 (*iv*) and 0.008 (*v*). Roughly 15 reversals are shown. Red, blue and white areas correspond to positive, negative and vanishing mean flow respectively. **b.** Power spectrum of the bottom mean flow $\overline{u}(Z = 0.1, T)$. The frequency axis is rescaled by the frequency of the reversals. The values 1, $1/3$ and $1/9$ are emphasised in red, orange and yellow respectively. Logarithmic axes are used.

show the time-height sections of the associated mean flows $\overline{u}(Z,T)$ while the right panels show the power-spectrum of the mean flow signal at the bottom, $\overline{u}(Z=0.1,T)$.

We observe a first transition from the periodic regime to a quasiperiodic with the emergence of an additional lower frequency in the spectrum. Then, for a higher forcing parameter, we observe a frequency locked state where the second frequency is locked at one-third of the primary frequency. In this case, the mean flow is thus periodic with an overall period three times bigger than the mean reversals period at the bottom.

After increasing again the forcing, a third frequency arises lower than the two previous ones leading back to a quasiperiodic or to a chaotic state (depending on the Lyapunov exponents). Finally, we report an additional frequency locked regime is obtained at even greater forcing where the three primary frequencies have rational ratios. In this case, the overall period of the mean flow is nine times bigger than the mean reversals period.

These observations suggest building a bifurcation diagram highlighting the different critical values for the forcing parameter $\widetilde{F}$. This work led to the redaction of a scientific article currently under peer-review. The preprint is included hereinbelow.

In this work, we consider the additional effect of the viscous damping on the wave beam. This leads to the consideration of a second parameter α in the model measuring the relative strength of the viscous damping compared against the radiative damping (solely considered so far). This additional parameter allowed us to compute a 2D bifurcation diagram of the 1D QBO-model unveiling an unforeseen complexity in the bifurcation structure (see Fig. 1 of the preprint). We also use the MIT GCM - a widely used general circulation model [96] resolving the primitive equations - to account for the full nonlinear dynamics of the waves and showed that the bifurcations persist in these nonlinear simulations (see Fig. 2 of the preprint). Based on the phenomenon of critical slowing down associated with the existence of bifurcations in systems [141], we show the enhancement of the variability provoked by external perturbations - such as the one observed in the 2016 QBO (see Fig. 4.1) - in association to an intrinsic dynamical variability (see Figs. 3 and S5 of the preprint).

We invite the reader to take notice that the parameter $\widetilde{F}$ is interpreted as a Reynolds number Re in the preprint. To accompany the reading of this article, we provide figure 4.11 and appendix C illustrating and summarising the method used to compute the bifurcation diagrams shown and discussed in the preprint.

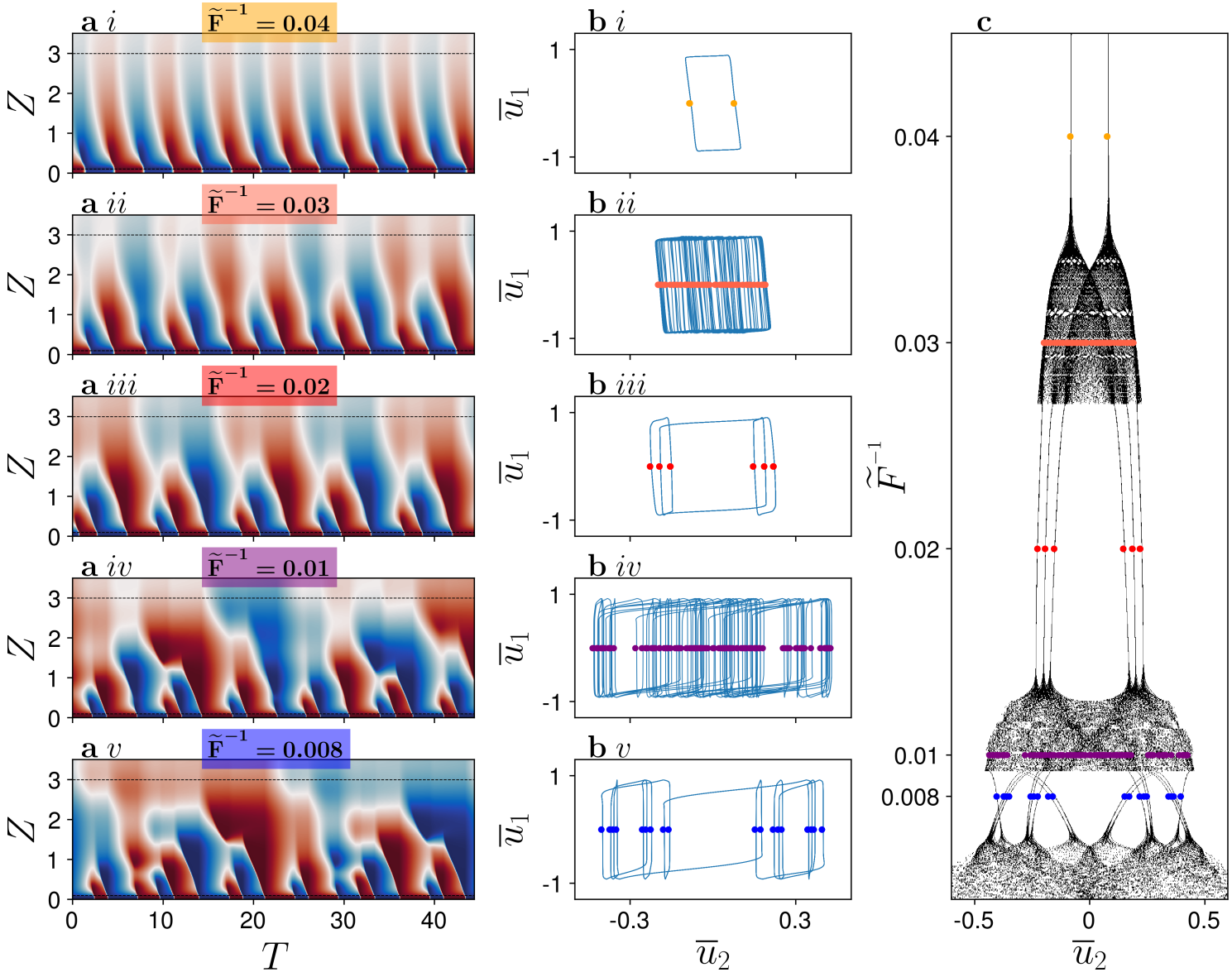

Figure 4.11: **From time-height sections to bifurcation diagram. a.** Time-height sections of the stationary mean flows $\overline{u}(Z,T)$ of the 1D QBO-model for $\widetilde{F}^{-1} = 0.04$ (*i*), 0.03 (*ii*), 0.02 (*iii*), 0.01 (*iv*) and 0.008 (*v*). Roughly 15 reversals are shown. Red, blue and white areas correspond to positive, negative and vanishing mean flow respectively. **b** Phase space trajectories projected on a 2D space defined by mean flows at two different heights: $\overline{u}_1(T) = \overline{u}(Z = 0.1, T)$ and $\overline{u}_2(T) = \overline{u}(Z = 3, T)$. Horizontal dashed black line are plotted over the time-height sections to highlight the heights $Z = 0.1$ and $Z = 3$. **c** Poincaré sections of the 1D model solutions as a function of $\widetilde{F}$ (see appendix C for details).

Periodicity disruption of a model quasi-biennial oscillation

Antoine Renaud[a], **Louis-Philippe Nadeau**[b], **and Antoine Venaille**[a]

[a]Univ Lyon, Ens de Lyon, Univ Claude Bernard, CNRS, Laboratoire de Physique, F-69342 Lyon, France; [b]Institut des Sciences de la Mer de Rimouski, Université du Québec à Rimouski. Rimouski, Québec, Canada

This manuscript was compiled on September 19, 2018

The quasi-biennial oscillation (QBO) of equatorial winds on Earth is the clearest example of the spontaneous emergence of a periodic phenomenon in geophysical fluids. In recent years, observations have revealed intriguing disruptions of this regular behaviour that have been attributed to extra-tropical perturbations. However, the mechanism by which these disturbances may affect the oscillation has remained elusive. Here, it is shown that part of the observed variability of the QBO can be attributed to the intrinsic dynamics of wave-mean flow interactions in stratified fluids. Using a constant-in-time monochromatic wave forcing, bifurcation diagrams are mapped for a hierarchy of simplified models of the QBO, ranging from a simplified quasilinear model to fully nonlinear simulations. The existence of a rich variety of dynamical regimes as well as a quasiperiodic route to chaos is reported in these models as the forcing amplitude is increased. The possibility for periodicity disruptions of a given QBO-like dynamical regime is then investigated by probing its resilience to time-varying external perturbations and ambient noise. Results show a clear signature of "critical slowing down", i.e. the recovery rate of the periodic oscillation to both external perturbations and ambient noise decreases as the system approaches a bifurcation point, thus suggesting a key role of the intrinsic dynamics in interpreting the observed variability of the QBO.

Stratified Fluids | Dynamical Systems | Quasi-Biennial Oscillation

Earth's equatorial stratospheric winds oscillate between westerly and easterly every 28 months. These low-frequency reversals known as quasi-biennial oscillations are driven by high-frequency waves emitted in the lower part of the atmosphere (1). It is an iconic example of the spontaneous emergence of a periodic phenomenon in a turbulent geophysical flow (2), with analogues in other planetary stratospheres (3–6), in laboratory experiments (7), as well as in idealized numerical simulations (8, 9).

In recent years, increasing attention has been given to the robustness of these regular reversals to external wave forcing and perturbations. Disruptions of this type of oscillations have been observed both in the Earth's atmosphere (10–12) and in Saturn's atmosphere (13). In addition, a variety of oscillatory regimes, including non-periodic ones, have been reported in direct numerical simulations of a stratified fluid forced by an oscillating boundary (8) or driven by an explicitly resolved turbulent convective layer (9). Non-periodic oscillations have also been reported in global circulation model simulations of the solar interior and Giant planets (14, 15).

Until now, the non-periodic nature of the reversals were interpreted as the system's response to transient external variations. For example, the non-periodic disruption of the Earth's QBO and Saturn's QBO-like oscillation have been attributed to the response of equatorial stratospheric dynamics to extratropical perturbations (10, 11, 13). Also, the existence of nonperiodic regimes in direct numerical simulations of stratified flows has been related to the time variability of the underlying turbulent convective layer (9, 15). Here, we show that the non-periodic nature of the reversals is a fundamental characteristic of stratified fluids by revealing the existence of a vast diversity of oscillatory regimes obtained using a simple steady monochromatic forcing. We further demonstrate that this rich intrinsic variability effectively controls to a large extent the system's response to a transient external variation. Periodicity disruptions are more easily triggered and are increasingly lengthened when the system approaches a bifurcation point.

Idealized models of the quasi-biennial oscillation

The simplest configuration capturing the dynamics of the quasi-biennial oscillation (QBO, Fig. 1a) is given by a vertical section of a stably stratified Boussinesq fluid, periodic in the zonal (longitudinal) direction, and forced by upward propagating internal gravity waves. This wave forcing is typically generated by an oscillating bottom boundary meant to represent the effect of tropopause height variations on the stratosphere. The evolution of the horizontally averaged zonal velocity, $\overline{u}$, is governed by a simplified version of the momentum equation

$$\partial_t \overline{u} - \nu \partial_{zz} \overline{u} = -\partial_z \overline{u'w'}, \qquad [1]$$

where ν is the kinematic viscosity, z is the upward direction, and $\overline{u'w'}$ is the Reynolds stress due to velocity fluctuations

Significance Statement

Oscillatory reversals of equatorial winds are ubiquitous in planetary atmospheres. On Earth, recent observations of the disruption of the quasi-biennial oscillations have been attributed to external perturbations, but the mechanism explaining the disrupted response has remained poorly understood. Here we show that part of the observed response can be attributed to intrinsic variability. First, we demonstrate the existence of a vast variety of oscillatory modes separated by bifurcation points in simplified models of the equatorial atmosphere. Second, we show that the proximity to a bifurcation point has crucial consequences on the system's response to ambient noise as well as external perturbations, which has important implications for interpreting perturbations of this regular phenomenon on Earth and in other planetary atmospheres.

All the authors participated in the design of numerical experiments, in the discussion of the physics, and in the redaction of the paper. AR performed the simulations with the help of LPN. AR performed data analysis. AV initiated the project.

The authors declare no conflict of interest.

[2]To whom correspondence should be addressed. E-mail: antoine.venailleens-lyon.fr

around the zonal average. In weakly nonlinear regimes, this stress is carried by internal gravity waves, and any process damping the wave amplitude leads to a transfer of momentum from the waves to the mean-flow through the Reynolds stress divergence. Wave properties are also affected by the mean-flow and this interplay results in a complex coupled system.

To close the dynamical system, one needs to compute the Reynolds stress in (1). In this study, the wave field is simulated either by taking into account for all nonlinear interactions between waves and mean-flow (hereafter "nonlinear 2D or 3D model") or by considering a simplified closure that neglects wave-wave interactions, together with a WKB approach (16). The latter approach (hereafter "quasilinear 1D model") has proven to be successful in explaining the spontaneous emergence of low-frequency periodic flow reversals (2, 16). Therefore, it is natural to ask whether periodicity disruptions can be understood in this framework as a minimal starting point.

We consider a standing wave pattern with wavenumber k and frequency ω, forcing a stratified fluid with buoyancy frequency N, for which the background stratification is maintained by Newtonian cooling with damping rate γ. Together, the Newtonian cooling γ, and the viscosity ν, damp the wave amplitude over a characteristic e-folding length $\Lambda = \alpha k c^4/(\nu N^3)$, where $c = \omega/k$ is the zonal phase speed, and where $\alpha = \nu N^2/(\nu N^2 + \gamma c^2)$ is the ratio of viscosity to Newtonian cooling in wave damping. Another essential parameter of the problem is the effective Reynolds number $\mathrm{Re} = \mathcal{F}_0 \Lambda/(c\nu)$, where $\mathcal{F}_0 = (u_0' w_0')_{\mathrm{r.m.s.}}$ is the wave forcing amplitude at the bottom boundary. This wave forcing amplitude further sets a characteristic time scale of low-frequency flow reversals $\mathcal{T} = c\Lambda/\mathcal{F}_0$ (2). Table 1 in methods provide estimates for the quasilinear and nonlinear models, as well as for the Earth's stratosphere.

Bifurcation diagrams

To uncover the vast complexity of dynamical regimes occurring in the quasilinear 1D model, we performed a large number of simulations spanning effective Reynolds numbers between $\mathrm{Re} = 2$ and 330, covering roughly the relevant range for the Earth's stratosphere (Table 1). For sufficiently low values of Re, the system has only one attractor: a stable point at $\overline{u} = 0$. A first bifurcation occurs above the critical value $\mathrm{Re}_{c1} \approx 4.25/(1+\alpha)$ (18), for which the zonally averaged velocities are attracted towards a limit cycle (16, 18) corresponding to horizontal mean-flow reversals and downward phase propagation (Fig. 1b). This period-1 cycle arguably reproduces the salient features of the observed QBO before the disruption event of 2016 (Fig. 1a). Figure 1d shows Poincaré sections plotted for increasing Reynolds numbers (see Methods). A second bifurcation from periodic to quasi-periodic regimes occurs above the critical value Re_{c2}. Additional bifurcations occur at higher Reynolds numbers, with transitions to frequency-locked regimes, and chaotic regimes. As Re increases, new oscillating modes appear in the vertical structure of the mean flow. For example, a unique frequency is observed at all heights for the period-1 limit cycle shown in Fig. 1b, while faster reversals are observed in the lower levels for the frequency-locked regime shown in Fig. 1c. Ultimately, in chaotic regimes, the superposition of these modes yields a fractal-like structure of nested flow reversals (see Fig S1 in Supplementary Information). Notice that similar regimes with faster reversals in the lower layers have also been reported in direct numerical simulations driven by a convective boundary layer (9, 15).

The quasiperiodic regime occurring at $\mathrm{Re} > \mathrm{Re}_{c2}$ is embedded with a complicated set of frequency-locked regimes (Fig. 1d). The global structure of the bifurcation diagrams is better appreciated by considering, in Fig. 1e, the two-dimensional parameter space spanned by the Reynolds number Re and the parameter α. This figure shows a range of parameters where frequency locked regions are organized into a sequence of staircases, qualitatively similar to Arnold's tongues (19).

Transition to chaos in a similar 1D quasilinear model was reported in Ref. (20), which focused only on the purely viscous case, $\alpha = 1$, with other boundary conditions relevant for the solar tachocline. Arnold's tongues were found when the 1D quasilinear model is coupled to an external low frequency forcing mimicking seasonal forcing (21), which is reminiscent of synchronisations phenomena in El Nino Southern Oscillations (22, 23). Here, by considering a simple monochromatic forcing, and by covering the full parameter space $Re - \alpha$, we bring to light an unforeseen intrinsic dynamical structure of the underlying quasilinear model.

The 1D quasilinear model is a highly truncated version of the original flow equations. It is thus crucial to see whether the aforementioned bifurcations occur in Navier-Stokes simulations of the fully nonlinear dynamics, including both wave-mean and wave-wave interactions. In Fig. 2a, we performed more than 200 two-dimensional numerical simulations to build a diagram similar to the one obtained with the 1D quasilinear model. These simulations show that the route to chaos is robust to the presence of nonlinear interactions between waves and mean-flow, with transitions from periodic solutions (Fig. 2b) to quasiperiodicity (Fig. 2c), to frequency locking (Fig. 2d) and eventually to chaos. However, significant differences from the quasilinear case are observed in the nonlinear simulations, where bifurcations occur at different Reynolds numbers, and where new dynamical regimes emerge. For instance, the large region of period-3 frequency locking obtained in the 1D quasilinear model (Fig. 1c) is replaced by a thin region of period-2 frequency locking for which the symmetry $U \to -U$ is broken (Figs. 2a and 2d).

Response to external perturbations

By considering a fixed monochromatic wave forcing, we show above that quasi-periodicity arises naturally at steady state in the stratified fluid. This fixed forcing contrasts however with the actual QBO signal, which is driven by time-varying wave forcing and extra-tropical perturbations. In the following, we investigate how the presence of a bifurcation point influences the resilience of a given period-1 QBO-like oscillation to external variability by considering the effect of time-dependent perturbation superimposed on its reference monochromatic wave forcing.

We first consider the effect of a time-dependent pulse in wave amplitude, $\mathcal{F}_0$, mimicking the reported sudden increase in wave activity at the equator in the winter preceding the observed periodicity disruption of 2016. From a dynamical point of view, this perturbation suddenly drives the system out of its limit cycle, until it eventually relaxes back to its original period-1 oscillation over a characteristic time τ. Figures 3a and 3b show examples of transient recovery periods for two values of the Reynolds number using the nonlinear model.

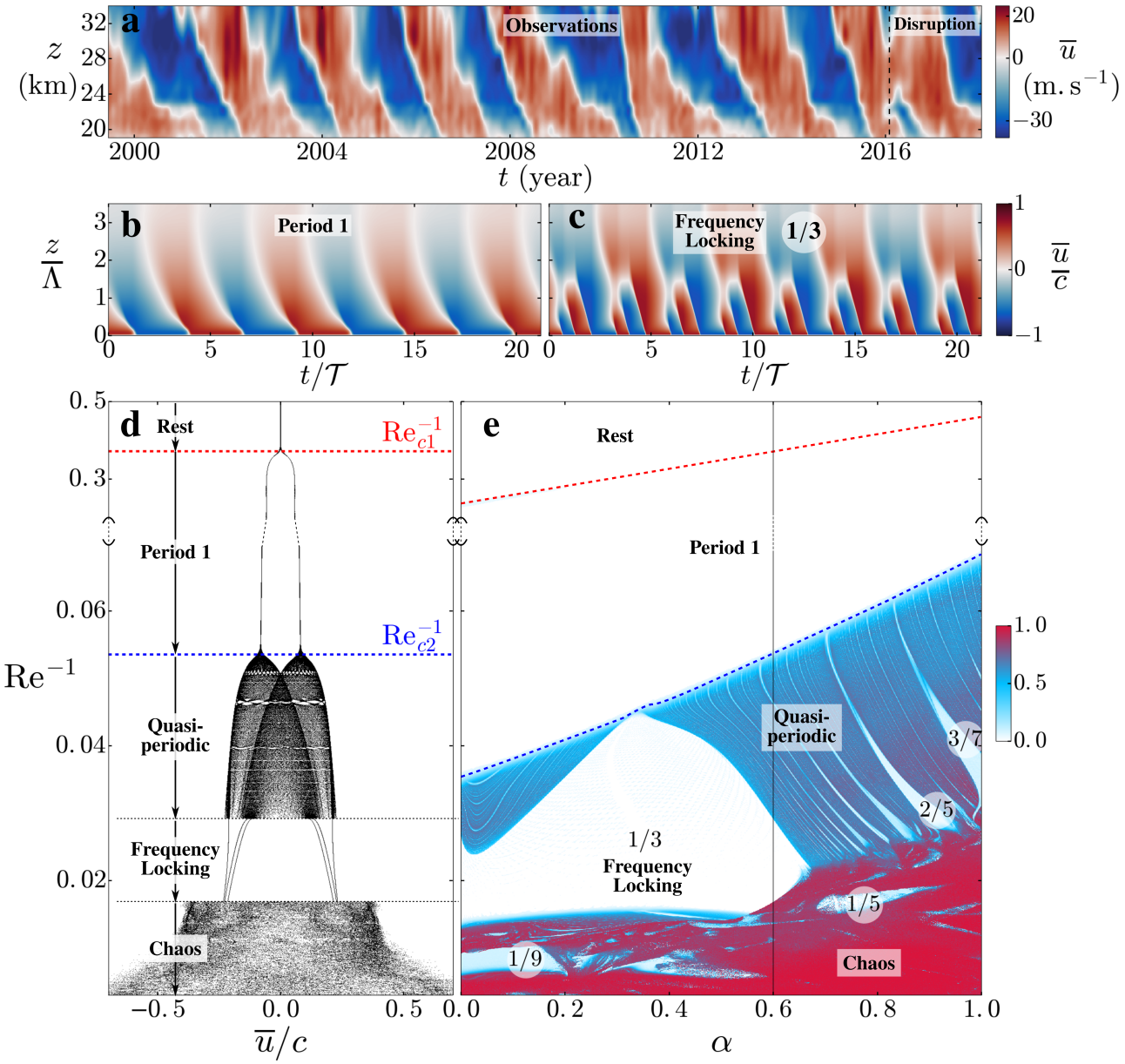

Fig. 1. Bifurcations in the 1D quasilinear model. a. Observations of the Earth's atmospheric quasi-biennial oscillations. Hovmöller diagram of monthly averaged zonal winds measured by radiosonde in the lower stratosphere above Singapore (1.4°N) (17). **b.** Hovmöller diagram of the mean-flow $\overline{u}(z,t)$ in stationary regime for $\alpha = 0.6$ and $\mathrm{Re}^{-1} = 0.06$, using the 1D quasilinear model. **c.** Same as b, but using $\mathrm{Re}^{-1} = 0.025$. **d.** Bifurcation diagram for $\alpha = 0.6$: a Poincaré section is shown for each value of Re^{-1} (see Methods). The dashed red line corresponds to the first bifurcation (from rest to period-1) occurring at Re_{c1}. The dashed blue line corresponds to the second bifurcation (from period-1 to quasiperiodic) occurring at Re_{c2}. **e.** Bifurcation diagram in parameter space $\left(\alpha, \mathrm{Re}^{-1}\right)$. The coloured field is an empirical estimate of the area of the attractor projected on the Poincaré section. Low values (in white) correspond to QBO-like regions (period-1) and frequency locked regions (rational numbers). Colours from blue to red correspond to quasiperiodic and chaotic regions. The main frequency locked regions are labelled by rational numbers corresponding to the ratio of lower levels to upper levels reversals periods. The vertical black line at $\alpha = 0.6$ corresponds to the bifurcation diagram plotted in panel c. The slanted dashed red and blue lines correspond to the first and second bifurcations respectively.

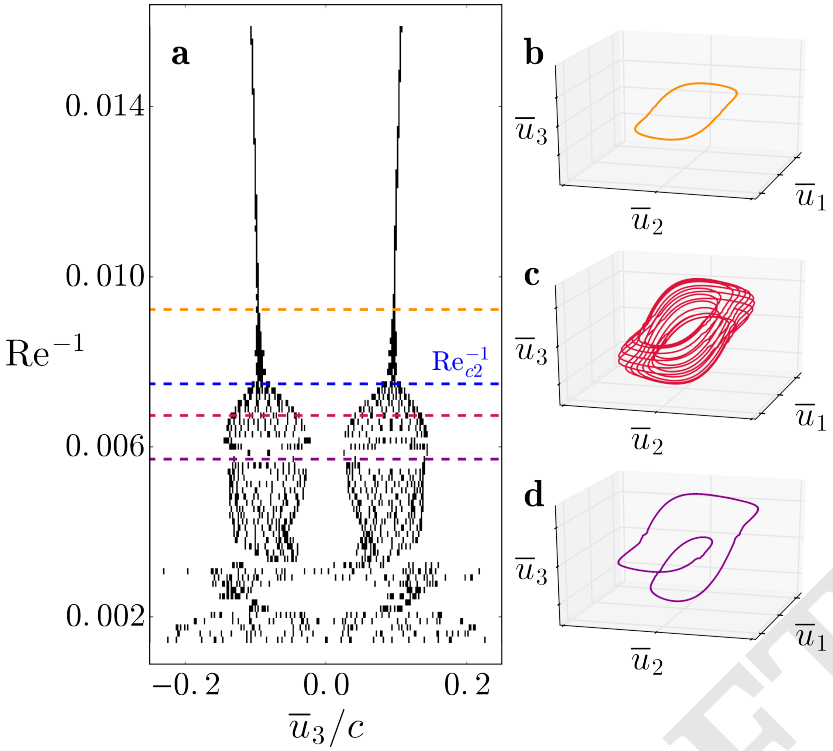

Fig. 2. Bifurcations in Navier-Stokes simulations. a. As in Fig 1d, but showing the bifurcation diagram obtained with the nonlinear simulations, using $\alpha = 0.6$. Selected values of Re (marked in orange, red and purple) correspond to panels b, c, and d. The dashed blue line corresponds to the second bifurcation (from period-1 to quasiperiodic) occuring at Re_{c2}. **b.** Phase space trajectory for $\mathrm{Re}^{-1} = 0.009$, projected on a 3D space defined by velocities at three different heights: $(\overline{u}_1, \overline{u}_2, \overline{u}_3) = (\overline{u}(z = 0.5\Lambda, t), \overline{u}(z = 1.5\Lambda, t), (z = 3\Lambda, t))$. **c.** Same as b, but using $\mathrm{Re}^{-1} = 0.0068$. **d.** Same as b, but using $\mathrm{Re}^{-1} = 0.0058$.

In each case, the time evolution of the mean-flow displays short eastward-flow structures sandwiched between broader westward wind patterns. This is reminiscent of the periodicity disruption observed in 2016.

Figure 3d shows that the characteristic timescale for recovery diverges as the system approaches the bifurcation point Re_{2c}. This divergence is observed both in the quasilinear model and the nonlinear model. Because of numerical constraints, longer time integrations were performed only with the quasilinear model. We found similar responses to a pulse in zonal mean momentum (see supplementary information).

The swift increase in recovery timescale observed as the system approaches a bifurcation point is often referred to as "critical slowing down" (24). In the climate system context, critical slowing down has proven to be useful in detecting early warnings of a bifurcation point (25). We are not aware of previous studies describing a critical slowing down for a transition from a limit cycle to a quasiperiodic oscillation.

We also investigated the effect of adding ambient noise and found an increase in variability as the Reynolds number approaches the critical value, consistent with the observed critical slowing down (see supplementary information).

Discussion and Conclusions

Non-periodic oscillations similar to those presented in this work have been reported in configurations using more complex wave forcing (8, 9, 14, 15). Our study demonstrates that part of the observed variability can be attributed to nonlinear wave-mean flow interactions, independently from the forcing. Because the quasiperiodic route to chaos is expected to be generic for a wide class of systems, we are confident that similar bifurcations will be found in more complex models. Our preliminary results show that adding the effect of rotation does not change the global structure of the bifurcation diagrams, both for the celebrated quasilinear Holton-Lindzen model and 3D nonlinear simulations (see supplementary information). Future work is needed to test this hypothesis in comprehensive general circulation models including realistic wave forcing. These comprehensive general circulation models describe nonlinear 3D flows but rely on parametrisations for internal gravity waves (26). In that respect, they are of intermediate complexity between the 1D quasilinear model and the fully nonlinear simulations used in this study.

Our study also elucidates possible dynamical mechanisms by which external perturbations may affect the QBO on Earth: the observed critical slowing down in response to external perturbations results from the existence of critical values in the bifurcation diagrams of the various simplified models of the equatorial atmosphere used in this study. In practice, evaluating how far the Earth's QBO is from a bifurcation point is challenging, considering both the idealized nature of the models and the large uncertainties in estimating the stratospheric value of eddy diffusivity ν, leading to a large range of possible Re and α. The fact that the oscillations have been remarkably stable — with well defined period and vertical structure before 2016 — suggests that the actual QBO is far from a bifurcation point. Nevertheless, our results show that the period-1 oscillation corresponding to the observed QBO is within an order of magnitude of the critical value Re_{c2}. This suggests that the variability of the QBO may be significantly altered under a changing climate, as the stratosphere approaches the bifurcation point following a possible increase in tropical wave activity. The recovery period following disruptions similar to the one observed in 2016 could then be much longer and be characterized by a very different vertical structure than what was previously observed.

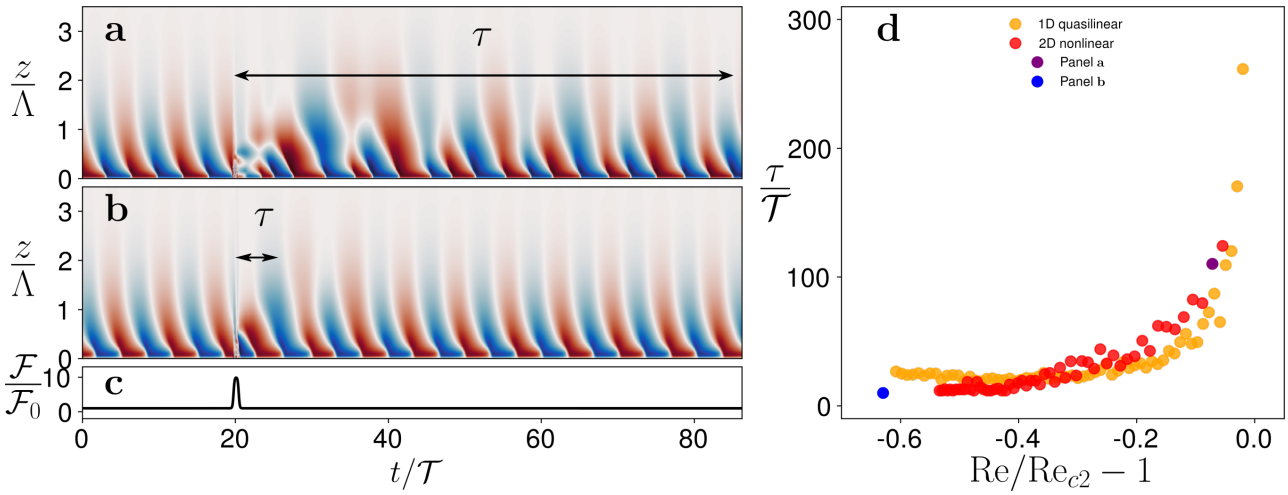

Fig. 3. Critical slowing down. **a.** Hovmöller diagrams of the mean-flow, $\overline{u}(z,t)$, in the Navier-Stokes simulations, perturbed by a pulse in wave forcing for $\mathrm{Re} = 125$ (see Methods for other parameters). **b.** Same as a, but using $\mathrm{Re} = 50$. **c.** Time evolution of the wave forcing amplitude $\mathcal{F}(t)$. **d.** Characteristic recovery timescale as a function of relative distance to the second bifurcation point, $1 - \mathrm{Re}/\mathrm{Re}_{c2}$, computed using the 1D quasilinear model (orange markers) and the 2D nonlinear model (red markers). The purple and blue markers correspond to the two points associated with the nonlinear computations of panels a and b, respectively. We used $\mathrm{Re}_{c2} = 24.3$ for the 1D quasilinear model and $\mathrm{Re}_{c2} = 135$ for the 2D nonlinear model.

$$\overline{u'w'}(z) = \sum_{i=1}^{2} (-1)^i \mathcal{F}_0 \exp\left\{ -\frac{1}{\Lambda} \int_0^z \mathrm{d}z' \left(\frac{\alpha}{\left(1-(-1)^i \overline{u}(z')/c\right)^4} + \frac{1-\alpha}{\left(1-(-1)^i \overline{u}(z')/c\right)^2} \right) \right\}. \quad [2]$$

Materials and Methods

1D quasilinear simulations. Using a static Wentzel-Kramers-Brillouin (WKB) approximation to compute the wave field for a given mean-flow (7), the wave-induced Reynolds stress in Eq. (1) is parametrised by the formula given in Eq. (2).

This formula is derived under the hydrostatic balance assumption (valid in the limit $k|c \pm \overline{u}|/N \to 0$) and the weak damping assumption (valid in the limit $\gamma/(k|c \pm \overline{u}|) \ll 1$ and $\nu N^2/(k|c \pm \overline{u}|^3) \ll 1$). Assuming that the characteristic vertical length for $\overline{u}$ is Λ, then the small parameter needed in the WKB approach is the Froude number $Fr = c/(\Lambda N) \to 0$. In practice, the different assumptions are most certainly violated. However, this set of equations has long been recognized as a useful model to probe the salient features of QBO reversals.

We solve numerically using a centred second-order finite difference method with grid size $\delta_z = H/60$, and a second-order Adams-Bashforth scheme with time-step $\delta_t = 0.005\mathcal{T}$; $\mathcal{T} = c\Lambda/\mathcal{F}_0$. A no-slip condition is used at the bottom boundary, $z = 0$, and a free-slip condition is used at the upper boundary, $z = H$. Singularities in Eq. (2) appear when $\overline{u} = c$ (critical layers). These singularities are treated as follows: at a given height $z = z_c$, if the absolute value of $\overline{u}$ reaches locally a value higher than c, then the corresponding exponential is set to zero for all $z \geq z_c$. The definition and value of each of the model's dimensionless numbers are given in table 1.

2D and 3D nonlinear simulations. The fully nonlinear simulations are conducted using the Massachusetts Institute of Technology general circulation model (MITgcm, (27)) solving the 3D Navier-Stokes equations under the Boussinesq and hydrostatic approximations

$$\begin{cases} \partial_t \mathbf{u}_\mathrm{h} + \mathbf{u}\cdot\nabla\mathbf{u}_\mathrm{h} + \beta y \hat{\mathbf{k}} \times \mathbf{u}_\mathrm{h} &= -\nabla\phi + \hat{\mathbf{k}} b + \nu\nabla^2 \mathbf{u}_\mathrm{h} - \hat{\mathbf{i}}\gamma_u (u - u_0) \\ \partial_t b + \mathbf{u}\cdot\nabla b &= \kappa\nabla^2 b - \gamma (b - b_0) \\ \nabla\cdot\mathbf{u} &= 0 \end{cases} \quad [3]$$

where $\mathbf{u} = u\hat{\mathbf{i}} + v\hat{\mathbf{j}} + w\hat{\mathbf{k}}$ is the 3D velocity, $\mathbf{u}_\mathrm{h}$ is its projection on the horizontal plane (x,y); $b = g(\rho_0 - \rho)/\rho_0$ is the buoyancy; ρ is the density and ρ_0 is a reference density; g is the gravitational acceleration; $\phi = P/\rho_0 + gz$; P is the pressure; ν is the viscosity coefficient; κ is the buoyancy diffusion coefficient; γ_u and γ are the rates at which the momentum and buoyancy are linearly restored to the reference profiles u_0 and b_0, respectively.

The domain is a Cartesian grid, periodic in the zonal direction, with zonal length $L_x = 2\pi/k$, height H and meridional extent L_y. In its 2D configuration, the horizontal and vertical resolutions are respectively $\delta_x = L/26$ and $\delta_z = H/200$. A free-slip condition is used at the bottom boundary, while a free-surface condition is used at the top.

Advection of buoyancy is achieved through the 7th order one-step method with monotonicity preserving limiter. The zonal momentum equation is forced at the bottom boundary using a linear velocity relaxation $\gamma_u = \delta_b/\tau_u$, where τ_u is a relaxation timescale, and δ_b is a delta function equal to 1 for the bottom grid-point and 0 for all other vertical levels. In this last grid-point, velocity is relaxed to a zonally periodic standing wave pattern $u_0 = \sqrt{4N\mathcal{F}/\omega}\cos(kx)\cos(\omega t)$, where $\mathcal{F}$ controls the wave momentum flux amplitude at the bottom. This forcing is thought to generate a standing internal gravity wave field while enforcing an effective no-slip condition for the mean flow $\overline{u}$. Buoyancy is relaxed to the linear profile $b_0 = N^2 z$. To avoid any wave reflection at the upper free-surface, the vertical grid spacing and the Newtonian colling are both increased in the 20 upper grid layers.

We also performed few 3D runs including weak rotation, by considering an equatorial beta-plane, i.e. a linear increase of the Coriolis parameter with latitude (see Supplementary Information). A summary of the relevant dimensionless numbers in the nonrotating case is provided in table 1.

Poincaré sections.. For each combination of parameters (Re, α), experiments are first spun-up over a time $t_\mathrm{e} = 1500\mathcal{T}$ where $\mathcal{T} = c\Lambda/\mathcal{F}_0$. This time is sufficient for the system to reach its attractor.

To combine the information of more than 10^6 simulations into a single bifurcation diagram, we first select two vertical levels: z_1 near the surface and z_2 aloft. Resuming the simulation at statistical equilibrium $(t > t_\mathrm{e})$, we store the values of $\overline{u}(z_2)$ that intersects

		1D quasilinear simulations	2D Nonlinear simulations	Stratosphere
Re	$= F_0\Lambda/(c\nu)$	$15-350$	$50-600$	$10-400$
α	$= \nu N^2/(\nu N^2+\gamma c^2)$	$0-1$	0.25	$0.1-0.9$
Pr	$= \nu/\kappa$	∞	740	~ 1
Fr	$= c/(\Lambda N)$	$\mathrm{Fr}\to 0$	0.06	0.1
	ω/N	$\omega/N\to 0$	0.1	$10^{-4}-10^{-3}$
	$\omega\tau_u$	0	0.1	N.A.
	H/Λ	3.5	4.1	1.5

Table 1. Dimensionless parameters. Viscosity, ν, and thermal diffusion coefficient, κ, are interpreted as effective turbulent eddy-diffusivities. Values corresponding to the stratosphere are based on the estimates given in (28), with updated ranges of vertical eddy-viscosity provided by (29). The closure used in the 1D quasilinear model reduces the number of dimensionless parameters down to three by assuming $\omega/N\to 0$ (hydrostatic approximation) and a low Froude limit $Fr\to 0$ (WKB approximation).

$\overline{u}(z_1)=0$ in the set

$$\mathbb{O}_{\mathrm{Re},\alpha}=\left\{\,\overline{u}\,(z_2,t)\,|\,\overline{u}\,(z_1,t)=0\,\right\}. \qquad [4]$$

The simulations are stopped once 200 values are stored (i.e. after 200 reversals of the lower-level mean-flow $\overline{u}\,(z_1)$). For each simulation associated with couples of parameters (Re,α), we build an histogram of the values stored in (4), using 1000 bins in the range $[-c,c]$. Histograms corresponding to all values of Re for a fixed $\alpha=0.6$ are drawn horizontally in figure 1c using a binary colour-map.

To collapse the information of the Poincaré sections into a 2D bifurcation diagram $(\alpha,\mathrm{Re}^{-1})$, we compute the ratio of populated bins to the total number of reversals for each histogram in the set (4). This ratio with values in $[0,1]$ provides an empirical estimate of each histogram's distribution and allows for an extensive classification of the different dynamical regimes in Fig. 1d.

Implementation of the pulse (figure 3a and 3b). To generate a pulse in external wave forcing, we consider a time-dependent momentum flux amplitude (see u_0 in Eq. (3))

$$\mathcal{F}\,(t)=\mathcal{F}_0\left(1+9\exp\left\{-\frac{1}{2}\left(10\frac{t-t_p}{T_{\mathrm{qbo}}}\right)^{10}\right\}\right), \qquad [5]$$

where T_{qbo} is the period of the limit cycle and t_p sets the timing of the pulse.

Estimation of the recovery timescale (Figure 3). We consider a large pulse in momentum flux such that the system is driven away from its initial period-1 limit cycle and then freely recovers back to the cycle. To estimate the recovery timescale, we first introduce the running mean-square

$$\left\langle\overline{u}^2\right\rangle(t)=\frac{1}{T_{\mathrm{qbo}}H}\int_{t-T_{\mathrm{qbo}}/2}^{t+T_{\mathrm{qbo}}/2}\int_0^H\overline{u}^2\left(z,t'\right)\mathrm{d}z\mathrm{d}t', \qquad [6]$$

where T_{qbo} is the period of the limit cycle. At steady state equilibrium, this running mean-square has a constant value $\langle\overline{u}^2\rangle_\infty$. Assuming a pulse shorter than the period of the limit cycle (see Fig. 3c), occurring at time t_p, the recovery timescale is then defined by

$$\tau=\min\left\{\frac{\langle\overline{u}^2\rangle\,(t_p+\Delta t)-\langle\overline{u}^2\rangle_\infty}{\langle\overline{u}^2\rangle_\infty}\leq 0.2\right\}, \qquad [7]$$

where $\Delta t\geq 0$.

We argue that the recovery timescale is of the same order of magnitude as the spin-up time required to reach the limit cycle starting from small random initial perturbations. In the supplementary materials, we show that both methods are equivalent assuming a large enough pulse. In Fig. 3d, we computed the recovery timescale using this spin-up timescale and in Fig. S4 using Eq. (7).

1. Baldwin M, et al. (2001) The quasi-biennial oscillation. Reviews of Geophysics 39(2):179–229.
2. Vallis GK (2017) Atmospheric and oceanic fluid dynamics. (Cambridge University Press).
3. Leovy CB, Friedson AJ, Orton GS (1991) The quasiquadrennial oscillation of jupiter's equatorial stratosphere. Nature 354(6352):380.
4. Dowling TE (2008) Planetary science: Music of the stratospheres. Nature 453(7192):163.
5. Fouchet T, et al. (2008) An equatorial oscillation in saturnś middle atmosphere. Nature 453(7192):200.
6. Orton GS, et al. (2008) Semi-annual oscillations in saturn's low-latitude stratospheric temperatures. Nature 453(7192):196.
7. Plumb R, McEwan A (1978) The instability of a forced standing wave in a viscous stratified fluid: A laboratory analogue of. the quasi-biennial oscillation. Journal of the Atmospheric Sciences 35(10):1827–1839.
8. Wedi NP, Smolarkiewicz PK (2006) Direct numerical simulation of the Plumb–McEwan laboratory analog of the QBO. Journal of the Atmospheric Sciences 63(12):3226–3252.
9. Couston LA, Lecoanet D, Favier B, Le Bars M (2018) Order out of chaos: slowly-reversing mean flows emerge from turbulently-generated internal waves. Accepted for Physical Review Letters 00(00).
10. Osprey SM, et al. (2016) An unexpected disruption of the atmospheric quasi-biennial oscillation. Science 353(6306):1424–1427.
11. Newman P, Coy L, Pawson S, Lait L (2016) The anomalous change in the qbo in 2015–2016. Geophysical Research Letters 43(16):8791–8797.
12. Dunkerton TJ (2016) The quasi-biennial oscillation of 2015–2016: Hiccup or death spiral? Geophysical Research Letters 43(19).
13. Fletcher LN, et al. (2017) Disruption of saturn?s quasi-periodic equatorial oscillation by the great northern storm. Nature Astronomy 1(11):765.
14. Rogers TM, Glatzmaier GA (2006) Angular momentum transport by gravity waves in the solar interior. The Astrophysical Journal 653(1):756.
15. Showman AP, Tan X, Zhang X (2018) Atmospheric circulation of brown dwarfs and jupiter and saturn-like planets: Zonal jets, long-term variability, and qbo-type oscillations. arXiv preprint arXiv:1807.08433.
16. Plumb RA (1977) The interaction of two internal waves with the mean flow: Implications for the theory of the quasi-biennial oscillation. Journal of the Atmospheric Sciences 34(12):1847–1858.
17. (year?) The quasi-biennial-oscillation (qbo) data series (www.geo.fu-berlin.de/en/met/ag/strat/produkte/qbo/index.html). Accessed: 2018-03.
18. Yoden S, Holton JR (1988) A new look at equatorial quasi-biennial oscillation models. Journal of the atmospheric sciences 45(19):2703–2717.
19. Arnold VI (1961) Small denominators. i. mapping the circle onto itself. Izvestiya Rossiiskoi Akademii Nauk. Seriya Matematicheskaya 25(1):21–86.
20. Kim Ej, MacGregor K (2001) Gravity wave-driven flows in the solar tachocline. The Astrophysical Journal Letters 556(2):L117.
21. Rajendran K, Moroz IM, Read PL, Osprey SM (2015) Synchronisation of the equatorial qbo by the annual cycle in tropical upwelling in a warming climate. Quarterly Journal of the Royal Meteorological Society 142(695):1111–1120.
22. Tziperman E, Stone L, Cane MA, Jarosh H (1994) El nino chaos: Overlapping of resonances between the seasonal cycle and the pacific ocean-atmosphere oscillator. Science 264(5155):72–74.
23. Jin FF, Neelin JD, Ghil M (1994) El Niño on the devil's staircase: annual subharmonic steps to chaos. Science 264(5155):70–72.
24. Scheffer M, et al. (2009) Early-warning signals for critical transitions. Nature 461(7260):53.
25. Lenton TM (2011) Early warning of climate tipping points. Nature Climate Change 1(4):201.
26. Lott F, et al. (2014) Kelvin and rossby-gravity wave packets in the lower stratosphere of some high-top cmip5 models. Journal of Geophysical Research: Atmospheres 119(5):2156–2173.
27. Marshall J, Adcroft A, Hill C, Perelman L, Heisey C (1997) A finite-volume, incompressible navier stokes model for studies of the ocean on parallel computers. J. Geophys. Res. 102:5753 – 5766.
28. Holton JR, Lindzen RS (1972) An updated theory for the quasi-biennial cycle of the tropical stratosphere. Journal of the Atmospheric Sciences 29(6):1076–1080.
29. Haynes P (2005) Stratospheric dynamics. Annual Review of Fluid Mechanics 37(1):263–293.

PNAS
www.pnas.org

Supplementary Information for

Periodicity disruption of a model quasi-biennial oscillation

Antoine Renaud, Louis-Philippe Nadeau and Antoine Venaille

A. Venaille
E-mail: antoine.venaille@ens-lyon.fr

This PDF file includes:

Supplementary text
Figs. S1 to S7
References for SI reference citations

Supporting Information Text

1. Bifurcations in the 1D quasilinear model

Figure S1 shows phase space trajectories and hovmöller diagrams of the mean-flow for four selected values of the Reynolds number in the bifurcation diagram presented in Fig. 1d. Shown are examples of transitions from the period-1 limit cycle (panels b and f), to quasiperiodicity (panels c and g), to frequency locking with frequency ratio 1/3 (panels d and h), and to chaos (panels e and i).

Additional bifurcation diagrams obtained for different values of α are shown in Fig. S2. Although sharing a common qualitative structure, each bifurcation diagrams show interesting specific features. For instance, panel *d* shows that the first quasiperiodic region vanishes almost entirely when α approaches 1/3. In the case $\alpha = 1$ (Fig. S2d), spontaneous breaking of the symmetry $U \leftrightarrow -U$ occurs in one of the frequency locked states ($\mathrm{Re}^{-1} \sim 0.045$), while all the frequency-locked regimes preserve this symmetry at lower values of α in panels a, b and c.

2. Effect of the resolution

Figure S3 shows the effect of changing vertical resolution when solving the 1D quasilinear model numerically (see methods in the main article).

From panel a to panel e, the vertical grid step is successively divided by two. The resolution used for panel c corresponds to the one used in the main paper.

We see that the critical Reynolds number Re_{c2} for the second bifurcation does not change significantly from case b to d. However, the details of the route to chaos are affected by changes in vertical resolution, in particular, for the structure of the embedded frequency locked regimes.

3. Spin-up and recovery times equivalence

In this section, using the 1D quasilinear model, we show the equivalence between the spin-up time from a random initial state and the relaxation time following an external perturbation, either in wave forcing amplitude or in the bulk of momentum equations.

The spin-up time corresponds to the time it takes for the system to reach the limit cycle starting from a small random perturbation. The recovery time corresponds to the time it takes for the system to recover the limit cycle after having been strongly perturbed by an external forcing. The precise definition of the recovery time is provided in the methods of the main article. Here, we consider two types of external forcing. The first one corresponds to a pulse in the wave amplitude (see Eq. (5) in the main article). The second one corresponds to a body force acting directly on the mean flow:

$$f_{\mathrm{ext}}\left(z,t\right) = \frac{10}{T_{\mathrm{qbo}}} \exp\left\{-\frac{1}{2}\left(10\frac{t-t_p}{T_{\mathrm{qbo}}}\right)^{10}\right\} \exp\left\{-800\left(\frac{z-z_p}{z_{\max}}\right)^2\right\}, \qquad [1]$$

where T_{qbo} is the period of the limit cycle. Parameters t_p and z_p control the timing and the height of the perturbation respectively. We chose $z_p = 0.2 z_{\max}$. We checked that t_p does not have any significant influence on the recovery time.

Figures S4 compares the spin-up and recovery timescales for different Reynolds numbers. It demonstrates the equivalence between these different timescales.

4. Response to stochastic forcing

In this section, we investigate how the response to an external ambient noise can be influenced by the presence of a bifurcation point. We introduce for that purpose a stochastic force term into the mean flow dynamics:

$$\partial_t \overline{u} - \nu \partial_{zz} \overline{u} = -\partial_z \overline{u'w'} + \sigma \xi\left(t\right) \sin\left\{2\pi\left(\frac{z}{H} + \varphi\left(t\right)\right)\right\}, \qquad [2]$$

where ξ and φ are noise functions correlated over the numerical time-step. ξ is Gaussian with unit variance and φ is uniform in $[0,1]$. The strength of the stochastic forcing is controlled by the additional dimensionless number $\tilde{\sigma} = \sigma\Lambda/\mathcal{F}_0$. To measure the variability of the response when the deterministic dynamics is on the periodic regime, we compute the ratio of the standard deviation for the reversals periods, ΔT_{qbo}, over the steady period obtained in the absence of noise, T_{qbo}.

Figure S5 shows the effect of the noise on the mean flow oscillations when the Reynolds number approaches the critical value for the transition towards quasiperiodic regimes. The strength of the noise in the forcing term is kept constant at $\tilde{\sigma} = 0.5$. We observe an amplification of the variability in the mean flow oscillations when the Reynolds number approaches the critical value. This amplification is the stochastic counterpart of the critical slowing down observed in figure 3. We observed a similar amplification for other types of noise.

5. Effect of rotation

We provide here two sets of simulations supporting the idea that the bifurcation observed in the non-rotating case persist in the presence of rotation. The first set of simulations deals with Holton-Lindzen 1D quasilinear model with a parameterisation for the effect of equatorial waves. (1, 2). The second set of simulations are direct numerical simulations of the fully nonlinear 3D equations including the effect of rotation.

A. Bifurcation diagram for Lindzen-Holton model. We consider here the 1972 Holton-Lindzen model (2, 3). In this model, the two counterpropagating internal gravity waves of the non-rotating case discussed in the main text are replaced by an eastward propagating Kelvin wave and a westward propagating Rossby waves, both of them being supported by the presence of an equatorial beta plane (The Corolis parameter is assumed to vary linearly with latitude as $f = \beta y$). The dispersion relation of these waves differ from the internal gravity waves, and lead to a different vertical wave momentum flux:

$$\overline{u'w'}\left(z\right) = \mathcal{F}_0 \left(\underbrace{\exp\left\{ -\frac{1}{\Lambda} \int_0^z \mathrm{d}z' \frac{1}{\left(1-\overline{u}\left(z'\right)/c\right)^2} \right\}}_{\text{Kelvin wave}} - \underbrace{\exp\left\{ -\frac{A}{\Lambda} \int_0^z \mathrm{d}z' \left(\frac{B}{\left(1+\overline{u}\left(z\right)/c\right)^3} + \frac{1-B}{\left(1+\overline{u}\left(z'\right)/c\right)^2} \right) \right\}}_{\text{Mixed Rossby-gravity wave}} \right). \qquad [3]$$

. The paramter Λ is the characteristic vertical damping length of the Kelvin wave when the mean flow is at rest. The parameter A is the ratio of the damping length of the Kelvin wave over the damping length of the mixed Rossby-gravity wave. $B = \beta/(\beta - k^2 c)$ is a dimensionless number depending on the beta plane coefficient β. Considering the values proposed by Holton and Lindzen (3) (see also Vallis' book (2)), we set $A = 0.23$ and $B = 2.09$. The major difference with the model we used in Eq (2) of the main text is the asymmetry between the two associated momentum fluxes.

Figure S6 shows the 1D bifurcation diagram computed using this Holton-Lindzen parameterisation. The symmetry $\overline{u} \to -\overline{u}$ is broken as expected from the form of the wave forcing. However, the quasiperiodic route to chaos remains the same as in the non-rotating case.

B. 3D fully nonlinear simulations with rotation. We show that the bifurcation from periodic to quasiperiodic regimes observed in the 2D nonlinear configuration (see main text) persists in a 3D nonlinear simulations with rotation.

We consider a domain geometry with horizontal aspect ratio $L_y/L_x = 1$ and resolution ratio $\delta_y/\delta_x = 1$, with free-slip lateral boundary condition at $y = \pm L_y/2$. To model the effect of rotation, we consider an equatorial beta-plane: the Coriolis parameter varies linearly with latitude, $f = \beta y$. We explore a weak rotation case, for which the equatorial Radius of deformation $L_d = \sqrt{N\Lambda/\beta}$ is much larger than the meridional extension of domain: $L_d/L_y = 96$. All other parameters are identical to the 2D nonlinear simulations, including the forcing, constant along the y direction.

Fig. S7 shows that bifurcation from a periodic regime (panel a) to a quasiperiodic regime (panel b) occurs when the Reynolds number is increased from $\mathrm{Re} = 125$ to $\mathrm{Re} = 250$. This demonstrates that the intrinsic variability observed in the 1D quasilinear model is robust to the presence of 3D wave-wave interactions.

In the Earth's stratosphere, the parameter L_d/L_y is smaller than one, and equatorial waves are trapped along the equator over a typical scale of the order of the deformation radius. Future work is needed to explore the robustness of the second bifurcation point in the presence of strong rotation.

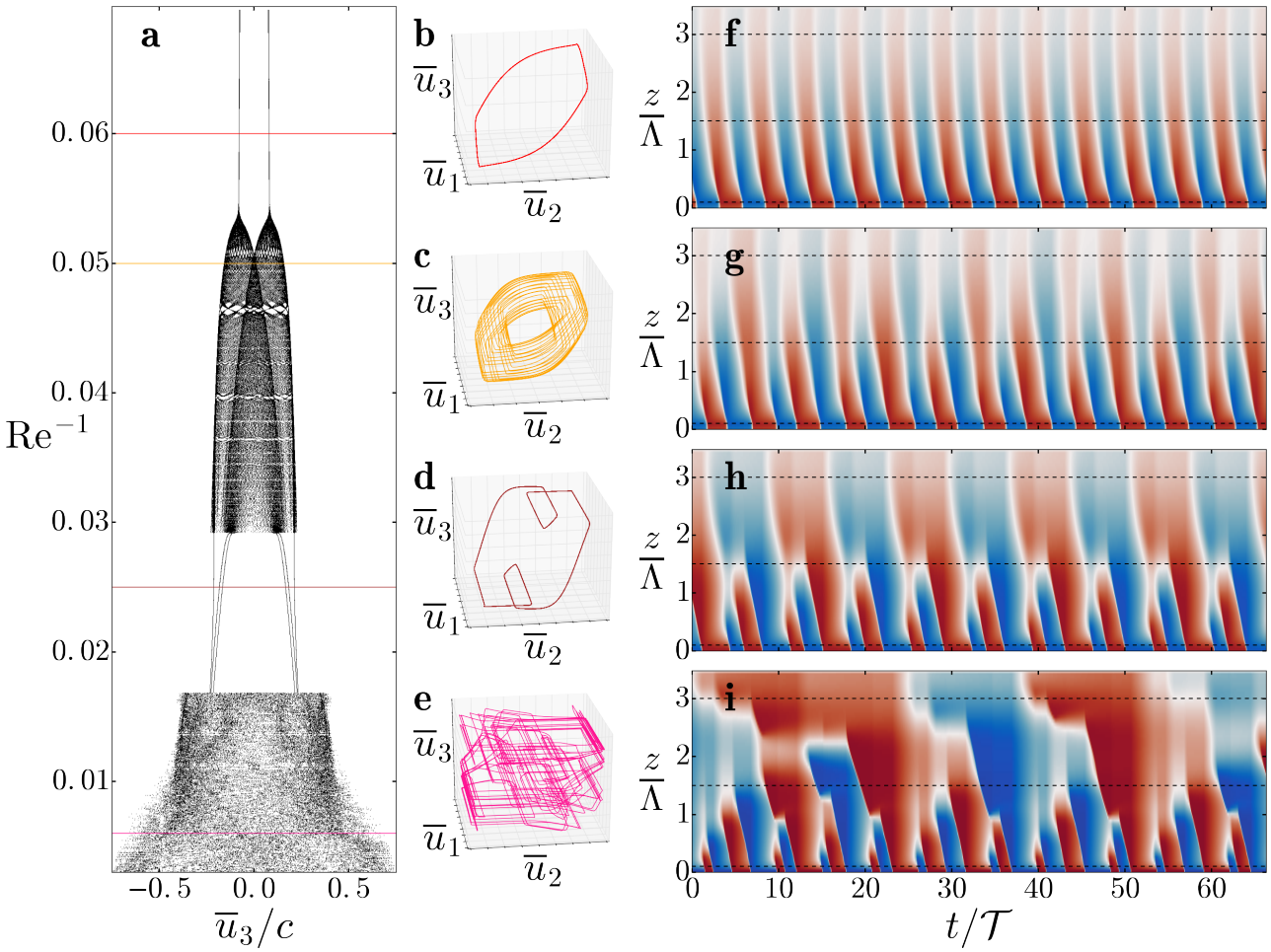

Fig. S1. Bifurcations in the 1D quasilinear model. a. A Poincaré section is shown for varying values of Re^{-1} and $\alpha = 0.6$ (see Methods). **b.** Projection of phase-space trajectory in a 3D space $(\overline{u}_1, \overline{u}_2, \overline{u}_3) = (\overline{u}(z = 0.1\Lambda), \overline{u}(z = 1.5\Lambda, t), \overline{u}(z = 3\Lambda, t))$ for $\mathrm{Re}^{-1} = 0.059$. **c.** Same for $\mathrm{Re}^{-1} = 0.045$. **d.** Same for $\mathrm{Re}^{-1} = 0.025$. **e.** Same for $Re^{-1} = 250$. **f.** Hovmöller diagram of the mean-flow $\overline{u}\,(z, t)$ for $\mathrm{Re}^{-1} = 0.059$. Time is rescaled by $\mathcal{T} = c\Lambda/\mathcal{F}_0$. The velocity $\overline{u}$ ranges from to $-c$ (blue) to $+c$ (red). The horizontal dotted lines highlight the height $z = 0.1\Lambda$, $z = 1.5\Lambda$ and $z = 3\Lambda$, associated with the 3D projections plotted in panels b to e. **g.** Same for $\mathrm{Re}^{-1} = 0.045$. **h.** Same for $\mathrm{Re}^{-1} = 0.025$. **i.** Same for $\mathrm{Re}^{-1} = 0.0004$.

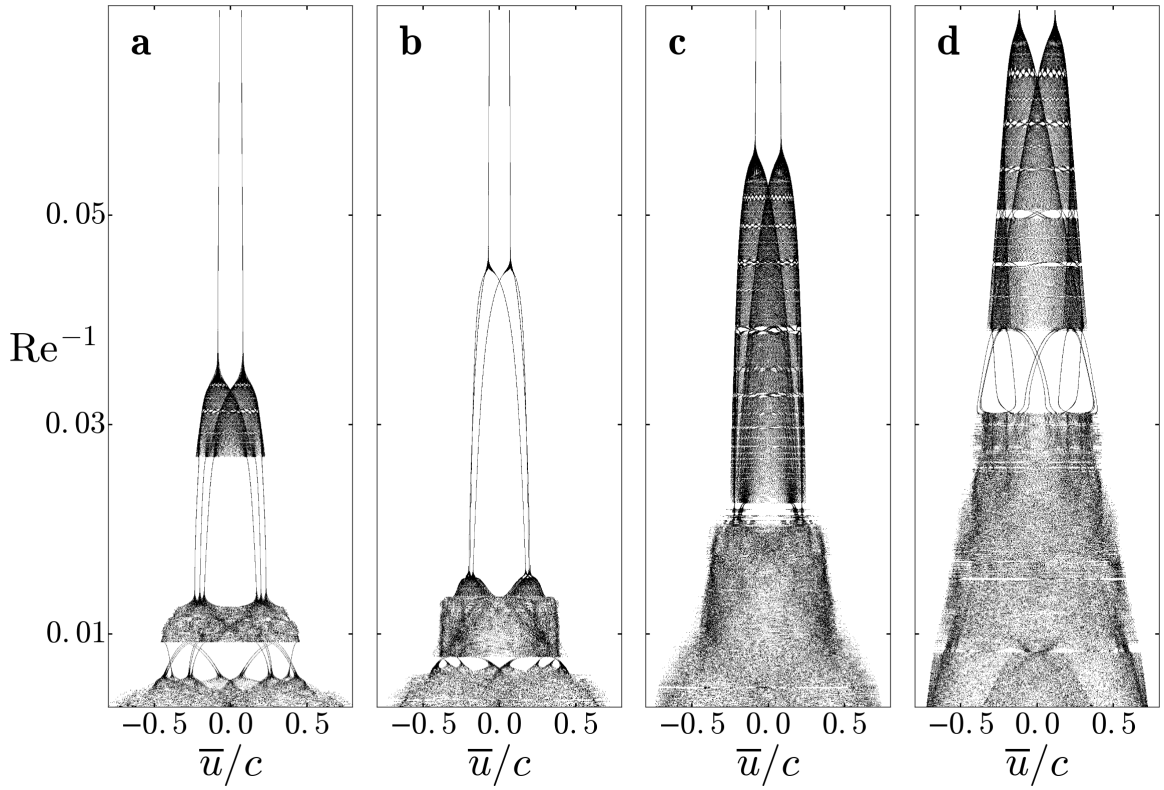

Fig. S2. Additional bifurcation diagrams of the 1D quasilinear model. a. Poincaré sections for each value of Re^{-1} using $\alpha = 0$ (see Methods). **b.** Same for $\alpha = 1/3$. **c.** Same for $\alpha = 2/3$. **d.** Same for $\alpha = 1$.

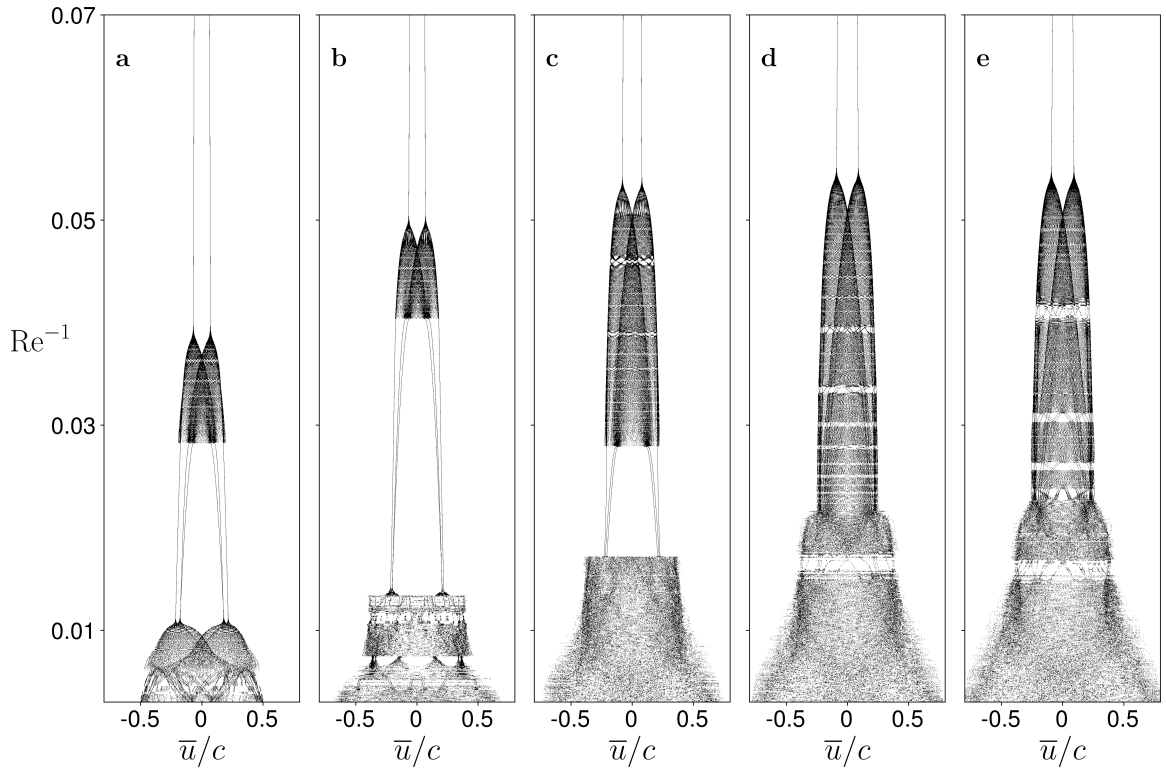

Fig. S3. Resolution dependence in the 1D quasilinear model a Poincaré sections for each value of Re^{-1} with $\alpha = 0.6$. The spatial resolution used is $\delta_z = 3.5/15$. **b.** Same for $\delta_z = 3.5/30$. **c.** Same for $\delta_z = 3.5/60$. **d.** Same for $\delta_z = 3.5/120$. **e.** Same for $\delta_z = 3.5/240$.

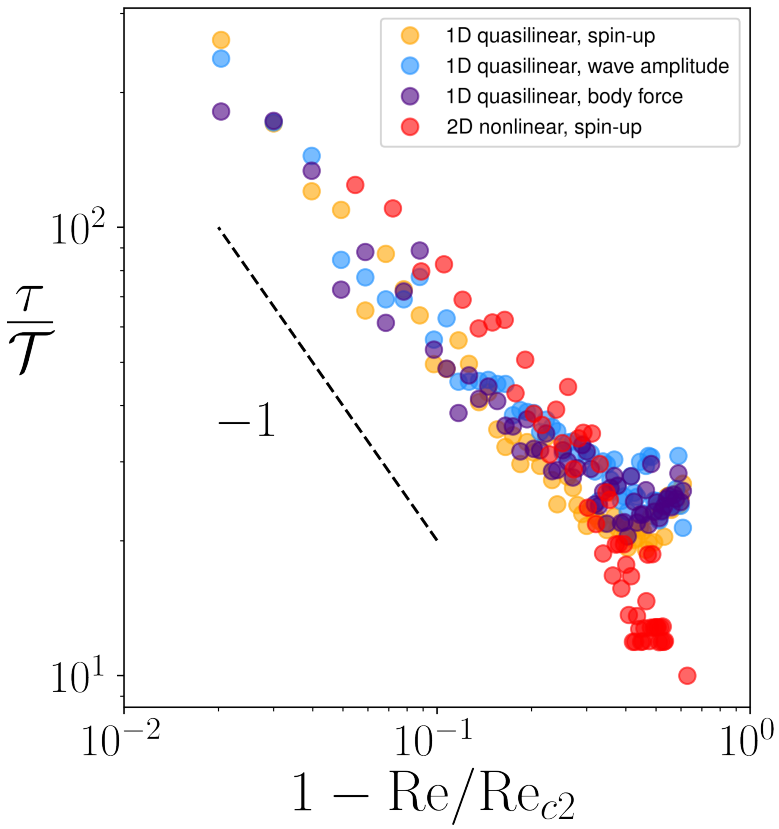

Fig. S4. Spin-up and recovery times equivalence. Characteristic recovery and spin-up timescales as a function of the relative distance to the second bifurcation point, $1 - \mathrm{Re}/\mathrm{Re}_{c2}$, represented in log-scale. The orange markers correspond to the spin-up time for the 1D quasi-linear model. The blue and purple markers are obtained with the quasilinear model, and correspond to the recovery from a pulse in the wave amplitude and from a direct body force, respectively. The red markers correspond to the spin-up time with the 2D nonlinear model. We used $\mathrm{Re}_{c2} = 24.3$ for the 1D quasilinear model and $\mathrm{Re}_{c2} = 135$ for the 2D nonlinear model.

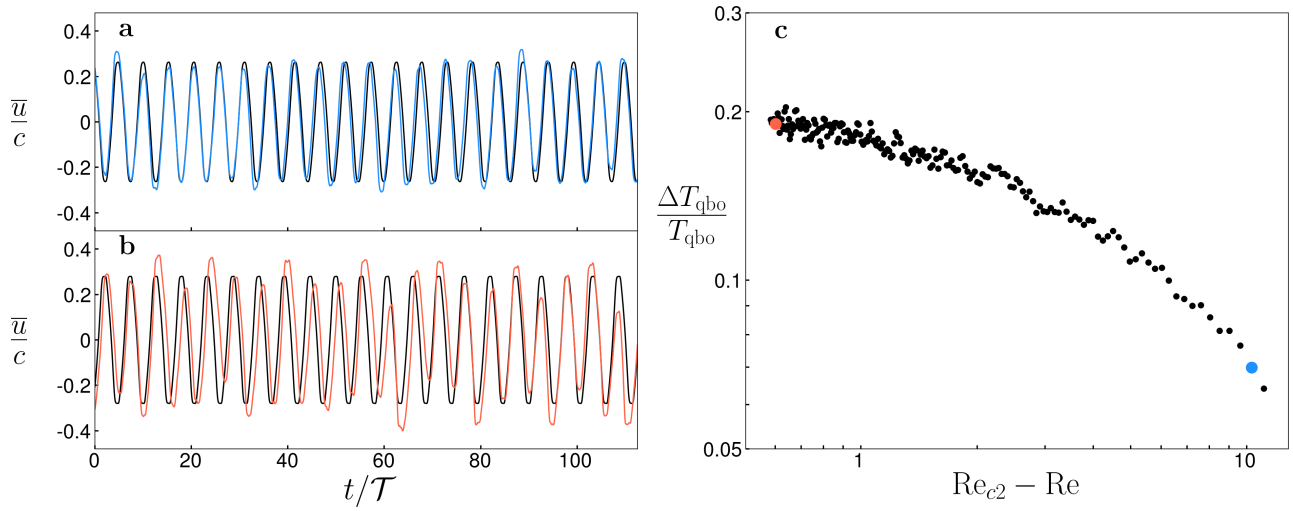

Fig. S5. Response to ambient noise. a. Temporal evolution of the mean flow $\overline{u}$ at $z = 1.5$, computed without noise (black color) and with noise (blue color), for $Re = 8.8$. **b.** Same for $Re = 18.5$, the case with noise is represented in red color. **c** Standard deviation $\Delta T_{\rm qbo}$ of the period of the signal in the case with noise, normalized by the steady period of the signal in the case without noise $T_{\rm qbo}$, for different values of Reynolds numbers $\mathrm{Re}_{c2} - \mathrm{Re}$.

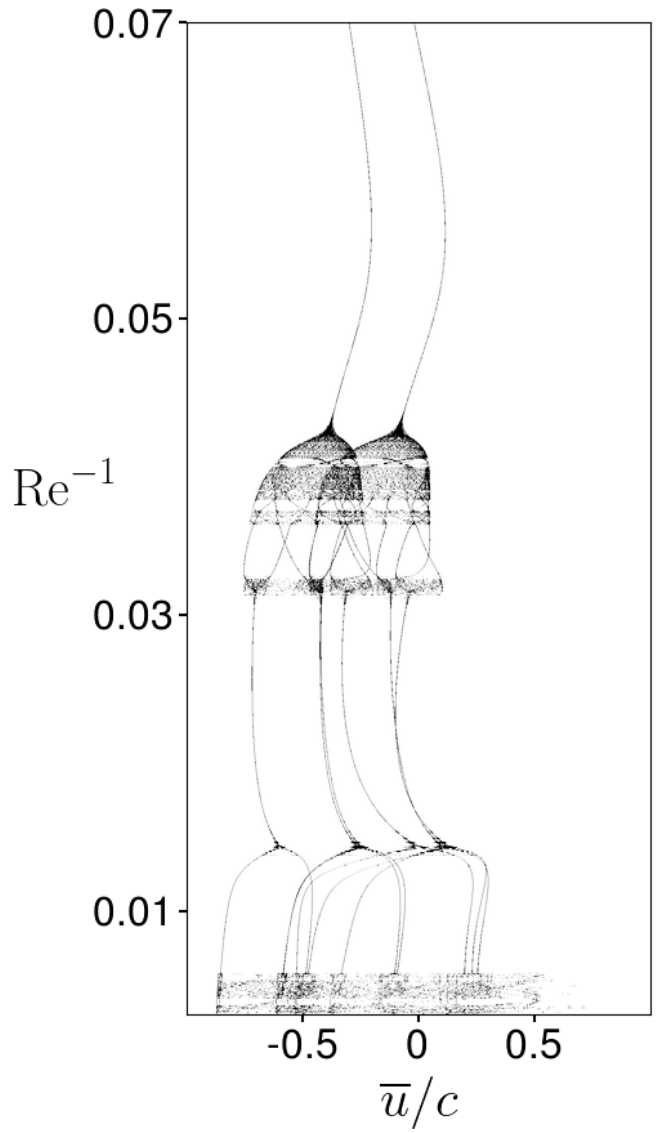

Fig. S6. Bifurcations in the Holton-Lindzen 1D quasilinear model. Poincaré sections for each value of Re^{-1}.

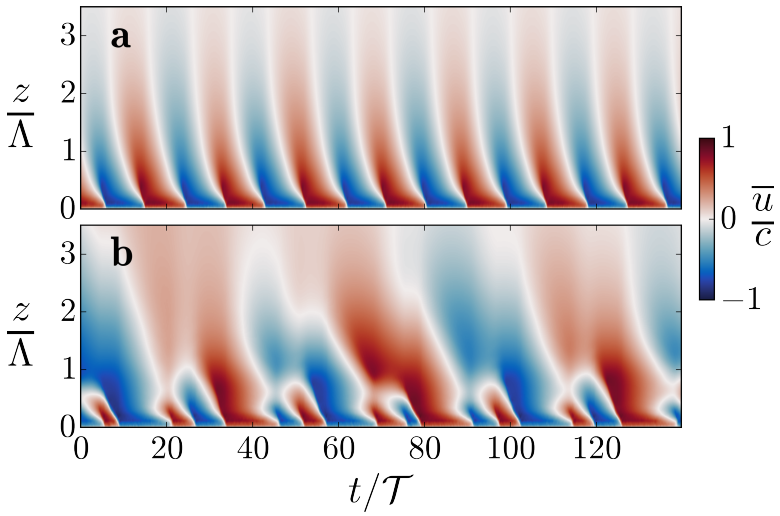

Fig. S7. Bifurcations in 3D nonlinear simulation with weak rotation. a. Hovmöller diagrams of the mean-flow $\overline{u}(z,t)$ for $\mathrm{Re}^{-1} = 0.08$. **b** Same for $\mathrm{Re}^{-1} = 0.04$.

References

1. Holton JR, Lindzen RS (1972) An updated theory for the quasi-biennial cycle of the tropical stratosphere. *Journal of the Atmospheric Sciences* 29(6):1076–1080.
2. Vallis GK (2017) *Atmospheric and oceanic fluid dynamics*. (Cambridge University Press).
3. Holton JR, Lindzen RS (1972) An updated theory for the quasi-biennial cycle of the tropical stratosphere. *Journal of the Atmospheric Sciences* 29(6):1076–1080.

4.3.3 Discussion about the effect of planetary rotation

In the previous section, the planetary rotation has barely been discussed. However, this rotation is essential to the QBO dynamics. Indeed, as we already discussed in section 4.1, rotation plays a major role in the confinement of the QBO signal to the equatorial region. Moreover, equatorial Rossby, Kelvin and Yanai gravity waves - which need a meridional gradient of planetary vorticity to propagate - are major contributors to momentum flux divergence driving the QBO. **This brings an important question regarding the results of the previous section: do the bifurcations towards altered regimes persist in the presence of rotation?**

In their 1972 paper, Holton & Lindzen [75] proposed a simple one-dimensional model, similar to the one discussed earlier, accounting for these equatorial waves. They considered the forcing coming from two equatorial waves: an easterly mixed Rossby-gravity wave and a westerly Kelvin waves. While these waves have a meridional extent, they mapped their effect into a one-dimensional equation for the zonal wind (following roughly the approach presented in Chapter 3). Their model successfully reproduced the salient periodic feature of the QBO while accounting for rotation via the consideration of equatorial wave. To probe the resilience of the bifurcations discussed in the previous section to the rotational effect, an easy first step is to explore the phase diagram of this simple model.

Ignoring the effect of the semi-annual oscillation and the vertical variation of density and radiative cooling, the Holton & Lindzen model writes in the nondimensionalised form

$$\partial_T \overline{u} - \frac{1}{\widetilde{F}} \partial_Z^2 \overline{u} = -\partial_Z \left(e^{-\int_0^Z \mathrm{d}Z' (1-\overline{u})^{-2}} - e^{-B\int_0^Z \mathrm{d}Z' (1+\overline{u})^{-2}\left(C(1+\overline{u})^{-1}-1\right)} \right), \tag{4.11}$$

where $B = k_0/k_1$ and $C = \beta/(k_1^2 c_1)$ are two parameters depending on the zonal wave numbers of the Kelvin wave k_0 and the Rossby wave k_1, the zonal phase speed of the of the Rossby wave c_1 and the meridional gradient of planetary vorticity at the equator β. To recover the model of frame 4.2.1, one simply need to set $B = 1$ and $C = 0$. In their paper, Holton & Lindzen considered $B = 0.25$ and $C = 1.92$ along with $\widetilde{F} \approx 10$.

The figure S6 of the preprint shows a bifurcation diagram obtain with this model (following the same method given in subsection 4.3.2; see also appendix C). We observe similar bifurcations from periodic to quasiperiodic regimes along with a large band of frequency locked regimes. Although the symmetry between the contra-propagating waves is broken, the bifurcation towards regimes of altered periodicity holds here. This first step into the investigation of the effect of rotation suggests that there is a good chance that altered periodicity regimes exist in more comprehensive 3D models of the QBO on a rotating planet.

Another important and interesting question is how the rotation sets the meridional profile of the QBO. Beyond equatorial waves that are intrinsically trapped at the equator, it would be interesting to investigate how the interplay between the planetary rotation and a broad meridional distribution of gravity wave activity would affect the meridional extent of the mean zonal flow reversals.

4.4 Conclusion of Chapter 4

In this chapter, inspired by the recently observed periodicity disruption of the quasi-biennial oscillation (QBO) on Earth [118] with analogues on Saturn [48], we investigated whether the variability of the reversals may come in part from its intrinsic underlying dynamics. To do so, we revisited a standard model of the QBO derived by [122] and highlighted a possible intrinsic nature of its variability.

Results summary

We exhibited the existence of regimes with disrupted periodicity obtained when the wave forcing is increased further above the threshold for the spontaneous emergence of the periodic reversals. These regimes had been foreseen by Kim & McGregor [81] within a similar model applied to the solar tachocline (involving different boundary conditions). However, they did not provide any bifurcation diagram. Here, we have filled this gap. Introducing an additional parameter, measuring the relative strength of the viscous damping to the radiative damping of the waves, we computed the complete bifurcation diagrams and unveiled a rich and complex quasiperiodic route to chaos in this 1D setting.

We observed similar transitions in fully nonlinear numerical simulations of a forced-dissipated stratified fluid, showing the robustness of these additional bifurcations to wave-wave interactions. Based on these bifurcation diagrams and the phenomenon of critical slowing down [88], we demonstrated an increase in sensitivity to external disturbance when approaching the bifurcation from periodic to quasi-periodic regimes.

Along the way, we revisited, the first bifurcation from a stable rest state towards periodic solutions. Building upon the work of Yoden & Holton [171], we considered a free-slip bottom condition for the zonal mean flow and offered an analytical prediction for the critical parameter at which the bifurcation occurs. We also showed that the nature of the transition is significantly different from the Hopf bifurcation observed in the no-slip scenario. In particular, we exhibit a divergence of the period of the reversals in the vicinity of the bifurcation point.

Perspectives

This last result invites us to better characterise the QBO bifurcation. For instance, it would be useful to derive normal forms for the one-dimensional QBO model in order to obtain scaling laws for the vicinity of the bifurcation point, particularly regarding the divergence of the limit cycle period observed in the free-slip case. A possible approach can be to resume the work of Yoden & Holton [171] who derived a simplified two-layer model reproducing the Hopf bifurcation and extend it to the free-slip case. Moreover, the addition of a third layer could capture the observed secondary bifurcations towards quasiperiodic regimes. We are currently carrying out this program.

As Plumb & McEwan had been able to replicate the reversals in laboratory, it would be interesting to know if the quasiperiodic route to chaos can be similarly reproduced (using, for instance, one of the experimental setups shown in figures 2.9b and 4.4a). The main issue would probably come from the large amplitude required for the wave. The accompanying strong mixing would make this experimental observation challenging.

To address the relevance of this route to chaos for the actual QBO, it will be necessary

to consider more comprehensive atmospheric numerical models, including rotation, 3D effects and realistic forcing. This study could build upon the recent 3D simulations of gas giants conducted by Showman and al. [1] who observed low-frequency reversals of equatorial zonal winds. It would also be interesting to see how the synchronisations on the seasonal cycle [126] coexist with the quasiperiodic route to chaos.

The effect of planetary rotation should deserve a particular attention. Indeed, the different idealised QBO models studied in the literature and the present work fail to explain the mechanism setting the meridional extent of equatorial reversals. To investigate this issue, a first step could be the study of an idealised atmosphere on an equatorial β-plane forced zonally by damped upward propagating gravity waves. This would allow probing the relative importance of the meridional circulation against the meridional extent of the wave forcing in determining the meridional extent of the QBO itself.

5. Boundary streaming

This chapter essentially provides a clone of a preprint, in section 5.2, which is currently under peer-review for an eventual publication in Journal of Fluid Mechanics. *The goal of this paper is to investigate the boundary streaming associated with viscous boundary layers of internal gravity waves using a quasilinear model. In section 5.1, we highlight the relevance of this investigation and summarise the main findings.*

5.1 Foreword

5.1.1 Internal gravity wave and acoustic wave streaming

In the previous chapter, we demonstrated the existence of a quasiperiodic route to chaos in idealised models of equatorial flow reversals driven by internal wave streaming. Let us mention recent works by Launay and collaborators highlighting a strong analogy with acoustic wave streaming. In their numerical simulations of cavity-flows driven by acoustic wave streaming, they unveiled a similar route to chaos [84]. Their numerical study focused on the unsteady flow regimes forced by a damped acoustic beam reflected several times in a cubic cavity. Figure 5.1 provides a sketch of the geometry and the beam and presents a periodic and a frequency locked flow regimes obtained by Launay et al. The analogy between the generation of slowly evolving mean flows by damped internal waves and acoustic streaming has already been mentioned in section 2.2. This additional example stresses it once again.

We suggest here to extend the analogy to the mean flow generated in the viscous boundary layers. This aspect has already been thoroughly studied in the context of acoustic waves.

5.1.2 Boundary layers and boundary flows in acoustic streaming

The study of acoustically driven flows led to a further consideration of **viscous boundary layers** of the wave field with pioneering work from Rayleigh at the end of 19th century [127]. The characteristic thickness of those boundary layers is equivalent at the linear level to the classical stokes layer thickness associated with the sliding oscillation of a solid plane

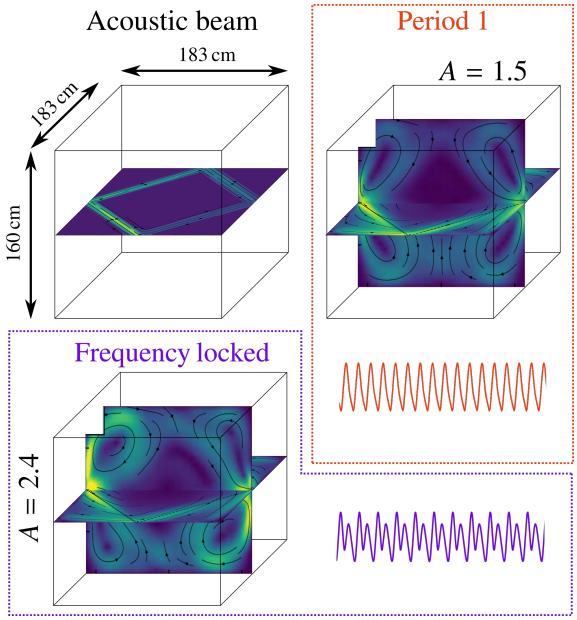

Figure 5.1: **Periodic and frequency locked regimes in acoustically-driven cavity flow** (Borrowed and adapted from [84])**. Upper-left.** Sketch of the cavity and horizontal section of the acoustic beam. **Upper-right.** Horizontal and vertical sections the time-averaged velocity magnitude for $A = 1.5$, where A is the normalised incoming power of the acoustic-beam. A single point time signal is shown whose period is of the order of 3 min. **bottom.** Same for $A = 2.4$. In this case, the period of the signal is of the order of 20 min.

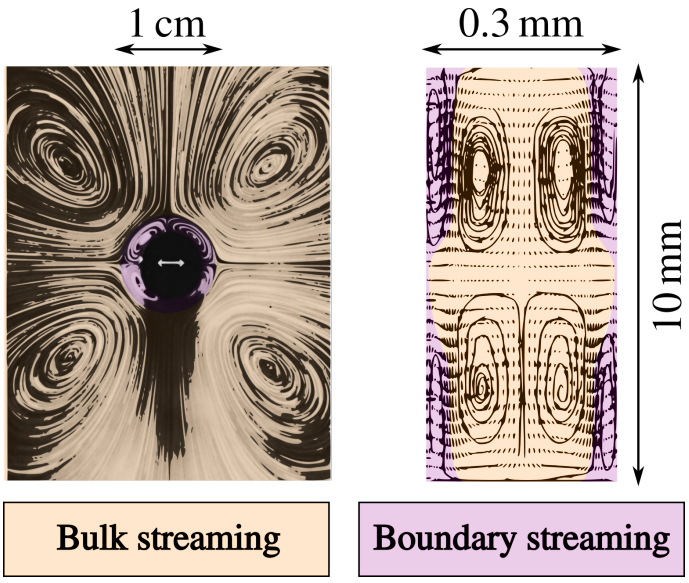

Figure 5.2: **Boundary flows driven by acoustic viscous boundary layers** (Borrowed and adapted from [139] and [4]). **Left.** Observation of the steady streaming induced by oscillating cylinder [139]. **right.** Numerical simulation of the steady streaming induced by a mode-one acoustic wave in a 2D rectangular domain. To distinguish them, bulk and boundary streaming regions have been highlighted in different colours.

boundary

$$\delta_\nu = \sqrt{\frac{2\nu}{\omega}}, \tag{5.1}$$

where ν is the kinematic viscosity and ω the angular frequency of the acoustic wave [172]. These viscous boundary layers have been shown to significantly force a mean flow in its vicinity [127, 172]. This phenomenon is known as **boundary streaming**. While this boundary streaming turned out to be essential to the intensity and structure of the steady Rayleigh streaming cells, in certain flow regimes it can lead to smaller recirculation cells localised in the vicinity of the viscous boundary layers called Schlichting cells [142]. Figure 5.2 shows two instances of such Schlichting cells. Acoustic boundary streaming has been thoroughly studied experimentally, numerically and analytically [12].

This extensive research contrast with the little attention paid to internal wave boundary streaming.

5.1.3 Boundaries and internal gravity waves

So far, in the context of internal gravity wave streaming, the effect of viscous boundary layers has been largely ignored. This is surprising given the importance of boundaries for internal gravity waves in experimental or geophysical contexts: In laboratory, internal gravity waves are generated by moving boundaries [60, 59, 123, 147] and wall-reflections have prompted a recent renewed scientific interest [99, 62]. In the oceans, an important source of internal gravity waves comes from the tides moving water mass above bathymetry [9, 6]. Besides, internal gravity waves are often generated through the interaction between a mean flow and the bathymetry (equivalently orography in the atmosphere). Reflections on continental shelves or topography are thought to play an important role in the global gravity wave spectrum and their breaking [40, 43, 20, 63]. The undulations of the tropopause may play the role of a bottom boundary for the stratosphere [28].

In the geophysical context, boundary layers are mostly of nonlinear or even turbulent nature. Indeed, the ocean floors present intensified turbulence which is reflected by an enhanced eddy diffusivity, several orders of magnitude larger than the molecular value [124]. In the stratosphere, measurements also suggest large turbulent diffusivities especially close to the tropopause [87]. These turbulent boundary layers might have significant implications for the generation of boundary flows. Streaming is generally well-captured by quasilinear models considering a linear propagation of the waves. Therefore, following the common practice (see e.g. the Ekman layers theory among others [161]), the effect of turbulent boundary layers to internal wave streaming can first be explored with the use of high eddy-viscosities in these quasilinear models.

In oceanic or atmospheric numerical models, a high eddy-viscosity is often used either as a tool to parametrise subgrid-scale turbulent mixing [148, 82] or for numerical stability purposes. In laboratory, internal wave viscous boundary layers are closer to the linear regime. For instance, in the experimental setups of Plumb & McEwan [123] and Sémin et al. [147] (see also figs. 2.9 and 4.4), we have $\delta_\nu \approx 3\,\text{mm}$ which is of the same order of their wave generator amplitude.

5.1.4 Results summary

In sections 5.2, we include a copy of a preprint which is currently under peer-review for publication in *Journal of Fluid Mechanics*. The goal of this paper is to investigate the boundary streaming associated with the viscous boundary layers of internal gravity waves using a quasilinear model. We extend the quasilinear framework developed in Chapter 3 considering viscous diffusion for both the mean flow and the wave field. The periodic geometry is akin to the cylindrical geometry of the experimental setups of Plumb & McEwan [123] and Sémin et al. [147]. Just as in the case of acoustic waves, we report the generation of boundary flows within the boundary layers of internal gravity waves. We consider both a no-slip boundary condition - relevant to laboratory contexts - and a free-slip boundary condition - relevant to some numerical contexts [86]. We exhibit important differences in the boundary streaming associated with these two boundary conditions.

An important difference from past studies of acoustic boundary streaming is that we look at the dynamics rather than at the steady regime. This way, we show that boundary streaming dominates over bulk streaming at early times. In particular, in the no-slip scenario, we show that the integrated Reynolds stress divergence vanishes. Then, the streaming in bulk must necessarily be compensated by an strong and opposite streaming in the boundary layer. Consequently, the boundary streaming is more intense in the no-slip case than in the free-slip case.

On the contrary to acoustic wave streaming, internal wave streaming can lead to flow velocities of the order of the phase speed of the waves such that the interplay between the mean flow and the wave is important. To address this issue, we develop a novel geometrical optics treatment including viscosity and treat the case of the mean flow reversals driven by a standing internal gravity wave forcing [123]. In this configuration, the effect of the mean flow on the wave is essential. We show that the presence of viscous boundary layers significantly impacts the reversals.

5.1.5 Perspectives

This work should be extended to further assess the importance of boundary streaming in the context of internal gravity waves. Addressing the boundary streaming generated by the reflection of an internal wave on a plane wall would be a first straightforward extension of the present quasilinear calculations. Then, it would be important to go beyond the quasilinear approximation and conduct fully nonlinear simulations. This would allow probing the robustness of our quasilinear prediction and ultimately exploring the streaming induced by a turbulent boundary layer.

In would be interesting to see whether the prediction that the integral of Reynolds stress divergence vanishes still holds when the boundary layer is nonlinear. An analytical result could be attainable with the use of Lagrangian-mean approaches which are better suited to deal with finite amplitude waves.

5.2 Boundary streaming by internal waves (*submitted publication*)

Boundary streaming by internal waves

A. Renaud†, A. Venaille

Univ Lyon, Ens de Lyon, Univ Claude Bernard, CNRS, Laboratoire de Physique, F-69342 Lyon, France

(Received xx; revised xx; accepted xx)

Damped internal wave beams in stratified fluids have long been known to generate strong mean flows through a mechanism analogous to acoustic streaming. While the role of viscous boundary layers in acoustic streaming has thoroughly been addressed, it remains largely unexplored in the case of internal waves. Here we compute the mean flow generated close to an undulating wall that emits internal waves in a viscous, linearly stratified two-dimensional Boussinesq fluid. Using a quasi-linear approach, we demonstrate that the form of the boundary conditions dramatically impacts the generated boundary streaming. In the no-slip scenario, the early time Reynolds stress divergence within the viscous boundary layer is much stronger than within the bulk while also driving flow in the opposite direction. Whatever the boundary condition, boundary streaming is however dominated by bulk streaming at large time. Using a WKB approach, we investigate the consequences of adding boundary streaming effects to an idealised model of wave-mean flow interactions known to reproduce the salient features of the quasi-biennial oscillation. The presence of wave boundary layers has a quantitative impact on the flow reversals.

Key words: Internal Gravity Waves; Streaming; Boundary Layers

1. Introduction

Internal gravity waves play a crucial role in the dynamics of atmospheres and oceans by redistributing energy and momentum (Sutherland 2010). In particular, strong mean flows can be generated by non-linear effects within internal wave beams (Lighthill 1978), a phenomenon analogous to acoustic streaming (Riley 2001; Eckart 1948). Internal wave streaming is central to the quasi-biennial oscillation of zonal winds in the equatorial stratosphere (Baldwin *et al.* 2001). The salient features of this robust phenomenon have been reproduced in a celebrated laboratory experiment (Plumb & McEwan 1978) and in direct numerical simulations (Wedi & Smolarkiewicz 2006). Since then, other instances of internal wave streaming have been reported in various experimental and numerical configurations: Semin *et al.* (2016) used a quasi two-dimensional experimental setting similar to Plumb & McEwan (1978) to describe internal wave streaming in the absence of flow reversal; Grisouard & Bühler (2012); Bordes *et al.* (2012); Kataoka & Akylas (2015) showed that three-dimensional effects lead to vortical streaming in the domain bulk. However, those previous studies have not addressed the role of viscous boundary layers and their potential implications for the generation of mean flows confined to the boundary. This contrasts with acoustic waves which have long been known to produce strong mean flows within their viscous boundary layers (Rayleigh 1884; Nyborg 1958). Boundaries are essential to the generation of the waves in laboratory experiments

† Email address for correspondence: antoine.renaud@ens-lyon.fr

(Gostiaux *et al.* 2006) or numerical models (Legg 2014), and to energy focusing (Maas *et al.* 1997). In the atmosphere and oceans, internal gravity waves are often generated through the interaction between a mean flow and a solid boundary (orography in the atmosphere, bathymetry in the oceans). Viscous effects are negligible at those geophysical scales, but numerical simulations of these flows are usually performed with larger effective turbulent viscosities. It is therefore crucial to understand the effect of viscous boundary layers.

Viscous internal wave beams generated by boundaries have been extensively studied (Voisin 2003), together with their consequences on the bulk energy budget of numerical ocean models (Shakespeare & Hogg 2017). The role of viscous boundary layers has been addressed by Beckebanze & Maas (2016) to close the energy budget of internal wave attractors; Chini & Leibovich (2003) described the viscous boundary layers in the case of Klemp and Durran boundary conditions; Passaggia *et al.* (2014) studied the structure of a stratified boundary layer over a tilted bottom with a small stream-wise undulation. The effect of the viscous boundary layers on the mean flow, however, is not discussed in those works. By contrast, Grisouard & Thomas (2015, 2016) carried out full nonlinear simulations of internal wave reflections and showed the existence of strong mean flows induced by the waves in the vicinity of a reflecting boundary. They also showed the importance of the wave boundary layers in the energy budget of the mean flow. This provides a strong incentive to revisit the mean flow generation associated with internal gravity wave boundary layers.

Here, using a two-dimensional and quasi-linear framework, we compute the mean flow generated by internal gravity waves close to a boundary, paying particular attention to the role of boundary conditions. The importance of changing the boundary condition in numerical models of internal wave dynamics close to bottom topography has been noticed in previous work related to mixing and wave dissipation (Nikurashin & Ferrari 2010). We will show that changing boundary conditions also substantially affects wave-driven mean flows. The quasi-linear approach is introduced in section 2. The structure of the viscous linear waves, their induced Reynolds stress divergences and the consequences for mean flow generation are discussed in section 3. An application to an idealised model of a quasi-biennial oscillation analogue is presented in section 4. A WKB treatment of the problem is provided in appendix A.

2. Internal gravity wave-mean flow interactions with zonal symmetry

We consider a fluid within a two-dimensional domain, periodic in the zonal x-direction with period L and semi-infinite in the vertical z-direction. The bottom boundary is a vertically undulating line located on average at $z = 0$. The fluid is considered incompressible, Boussinesq, viscous with viscosity ν and linearly stratified with buoyancy frequency N. For the sake of simplicity, we ignore any buoyancy diffusion process. This approximation is relevant for experimental configurations where the stratification agent is salt, given the low diffusivity $\kappa = \nu/1000$, but it does not apply to the atmosphere and the ocean, where turbulent viscosity and diffusivity have the same order of magnitude.

Throughout this work, we solely consider monochromatic waves. Let us introduce the typical zonal wave number $k = 2\pi/L$, angular frequency ω and amplitude of the bottom undulation h_b. There are three independent dimensionless numbers in the problem. The Froude number $Fr = \omega/N$ controls the angle of propagation of the wave. The wave Reynolds number $Re = \omega/\left(k^2\nu\right)$ controls the viscous damping and the viscous boundary layer thickness of the wave field. When considering the lee wave generation case, this wave Reynolds number scales as UL/ν, where U is the typical mean zonal velocity. The

third parameter is the dimensionless amplitude of the wave $\epsilon = h_b k$, which corresponds to the typical slope of the bottom boundary and controls the linearity of the wave. In numerical simulations, an additional aspect ratio $r = kH$ and a wave Péclet number $\omega/(k^2\kappa)$ have to be taken into account, because the domain has a finite height H, and because it includes a buoyancy diffusivity κ. Both parameters will be much larger than one in the numerical simulations presented in this paper, and we will assume that they do not play a significant role in this limit. We use k^{-1}, ω^{-1} as reference length and time for the space-time coordinates, $c = \omega/k$ as a reference velocity, N^2/k as a reference buoyancy, and write the dynamical equation in a dimensionless form

$$\left\{ \begin{array}{ll} \partial_t \mathbf{u} + (\mathbf{u}\cdot\nabla)\,\mathbf{u} & = -\nabla p + Fr^{-2} b \mathbf{e}_z + Re^{-1}\nabla^2 \mathbf{u} \\ \partial_t b + \mathbf{u}\cdot\nabla b + w & = 0 \\ \nabla\cdot\mathbf{u} & = 0 \end{array} \right. , \tag{2.1}$$

where $\mathbf{u} = (u, w)$ is the two-dimensional velocity, p the renormalised pressure, b the buoyancy anomaly, $\mathbf{e}_z$ the unit vector of the vertical direction pointing upward, and $\nabla^2 = \partial_{xx} + \partial_{zz}$ the standard Laplacian operator.

Previous studies in the context of acoustic streaming have investigated the effect of changing boundary conditions on mean flow properties (Xie & Vanneste 2014). In this paper devoted to internal wave streaming, we discuss two different bottom boundary conditions on $z = \epsilon h\,(x,t)$:

$$\text{free-slip:}\quad w = \epsilon\left(\partial_t h + u\partial_x h\right),\ \boldsymbol{G}\left[\mathbf{n}_h\right]\cdot\mathbf{n}_h^{\perp} = 0 \quad ; \quad \text{no-slip:}\quad \mathbf{u} = \epsilon\partial_t h\mathbf{e}_z, \tag{2.2}$$

where $\mathbf{n}_h = \nabla\left(z - \epsilon h\,(x,t)\right)$ is a local normal vector of the bottom boundary, $\mathbf{n}_h^{\perp}$ a local tangent vector and $\boldsymbol{G}$ the velocity gradient tensor ($G_{ij} = \partial_j u_i$). This free-slip condition is the one implemented in the numerical model considered in this paper (see MITgcm user's manual 2018). It is equivalent to the stress-free condition when boundary curvature can be neglected. In the stress-free case, $\boldsymbol{G}$ is replaced by its symmetric part only. Regarding the boundary streaming, we confirmed that the discrepancies between stress-free and our free-slip condition arise only in non-hydrostatic regimes of internal waves. Therefore, in most practical cases, the results obtained by considering the free-slip condition (2.2) will also be relevant for numerical simulation using the stress-free condition. Finally, we require all gradients with respect to z to vanish as $z \to \infty$.

When considering a progressive pattern ($h\,(x,t) = h\,(x-t)$) in (2.2), a Galilean change of reference yields the case of lee-wave generation by a depth-independent mean flow passing over bottom topography. Then, the free-slip bottom boundary condition for the generation of lee waves obviates the need to treat the near-bottom critical layer induced by a more realistic no-slip condition (Passaggia *et al.* 2014). Regarding the free-slip condition, the predictions will be compared against direct numerical simulations of monochromatic lee waves generation using the MIT global circulation model (Adcroft *et al.* 1997) which specifically uses our definition for the free-slip condition. The no-slip boundary condition in (2.2) is relevant to model the generation of internal gravity waves in laboratory experiments using vertically oscillating bottom membranes (Plumb & McEwan 1978; Semin *et al.* 2016) or a system of plates and camshafts (Gostiaux *et al.* 2006). We will, however, consider limiting cases where the viscous boundary layer is larger than the boundary height variations, which is not always the case in actual experiments.

We decompose any field ϕ into a mean flow part $\overline{\phi}$ and a wave part ϕ' using the zonal

averaging procedure (see Bühler 2014):

$$\overline{\phi}\,(z,t) = \frac{1}{2\pi}\int_0^{2\pi} \mathrm{d}x\;\phi\,(x,z,t)\,, \quad \phi' = \phi - \overline{\phi}. \tag{2.3}$$

The averaging of the zonal momentum equation in (2.1) leads to the mean flow evolution equation:

$$\partial_t \overline{u} = -\partial_z \overline{u'w'} + Re^{-1}\partial_{zz}\overline{u}. \tag{2.4}$$

The source of streaming is the divergence of the Reynolds stress $-\partial_z\overline{u'w'}$. To compute this term, we subtract the averaged equations from (2.1) and linearise the result assuming $(u', w', b', p') = O(\epsilon)$ with $\epsilon \ll 1$. In the limit $\epsilon \ll 1$, in the absence of dissipation in the buoyancy equation, it turns out that $\overline{b}$ scales with ϵ^2 at all time (see Bühler 2014). In the following, we will ignore $\overline{b}$ and its evolution.

At this stage, we assume that $|\overline{u}| \ll 1$. Starting from a state of rest, at early times of its evolution, the mean flow is weak, which justifies this assumption. At later times, the feedback of the mean flow on the wave can no longer be ignored (Kataoka & Akylas 2015; Fan *et al.* 2018), as will be discussed in more detail in section 4 (see also equation (A 1) in appendix A). This case without feedback from the mean flow leads to homogeneous wave equations, which provides a simple framework to describe essential features of boundary streaming:

$$\begin{cases} \partial_t u' + \partial_x p' - Re^{-1}\nabla^2 u' & = 0 \\ \partial_t w' + \partial_z p' - Fr^{-2}b' - Re^{-1}\nabla^2 w' & = 0 \\ \partial_t b' + w' & = 0 \\ \partial_x u' + \partial_z w' & = 0 \end{cases}. \tag{2.5}$$

The coupled equations (2.4) and (2.5) form a quasi-linear model for the interaction between boundary generated viscous waves and the zonal mean flow. The Reynolds stress divergence, $-\partial_z\overline{u'w'}$, at the origin of streaming, is the only non-linear term remaining in the problem. It acts as a forcing term and is computed from the wave field.

We perform the wave-mean decomposition on the boundary conditions (2.2) and we linearise the result assuming as above a wave amplitude of order ϵ on an asymptotically flat boundary at $z = 0$:

$$\text{free-slip:} \quad \begin{cases} \partial_z\overline{u} & = 0 \\ w' - \partial_t h & = 0 \\ \partial_z u' & = 0 \end{cases} \quad ; \quad \text{no-slip:} \quad \begin{cases} \overline{u} & = 0 \\ w' - \partial_t h & = 0 \\ u' & = 0 \end{cases}. \tag{2.6}$$

In the free-slip case, the Reynolds stress divergence vanishes at the bottom ($\partial_z\overline{u'w'}|_{z=0} = 0$) while, in the no-slip case, the Reynolds stress itself vanishes at the bottom ($\overline{u'w'}|_{z=0} = 0$). Given that $\overline{u'w'}|_{z\to\infty} = 0$ for damped waves, the integrated streaming in the no-slip case has to be zero: $\int_0^\infty \partial_z\overline{u'w'}\,\mathrm{d}z = 0$. Consequently, all the streaming far from the bottom boundary has to be compensated for by an opposite boundary streaming.

3. From viscous waves to boundary streaming

3.1. *Viscous internal gravity waves*

We describe in this section the detailed structure of the Reynolds stress divergences for both the free-slip and the no-slip boundary conditions, when the mean flow can be neglected. Inserting the ansatz $(u', w', b', p') = \Re\left[\left(\tilde{u}, \tilde{w}, \tilde{b}, \tilde{p}\right) e^{i(x+mz-t)}\right]$ into equation

(2.5) leads to the dispersion relation for viscous internal gravity waves, expressed here as

$$m^2 = \frac{iRe}{2}\left(1 \pm \sqrt{1 + \frac{4i}{Fr^2 Re}}\right) - 1. \tag{3.1}$$

Among the four possible solutions for m, we retain only the two upward propagating ones, by discarding the solutions with a negative imaginary part. To simplify the discussion, it will be useful to express these solutions in the asymptotic regime $Fr^2Re \gg 1$, followed by $Fr \ll 1$:

$$\begin{cases} m_w &= -1/Fr + i/\left(2L_{Re}\right) + o\left(\left(ReFr^3\right)^{-1}\right) \\ m_{bl} &= (1+i)/\delta_{Re} + o\left(Re^{1/2}\right) \end{cases}, \tag{3.2}$$

with

$$L_{Re} = ReFr^3 \quad \text{and} \quad \delta_{Re} = \sqrt{2/Re}\,. \tag{3.3}$$

The solution m_w corresponds to the propagating solution converging toward the inviscid solution in the limit $Re \to \infty$. L_{Re} is the damping length-scale of the wave-beam, scaling linearly with the wave Reynolds number. The solution m_{bl} corresponds to the wave boundary layer. The boundary layer thickness, given by δ_{Re}, scales as $Re^{-1/2}$ as in the classical case of a horizontally oscillating flat boundary. This last solution is needed to match the propagating solution with the viscous boundary conditions and is analogous to the one discussed in acoustic boundary streaming (Nyborg 1958). Importantly the ratio L_{Re}/δ_{Re} diverges in the limit $Fr^2Re \to +\infty$. This limit, therefore, allows for a clear separation between bulk and boundary effects.

The viscous internal-wave dispersion relation has already been extensively studied. Chini & Leibovich (2003) considered a finite Prandtl number, which provides an additional branch of boundary layer solutions associated with the diffusion operator in the buoyancy equation. They also gave asymptotic expansions for large Reynolds number. Grisouard & Thomas (2016) considered the effect of a Coriolis force, which also gives rise to an additional branch of boundary layer solutions. Although rotation, buoyancy diffusion, and their associated boundary layer solutions undoubtedly impact boundary streaming, we do not consider these additional effects, to simplify the presentation.

In the case of a progressive sine-shaped bottom undulations, $h\left(x,t\right) = \Re\left[e^{i(x-t)}\right]$, the general expression of the wave field is given by the linear combination of a propagating (w) and a boundary layer (bl) part

$$[u', w', b', p'] = \Re\left\{\left(\phi_w \mathbf{P}[m_w]\, e^{im_w z} + \phi_{bl}\mathbf{P}\left[m_{bl}\right] e^{im_{bl}z}\right) e^{i(x-t)}\right\}, \tag{3.4}$$

with

$$\mathbf{P}[m] = \left[1, -m^{-1}, iFr^{-2}m^{-1}, Fr^{-2}\left(1+m^2\right)^{-1}\right]. \tag{3.5}$$

$\mathbf{P}[m]$ is the polarisation of the wave obtained from (2.5), (m_w, m_{bl}) are given in equation (3.2), and (ϕ_w, ϕ_{bl}) are scalars determined by the boundary conditions (2.6):

$$\text{free-slip:} \begin{cases} \phi_w &= i\epsilon\frac{m_w m_{bl}^2}{m_{bl}^2 - m_w^2} \\ \phi_{bl} &= i\epsilon\frac{m_{bl} m_w^2}{m_w^2 - m_{bl}^2} \end{cases} ; \quad \text{no-slip:} \begin{cases} \phi_w &= i\epsilon\frac{m_w m_{bl}}{m_{bl} - m_w} \\ \phi_{bl} &= i\epsilon\frac{m_w m_{bl}}{m_w - m_{bl}} \end{cases}. \tag{3.6}$$

The generic vertical profiles of the wave field u' are drawn in figure 1 for both boundary conditions. Most of the differences between the two profiles are located in the boundary layer close to the bottom. We will see that these different profiles lead to very different boundary streaming behaviours, by computing the Reynolds stress divergence of the corresponding wave fields.

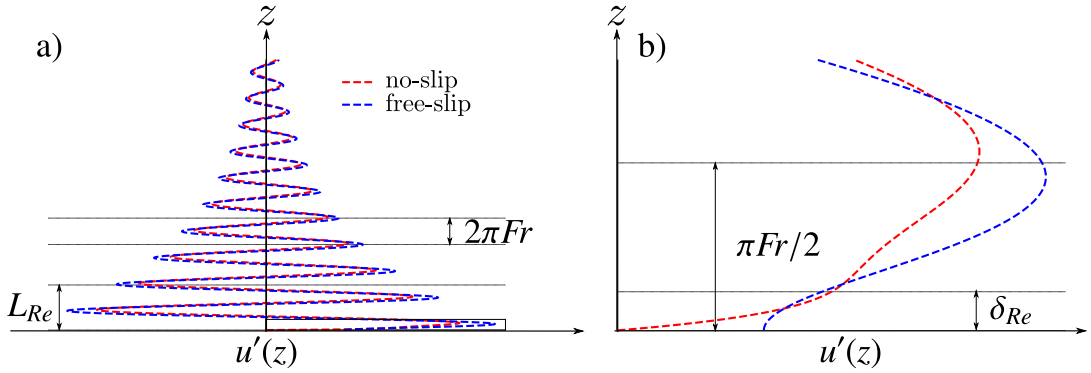

Figure 1: a) Example of a linear computation of the vertical profile of the fully established wave field, u', in the absence of a mean flow, with the free-slip (blue) and no-slip (red) boundary conditions. b) Zoom on the boundary layer of the wave. The wave damping length, L_{Re}, and the boundary layer thickness, δ_{Re}, are represented on the graph along with the inviscid vertical wavelength, $\lambda_z = 2\pi Fr$.

3.2. *Reynolds stress divergence*

The Reynolds stress $\overline{u'w'}$ is composed of cross terms involving both the propagative and the boundary layer contributions. In the limit of small viscosity, the "self-interaction" of the propagating contribution decreases exponentially over a scale L_{Re}. This effect is responsible for bulk streaming. All the other terms involve a pairing with the boundary layer contribution that decay exponentially over the scale δ_{Re}. The sum of these terms induces the boundary streaming. We thus decompose the Reynolds stress into a bulk and a boundary term

$$\overline{u'w'}\,(z) = F_w\,(z) + F_{bl}\,(z)\,. \tag{3.7}$$

In the remainder of this section, the quasi-linear computations will be performed by using the exact solutions of (3.1). In order to get insights on the basic differences between the free-slip and the no-slip case, it is useful, however, to estimate the Reynolds stress by using the asymptotic expression (3.2) for both boundary conditions in (2.6):

$$\text{free-slip:} \quad \begin{cases} F_w\,(z) &= \frac{\epsilon^2}{2Fr}\exp\left\{-\frac{z}{L_{Re}}\right\} \\ F_{bl}\,(z) &= \frac{\epsilon^2}{Fr^2 2\sqrt{2Re}}\exp\left\{-\frac{z}{\delta_{Re}}\right\}\left(\sin\frac{z}{\delta_{Re}} + \cos\frac{z}{\delta_{Re}}\right) \end{cases} \quad . \tag{3.8}$$

$$\text{no-slip:} \quad \begin{cases} F_w\,(z) &= \frac{\epsilon^2}{2Fr}\exp\left\{-\frac{z}{L_{Re}}\right\} \\ F_{bl}\,(z) &= -\frac{\epsilon^2}{2Fr}\exp\left\{-\frac{z}{\delta_{Re}}\right\}\cos\frac{z}{\delta_{Re}} \end{cases}$$

The bulk Reynolds stress F_w is the same at leading order for both the free-slip and the no-slip case. The difference lies in the boundary-driven Reynolds stress F_{bl}. The corresponding asymptotic expressions for the streaming body forces are:

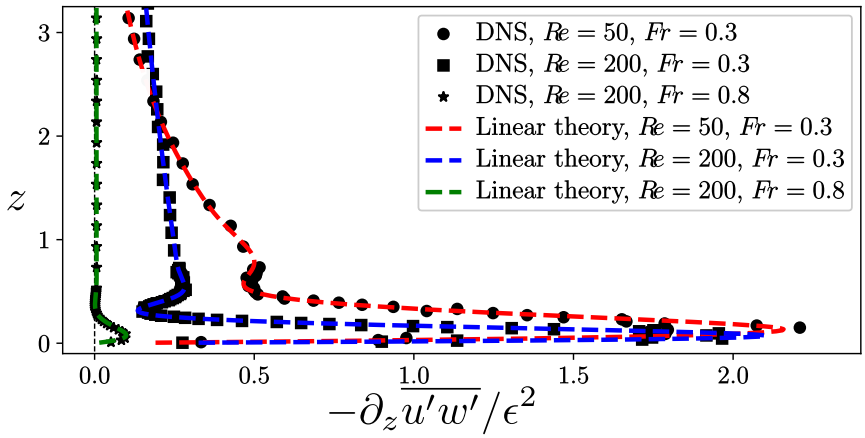

Figure 2: Plot of the vertical profile of the Reynolds stress divergence in the absence of mean flow ($\overline{u} = 0$) considering the free-slip boundary condition for different couples (Re, Fr). The markers plots come from high-resolution direct numerical simulations (DNS) while the dashed lines plots come from the full linear theory without mean flow. The other dimensionless parameters for the simulation are $\epsilon = 0.01$ (wave amplitude) and $r = 6L_{Re}$ (domain aspect ratio); the resolution is $\Delta x = \Delta z = \delta_{Re}/50$; the grid is stretched above $z = 6L_{Re}$ to avoid wave reflection; the simulated data have been smoothed over ten time steps of the simulation to get rid of the fast motion coming from surface waves present in the numerical model.

$$\text{free-slip:} \quad \begin{cases} -\partial_z F_w(z) &= \frac{\epsilon^2}{2Fr^4 Re} \exp\left\{-\frac{z}{L_{Re}}\right\} \\ -\partial_z F_{bl}(z) &= \frac{\epsilon^2}{2Fr^2} \exp\left\{-\frac{z}{\delta_{Re}}\right\} \sin\frac{z}{\delta_{Re}} \end{cases}$$

$$\text{no-slip:} \quad \begin{cases} -\partial_z F_w(z) &= \frac{\epsilon^2}{2Fr^4 Re} \exp\left\{-\frac{z}{L_{Re}}\right\} \\ -\partial_z F_{bl}(z) &= -\frac{\epsilon^2\sqrt{Re}}{2Fr\sqrt{2}} \exp\left\{-\frac{z}{\delta_{Re}}\right\} \left(\cos\frac{z}{\delta_{Re}} + \sin\frac{z}{\delta_{Re}}\right) \end{cases} \quad . \tag{3.9}$$

In the free-slip case, the boundary forcing amplitude does not depend on the wave Reynolds number at leading order, only its e-folding height does. This amplitude decreases with the Froude number. This effect can be seen in figure 2 where the free-slip Reynolds stress divergence $\partial_z \overline{u'w'}$ is plotted for three different values of Reynolds and Froude numbers. These quasi-linear calculations are successfully compared to high resolution direct numerical simulations of the established wave pattern generated by a depth-independent flow above a sine-shaped topography in a linearly stratified fluid.

In the no-slip case, boundary forcing is opposite (and much stronger) than the bulk forcing, as shown in figure 3-a. The underlying reason is the vanishing of the integral of the Reynolds stress divergence over the whole domain, as discussed at the end of section 2. According to equation (3.9), the amplitude of the boundary forcing evaluated at the bottom scales as $\epsilon^2 Re^{1/2}/Fr$. In the limit $ReFr^2 \gg 1$, this amplitude is much larger than in the free-slip case. In addition, it increases with the Reynolds number. However, we will see in section 3.3 that the amplitude does not blow up in a distinguished limit that is consistent with the linearization of the equations.

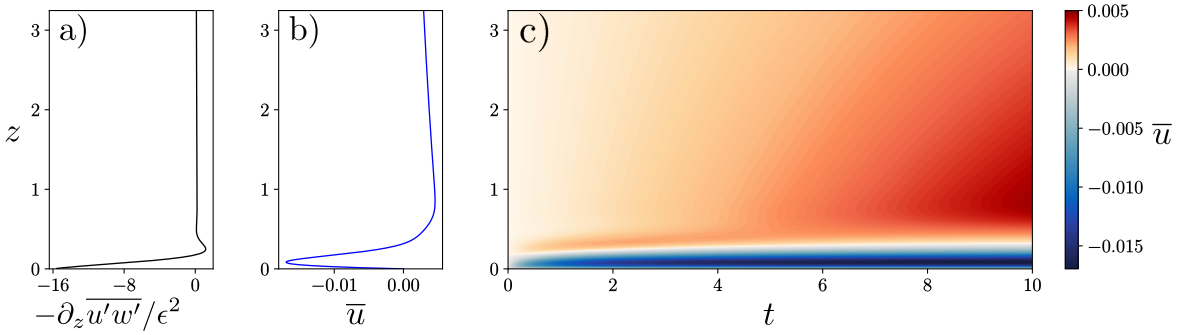

Figure 3: a) Plot of the vertical profile of the Reynolds stress divergence for the no-slip boundary condition computed using the full linear theory without mean flow. b) Plot of the vertical profile of the mean flow at $t = 10$ computed using the quasi-linear model for the no–slip boundary condition. c) Hovmöller diagrams of the mean flow , $\overline{u}\,(z,t)$, computed using the quasi-linear theory for the scenario in which the lower boundary condition is no-slip. The parameters are $Re = 200$, $Fr = 0.3$ and $\epsilon = 0.005$.

3.3. *Boundary flows*

We now look for the mean flow response to the Reynolds stress divergences, by inserting the linear predictions for wave fields into equation (2.4). When ignoring the influence of the mean flow on the wave fields, equation (2.4) becomes a linear diffusion equation with a steady forcing, that can be decomposed into a bulk and a boundary contribution, as in equation (3.7).

The typical time scales τ_w and τ_{bl} for the mean flow to reach a given velocity U in the presence of either bulk or boundary streaming forcing terms are obtained by balancing $\partial_t\overline{u}$ with $\partial_z F_w$ and $\partial_z F_{bl}$, respectively. Using the large Reynolds number asymptotic estimates given in equation (3.9) leads then to $\tau_{bl}/\tau_w \sim 1/(Fr^2 Re)$ in the free-slip case and $\tau_{bl}/\tau_w \sim 1/(Fr^2 Re)^{3/2}$ in the no-slip case. We thus expect the boundary streaming to dominate over the bulk streaming at the early stage of the mean flow evolution in both cases.

At a quasi-linear level, the early stage of the mean flow evolution is obtained for both the free-slip and the no-slip conditions by solving equation (2.4) numerically, assuming that the wave field is described by equations (3.1), (3.4), (3.5) and (3.6). A finite size domain is considered in the simulations with an aspect ratio $r = 6L_{Re}$. The waves are computed as if the domain were semi-infinite and a free-slip upper boundary condition is considered for the mean flow.

In figure 4, we compare the quasi-linear predictions for the free-slip boundary condition against direct numerical simulations. The parameters are $Re = 200$, $Fr = 0.3$ and $\epsilon = 0.01$. For those parameters, the wave boundary layer thickness is $\delta_{Re} = 0.1$ and the viscous damping length is $L_{Re} = 5.15$. The Hovmöller diagrams focus on an area close to the bottom boundary. We use a vertical resolution of $\mathrm{d}z = 0.0067$ which resolves properly the wave boundary layer. In the DNS, a stretched grid has been implemented on the vertical to avoid any downward reflection. The quasi-linear model captures well the boundary streaming effect. To emphasise the crucial role of the boundary streaming term, we added a diagram in figure 4 of a quasi-linear computation where the boundary forcing has been removed in (2.4) ($F_{bl} = 0$ in (3.7)). We clearly see that the presence of boundary streaming is important to predict accurately the early evolution of the mean flow in this case.

In figure 3-c, we show a Hovmöller diagram of the mean flow computed using the quasi-

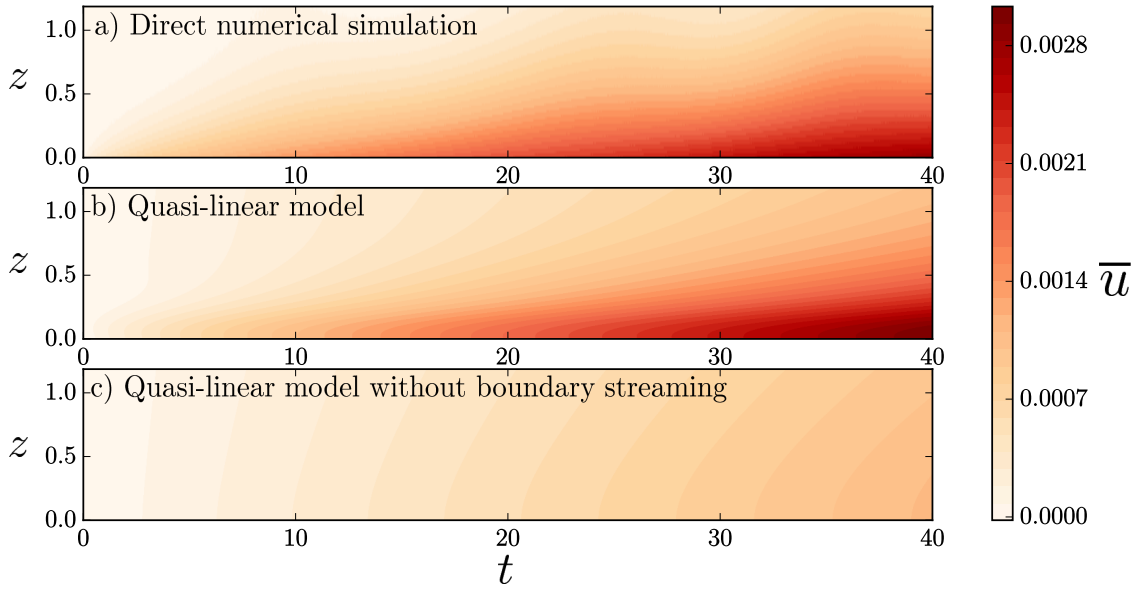

Figure 4: Hovmöller diagrams of the mean flow, $\overline{u}\,(z,t)$, for the scenario in which the bottom boundary condition is free-slip. a) Direct numerical simulation (DNS) b) quasi-linear model c) quasi-linear model without the boundary streaming terms in the Reynolds stress divergence. The parameters are $Re = 200$, $Fr = 0.3$ and $\epsilon = 0.01$, $\mathrm{d}x = \mathrm{d}z = \delta_{Re}/15$. The grid is exponentially stretched on the vertical axis above $z = 6L_{Re}$ in the DNS. At larger time, around $t \sim 300$, the mean flow induced by bulk streaming becomes larger than the mean flow induced by boundary streaming.

linear model in the case of no-slip boundary condition. The parameters are $Re = 200$, $Fr = 0.3$ and $\epsilon = 0.005$. As expected from the discussion following equation (3.9), the boundary forcing generates a strong boundary mean flow going in a direction opposite to the direction of the bulk mean flow. Consistently with our previous estimates of typical timescales for the mean flow evolution, the establishment of the bulk flow occurs at a time scale larger than the establishment of the quasi-stationary boundary flow.

In the no-slip case, the mean flow eventually reaches a stationary state given by

$$\overline{u}_\infty\,(z) = Re \int_0^z \overline{u'w'}\,(z')\,\mathrm{d}z'. \tag{3.10}$$

Then, the contribution from the boundary streaming is negligible with respect to the contribution from the bulk streaming. This can be quantified by computing the order of magnitude of typical mean flow amplitudes U_w and U_{bl} obtained by splitting Reynolds stresses in (3.10) into a bulk and a boundary contribution, respectively. Using the large Reynolds asymptotic expressions obtained in (3.8) assuming $ReFr^2 \to +\infty$ and $Fr \to 0$, we get $U_w \sim (\epsilon ReFr)^2$ and $U_{bl} \sim \epsilon^2 Re^{1/2} Fr^{-1}$. Their ratio scale as $(ReFr^2)^{3/2}$, and thus tends diverges: the bulk flow is dominant in the longtime limit.

In the free-slip case, no stationary regime is reached and the mean flow amplitude keeps increasing in time. It can be assessed by considering the z-integrated momentum, $P\,(t) = \int_0^\infty \overline{u}\,(z,t)\,\mathrm{d}z$. Using the free-slip boundary condition and integrating (2.4), we get $P\,(t) = \left(\overline{u'w'}|_{z=0}\right) t$. At sufficiently large times, the mean flow varies over the characteristic length scale $\sqrt{t/Re}$. Consequently, the mean flow amplitude $P/\sqrt{t/Re}$ increases as $t^{1/2}$: eventually, the feedback of the mean flow on the wave will no longer be negligible. We can however use this mean flow amplitude estimate, together with the large Reynolds asymptotic expressions in (3.8), to infer $U_{bl}/U_w \sim 1/(FrRe^{1/2})$. This

scaling has been obtained under the assumption $Fr^2Re \to +\infty$. This means that the bulk flow is dominant in the long time limit, just as in the no-slip case. It is also possible to estimate the time scale τ for which the mean flow induced by the bulk streaming becomes of the same order as the mean flow induced by the boundary streaming. When this occurs, the long time limit is relevant for the estimate of the mean flow induced by boundary streaming, as above: $U_{bl} \sim F_{bl}(0)\sqrt{\tau/Re}$. By contrast, assuming $L_{Re} \gg \delta_{Re}$, the flow induced by the bulk streaming must be estimated using an early time limit: $U_w \sim \tau \partial_z F_w|_{z=0}$. Then, using $U_{bl} \sim U_w$ yields $\tau \sim Fr^4Re^2$. Using the parameters corresponding to figure 4 yields $\tau \sim 300$.

3.4. *Limitation of the quasi-linear model*

To derive the quasi-linear model around a state of rest presented above, the only necessary assumption is $\epsilon \to 0$, with all other parameters fixed. The quasi-linear numerical calculations have been made using the actual solution of the dispersion relation (3.1), but we obtained scalings by assuming simplified expressions for the wave field in the inviscid limit $Fr^2Re \to +\infty$, together with the hydrostatic limit $Fr \to 0$. These two conditions imply $\delta_{Re}/L_{Re} \sim \left(ReFr^2\right)^{-3/2} \to 0$, and therefore make possible a clear distinction between a bulk and a boundary contribution to streaming. To establish a self-consistent distinguished limit, we write

$$(\epsilon, Fr, Re) = (\epsilon, \epsilon^{\alpha}, \epsilon^{-\beta}). \tag{3.11}$$

The two simplifying assumptions above correspond to $\beta > 2\alpha$ and $\alpha > 0$. With these assumptions, the wave amplitudes scale as $(\phi_w, \phi_{bl}) \sim (\epsilon^{1-\alpha}, \epsilon^{1-2\alpha+\beta/2})$ in the free-slip case and $(\phi_w, \phi_{bl}) \sim (\epsilon^{1-\alpha}, \epsilon^{1-\alpha})$ in the no-slip case. We now list the conditions required for the validity of the linearisation procedure.

In the bulk, neglecting the nonlinear (advection) terms with respect to the viscous terms and the time derivative terms yields to the conditions $\beta < 1 + \alpha$ and $\alpha < 1$, respectively. Within the boundary layer, the full solution is composed of a bulk and a boundary term. Neglecting nonlinear terms involving both bulk and boundary components leads to an additional constraint $\beta < 2$. Neglecting nonlinear terms involving only boundary components leads to an additional constraint $\beta > 4\alpha - 2$ only in the free slip case. Neglecting nonlinear terms in the bottom boundary conditions (2.2) does not add any new constraint. There are therefore six inequalities to be satisfied for α and β in the free-slip case, five inequalities for the no-slip case. For the latter case, regimes of parameters for which these conditions are all fulfilled in presented in figure 5. The black area corresponds to regimes fulfilling all the constraints. The additional condition required for the free-slip case is also fulfilled within this black area.

In all the above analysis, we have neglected the feedback of the mean flow on the wave field. This is always valid at sufficiently short times. However, we saw that this can never be satisfied at large time in the free-slip case since the mean flow keeps increasing in time. In the no-slip case, we found that both the bulk and the boundary mean flow are indeed negligible with respect to the horizontal phase speed ($|\partial_t| \gg |\overline{u}\partial_x|$), as $U_w \sim (\epsilon ReFr)^2 \to 0$ and $U_{bl} \sim \epsilon^2 Re^{1/2} Fr^{-1} \to 0$ in the distinguished limit.

In the no-slip case, we expect a two-way coupling between waves and mean flow when the induced flows are of order one - with $\epsilon ReFr \sim 1$ for the bulk flow and $\epsilon Re^{1/4}Fr^{-1} \sim 1$ for the boundary-driven flow - since the terms involving the mean flow can no longer be ignored to compute the wave field in that case. These additional conditions are represented by the dashed red lines in figure 5. The red dot corresponds to the regime $(\alpha, \beta) = (1, 2)$ satisfying marginally the distinguished limit while allowing for order one

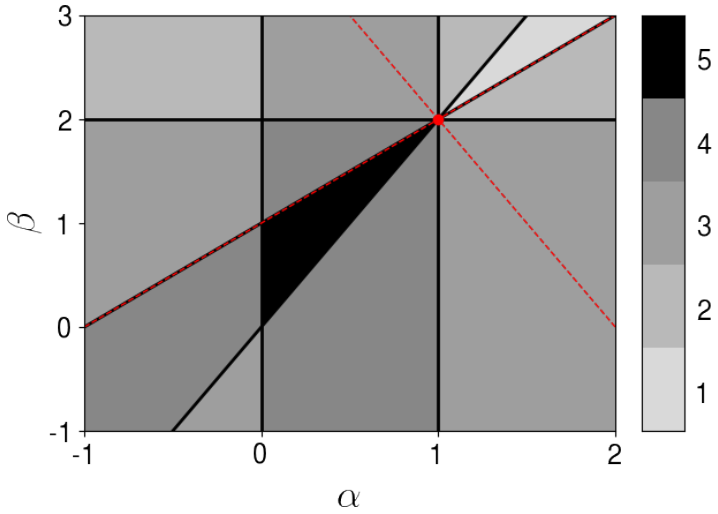

Figure 5: Distinguished limit for the validity of the linear dynamics around a state of rest in the no-slip case: $(Fr, Re) = (\epsilon^{\alpha}, \epsilon^{-\beta})$. Each line delimitates a half plane where one of the constraints is satisfied. The colourmap shows the number of constraints that are satisfied. The black region corresponds to the range of exponents (α, β) for which the asymptotic approach is self-consistent: all the constraints are satisfied for those scalings. In the free-slip case, there is an additional constraint $\beta < 4\alpha - 2$ which is not represented here, but that is fulfilled within the black area. The dashed red lines correspond to limit cases above which the mean flows induced by the bulk streaming and boundary streaming impact the wave field. The red dot corresponds to the regime $(\alpha, \beta) = (1, 2)$ where the distinguished limit is marginally satisfied, and where two-way coupling between waves and mean flow can no longer be neglected.

mean flows induced by both the bulk and the boundary forcing. Within this regime the viscous terms are of the order of nonlinear terms in the bulk wave equation, thus invalidating the quasi-linear approach. This limitation can be bypassed by introducing additional dissipative terms, such as a linear friction term in the zonal flow equation or the buoyancy equation. Such terms would allow us to control the typical vertical length scale for wave attenuation, related to the intensity of the bulk internal wave streaming, without varying the Reynolds number that constrains the mean flow vertical gradients. To avoid the introduction of such additional parameters, we choose in the following to consider the quasi-linear equations as an *ad hoc* model for wave-mean flow interactions. This simplified model will illustrate how boundary streaming can affect mean flow properties in the bulk when the feedback of the mean flow on the wave field is taken into account.

4. Application to an idealised analogue of the quasi-biennial oscillation

We consider a standing wave pattern imposed at the bottom boundary: $h(x,t) = \cos(x)\cos(t)$ with a no-slip boundary condition. This idealised configuration is thought to capture the essential mechanism at the origin of the equatorial stratospheric quasi-biennial oscillation (Plumb 1977), and has been experimentally studied by Plumb & McEwan (1978). Two linear waves with equal amplitude and opposite zonal phase speeds are emitted by such a bottom excitation. The resulting Reynolds stress is simply the sum of the Reynolds stresses computed from each individual wave plus a rapidly oscillating term that can be smoothed out by averaging over this fast oscillation. The Reynolds

stress divergences induced by the two waves are opposite and annihilate each other in the absence of mean flow. Above a certain value of the amplitude of the waves, a Hopf bifurcation occurs: a vacillating mean flow is generated and approaches a limit cycle (Plumb 1977). Plumb & McEwan (1978) reported the spontaneous generation of an oscillating mean flow in laboratory experiments when the wave amplitude exceeds a threshold, and compared their measurements against quasi-linear computations. They considered a no-slip bottom boundary condition for the mean flow but inviscid impermeability condition for the wave field, allowing them to ignore any boundary layer effect. Here, we investigate the effect of the viscous boundary layers and the associated boundary streaming on the oscillation arising with the standing wave excitation, assuming a no-slip condition for both the mean flow and the waves. We show that the inclusion of boundary streaming induces important alterations on the mean flow in this idealised model of wave-mean flow interactions.

In section 3, we ignored the effect of the mean flow on the wave field. We need here to take this feedback into account, as the initial instability arises from a perturbation of the mean flow itself. The effect of the mean flow on the wave is included by performing a WKB expansion of the wave field following the method of Muraschko *et al.* (2015), but including dissipative effects. The full calculation is detailed in appendix A. The Reynolds stress divergence is then computed and inserted into the mean flow equation (2.4) in order to compute the long-time evolution of $\overline{u}$. This task is done numerically using the results of appendix A and for the no-slip boundary condition in (3.6). While Plumb & McEwan (1978) considered asymptotic expression for the bulk solution of the dispersion relation (A 5), our numerical calculations use the actual solutions. As discussed at the end of Appendix A, this solution captures important corrections close to the critical layers, where the mean flow is of the order of the wave zonal phase speed.

The resulting Hovmöller diagrams of mean flows time series are showed on figure 6 for different values of the Reynolds number. The time series used for the upper plots have been computed using the full quasi-linear model while the one used for the bottom plots have been computed without the boundary layer contributions. All simulations start with the same initial perturbation. In figure 6a, we see that the inclusion of boundary streaming has altered the critical parameter values at which the bifurcation to mean-flow reversals occurs. In figure 6b, the Reynolds number is increased and the oscillation is present in both cases. However, the oscillation period is decreased by 20% when the boundary streaming is included. By further increasing the Reynolds number we see in figure 6c that the inclusion of the boundary streaming significantly changes the mean flow oscillation. This new regime exhibiting an additional frequency in the signal can actually be reached without the boundary streaming but at a larger Reynolds number. A similar regime has been reported by Kim & MacGregor (2001), and we will more thoroughly study these bifurcations in a companion paper. Our aim is here to show that the presence of the wave boundary layer has an impact on such bifurcation diagrams, in addition to significantly altering the period of oscillations in the periodic case.

For the range of parameters corresponding to figures 6b and 6c, the mean flow reaches an amplitude close to the phase speed of the waves. To investigate the effect of the boundary layers in these cases, we consider two mean flow snapshots, plotted in figure 7, taken from the two time-series plotted in figure 6b. The snapshots are taken at the same stage of the oscillation cycle.

The Reynold stress divergences computed using the two mean flow snapshots shown in figure 7-a and considering the counter-propagating waves separately are plotted in figure 7-b. The total Reynolds stress divergences are plotted in figure 7-c. As expected, the boundary layers significantly modify the streaming vertical profiles. Interestingly, while

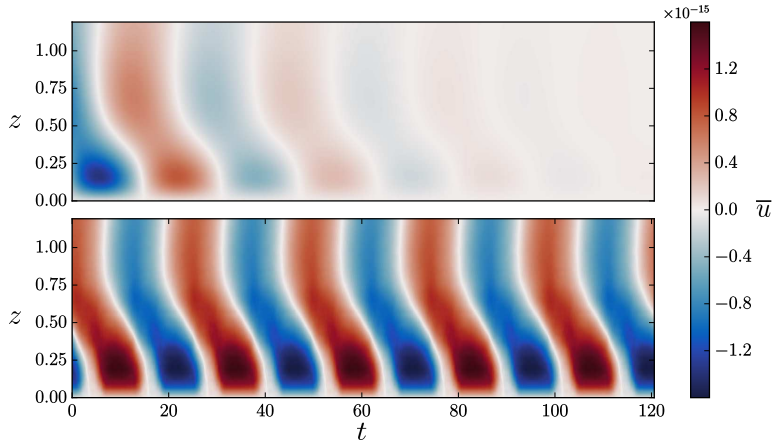

(a) $Re = 67$, $L_{Re} = 0.44$ and $\delta_{Re} = 0.13$

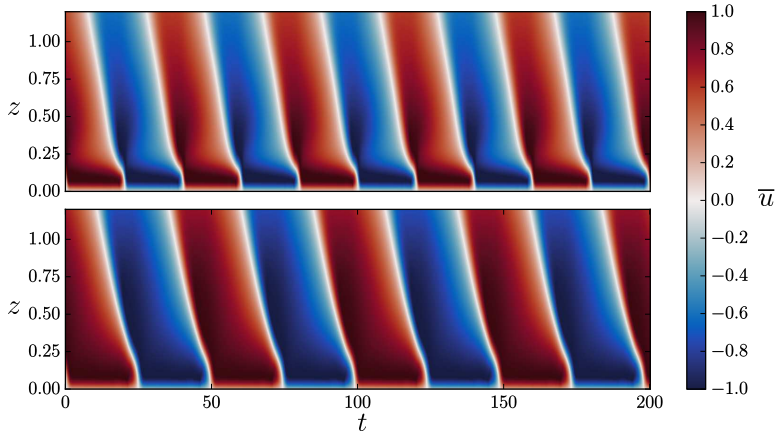

(b) $Re = 154$, $L_{Re} = 0.65$ and $\delta_{Re} = 0.10$

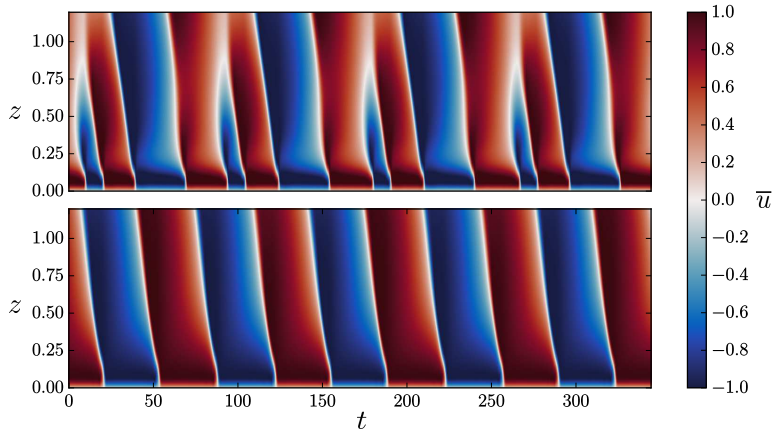

(c) $Re = 200$, $L_{Re} = 0.78$ and $\delta_{Re} = 0.089$

Figure 6: The mean flow, $\overline{u}\,(z,t)$, is generated by the streaming coming from two counter propagative waves with the same amplitude and opposite horizontal phase speed, generated by a vertically oscillating bottom boundary with no-slip condition using the quasi-linear model. Hovmöller diagrams of the mean flow time series are shown for three different Reynolds numbers. In each panel (a,b,c) the upper plot corresponds to a case where the boundary streaming has been included in the computation while the lower plot corresponds to a computation with same parameters but without the contribution of the boundary streaming terms. In all cases, $Fr = 0.15$ and $\epsilon = 0.3$. In figure b), the mean flow oscillates with an oscillation period of about 40 and 50 time units for the case with (upper plot) and without (lower plot) boundary streaming respectively.

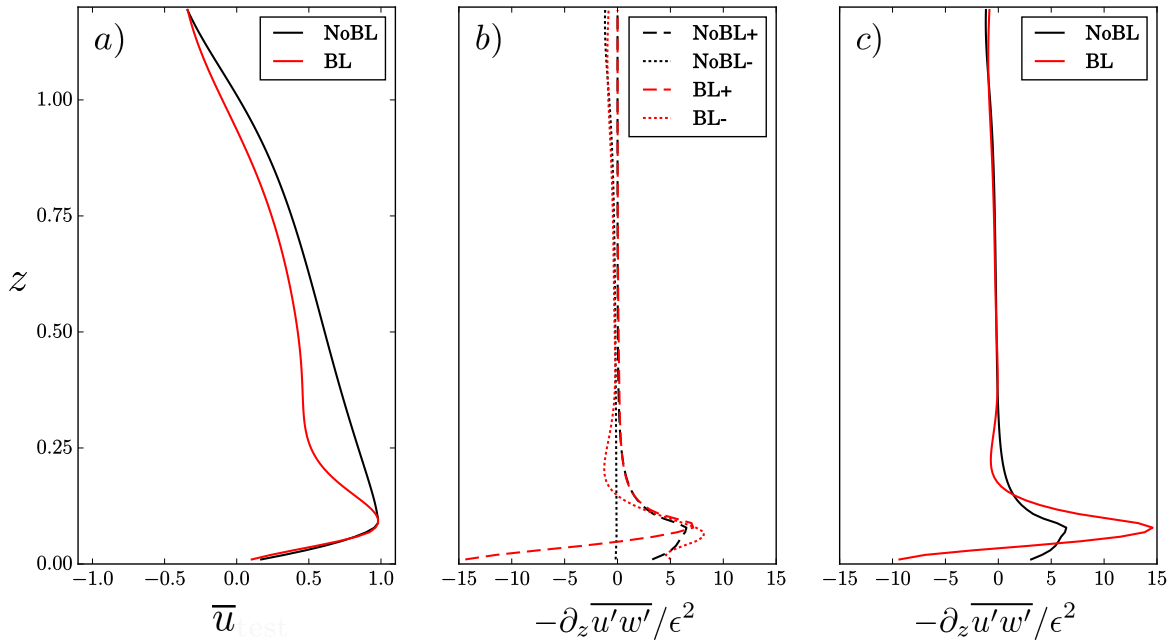

Figure 7: *a*) Mean flow snapshots extracted from the two time series plotted in figure 6b computed with (BL) and without (NoBL) boundary streaming and taken at $t = 10$ and $t = 12.5$ respectively. *b*) Plot of the associated Reynolds stress divergences obtained for the wave propagating in the direction of positive mean flow ("+") and for the counter-propagating one ("-") considering the mean flow profile obtained by either including (BL) or ignoring (NoBL) the boundary streaming. *c*) Plot of the total Reynold stress divergences, the sum of the two counter propagative waves contributions for the case with boundary streaming (BL) and without boundary streaming (NoBL).

bulk streaming is dominated by the wave travelling in the same direction as the mean flow, the main discrepancy between the case with and without boundary streaming comes from the boundary forcing associated with the wave going in a direction opposite to the mean flow near the bottom boundary.

In figure 6b, we see that the bottom profile of the mean flow is approximately steady before a reversal. Let us call λ_{Re} the typical length over which the mean flow reaches its extremum value This velocity is of order one as it is close to the gravity wave zonal phase speed. Using equation (2.4), we infer the typical scaling of λ_{Re} by balancing the viscous term $Re^{-1}\partial_{zz}\overline{u}$ and the streaming term $\partial_z\overline{u'w'}$. This last term is dominated by the bulk contribution F_w associated with the wave that propagates in the same direction as the mean flow. This yields $\lambda_{Re} \sim (Re\, F_w(0))^{-1}$. The order of magnitude of $F_w(0)$ can be obtained by using the asymptotic expression in equation (3.8), under the assumption $Fr \to 0$ and $Re^2 Fr \to \infty$. This yields $\lambda_{Re} \sim Fr/(\epsilon^2 Re)$. Using parameters of figure 7, we find $\lambda_{Re} \sim 0.1$.

The presence of the mean flow thus leads to a new "bulk scale" λ_{Re} that differs from the bulk dissipative scale L_{Re} for the flow at rest; in particular, in our distinguished limit (i.e. an inviscid limit), the former tends to zero, while the latter tends to infinity. In the bulk, the wave propagating in the same direction as the mean flow is controlled by λ_{Re}; the wave propagating in the other direction is controlled by L_{Re}. The typical scale of bulk flow reversals is thus given by λ_{Re}. We expect boundary streaming to have a significant impact on these reversals when they occur within the boundary layer, i.e. when $\lambda_{Re} \sim \delta_{Re}$ or $\lambda_{Re} \ll \delta_{Re}$. This is indeed the case in figure 6c, where $\delta_{Re} \approx 0.1$.

It is instructive to establish the range of parameter for which this condition is satisfied. Using $\delta_{Re} \sim 1/Re^{1/2}$, we find that this length scale is larger or of the order of λ_{Re} when $Fr/(\epsilon^2 Re^{1/2}) \to 0$. The above analysis suggests the possibility for active control of the boundary layer on the bulk flow when $(Fr, Re) = (\epsilon^{\alpha}, \epsilon^{-\beta})$ with $\beta \geqslant 4 - 2\alpha$, $\alpha > 0$ and $\beta > 2\alpha$.

As seen on figure 5, the distinguished limits consistent with an active control of the boundary layer on bulk flow reversal in the *ad hoc* quasi-linear model do not overlap with the distinguished limits ensuring the validity of the quasi-linear dynamics around a state of rest. In fact, both sets of constraints can only be marginally satisfied at the point $(\alpha, \beta) = (1, 2)$. This is the main caveat of the analysis presented in this section and illustrated in figure 7: because $\epsilon ReFr \sim 1$, the nonlinear terms involving bulk waves are not negligible with respect to the bulk viscous term. Furthermore, since $\epsilon Re^{1/2} \sim 1$, the boundary layer can hardly be considered as linear. Whether active control of the boundary on the bulk flow persists when nonlinear effects are reincorporated into the problem needs to be addressed in a future work.

Another caveat of the quasi-linear model presented here comes from the assumptions underlying the WKB approach used to compute the wave-field. We assumed that there is a vertical scale separation between the wave and the mean flow and that the wave field reaches its steady state in a time much shorter than the typical time of evolution of the mean flow. The wave field is thus computed using a static WKB approximation with a frozen in time mean flow. Since the mean flows shown in figure 6 exhibit sharp shear at the bottom, and since they reach values of the order of the zonal phase speed of the waves, those hypotheses are not valid. Nevertheless, this WKB approximation is the simplest way of accounting for the mean flow effect on the wave field, and a useful first step to understand their interactions.

We should finally stress that the no-slip bottom boundary condition is most certainly irrelevant to the actual quasi-biennial oscillation occurring in the upper atmosphere and that our model has been derived in a distinguished limit for which the viscous boundary layer is much larger than the boundary height variations, which is not satisfied in laboratory experiments. However, despite these limitations, our results show that the boundary conditions and the associated wave boundary layers should not be overlooked, since boundary streaming may have a quantitative impact on mean flow reversals in the domain bulk.

5. Conclusion

We have shown that changing the boundary conditions has a significant impact on the boundary mean flow generated by internal waves emitted from an undulating wall in a viscous stratified fluid. We first compared the effect of no-slip and free-slip boundary conditions by considering a distinguished limit that makes possible a clear separation between the bulk and a viscous boundary layer. In the no-slip scenario, the Reynolds stress divergence scales at early time in direct proportion to $\epsilon^2\sqrt{Re}/Fr$, where ϵ is the dimensionless wave amplitude, Re is the wave Reynolds number, and Fr the wave Froude number. However, bulk streaming dominates over boundary streaming in the large time limit, and the system reaches a stationary state with a mean flow that remains negligible with respect to the wave-field. In the free-slip scenario, boundary forcing amplitude does not depend on the Reynolds number, only its e-folding depth does. The presence of the boundary layer qualitatively alters the early time flow evolution. Just as in the no-slip case, bulk streaming has a dominant contribution at large-time. However, contrary to the no-slip case, the system does not reach a stationary state. In both cases, the distinguished

limit considered to derive these results prevent a two-way coupling between waves and mean flows.

To address the interplay between boundary streaming, waves and mean-flows, we treated the case of a forced standing wave with an ad hoc truncation of the dynamics based on a quasi-linear approach. This model captures the basic mechanism responsible for the quasi-biennial oscillation (Plumb 1977). Using a novel WKB treatment of the waves that takes into account viscous effects, we investigated the effect of boundary streaming on mean flow reversals in this model. We found that boundary streaming significantly alters the mean flow reversals by either inhibiting them, decreasing their period or altering their periodicity depending on the wave amplitude. Further work will be needed to determine whether this active control of bulk properties by boundary streaming is robust to the presence of wave-wave interactions.

Beyond these particular examples, our results show the importance of describing properly the physical processes taking place in the boundary layers where waves are emitted to model correctly the large-scale flows induced by these waves. We have neglected the effects of rotation and diffusion of buoyancy which are known to change the properties of the wave fields close to boundaries (Grisouard & Thomas 2015, 2016), and will, therefore, affect boundary streaming. By restricting ourselves to a quasi-linear approach, we have also neglected nonlinear effects that may become important close to the boundary, even in the limit of weak undulations, due to the emergence of strong boundary currents. All these effects could deserve special attention in future numerical and laboratory experiments.

The authors warmly thank Louis-Philippe Nadeau for his help with the MIT-GCM, and express their gratitude to Freddy Bouchet and Thierry Dauxois for their useful insights. This paper also benefited greatly from the significant involvement of an anonymous reviewer.

Appendix A. WKB expansion of viscous internal gravity wave within a frozen in time mean flow

We compute here the leading order terms of a Wentzel-Kramers-Brillouin (WKB) expansion of the viscous wave field within a weakly sheared mean flow frozen in time. We follow the method developed in Muraschko *et al.* (2015), the novelty being the presence of viscosity, in the wave equation (2.5). The internal wave equations write

$$\begin{cases} \partial_t u' + \overline{u}\partial_x u' + w'\partial_z \overline{u} + \partial_x p' - Re^{-1}\nabla^2 u' &= 0 \\ \partial_t w' + \overline{u}\partial_x w' + \partial_z p' - Fr^{-2} b' - Re^{-1}\nabla^2 w' &= 0 \\ \partial_t b' + \overline{u}\partial_x b' + w' &= 0 \\ \partial_x u' + \partial_z w' &= 0 \end{cases} . \tag{A 1}$$

We assume that the mean flow is time independent and varies over a vertical scale L_u much larger than the inverse of the vertical wave number modulus $1/|m|$. None of those quantities is known prior to our problem. For the present calculation, we assume $L_u \gg 1$ and $|m| \sim 1$ but the final result will apply for different scalings as long as $L_u m \gg 1$ is fulfilled. We therefore assume that $\overline{u}$ depends on a smooth variable $Z = az$ with $a = 1/L_u \ll 1$.

We introduce the WKB ansatz for a monochromatic wave solution

$$\begin{bmatrix} u' \\ w' \\ b' \\ p' \end{bmatrix} = \Re\left\{ \sum_{j=0}^{+\infty} a^j \begin{bmatrix} \tilde{u}_j(Z) \\ \tilde{w}_j(Z) \\ \tilde{b}_j(Z) \\ \tilde{p}_j(Z) \end{bmatrix} e^{i(x-ct) + \frac{i\Phi(Z)}{a}} \right\}, \tag{A 2}$$

with $c = \pm 1$. The function $\Phi(Z)$ accounts for the vertical phase progression of the wave. The local vertical wave number is defined by $m(Z) = \partial_Z \Phi$. Inserting this expansion into the previous equation and collecting the leading order terms in a leads to:

$$\boldsymbol{M} \begin{bmatrix} \tilde{u}_0 \\ \tilde{w}_0 \\ \tilde{b}_0 \\ \tilde{p}_0 \end{bmatrix} + a \left(\boldsymbol{M} \begin{bmatrix} \tilde{u}_1 \\ \tilde{w}_1 \\ \tilde{b}_1 \\ \tilde{p}_1 \end{bmatrix} + \begin{bmatrix} \tilde{w}_0 \partial_Z \overline{u} - iRe^{-1}\left(\tilde{u}_0 \partial_Z m + 2m\partial_Z \tilde{u}_0\right) \\ \partial_Z \tilde{p}_0 - iRe^{-1}\left(\tilde{w}_0 \partial_Z m + 2m\partial_Z \tilde{w}_0\right) \\ 0 \\ \partial_Z \tilde{w}_0 \end{bmatrix} \right) + o(a) = 0, \tag{A 3}$$

with

$$\boldsymbol{M} = \begin{bmatrix} Re^{-1}\left(1+m^2\right) - i(c-\overline{u}) & 0 & 0 & i \\ 0 & Re^{-1}\left(1+m^2\right) - i(c-\overline{u}) & -1 & im \\ 0 & Fr^{-2} & -i(c-\overline{u}) & 0 \\ i & im & 0 & 0 \end{bmatrix}. \tag{A 4}$$

We introduce the polarisation $\mathbf{P}[m]$ defined by $\left[\tilde{u}_0, \tilde{w}_0, \tilde{b}_0, \tilde{p}_0\right] = \phi_0(Z)\,\mathbf{P}[m]$, where $\phi_0(Z)$ is the amplitude of the wave mode. The cancellation of the zeroth order term in equation (A 2) yields to $\det \boldsymbol{M} = 0$. This gives the local dispersion relation

$$Fr^2 (c-\overline{u})^2 \left(1+m^2\right)\left(1 + iRe^{-1}\frac{1+m^2}{c-\overline{u}}\right) = 1\ . \tag{A 5}$$

Then, using $\boldsymbol{M}\mathbf{P} = 0$ we obtain the polarisation expression

$$\mathbf{P}[m] = \left[c-\overline{u}, -\frac{1}{m}(c-\overline{u}), \frac{i}{Fr^2 m}, \frac{1}{Fr^2\left(1+m^2\right)}\right]. \tag{A 6}$$

The cancellation of the terms proportional to a in (A 3) provides an equation for the amplitude $\phi_0(Z)$. To get rid of the terms involving components of the order one wave, let us introduce the vector $\mathbf{Q} = \left[\tilde{u}_0, \tilde{w}_0, -\tilde{b}_0 Fr, \tilde{p}_0\right]$ such that $\mathbf{Q}^{\perp}\boldsymbol{M} = \mathbf{0}$. We then take the inner product between $\mathbf{Q}$ and the terms proportional to a in (A 3). This gives

$$\tilde{u}_0\tilde{w}_0\partial_Z\overline{u} + \partial_Z\left(\tilde{w}_0\tilde{p}_0\right) = iRe^{-1}\partial_Z\left(m\left(\tilde{u}_0^2 + \tilde{w}_0^2\right)\right). \tag{A 7}$$

By introducing $\varphi_0^2 = \phi_0^2 (c-\overline{u})^2 / m$ and using the dispersion relation (A 5), we obtain after some algebra:

$$\partial_Z \log\varphi_0^2 + \frac{2iRe^{-1}\left(1+m^2\right)}{c-\overline{u}+2iRe^{-1}\left(1+m^2\right)}\partial_Z \log\left(1+m^2\right) = 0. \tag{A 8}$$

This last equation has to be solved for every solution $m(Z)$ of the dispersion relation. This is done numerically in general.

By solving the dispersion relation (A 5), we find that in the limit of large Reynolds number the bulk solution is independent of Re and we recover the amplitude equation obtained by Muraschko *et al.* (2015)

$$\partial_Z \varphi_0 = 0. \tag{A 9}$$

However, for the boundary layer solution we find the scaling $m_{bl}^2 \sim = iRe\,(c-\overline{u})$ at leading order in the large Reynolds limit. In this case, the amplitude equation for the boundary layer solution reduces to

$$\partial_Z \left(\varphi_0^2 \,(c-\overline{u})^2 \right) = 0. \tag{A 10}$$

These results fail close to critical layers where $|c-\overline{u}| \ll 1$.

Let us consider the momentum flux computed from the self-interaction of the upwardly propagating bulk solution of (A 5), i.e. the one converging toward the inviscid solution when we take the limit $Re \to \infty$. If we assume $Fr\,|c-\overline{u}| \ll 1$ and $Re\,|c-\overline{u}| \sim (Fr\,|c-\overline{u}|)^{-3}$ for every z, we recover the expression of equation (2.1) of Plumb & McEwan (1978) with $a_1 = 0$:

$$\overline{u'w'}\,(z) = \mathrm{sign}\,(c)\,|\varphi_0\,(z=0)|^2 \exp\left\{ -\frac{1}{Fr^3 Re} \int_0^z \frac{\mathrm{d}z'}{\left(c-\overline{u}\,(z')\right)^4} \right\}. \tag{A 11}$$

This expression fails close to critical layers where the scaling assumption $Re\,|c-\overline{u}| \sim (Fr\,|c-\overline{u}|)^{-3}$ can not remain valid.

REFERENCES

Adcroft, A., Campin, J.M., Doddridge, E., Dutkiewicz, S., Evangelinos, C., Ferreira, D., Follows, M., Forget, G., Fox-Kemper, B., Heimbach, P., Hill, C., Hill, E., Hill, H., Jahn, O., Klymak, J., Losch, M., Marshall, J., Maze, G., Mazloff, M., Menemenlis, D., Molod, A. & Scott, J. 2018 *MITgcm-s user manual*. Https://mitgcm.readthedocs.io/en/latest/.

Adcroft, A., Hill, C. & Marshall, J. 1997 Representation of topography by shaved cells in a height coordinate ocean model. *Monthly Weather Review* **125** (9), 2293–2315.

Baldwin, M.P., Gray, L.J., Dunkerton, T.J., Hamilton, K., Haynes, P.H., Randel, W.J., Holton, J.R., Alexander, M.J., Hirota, I., Horinouchi, T., Jones, D.B.A, Kinnersley, J.S., Marquardt, C., Sato, K. & Takahashi, M. 2001 The quasi-biennial oscillation. *Reviews of Geophysics* **39** (2), 179–229.

Beckebanze, F. & Maas, L. 2016 Damping of 3d internal wave attractors by lateral walls. *Proceedings, International Symposium on Stratified Flows* .

Bordes, G., Venaille, A., Joubaud, S., Odier, P. & Dauxois, T. 2012 Experimental observation of a strong mean flow induced by internal gravity waves. *Physics of Fluids* **24** (8), 086602.

Bühler, O. 2014 *Waves and mean flows*. Cambridge University Press.

Chini, G.P. & Leibovich, S. 2003 An analysis of the klemp and durran radiation boundary condition as applied to dissipative internal waves. *Journal of Physical Oceanography* **33** (11), 2394–2407.

Eckart, Carl 1948 Vortices and streams caused by sound waves. *Physical review* **73** (1), 68.

Fan, B., Kataoka, T. & Akylas, T.R. 2018 On the interaction of an internal wavepacket with its induced mean flow and the role of streaming. *Journal of Fluid Mechanics* **838**.

Gostiaux, L., Didelle, H., Mercier, S. & Dauxois, T. 2006 A novel internal waves generator. *Experiments in Fluids* **42**, 123–130.

Grisouard, N. & Bühler, O. 2012 Forcing of oceanic mean flows by dissipating internal tides. *Journal of Fluid Mechanics* **708**, 250–278.

Grisouard, N. & Thomas, L. N. 2015 Critical and near-critical reflections of near-inertial waves off the sea surface at ocean-fronts. *Journal of Fluid Mechanics* **765**, 273–302.

Grisouard, N. & Thomas, L. N. 2016 Energy exchanges between density fronts and near-inertial waves reflecting off the ocean surface. *Journal of Physical Oceanography* **46** (2), 501–516.

Kataoka, T. & Akylas, T.R 2015 On three-dimensional internal gravity wave beams and induced large-scale mean flows. *Journal of Fluid Mechanics* **769**, 621–634.

Kim, E. & MacGregor, K. B. 2001 Gravity wave-driven flows in the solar tachocline. *The Astrophysical Journal Letters* **556** (2), L117.

Legg, S. 2014 Scattering of low-mode internal waves at finite isolated topography. *Journal of Physical Oceanography* **44** (1), 359–383.

Lighthill, J. 1978 Acoustic streaming. *Journal of Sound and Vibration* **61** (3), 391 – 418.

Maas, L., Benielli, D., Sommeria, J. & Lam, F. A. 1997 Observation of an internal wave attractor in a confined, stably stratified fluid. *Nature* **388** (6642), 557–561.

Muraschko, J., Fruman, M. D., Achatz, U., Hickel, S. & Toledo, Y. 2015 On the application of Wentzel-Kramer-Brillouin theory for the simulation of the weakly nonlinear dynamics of gravity waves. *Quarterly Journal of the Royal Meteorological Society* **141** (688), 676–697.

Nikurashin, M. & Ferrari, R. 2010 Radiation and dissipation of internal waves generated by geostrophic motions impinging on small-scale topography: Application to the southern ocean. *Journal of Physical Oceanography* **40** (9), 2025–2042.

Nyborg, W.L. 1958 Acoustic streaming near a boundary. *The Journal of the Acoustical Society of America* **30** (4), 329–339.

Passaggia, P.-Y., Meunier, P. & Le Dizès, S. 2014 Response of a stratified boundary layer on a tilted wall to surface undulations. *Journal of Fluid Mechanics* **751**, 663–684.

Plumb, R. A. 1977 The interaction of two internal waves with the mean flow: Implications for the theory of the quasi-biennial oscillation. *Journal of the Atmospheric Sciences* **34** (12), 1847–1858.

Plumb, R. A. & McEwan, A. D. 1978 The instability of a forced standing wave in a viscous stratified fluid: A laboratory analogue of .the quasi-biennial oscillation. *Journal of the Atmospheric Sciences* **35** (10), 1827–1839.

Rayleigh, Lord 1884 On the circulation of air observed in kundt's tubes, and on some allied acoustical problems. *Philosophical Transactions of the Royal Society of London* **175**, 1–21.

Riley, N. 2001 Steady streaming. *Annual Review of Fluid Mechanics* **33** (1), 43–65.

Semin, B., Facchini, G., Pétrélis, F. & Fauve, S. 2016 Generation of a mean flow by an internal wave. *Physics of Fluids* **28** (9), 096601.

Shakespeare, C. J. & Hogg, A. McC. 2017 The viscous lee wave problem and its implications for ocean modelling. *Ocean Modelling* **113**, 22 – 29.

Sutherland, B. R. 2010 *Internal gravity waves*. Cambridge University Press.

Voisin, B. 2003 Limit states of internal wave beams. *Journal of Fluid Mechanics* **496**, 243–293.

Wedi, N. P & Smolarkiewicz, P. K. 2006 Direct numerical simulation of the Plumb–McEwan laboratory analog of the QBO. *Journal of the atmospheric sciences* **63** (12), 3226–3252.

Xie, J. & Vanneste, J. 2014 Boundary streaming with Navier boundary condition. *Physical Review E* **89** (6).

6. Statistical wave-mean flow equilibrium

In this chapter, we present research initiated before the PhD and completed during the first doctoral year. Although the adopted modelisation techniques are very different from the quasilinear approximations and asymptotic expansions employed so far, this investigation remains closely related to the general issue of wave-mean flow interaction in stratified fluids.

6.1 Foreword

6.1.1 Problematic

Up to now, this thesis addressed wave and mean flow interactions through the phenomenon of wave streaming which requires dissipative processes and is well-captured by the quasi-linear dynamics. In this chapter, **we investigate the inviscid problem where the wave-mean flow coupling is supported by the full nonlinear dynamics**. Let us denote this phenomenon by **inviscid streaming**. We had a first glimpse into this phenomenon when we studied critical layers in Chapter 3 (see subsection 3.3.4 in particular). The fully nonlinear processes underlying inviscid streaming cannot be addressed simply with expansions higher-order than the quasilinear approximation. Leaving aside the details of the wave-mean flow interaction dynamics, we consider here the simpler problem of **the equilibrium outcome of the free evolution of a given initial state - say a pure gravity wave field - and investigate the spontaneous emergence of a large-scale mean flow. We also ask about the possibility of the reverse scenario, namely the spontaneous radiation of waves from a large scale vortical flow.**

Posing the problem in such a way conveniently favours the deployment of the powerful machinery of **equilibrium statistical mechanics**. The statistical mechanical approach allows predicting equilibrium macroscopic quantities such as large-scale flow patterns or local flow statistics, without describing the detail of the microscopic dynamics, namely the nonlinear processes engendering inviscid streaming. It relies on the strong but single assumption that the flow evenly explores phase space at equilibrium, thanks to the high nonlinearities that couples a huge number of degrees of freedom. Then, equilibrium macroscopic quantities are predicted as the most probable outcome of this nonlinear stirring. In the context of geophysical fluid dynamics, equilibrium statistical mechanics has been applied first to 2D-Euler and quasi-geostrophic flows in the 90ties by Robert, Sommeria

and Miller [133, 109] with remarkable applications to Jovian flows [108, 17] and the vertical energy transfers in the ocean [163], among others. The program followed by Robert, Sommeria and Miller is reviewed by Bouchet and Venaille [18].

The statistical mechanics of 2D-Euler and quasi-geostrophic flows predicts a concentration of the initial energy at large scales at equilibrium, concomitant with the spontaneous emergence of large-scale flow structures. This prediction is associated with the so-called inverse cascade of energy observed in forced-dissipated 2D turbulence [138]. By contrast, three-dimensional flows are characterised by a small-scale energy transfer associated with the classical picture of a direct cascade of energy.

Geophysical flows are intermediate cases between 2D and 3D. On the one hand, the bi-dimensional flattening of the flow is strongly favoured by the small vertical-over-horizontal aspect ratio and the planetary rotation. On the other hand, the stratification of geophysical fluids supports the existence of gravity waves which are associated with motions in the third vertical dimension. The 2D-Euler and quasi-geostrophic models do not support the propagation of gravity waves. **It is natural to ask whether gravity waves trigger a small-scale energy transfer or, conversely, feed the emergence of large-scale flows by inviscid streaming.**

To address this question, we extend the application of statistical mechanics to one of the simplest models accounting for gravity waves: **the shallow-water model**. This model is an intermediate model between 3D and 2D flows describing the dynamics of a thin layer of fluid with homogeneous density and free-surface. The associated velocity field is two-dimensional but the third vertical dimension is represented by a dynamical height field supporting the propagation of gravity waves. These shallow-water gravity waves contrast with the internal gravity waves studied in previous chapters as they propagate at the upper surface rather than within a stratified bulk. Nevertheless, we expect a comparable phenomenology for both internal and surface gravity waves regarding inviscid streaming.

Here, we thus compute the statistical equilibrium of the inviscid shallow-water system. **This work and the associated results are presented hereinbelow in the form of a scientific article published in *Journal of Statistical Physics***. We first provide a brief summary of the main results and discuss them in relation to previous works.

6.1.2 Results summary

In order to compute the equilibrium states of the shallow-water model, we build upon Robert-Miller-Sommeria theory [18]. We first introduce a finite dimensional model of the continuous shallow-water fields and define the large-scale mean flow through a coarse-graining procedure, equivalent to a local spatial average. Then, using large-deviation tools, we compute the statistical equilibrium of the shallow-water system in the microcanonical ensemble. This leads to several important results.

We show that equilibrium states of the shallow-water system are associated with the coexistence of a large-scale mean flow which is a stationary state of the shallow-water dynamics, superimposed with gravity waves that may contain, in some cases, a substantial part of the initial energy. The case with both bottom topography and system rotation is particularly interesting. In this case, we show that a large-scale mean flow can emerge at equilibrium starting from an initial state with only waves. This highlights an inviscid

streaming contrasting with the streaming spawned by dissipation, studied in the previous chapters. We also provide an explicit computation of the equilibrium energy partition between the large-scale flow and the gravity wave motions.

Concomitantly, we also predict that, in the absence of bottom topography and lateral boundaries, initial large-scale vortical flows ultimately radiate all their energy into gravity waves. We also find that the presence of gravity waves implies a positive temperature for the equilibrium state which contrasts with the existence of negative temperature states for the previously studied 2D Euler or quasi-geostrophic models. In a weak energy limit, we obtain an interesting physical picture of the shallow-water equilibria, which may be interpreted in that limit as two subsystems in thermal contact: A first subsystem is the large-scale mean flow and the second one corresponds to gravity waves. Taking the quasi-geostrophic limit for the large-scale flow, we recover previously computed equilibrium states of the quasi-geostrophic system. In our case, however, the thermal contact with the gravity waves subsystem selects a subclass of the equilibria with positive temperature.

6.1.3 Previous works

There are few previous results on statistical equilibrium states of the shallow-water system. Warn studied the equilibrium states in a weak energy limit [167]. He showed that in the absence of lateral boundaries and in the absence of bottom topography, all the initial energy of a shallow-water flow is transferred towards small scales. Here we relax the hypothesis of a weak energy, generalise his conclusions and discuss the effect of bottom topography. In particular, we show that when there is a non zero bottom topography and when the flow is rotating, there is a large-scale flow at equilibrium. Chavanis & Sommeria [25] assumed that all the energy remain in the large-scale flow and proceeded through analogy to extend the 2D-Euler and quasi-geostrophic statistical equilibrium states to the shallow-water model. Here, with an approach based on statistical mechanics arguments, we confirm their results regarding the large-scale flow. However, we stress that a reduced large-scale energy needs to be considered as part of the initial energy is carried by the gravity waves at equilibrium.

We have also been inspired by the work of Weichman and Petrich [170]. In their work, the authors computed statistical equilibrium states of the shallow water system in the grand canonical ensemble. They recovered results from Chavanis and Sommeria [25] based on a statistical mechanics treatment. However, they also assumed that the equilibrium energy is concentrated at large-scale. Another caveat from their work is that starting from grand canonical distribution is questionable for flow systems which are associated with long-range interactions. Here, we solve the microcanonical problem.

6.1.4 Limitations and perspectives

The prediction of a vanishing large-scale flow in the absence of lateral boundaries and bottom topography seems to contradict some numerical results performed in such configurations, in which case long-lived vortex were reported [46]. In practice, the predicted equilibrium states may require a very large time to be reached in direct numerical simulations due to a very weak coupling between wave and mean motions. This highlight an important caveat of equilibrium statistical mechanics which fails to tell anything about the relaxation dynamics. A possible approach to overcome this issue could be to assume a time-scale separation between the large-scale mean flow and the waves and treat the wave motions with the tools of statistical mechanics keeping the dynamics of the large-scale

vortical flow. This idea, related to the geostrophic adjustment problem [160], could be explored in future work.

After publication of our work, Weichman proposed a competing theory [169]. Revisiting our approach, he built a different discretised model. While our model is consistent with the volume conservation of fluid particles, Weichman preferred to relax this constraint to have a model consistent with the invariant measure of the continuous shallow water system. None of these approaches is fully satisfactory. We stress, however, that our approach has the interest of yielding self-consistent results, such as equilibrium large-scale flows that are stationary state of the shallow-water model. This last property is not satisfied by the statistical equilibria obtained by Weichman's theory.

6.2 Equilibrium statistical mechanics and energy partition for the shallow water model (*published article*)

J Stat Phys (2016) 163:784–843
DOI 10.1007/s10955-016-1496-x

Equilibrium Statistical Mechanics and Energy Partition for the Shallow Water Model

A. Renaud[1] · **A. Venaille**[1] · **F. Bouchet**[1]

Received: 28 April 2015 / Accepted: 8 March 2016 / Published online: 25 March 2016

Abstract The aim of this paper is to use large deviation theory in order to compute the entropy of macrostates for the microcanonical measure of the shallow water system. The main prediction of this full statistical mechanics computation is the energy partition between a large scale vortical flow and small scale fluctuations related to inertia-gravity waves. We introduce for that purpose a semi-Lagrangian discrete model of the continuous shallow water system, and compute the corresponding statistical equilibria. We argue that microcanonical equilibrium states of the discrete model in the continuous limit are equilibrium states of the actual shallow water system. We show that the presence of small scale fluctuations selects a subclass of equilibria among the states that were previously computed by phenomenological approaches that were neglecting such fluctuations. In the limit of weak height fluctuations, the equilibrium state can be interpreted as two subsystems in thermal contact: one subsystem corresponds to the large scale vortical flow, the other subsystem corresponds to small scale height and velocity fluctuations. It is shown that either a non-zero circulation or rotation and bottom topography are required to sustain a non-zero large scale flow at equilibrium. Explicit computation of the equilibria and their energy partition is presented in the quasi-geostrophic limit for the energy–enstrophy ensemble. The possible role of small scale dissipation and shocks is discussed. A geophysical application to the Zapiola anticyclone is presented.

Keywords Equilibrium statistical mechanics · Shallow water model · Large deviations · Turbulence · Inertia-gravity waves · Geostrophic flows

✉ A. Venaille
antoine.venaille@ens-lyon.fr

A. Renaud
antoine.renaud@ens-lyon.fr

F. Bouchet
freddy.bouchet@ens-lyon.fr

[1] Laboratoire de Physique de l'École Normale Supérieure de Lyon, Université de Lyon, CNRS, 46 Allée d'Italie, 69364 Lyon Cedex 07, France

1 Introduction

Geophysical turbulent flows have the propensity to self-organize into large scale coherent structures such as cyclones, anticyclones and jets. These coherent structures are long lived, but can also loose energy, for instance through the radiation of waves that eventually break into small scale structures. The aim of this paper is to understand the energy partition into large scale structures and small scale fluctuations in the framework of freely evolving shallow water dynamics, using statistical mechanics arguments. Indeed, geophysical turbulent flows involve a huge number of degrees of freedom coupled through non-linear interactions, which strongly motivates a statistical mechanics approach. This approach allows to reduce the study of self-organization and energy partition down to a few parameters, such as the total energy of the flow and its total enstrophy.

In the case of the three dimensional Euler equations, equilibrium statistical mechanics predicts that all the energy is lost into small scales, consistently with the classical picture of a small scale energy transfer. By contrast, two-dimensional flows are characterized by a large scale energy transfer, and equilibrium tools are appropriate to describe the large scale structure resulting from self-organization at the domain scale, in the absence of forcing and dissipation. The idea goes back to Onsager [28], and has been mostly developed during the nineties after the work of Miller–Robert–Sommeria [23,33], see also Refs. [4,10,17] and references therein. Importantly, the theory predicts that the contribution of small scale fluctuations to the total energy are negligible in the two-dimensional case. Equilibrium statistical mechanics of two-dimensional and quasi-geostrophic flows is now fairly well understood. It has been applied to various problems in geophysical context such as the description of Jovian vortices [3,44], oceanic rings and jets [50,55], equilibria on a sphere [15], and to describe the vertical energy partition in continuously stratified quasi-geostrophic flows [19,48,52].

Due to the combined effect of stable stratification, thin aspect ratio and rotation, geophysical flows are very different from classical three-dimensional turbulence. However, such flows are not purely two-dimensional. Here we consider the shallow water equations, which is an intermediate model between three-dimensional and two-dimensional turbulence. This model describes the dynamics of a thin layer a fluid with homogeneous density. On the one hand, shallow water equations admit conservation laws similar to two-dimensional Euler equations, that lead to self-organization of the energy at large scale in the Euler case. On the other hand, shallow water dynamics support the presence of inertia-gravity waves that are absent from purely two-dimensional turbulence. A small scale energy transfer may exist due to the existence of these inertia-gravity waves in the shallow water system. The quasi-geostrophic model is recovered as a limit case of the shallow water model, when the Rossby parameter (comparing inertial terms to Coriolis forces) is small. A small Rossby number corresponds to a strong rotation limit. It is then natural to ask whether previously computed statistical equilibrium states of the quasi-geostrophic models remain equilibrium states of the shallow water model. More generally, given a certain amount of energy in an unforced, undissipated geophysical flow, will the flow self-organize into a large scale coherent structure, just as in two dimensional turbulence? Or will the energy be transferred towards the small scales, just as in three dimensional homogeneous turbulence? The aim of this paper is to answer these questions by computing statistical equilibrium states of the inviscid shallow water model.

The first step before computing equilibrium states is to identify a suitable phase space to describe microscopic configurations of the system. The phase space variables must satisfy a Liouville theorem, which ensures that the flow in phase space is divergence-less. Consequently, a uniform measure on a constant energy-Casimirs shell of phase space is invariant (microcanonical measure). The second step is to describe the system at a macroscopic level.

The macrostates will be the sets of microstates sharing the same macroscopic behavior. The third step is to find the most probable macrostate, and to show that almost all the microstates correspond to this macrostate for given values of the constraints. While these three steps may be straightforward for differential equations with a finite number of degrees of freedom, for continuous systems described by partial differential equations, these three steps require the introduction of discrete approximations of the continuous field and of the invariant measure, and to study the continuous field limit of these discrete approximations. This point will be further discussed in the following.

This program has been achieved in the 90s for the two-dimensional Euler equations. Indeed, a Liouville theorem is satisfied by the vorticity field, which describes therefore a microscopic configuration of the system. A macrostate can be defined as a probability field describing the distribution of vorticity levels at a given point, either through a coarse graining procedure [22,23] or directly by the introduction of Young measures [30,31,33].

For the shallow water dynamics, they are further issues that need to be overcome. The existence of a Liouville theorem for the shallow water flow was found by Warn [53] by describing the flow configurations on a basis given by the eigenmodes of the linearized dynamics. However, the constraints of the problem given by dynamical invariants are not easily expressed in terms of the variables satisfying this Liouville theorem (except in the weak flow limit discussed by Warn [53]). This difficulty has been overcome by Weichman and Petrich [56] who considered first a Lagrangian representation of the flow, and then used a formal change of variable to describe the flow configurations with Eulerian variables convenient to express the constraints of the problem. Using a different method that does not require a Lagrangian representation of the fluid, we will show the existence of a formal Liouville theorem.

A second difficulty concerns the choice of a relevant discrete approximation that allows to keep as much as possible geometric conservations laws of the continuous dynamics. Those geometric conservation laws include the Liouville property, the Lagrangian conservation laws (i.e. the conservation of the volume carried by each fluid particle), and global dynamical invariants. Unfortunately, we are not aware of a discrete model that does not break at least one of those geometric conservation laws. However, we will argue that there is no logical need for the discrete model to satisfy all the conservation laws of the continuous dynamics in order to guess the correct microcanonical measure of the continuous system by considering the limit of a large number of degrees of freedom.

A third difficulty is that local small scale fluctuations of the fields may have a substantial contribution to the total energy. This contrasts with 2D Euler dynamics, for which small scale fluctuations of the vorticity field have a vanishingly small contribution to the total energy in the continuous limit. In the shallow water case, it is not a priori obvious that the contribution of these small scale fluctuations to the total energy can be expressed in terms of the macroscopic probability density field.

In order to overcome the second and the third difficulty, we introduce in this paper a semi-Lagrangian discretization: one the one hand, we consider fluid particles of equal volume, which allows to keep track of the Lagrangian conservation laws of the dynamics. On the other hand, the particle positions are restricted to a uniform horizontal grid, and each grid node may contain many particles, which allows for an Eulerian representation of the macrostates and to keep track of global conservation laws, while taking into account the presence of small scale fluctuations contributing to the total energy. We then derive the statistical mechanics theory for this discrete representation of the shallow water model, using large deviation theory.

We will argue that in the limit of a large number of degrees of freedom, the equilibrium states of the semi-Lagrangian discrete model are the equilibrium states of the actual shallow

water system, and we will also show that we recover with this model results already obtained in several limiting cases. While the statistical mechanics treatment of our discrete model is rigorous, there is some arbitrariness in our definition of the discrete model, which is not fully satisfactory.

We stress that our approach to guess the invariant measure of the continuous shallow-water system is heuristic: there is to our knowledge no simple way to define mathematically the microcanonical measure or the Gibbs measure of an Hamiltonian infinite dimensional system. As far as we know the only example of a rigorous work for defining invariant measures in the class of deterministic partial differential equations of interest, is a work by [5] on the periodic nonlinear Schrodinger equation. For the 2D Euler equations, the microcanonical measure seems clear from a physical point of view because different discretizations, for instance either Eulerian ones [22,32] or Lagrangian ones (see [8], lead to a consistent picture in the thermodynamics limit, but even in that case no clear mathematical construction of the invariant measure exists.

There exist only a very limited number of results on statistical equilibrium states of the shallow water system. Warn [53] studied the equilibrium states in a weak flow limit in the energy–enstrophy ensemble. He showed that in the absence of lateral boundaries and in the absence of bottom topography, all the initial energy of a shallow water flow is transferred towards small scales. Here we relax the hypothesis of a weak flow, generalizing the conclusions of Warn [53] for any flow, and we discuss the effect of bottom topography. We show that when there is a non zero bottom topography and when the flow is rotating, there is a large scale flow associated with the equilibrium states.

References [7,20] did compute statistical equilibrium states of "balanced" shallow water flows, by assuming that all the energy remain in the large scale flow. The equilibria described by Merryfield et al. [20] were obtained in the framework of the energy–enstrophy theory, neglecting any other potential vorticity moments than the potential enstrophy. Similar states were described as minima of the potential enstrophy for the macroscopic potential vorticity field by Sanson [37].

Chavanis and Sommeria [7] proposed a generalization of the 2D-Euler variational problem given by the Miller–Robert–Sommeria theory to the shallow water case. Their main result is a relationship between the large scale streamfunction and height field. This result was very interesting and inspiring to us. However, Chavanis and Sommeria did not derive their variational problem from statistical mechanics arguments but proceeded through analogy. They were moreover neglecting height fluctuations. This does not allow for energy partition between vortical flow and fluctuations, and moreover leads to inconsistencies for some range of parameters, as the Chavanis–Sommeria constrained entropy can be shown to have no maxima for negative temperatures (the negative temperature critical points of this variational problem are saddles rather than maxima). As a consequence a range of possible energy values can not be achieved in this phenomenological framework. Nevertheless, with an approach based on statistical mechanics, we will confirm, in this study, the form of the variational problem proposed by Chavanis and Sommeria [7] for describing part of the field, for a restricted range of parameters. We stress however, that generically part of the energy will be carried by the fluctuations, and thus that the Chavanis–Sommeria variational problem should be considered with an energy value which is not the total one. Determining which part of the energy should be taken into account requires a full statistical mechanics treatment, taking into account height fluctuations. We also note that for some other ranges of parameters, all the energy will be carried by the fluctuations, and thus the Chavanis–Sommeria variational problem then does not make sense.

In the preparation of this work, we have also been inspired by the work of Weichman and Petrich [56]. In this work, the authors computed a class of statistical equilibrium states of the shallow water system, starting from a grand canonical distribution. The main result of their work is the same equation describing the relation between the large scale stream function and height field, as the one previously obtained by Chavanis and Sommeria [7]. The Weichman–Petrich approach seemed more promising than the Chavanis–Sommeria one as it was based on a statistical mechanics treatment. However it also fails to predict which part of the energy goes into fluctuations, and to recognize the range of parameters for which the mean field equation for the largest scale is relevant. The reason is that, while natural in condensed matter physics, the hypothesis of a Gibbs or a grand canonical distribution, is questionable for an inertial flow equation which is in contact neither with an energy bath, nor with a potential vorticity bath. Related to this issue, Weichman and Petrich had to assume an ad hoc scaling for the thermodynamical parameters, in order to obtain statistical ensembles where entropy actually balances conservation laws. It has been recognized for a long time that this kind of theoretical difficulties are related to the Rayleigh–Jeans paradox. The proper way to address these issues, in some fluid models like for instance the two-dimensional Euler equation, is to start from the microcanonical measure rather than from a canonical or grand canonical one [4]. We will overcome all these problems in this work by solving the microcanonical problem, which may seem more difficult, but which can be handled using large deviation theory. It also leads to a more precise description of macrostate probabilities.

In this paper, starting from the microcanonical measure, we propose a complete computation of the macrostate entropy for the shallow water equations. In order to achieve this goal, we consider a large-deviation approach that allows to perform the statistical mechanics computation in an explicit and clear way, and that gives a precise description of most-probable macrostates. Moreover, we compute explicitly both the large scale flow and the small scales fluctuations of the equilibrium states. Our results are thus a complete statistical mechanics treatment of the shallow water equations.

We also connect our general results to some of the partial treatment discussed in the previous literature. For instance, we show that only one subclass of the states described by [7,20,56] are actual statistical equilibria of the shallow water model. More precisely, we will see that the large scale flow and the small scales fluctuations can be interpreted as two subsystems in thermal contact, and that the temperature of small scales fluctuations is necessarily positive. The large scale flow is therefore also characterized by a positive temperature.

The paper is organized as follows. The shallow water model and its properties are introduced in Sect. 2. Equilibrium statistical mechanics of a discrete flow model arguably relevant to describe the continuous shallow water system is derived in Sect. 3. Computation of the equilibrium states and a description of their main properties are presented in Sect. 4. Energy partition between a large scale flow and small scale fluctuations is computed analytically in the quasi-geostrophic limit in Sect. 5, which also includes a geophysical application to the Zapiola anticyclone. The main results are summarized and discussed in the conclusion.

2 Shallow Water Model

2.1 Dynamics

The shallow water equations describe the dynamics of a fluid layer with uniform mass density, in the limit where the layer depth is very small compared to the horizontal length scales of the

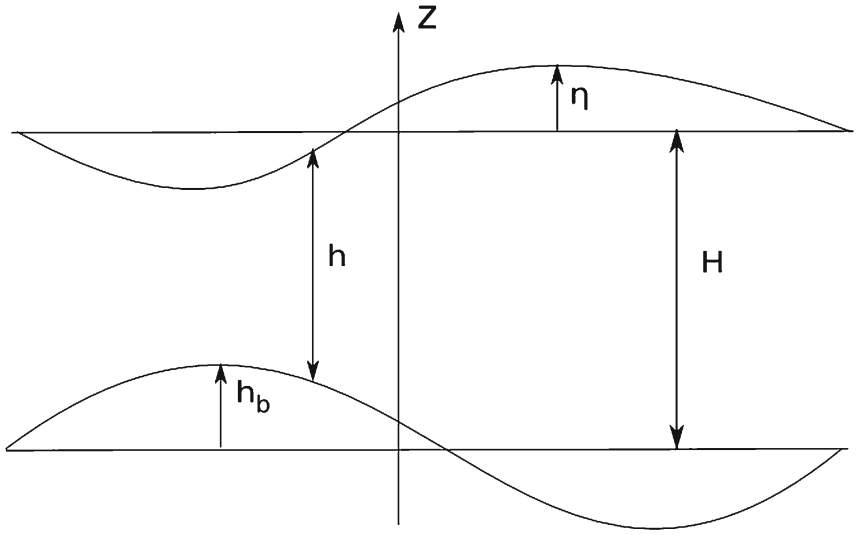

Fig. 1 Scheme of a vertical slice of fluid, η is the upper interface displacement, h_b is the bottom topography, h is the height field and H is the mean height of the fluid ($\langle h \rangle$)

flow [29,46]. In this limit the vertical momentum equation yields hydrostatic equilibrium, and the horizontal velocity field $(u, v) = \mathbf{u}(\mathbf{x}, t)$ is depth independent, where $\mathbf{x} = (x, y)$ is any point of a two-dimensional simply connected domain $\mathscr{D}$. We consider the Coriolis force in the f-plane approximation, i.e. with a constant Coriolis parameter f and a rotation axis along the vertical direction. We denote $\eta(\mathbf{x}, t)$ the vertical displacement of the upper interface and $h_b(\mathbf{x})$ the bottom topography (see Fig. 1). The origin of the z axis is chosen such that

$$\int_{\mathscr{D}} \mathrm{d}\mathbf{x}\, h_b(\mathbf{x}) = 0, \tag{1}$$

and the vertical displacement is defined such that

$$\int_{\mathscr{D}} \mathrm{d}\mathbf{x}\, \eta(\mathbf{x}, t) = 0 \tag{2}$$

as well. We introduce the total depth

$$h = H - h_b + \eta(\mathbf{x}, t), \tag{3}$$

where

$$H = \frac{1}{|\mathscr{D}|} \int_{\mathscr{D}} \mathrm{d}\mathbf{r}\, h(\mathbf{r}) \tag{4}$$

is the mean depth of the fluid, with $|\mathscr{D}|$ the area of the flow domain. The horizontal and vertical length units can always be chosen such that the domain area and the mean height H are equal to one ($|\mathscr{D}| = 1$, $H = 1$), and this choice will be made in the remainder of this paper.

The dynamics is given by the horizontal momentum equations

$$\begin{cases} \partial_t u + u\partial_x u + v\partial_y u - fv = -g\partial_x(h + h_b) \\ \partial_t v + u\partial_x v + v\partial_y v + fu = -g\partial_y(h + h_b) \end{cases} \tag{5}$$

and the mass continuity equation

$$\partial_t h + \nabla \cdot (h\mathbf{u}) = 0, \tag{6}$$

where $\nabla = (\partial_x, \partial_y)$, with impermeability boundary conditions

$$\mathbf{u} \cdot \mathbf{n} = 0 \quad \text{on } \partial\mathscr{D}, \tag{7}$$

where $\mathbf{n}$ is the outward border-normal unit vector.

By introducing the Bernoulli function

$$B \equiv \frac{1}{2}\mathbf{u}^2 + g\,(h + h_b - 1)\,, \tag{8}$$

the relative vorticity field

$$\omega = \partial_x v - \partial_y u, \tag{9}$$

the divergence field

$$\zeta = \nabla \cdot \mathbf{u} = \partial_x u + \partial_y v, \tag{10}$$

and the potential vorticity field

$$q = \frac{\omega + f}{h}, \tag{11}$$

the momentum equations (5) can be recast into a conservative form

$$\begin{cases} \partial_t u - qhv = -\partial_x B \\ \partial_t v + qhu = -\partial_y B \end{cases}. \tag{12}$$

One can get from the momentum equations (12) a dynamical equations for the potential vorticity field (11) and for the divergence field (10), respectively:

$$\partial_t q + \mathbf{u} \cdot \nabla q = 0, \tag{13}$$

$$\partial_t \zeta - \nabla^\perp \cdot (qh\mathbf{u}) = -\Delta B, \tag{14}$$

where $\Delta = \nabla \cdot \nabla$ is the Laplacian operator and $\nabla^\perp = \left(-\partial_y, \partial_x\right)$. In order to show that the shallow water system described by $(h, \mathbf{u})$ is also fully described by the triplet (h, q, ζ), we introduce the velocity streamfunction $\psi(x, y, t)$ and the velocity potential $\phi(x, y, t)$ through the Helmholtz decomposition of the velocity[1]:

$$\mathbf{u} = \nabla^\perp \psi + \nabla\phi. \tag{15}$$

The boundary condition for the velocity given in Eq. (7) yields

$$\begin{cases} \mathbf{n} \cdot \nabla^\perp \psi = 0 \\ \mathbf{n} \cdot \nabla\phi = 0 \end{cases} \quad \text{on } \partial\mathscr{D}, \tag{16}$$

where $\mathbf{n}$ is the boundary normal vector. The relative vorticity (9) and the divergence (10) can be expressed in terms of the velocity streamfunction and velocity potential as

$$\omega = \Delta\psi, \quad \zeta = \Delta\phi\,. \tag{17}$$

[1] In the particular case of a bi-periodic domain, i.e. with periodic boundary conditions for the velocity $\mathbf{u}$, one would need to describe in addition the homogeneous part of the velocity field, which is both divergence-less and irrotational.

To the fields ω and ζ correspond a unique field ψ and a field ϕ defined up to a constant with the boundary condition (16). Thus, to the fields $\omega = qh - f$ and ζ corresponds a unique velocity vector written formally as

$$\mathbf{u} = \nabla^{\perp}\Delta^{-1}(qh - f) + \nabla\Delta^{-1}\zeta. \tag{18}$$

It will also be useful to consider the field μ defined as

$$\mu = \Delta^{1/2}\phi, \tag{19}$$

where $\Delta^{1/2}$ is the linear operator whose eigenmodes are Laplacian eigenmodes in the domain $\mathscr{D}$ with the boundary condition $\mathbf{n}\cdot\boldsymbol{\nabla} = 0$ on $\partial\mathscr{D}$, and whose eigenvalues are the negative square root of the modulus of Laplacian eigenvalues. The field μ can be interpreted as a measure of the amplitude of the potential contribution to the velocity field, given that $\int_{\mathscr{D}}\mu^2 = \int_{\mathscr{D}}(\nabla\phi)^2$. This field will also be referred to as the divergence field in the following. To the field μ correspond a unique field ϕ (up to a constant). Thus, the shallow water system is fully described by the triplet (h, q, μ), and the velocity vector can be written formally in terms of these fields as

$$\mathbf{u} = \nabla^{\perp}\Delta^{-1}[hq - f] + \nabla\Delta^{-1/2}[\mu]. \tag{20}$$

2.2 Stationary States

We investigate in this section the conditions for stationarity of the flow in the shallow water model following [7]. Using a Helmholtz decomposition, one can define the mass transport streamfunction $\Psi(x, y, t)$ and the mass transport potential $\Phi(x, y, t)$, not to be confused with ψ and ϕ defined in Eqs. (15) and (16):

$$h\mathbf{u} = \nabla^{\perp}\Psi + \nabla\Phi. \tag{21}$$

The boundary condition for the velocity given in Eq. (7) yields

$$\begin{cases}\mathbf{n}\cdot\nabla^{\perp}\Psi = 0\\ \mathbf{n}\cdot\nabla\Phi = 0\end{cases}\quad\text{on } \partial\mathscr{D}. \tag{22}$$

It will be useful in the remainder of the paper to express the vorticity field defined in Eq. (9) and the divergent field defined in Eq. (10) in terms of these transport streamfunction Ψ and transport potential Φ:

$$\omega = \nabla\cdot\left(\frac{1}{h}\nabla\Psi\right) + J\left(\frac{1}{h}, \Phi\right), \tag{23}$$

$$\zeta = \nabla\cdot\left(\frac{\nabla\Phi}{h}\right) - J\left(\frac{1}{h}, \Psi\right), \tag{24}$$

where

$$J(f, g) = \partial_x f\,\partial_y g - \partial_y f\,\partial_x g \tag{25}$$

is the Jacobian operator. The dynamics in Eqs. (6), (13) and (14) can also be written in terms of Ψ and Φ:

$$\partial_t h = -\Delta\Phi, \tag{26}$$

$$\partial_t q + \frac{1}{h}J(\Psi, q) + \frac{1}{h}\nabla\Phi\cdot\nabla q = 0, \tag{27}$$

$$\partial_t\zeta + J(\Phi, q) - q\Delta\Psi - \nabla q\cdot\nabla\Psi = -\Delta B. \tag{28}$$

We see that $\partial_t h = 0$ implies $\Phi = Cst$, and $\partial_t q = 0$ implies $J(\Psi, q) = 0$, which means that isolines of potential vorticity are the mass transport streamlines. This is the case if for instance $q = F(\Psi)$. Reciprocally, if $\Phi = Cst$ and if q and Ψ have the same isolines, then $\partial_t h = 0$ and $\partial_t q = 0$, which also implies $\partial_t \Psi = 0$. Thus, through the decomposition (21), the velocity field is also stationary, with $\mathbf{u} = (1/h)\,\nabla^{\perp}\Psi$. We conclude that a necessary and sufficient condition for a shallow water flow $(h, \mathbf{u})$ to be stationary is

$$\Phi = Cst, \quad q \text{ and } \Psi \text{ have the same isolines.} \tag{29}$$

There is an additional relation verified by the stationary flow. This relation may be obtained by considering stationarity of the kinetic energy. The dynamics of the kinetic energy is obtained from Eq. (12):

$$\partial_t \left(\frac{\mathbf{u}^2}{2} \right) = -\frac{1}{h} J(\Psi, B) - \frac{1}{h} \nabla\Phi \cdot \nabla B. \tag{30}$$

Stationarity of the kinetic energy field and Eq. (29) gives $J(\Psi, B) = 0$: the Bernoulli function defined in Eq. (8) and the mass transport streamfunction Ψ have the same isolines. In addition, in any subdomain where $q = F(\Psi)$, the stationarity of the velocity field and the momentum equations (12) give the relation

$$q = \frac{\mathrm{d}B}{\mathrm{d}\Psi}. \tag{31}$$

2.3 Conserved Quantities

Provided that the velocity and height fields remain differentiable, the shallow water dynamics in Eqs. (6), (13) and (14) conserves the total energy

$$\mathscr{E}[\mathbf{u}, h] = \frac{1}{2} \int \mathrm{d}\mathbf{x} \left[h\mathbf{u}^2 + g\,(h + h_b - 1)^2 \right], \tag{32}$$

which includes a kinetic energy contribution and a potential energy contribution. It is known that the shallow water dynamics sometimes leads to shocks that prevent energy conservation. We postpone a discussion of this important point to the last section of this paper.

As a consequence of particle relabeling symmetry there is an infinite number of other conserved quantities called Casimir functionals, see e.g. [35]. These functionals are written

$$\mathscr{C}_s = \int \mathrm{d}\mathbf{x}\, h s(q)\ , \tag{33}$$

where s is any distribution. This conservation can be easily checked from Eqs. (13) and (6). The conservation of all the Casimirs implies the conservation of all the potential vorticity moments

$$\forall k \in \mathbb{N},\ \mathscr{Z}_k = \int \mathrm{d}\mathbf{x}\, h q^k. \tag{34}$$

These Casimir functionals include the total mass conservation ($k = 0$), the conservation of the circulation[2] ($k = 1$) and the conservation of the enstrophy ($k = 2$).

[2] The actual circulation is usually defined as $\Gamma \equiv \int_{\partial D} \mathrm{d}\mathbf{l} \cdot \mathbf{u}$, where $\mathrm{d}\mathbf{l}$ is a vector tangent to the domain boundary. Stokes theorem yields to $Z_1 = \Gamma + f$.

The conservation of all the Casimirs is equivalent to the conservation of mass plus the conservation of the potential vorticity distribution $\mathscr{D}[q]$ defined through

$$\forall \sigma, \quad \mathscr{D}[q](\sigma)\,\mathrm{d}\sigma = \int \mathrm{d}\mathbf{x}\, h \mathscr{I}_{\{\sigma \le q \le \sigma + \mathrm{d}\sigma\}} \tag{35}$$

where $\mathscr{I}_{\{\sigma \le q \le \sigma + \mathrm{d}\sigma\}}$ is the characteristic function, i.e. it returns one if $\sigma \le q(\mathbf{x}) \le \sigma + \mathrm{d}\sigma$ and zero otherwise. It means that the global volume of each potential vorticity level σ_q is conserved through the dynamics.

We will restrict ourselves to initial states where the potential vorticity field has a distribution characterized by its moments only, then the knowledge of its global distribution given in Eq. (35) and of the total mass is equivalent to the knowledge of the moments given in Eq. (34).

Depending on the domain geometry, there could be additional invariants. For the sake of simplicity, we do not discuss the role of these additional invariant in this paper, but it would not be difficult to generalize our results by taking them into account.

In the quasi-geostrophic or two-dimensional Euler models, dynamical invariants have important consequences such as the large scale energy transfer, the self-organization at the domain scale, and the existence of an infinite number of stable states for the dynamics, see for instance Ref. [4] and references therein. We show in the present paper that these dynamical invariants play a similar role in the shallow water case, allowing for a large-scale circulation associated with the potential vorticity field, even if this process may be associated with a concomitant loss of energy toward small scales.

3 Equilibrium Statistical Mechanics of a Discrete Shallow Water Model

The aim of this section is to compute statistical equilibrium states of a discrete model of the shallow water system and to consider the thermodynamic limit for this model. In the first subsection, a formal Liouville theorem is given for the triplet of variables (h, hu, hv) and then the triplet (h, q, μ) after a change of variables. The derivation given with more details in Appendix 1 is made in the Eulerian representation. This allows to write formally the microcanonical measure of the shallow water model for these triplets of fields.

In the second subsection, a finite dimensional semi-Lagrangian discretization of the model is proposed to give a physical meaning to the formal measure. Other discretizations of the shallow water system may have been considered but any other choices we have tried were not taking into account the fluid particle mass conservation and led to inconsistent results (for instance the equilibrium states were not stationary, not stable by coarse-graining, and unbalanced, see Appendix 5).

Then the macroscopic states are defined through a coarse-graining procedure in a third subsection. The variational problem leading to the equilibrium states, i.e. the most probable macroscopic state, is introduced in the fourth subsection. This variational problem generalizes the Miller–Robert–Sommeria equilibrium theory to the shallow water system.

3.1 Liouville Theorem

The first step before computing equilibrium states is to define what is a microscopic configuration of the system, which requires to identify the relevant phase space. The simplest set of variables to consider are those that satisfy a Liouville theorem. A Liouville theorem means that the flow in phase space is non-divergent, which implies the time invariance of the

microcanonical ensemble. The existence of a Liouville theorem for the shallow water system was initially shown by Warn [53] who considered a decomposition of the flow fields on a basis given by the eigenmodes of the linearized dynamics. A Liouville theorem was shown by Weichman and Petrich [56] for a Lagrangian representation of the dynamics. Following a general method proposed by one of us and described by Thalabard [40], it is shown in Appendix 1 that the triplet (h, hu, hv) does satisfy a formal Liouville theorem. At a formal level, the microcanonical measure can then be written[3]

$$\begin{aligned} &\mathrm{d}\mu_{h,hu,hv}\left(E, \{Z_k\}_{k\geq 0}\right) \\ &= \frac{1}{\Omega\left(E, \{Z_k\}_{k\geq 0}\right)} \mathscr{D}[h]\,\mathscr{D}[hu]\,\mathscr{D}[hv]\,\delta\left(\mathscr{E} - E\right) \prod_{k=0}^{+\infty} \delta\left(\mathscr{Z}_k - Z_k\right), \end{aligned} \tag{36}$$

with the phase space volume

$$\Omega\left(E, \{Z_k\}_{k\geq 0}\right) = \int \mathscr{D}[h]\,\mathscr{D}[hu]\,\mathscr{D}[hv]\,\delta\left(\mathscr{E} - E\right) \prod_{k=0}^{+\infty} \delta\left(\mathscr{Z}_k - Z_k\right). \tag{37}$$

Here $\mathscr{E}$ is the energy of a microscopic configuration defined in Eq. (32), and the $\{\mathscr{Z}_k\}_{k\geq 0}$ are the potential vorticity moments of a microscopic configuration defined in Eq. (34). Those constraints are the dynamical invariants of the shallow water model. The notation $\int \mathscr{D}[h]\,\mathscr{D}[hu]\,\mathscr{D}[hv]$ means that the integral is formally performed over each possible triplet of fields $(h,\ hu,\ hv)$. The microcanonical measure allows to compute the expectation of an observable $A[h, hu, hv]$ in the microcanonical ensemble as

$$\langle \mathscr{A} \rangle_{d\mu_{h,hu,hv}} = \int \mathrm{d}\mu_{h,hu,hv}\, \mathscr{A}[h, hu, hv]. \tag{38}$$

Assuming ergodicity, the ensemble average $\langle \mathscr{A} \rangle_{d\mu_{h,hu,hv}}$ can finally be interpreted as the time average of the observable $\mathscr{A}$.

The triplet (h, hu, hv) is not a convenient one to work with, since the Casimir functionals $\{\mathscr{Z}_k\}_{k\geq 0}$ defined in Eq. (34) are not easily expressed in terms of these fields. Indeed, the expression of the Casimir functionals $\{\mathscr{Z}_k\}_{k\geq 0}$ involve not only the triplet (h, hu, hv), but also the triplet of the horizontal derivatives of these fields. We showed in Sect. 2.1 that the triplet of fields (h, q, μ) fully describes the shallow water dynamics in a closed domain, and the functionals $\{\mathscr{Z}_k\}_{k\geq 0}$ are much more easily expressed in terms of the fields h, q. It is therefore more convenient to use these fields as independent variables. The price to pay is that the simple form of the energy defined in Eq. (32) in terms of the triplet (h, hu, vh) becomes more complicated when expressed in terms of the triplet (h, q, μ). However, we will propose a simplified version of this energy functional, and argue in Appendix 2 that this is the relevant form of the energy to consider to compute the equilibrium state.

Unfortunately no direct proof of a Liouville theorem can be obtained for the triplet (h, q, μ). However, it is still possible to start from the microcanonical measure built with (h, hu, hv) in Eq. (36), and change variables at a formal level. It is shown in section "Change of variables from (h, hu, hv) to (h, q, μ)" in Appendix 1 that the Jacobian of the transformation is[4]

[3] The letter "μ" appearing in the measure denoted $\mathrm{d}\mu$ is not related to the divergent field denoted μ.

[4] The h^3 term that appears after the change of variables in the functional integral must be understood as a "functional product" $\prod_{\mathbf{x}\in\mathscr{D}} h^3(\mathbf{x})$, see also the finite-dimensional representation of this measure given in the next subsection.

$$\left| J\left[\frac{(h, hu, hv)}{(q, h, \mu)}\right]\right| = Ch^3. \tag{39}$$

where C is a constant. We conclude that the microcanonical measure can therefore be formally written

$$\mathrm{d}\mu_{h,q,\mu}\left(E, \{Z_k\}_{k\geq 0}\right) = \frac{1}{\Omega\left(E, \{Z_k\}_{k\geq 0}\right)} h^3 \mathscr{D}[h]\,\mathscr{D}[q]\,\mathscr{D}[\mu]\,\delta\left(\mathscr{E} - E\right)\prod_{k=0}^{+\infty}\delta\left(\mathscr{Z}_k - Z_k\right), \tag{40}$$

with

$$\Omega\left(E, \{Z_k\}_{k\geq 0}\right) = \int h^3 \mathscr{D}[h]\,\mathscr{D}[q]\,\mathscr{D}[\mu]\,\delta\left(\mathscr{E} - E\right)\prod_{k=0}^{+\infty}\delta\left(\mathscr{Z}_k - Z_k\right). \tag{41}$$

In that case, the expectation of an observable $A[q, h, \mu]$ in the microcanonical ensemble is given by

$$\langle \mathscr{A} \rangle_{d\mu_{q,h,\mu}} = \int \mathrm{d}\mu_{q,h,\mu} \mathscr{A}[q, h, \mu]. \tag{42}$$

A finite-dimensional projection of the fields will be given in the next subsection to give a meaning to the formal notations of this subsection.

3.2 A Discrete Model

In this section, we devise a discrete model of the shallow water system based on a semi-Lagrangian representation. This allows to give a finite dimensional representation of the formal measure given Eq. (40).

In order to keep track of the conservation properties of the continuous dynamics, we propose a convenient discretization of the shallow water system in terms of fluid particles. Since the fluid is considered incompressible, it is discretized into equal volume particles. The fluid particles do not have necessarily the same height, and the horizontal velocity field may be divergent. It is not possible to build a uniform grid with a single fluid particle per grid point since two particles with equal volume and different height can not occupy the same area. In order to bypass this difficulty, we define a uniform grid where several fluid particles can occupy a given site. To keep track that the actual fluid is continuous and incompressible, we add the condition that the area occupied by the particles inside a grid site fit the available area of the grid site.

In a first step the ensemble of microscopic configurations (the ensemble of the microstates of the discrete model) is defined. In a second step, the constraints of the discrete shallow water system are introduced, which allows to define the microcanonical measure of the discrete model in a third step.

3.2.1 Definition of the Ensemble of Microscopic Configurations

For the sake of simplicity, the domain $\mathscr{D}$ where the flow takes place is considered rectangular but generalizing the results to any shape would be straightforward. We recall that the horizontal and vertical length units have been chosen such that the domain area and the mean height are equal to one ($|\mathscr{D}| = L_x L_y = 1$, $H = 1$). The domain $\mathscr{D}$ is discretized into a uniform grid with $N = N_x \times N_y$ sites. The area of a grid site is $|\mathscr{D}|/N = 1/N$. Each site

can contain many fluid particles. It is assumed that the fluid contains $N \times M$ fluid particles of equal mass and volume (the fluid is incompressible), where M is the average number of particles per site. The volume of a fluid particle is therefore

$$\delta V = \frac{|\mathscr{D}|\, H}{NM} = \frac{1}{NM}. \tag{43}$$

The grid sites are indexed by (i, j) with $1 \leq i, j \leq N_x, N_y$ and the fluid particles by n with $1 \leq n \leq NM$.

Each fluid particle is characterized by its position (I_n, J_n) on the grid, by its potential vorticity $q_n \in [q_{min}, q_{max}]$, its divergence $\mu_n \in [-\mu_{max}, \mu_{max}]$ and its height $h_n \in [h_{min}, h_{max}]$. The cutoffs on the potential vorticity can be physically related to actual minimum and maximum in the global distribution of potential vorticity level defined in Eq. (35), since this distribution is conserved by the dynamics. Such a justification does not exist for the other cutoffs. We will consider first the limit of an infinite number of fluid particles per grid site ($M \to +\infty$), then the limit of an infinite number of grid site ($N \to \infty$) and finally the limit of infinite height and divergence cut-off $\mu_{max} \to +\infty$, $h_{max} \to +\infty$, $h_{min} \to 0$. We will see that the result does not depend on those cut-off.

Let us introduce M_{ij} the number of particles per grid site (i, j), defined as

$$M_{ij} = \sum_{n=1}^{NM} \delta_{I_n,i} \delta_{J_n,j}. \tag{44}$$

The set of the particles that belong to the site (i, j) is denoted

$$\mathscr{M}_{ij} = \{1 \leq n \leq NM \mid (I_n, J_n) = (i, j)\}, \tag{45}$$

whose cardinal is M_{ij}. Mass conservation states that the total number of particles filling the grid is a constant, which gives the constraint

$$\sum_{ij} M_{ij} = NM, \tag{46}$$

where $\sum_{ij}$ means that we sum over the all the sites of the grid. A fluid particle labeled by n and carrying the height h_n occupies an area $\delta V / h_n$. The constraint that the area of each grid site is covered by fluid particles leads to the constraint

$$\forall i, j \qquad \frac{1}{M} \sum_{n \in \mathscr{M}_{ij}} \frac{1}{h_n} = 1, \tag{47}$$

where $\mathscr{M}_{ij}$ is the set defined in Eq. (45).

The ensemble of microstates of the discrete model is given by the set of all reachable values of grid positions, potential vorticities, divergences and heights of each fluid particle in accordance with the constraint of particle filling the area of each grid site:

$$X_{micro} \equiv \left\{ \chi_{micro} = \{(I_n, J_n), q_n, \mu_n, h_n\}_{1 \leq n \leq MN} \;\middle|\; \forall i, j \; 1 \leq i, j \leq N_x, N_y \quad \frac{1}{M} \sum_{n \in \mathscr{M}_{ij}} \frac{1}{h_n} = 1 \right\}. \tag{48}$$

3.2.2 Coarse-Graining

Here we consider a microstate $\chi_{micro} = \{(I_n, J_n), q_n, \mu_n, h_n\}_{1 \le n \le MN}$ and an arbitrary function

$$g : n \to g_n = g(h_n, q_n, \mu_n). \tag{49}$$

We introduce two different coarse-graining procedures: an areal coarse-graining, and a volumetric coarse-graining.

The *areal coarse-graining* of the function g is defined at each grid point (i, j) as

$$\overline{g}_{ij} \equiv \frac{1}{M} \sum_{n \in \mathscr{M}_{ij}} \frac{1}{h_n} g_n \tag{50}$$

where $\mathscr{M}_{ij}$ is a set defined in Eq. (45). The terms $1/h_n$ appearing in Eq. (50) means that we consider local average of g_n weighted by the area occupied by each fluid particle. Note that we will only consider function g such that $\overline{g}_{ij}$ converges to a finite value in the limit of large $M_{ij} \sim M$. This means that the terms g_n should not be allowed to scale with M. This is the reason why we will consider first the large M limit, and then the limit of large cut-off μ_{max} and h_{max} for the fields μ and h.

The area filling constraint in Eq. (47) can then be written in terms of this areal coarse graining:

$$\overline{1}_{ij} = 1. \tag{51}$$

for any i, j. We also notice that the areal coarse-grained height field is simply the ratio of the number of particles in the site (i, j) over the averaged number of particles per site:

$$\overline{h}_{ij} = \frac{M_{ij}}{M}. \tag{52}$$

The *volumetric coarse-graining* of the function g is defined at each grid point (i, j) as

$$\langle g \rangle_{ij} \equiv \frac{1}{M_{ij}} \sum_{n \in \mathscr{M}_{ij}} g_n. \tag{53}$$

This field corresponds to the average of the function g carried by a fluid particle on site (i, j). The volumetric coarse-graining is related to the areal one through

$$\langle g \rangle_{ij} = \frac{\overline{hg}_{ij}}{\overline{h}_{ij}}. \tag{54}$$

3.2.3 Definition of a Velocity Field on the Grid

Let us now define a large scale velocity field (or mean flow) on the uniform grid of the discrete model. We will introduce later a field accounting for small scale fluctuations of the velocity at each grid point. In the case of the actual shallow water model, for a given triplet of continuous fields $h,\ q,\ \mu$, the velocity field is computed by using Eq. (20), which involves two spatial differential operators, namely $\nabla^{\perp}\Delta^{-1}$ and $\nabla\Delta^{-1/2}$. Discrete approximations of these spatial operators are well defined on the uniform grid of the discrete model. Discrete approximations of Eq. (20) can therefore be used to define a velocity field on the uniform grid. Let us consider a coarse-grained vorticity field $\widetilde{\omega} = \overline{h}\langle q \rangle - f$ and a coarse-grained divergent field $\widetilde{\mu} = \langle \mu \rangle$ defined on the same uniform grid. Discrete approximations of the operators

appearing in Eq. (20) can be written respectively as $\left\{\nabla^{\perp}\Delta^{-1}\left[\widetilde{\omega}\right]\right\}_{ij} = \sum_{kl} \mathbf{G}^{\omega}_{ij,kl}.\widetilde{\omega}_{kl}$ and $\left\{\nabla^{\perp}\Delta^{-1}\left[\widetilde{\mu}\right]\right\}_{ij} = \sum_{kl} \mathbf{G}^{\mu}_{ij,kl}.\widetilde{\mu}_{kl}$, where the sum $\sum_{kl}$ is performed over each grid site (k, l). In the remainder of this paper, we do not need the explicit expression of the kernels $\{\mathbf{G}^{\omega}\}$ and $\{\mathbf{G}^{\mu}\}$, which depend only on the domain geometry. Using these notations, we define the large scale velocity field as

$$\mathbf{u}_{mf,ij} = \left\{\nabla^{\perp}\Delta^{-1}\left[\overline{h}\,\langle q\rangle - f\right]\right\}_{ij} + \left\{\nabla\Delta^{-1/2}\left[\langle\mu\rangle\right]\right\}_{ij}, \tag{55}$$

where the index "mf" stands for "mean flow".

At this point one may wonder why the relevant coarse-grained fields used to define the large scale flow $\mathbf{u}_{mf}$ should be $\overline{h}, \langle\mu\rangle, \langle q\rangle$ (which, using Eq. (54) , is equivalent to either the triplet $\overline{h}, \overline{h\mu}, \overline{hq}$ or to the triplet $\left\langle h^{-1}\right\rangle, \langle\mu\rangle, \langle q\rangle$). Our motivation for such a choice is twofold. First, we will see *a posteriori* that this allows to recover previous results derived in several limit cases (weak flow limit, quasi-geostrophic limit), and to obtain consistent results in the general case. Second, in physical space, the number of fluid particles at each grid site is given by the areal-coarse-grained height field $\overline{h}$, according to the previous section. The relevant macroscopic potential vorticity field or divergent field is then given by the volumetric coarse-graining $\langle q\rangle = \overline{hq}/\overline{h}$ and $\langle\mu\rangle = \overline{h\mu}/\overline{h}$. In that respect, the phase space variable h does not play the same role as q and μ when considering macroscopic quantities in physical space, and this is why we do not consider the triplet $\langle h\rangle, \langle\mu\rangle, \langle q\rangle$ to describe the system at a macroscopic level.

3.2.4 Definition of the Microcanonical Ensemble for the Discrete Model

Here we introduce a set of constraints associated with the discrete model in order to define the microcanonical ensemble. These constraints are a discrete version of the Casimirs functional and the energy of the continuous shallow water model, defined in Eqs. (34) and (32), respectively. Additional assumptions on the form of the energy will be required, and we will discuss the relevance of such assumptions.

Note that we introduce here constraints for the discrete shallow water model, but we do not define what would be the dynamics of the discrete model. Indeed, it is not necessary to know the dynamics in order to compute the equilibrium state of the system. Only the knowledge of constraints provided by dynamical invariants is required.

Let us consider a given microstates $\chi_{micro} = \{(I_n, J_n), q_n, \mu_n, h_n\}_{1\leq n\leq MN}$, which belongs to the ensemble X_{micro} of possible configurations of the discrete model defined in Eq. (48). By construction of the ensemble X_{micro}, each element χ_{micro} satisfies the areal filling constraint given in Eq. (47).

The potential vorticity moments of the discrete model are defined as

$$\forall k \geq 0, \quad \mathscr{Z}_k \equiv \frac{1}{NM}\sum_{n=1}^{NM} q_n^k = \frac{1}{N}\sum_{ij}\overline{hq^k}_{ij}. \tag{56}$$

The notation $\sum_{ij}$ means that the sum is performed over each grid point, with $1 \leq i \leq N_x$, $1 \leq j \leq N_y$. It is shown in Appendix 2 that those discrete potential vorticity moments tend to the potential vorticity moments of the continuous dynamics defined in Eq. (34) in the limit of large number of fluid particles NM.

We also define the total energy of the discrete model as

$$\mathscr{E} \equiv \frac{1}{NM}\sum_{n=1}^{NM}\left(\frac{1}{2}\mathbf{u}_{mf,I_nJ_n}^2+\frac{1}{2}\left(\mu_n-\langle\mu\rangle_{I_nJ_n}\right)^2+g\left(\frac{h_n}{2}+h_{bI_nJ_n}\right)\right)-\mathscr{E}_{cst}. \tag{57}$$

where $h_{b,ij}$ is the discrete topography,[5] where $\mathbf{u}_{mf,ij}$ is the mean flow defined in Eq. (55), and where $\mathscr{E}_{cst}\left[h_{bij}\right]$ is an unimportant functional of h_b chosen such that $\mathscr{E}=0$ at rest (i.e. when $\mu_n=0$, $\mathbf{u}_{mfI_nJ_n}=0$, $h_n=1-h_{bI_nJ_n}$ for any n and $M_{ij}=M$ for any (i,j)):

$$\mathscr{E}_{Cst}=\frac{1}{N}\sum_{ij}\frac{g}{2}\left(1-h_{bij}^2\right). \tag{58}$$

A simple interpretation for this form of the total energy is that each fluid particle carries a kinetic energy associated with the mean flow $\mathbf{u}_{mf}$, as well as a kinetic energy associated with local fluctuations of the divergence field and finally a potential energy (the height of the center of mass of the fluid particle is $h_{bI_nJ_n}+h_n/2$).

It is argued in Appendix 2 that with only a few reasonable assumptions on the properties of the equilibrium state, the energy of the discrete model defined in Eq. (57) would also be the energy of the equilibrium state of the actual shallow water model defined in Eq. (32) in the limit of large number of fluid particles NM. Note also that according to Eq. (57), the vortical part of the velocity field does not contribute to local small scale kinetic energy, which is analogous to previous statistical mechanics results for non-divergent flow models such as two-dimensional Euler equations or quasi-geostrophic equations [23,33]. Qualitatively, this is due to the fact that inverting the Laplacian operator smooth out local fluctuations of the relative vorticity $\omega=hq-1$ so that the streamfunction associated with the microscopic vorticity field is the same as the streamfunction associated with the coarse-grained relative vorticity field, see Appendix 2 for more details.

The expression of the energy in Eq. (57) involves a sum over the NM fluid particles. This sum can be recast into a sum over the N points of the grid, by using the definition of the areal coarse-graining in Eq. (50) and the definition of volumetric coarse-graining in Eq. (53):

$$\begin{aligned}\mathscr{E}=\frac{1}{N}\sum_{ij}\Bigg(&\frac{1}{2}\overline{h}_{ij}\mathbf{u}_{mf,ij}^2+\frac{1}{2}\overline{h}_{ij}\left(\langle\mu^2\rangle_{ij}-\langle\mu\rangle_{ij}^2\right)\\&+\frac{g}{2}\left(\left(\overline{h}_{ij}+h_{b,ij}-1\right)^2+\left(\overline{h^2}_{ij}-\overline{h}_{ij}^2\right)\right)\Bigg).\end{aligned} \tag{59}$$

This Eulerian representation of the energy allows to identify three different contributions.

One first contribution to the total energy is given by the sum over each grid point (i,j) of the kinetic energy of the mean flow $\mathbf{u}_{mf}$ (which is carried by $M_{ij}=M\overline{h}_{ij}$ fluid particles), and of the potential energy of the areal coarse-grained height field $\overline{h}_{ij}$:

$$\mathscr{E}_{mf}\equiv\frac{1}{2N}\sum_{ij}\left[\overline{h}_{ij}\mathbf{u}_{mf,ij}^2+g\left(\overline{h}_{ij}+h_{b,ij}-1\right)^2\right]. \tag{60}$$

This contribution will be referred to as the total mean flow energy, or the energy of the large scale flow.

[5] Here, the bottom topography is assumed sufficiently smooth to be considered constant over a grid site. A fluctuating topography would require further discussion.

A second contribution to the total energy is given by the sum over each grid points of the variance of the divergence levels μ carried by fluid particles at site (i, j), times the number of fluid particles ($M_{ij} = M\overline{h}_{ij}$):

$$\mathscr{E}_{\delta\mu} \equiv \frac{1}{2N} \sum_{ij} \overline{h}_{ij} \left(\langle \mu^2 \rangle_{ij} - \langle \mu \rangle_{ij}^2 \right). \tag{61}$$

This term can be interpreted as a subgrid-scale (or small scale) kinetic energy term due entirely to the divergent part of the velocity field (see Appendix 2).

The last contribution to the total energy is the sum over each grid point of the potential energy associated with local fluctuations of the height field:

$$\mathscr{E}_{\delta h} \equiv \frac{g}{2N} \sum_{ij} \left(\overline{h^2}_{ij} - \overline{h}_{ij}^2 \right). \tag{62}$$

This term can be interpreted as a subgrid-scale (or small scale) potential energy term.

One can finally check that total energy defined in Eq. (59) is the sum of the three contributions given in Eqs. (60)–(62):

$$\mathscr{E} = \mathscr{E}_{mf} + \mathscr{E}_{\delta\mu} + \mathscr{E}_{\delta h}. \tag{63}$$

It is well known that for the 2D Euler model or the quasi-geostrophic model, there is no contribution to the energy from the sub-grid fluctuations of the potential vorticity in the limit of vanishing grid size (see [22,33]). For the shallow water model, this is also the case. However the sub-grid fluctuations of height and divergence do contribute to the energy (see Eqs. (61)–(63)). A qualitative reason for this contribution of local height and divergence fluctuations to the total energy is that those two fields may be decomposed on the basis of inertia-gravity waves, which are known to develop a small scale energy transfer [53], and consequently to a loss of energy at subgrid-scales in the discretized model.

Now that we have defined the configurations space in Eq. (48), the potential vorticity moments $\{\mathscr{Z}_k[\chi_{micro}]\}_{k\geq 0}$ of the discrete model in Eq. (56) and the energy $\mathscr{E}[\chi_{micro}]$ of the discrete model in Eq. (59), we introduce the microcanonical ensemble as the restriction of the configurations space X_{micro} to configurations with fixed values of energy E and Casimirs $\{Z_k\}_{k\geq 0}$:

$$\Big\{ \chi_{micro} = \{(I_n, J_n), q_n, \mu_n, h_n\}_{1\leq n\leq MN} \in X_{micro} \,|\, \mathscr{E}[\chi_{micro}] = E, \\ \forall k \in \mathbb{N} \quad \mathscr{Z}_k[\chi_{micro}] = Z_k \Big\}. \tag{64}$$

In our discrete model, we assume that the microcanonical measure over the ensemble of configurations X_{micro} is:

$$\mathrm{d}\mu^{N,M}_{E,\{Z_k\}_{k\geq 0}}(\chi_{\mathrm{micro}}) = \frac{\delta(\mathscr{E}[\chi_{\mathrm{micro}}] - E)}{\Omega(E, \{Z_k\}_{k\geq 0})} \prod_{k=0}^{\infty} \delta(\mathscr{Z}_k[\chi\,\mathrm{micro}] - Z_k) \prod_{ij} \delta(\overline{1}_{ij}[\chi\,\mathrm{micro}] - 1) \\ \times \prod_{n=1}^{NM} h_n^3 \mathrm{d}h_n \mathrm{d}q_n \mathrm{d}\mu_n \mathrm{d}I_n \mathrm{d}J_n, \tag{65}$$

where $\Omega(E, \{Z_k\})$ is the phase space volume defined as

$$\Omega(E, \{Z_k\}_{k\geq 0}) = \sum_{I_1=1}^{N_x} \cdots \sum_{I_n=1}^{N_x} \sum_{J_1=1}^{N_y} \cdots \sum_{J_n=1}^{N_y} \int \left[\prod_{n=1}^{NM} h_n^3 dh_n dq_n d\mu_n \right] \times \delta(\mathscr{E}[\chi_{\text{micro}}] - E) \prod_{k=0}^{\infty} \delta(\mathscr{Z}_k[\chi_{\text{micro}}] - Z_k) \times \prod_{ij} \delta(\overline{1}_{ij}[\chi_{\text{micro}}] - 1). \tag{66}$$

The terms $\mathrm{d}I_n$ and $\mathrm{d}J_n$ are discrete measures with support on the grid coordinates: $\mathrm{d}I_n(f) = \sum_{i=1}^{N_x} f_i$, $\mathrm{d}J_n(f) = \sum_{j=1}^{N_y} f_j$. The product $\prod_{ij}$ is performed over the grid sites (i, j) with $1 \leq i \leq N_x$ and $1 \leq j \leq N_y$. The constraint $\delta\left(\overline{1}_{ij}[\chi_{micro}] - 1\right)$ corresponds to the area filling constraint defined in Eq. (51), which must be satisfied by each microstate $\chi_{micro} \in X_{micro}$.

Note that Eq. (65) is a discrete version of the formal microcanonical measure given in Eq. (40) for the continuous case. The expectation of an observable $\mathscr{A}[\chi_{micro}]$ in the microcanonical ensemble is

$$\langle \mathscr{A} \rangle_{E,\{Z_k\}_{k\geq 0}}^{N,M} = \mathrm{d}\mu_{E,\{Z_k\}_{k\geq 0}}^{N,M}(\mathscr{A}) = \int \mathrm{d}\mu_{E,\{Z_k\}_{k\geq 0}}^{N,M}(\chi_{\text{micro}}) \mathscr{A}[\chi_{\text{micro}}]. \tag{67}$$

The problem is now to compute the macrostate entropy, which accounts for the logarithm of the number of microstates corresponding to the same macrostate. Although we do not need to consider this problem in the present work, it would be very interesting to have continuous or discrete approximation of the shallow water equation that have the invariant measure (65), in an analogous way as what was achieved for the 2D Euler equations [9,13].

3.3 Macrostates and Their Entropy

The aim of this section is to compute the equilibrium state of the discrete model introduced in the previous subsection. The first step is to define the macrostates of the system, the next step is to compute the most probable macrostates, using large deviation theory, which yields also a concentration property asymptotically for large N and M (almost all the microstates correspond to the most probable macrostate).

3.3.1 Definition of the Empirical Density Field

Let us consider a microstate $\chi_{micro} = \{(I_n, J_n), q_n, \mu_n, h_n\}_{1\leq n\leq MN}$ picked in the ensemble of configurations X_{micro} defined in Eq. (48). The empirical density field of this microstate is defined for each grid point (i, j) as

$$p_{ij}\left(\sigma_h, \sigma_q, \sigma_\mu\right)[\chi_{\text{micro}}] \equiv \overline{\delta\left(h - \sigma_h\right) \delta\left(q - \sigma_q\right) \delta\left(\mu - \sigma_\mu\right)}_{ij}, \tag{68}$$

where the overline operator is the areal coarse-graining defined in (50). This field contains all the statistical information of the system at the grid level. The constraint that each grid site (i, j) is covered by particles is given by Eq. (51), which ensures the normalization:

$$\int \mathrm{d}\sigma_h \mathrm{d}\sigma_q \mathrm{d}\sigma_\mu \; p_{ij} = 1. \tag{69}$$

Let us consider a function $g(h_n, q_n, \mu_n)$ depending on the height, potential vorticity and divergence carried by a fluid particle. Let us then consider the discrete microscopic field $n \to g_n = g(h_n, q_n, \mu_n)$ with $1 \leq n \leq NM$. Following Eqs. (50) and (68), the corresponding coarse-grained field $\overline{g}_{ij}$ is expressed solely in terms of the empirical density field p_{ij}:

$$\overline{g}_{ij} = \int \mathrm{d}\sigma_h \mathrm{d}\sigma_q \mathrm{d}\sigma_\mu \; g(\sigma_h, \sigma_q, \sigma_\mu) p_{ij}\left(\sigma_h, \sigma_q, \sigma_\mu\right). \tag{70}$$

If we consider for instance the function $g(h, q, \mu) = q$, then $g_n = q_n$ the microscopic potential vorticity field, and coarse-grained potential vorticity field $\overline{q}_{ij}$ is obtained by a direct application of Eq. (70): $\overline{q}_{ij} = \int \mathrm{d}\sigma_h \mathrm{d}\sigma_q \mathrm{d}\sigma_\mu \; \sigma_q \, p_{ij}$.

Importantly, the constraints $\{\mathscr{Z}_k[\chi_{micro}] = Z_k\}_{k\geq 0}$ and $\mathscr{E}[\chi_{micro}] = E$ defined in Eq. (56) and (59) depend only on the empirical density field p_{ij} (since they depend only on local areal coarse-grained moments of the different fields). The empirical density is therefore a relevant variable to fully characterize the system at a macroscopic level.

3.3.2 Definition of the Macrostates

The macrostates are defined as the set of microscopic configurations leading to a given value $p_{ij} = \rho_{ij}$ of the empirical density field:

$$\rho \equiv \left\{ \chi_{micro} \in X_{micro} \;\middle|\; \forall i, j \quad p_{ij}[\chi_{micro}] = \rho_{ij} \right\}. \tag{71}$$

For the sake of simplicity, we make a small abuse of notation by denoting ρ both the macrostate defined in Eq. (71) and the field $\rho = \left\{\rho_{ij}\right\}$. The values of the constraints are the same for all microstates within a given macrostate since they depend only on the local coarse-grained moments of the different fields, which remain unchanged for a prescribed empirical density field. The energy and the Casimirs, defined in Eqs. (57) and (56) respectively, have the same values for all the microstates within a single macrostate and will therefore be denoted by $\mathscr{E}[\rho]$ and $\{\mathscr{Z}_k[\rho]\}_{k\geq 0}$.

3.3.3 Macroscopic Observables and Empirical Density

Let us now consider an observable $\mathscr{A}[\chi_{micro}]$ on the configuration space X_{micro} defined in Eq. (48) such that their dependance on the microscopic configuration χ_{micro} occurs only through the empirical density field:

$$\mathscr{A}[\chi_{micro}] = \mathscr{A}\left[\left\{p_{ij}[\chi_{micro}]\right\}\right]. \tag{72}$$

This is actually the case for any observable written as a sum over the fluid particles, i.e. for any observable appearing in Eq. (67). It is therefore possible to change variables from χ_{micro} to the empirical density field values $\left\{\rho_{ij}\right\}_{1\leq i,j\leq N_x,N_y}$ in Eq. (67):

$$\begin{aligned}\langle \mathscr{A} \rangle^{N,M}_{E,\{Z_k\}_{k\geq 0}} = \int \left[\prod_{ij} \mathscr{D}\left[\rho_{ij}\right]\right] \mathscr{A}\left[\{\rho_{ij}\}\right] \frac{\Omega(\rho)}{\Omega\left(E, \{Z_k\}_{k\geq 0}\right)} \\ \times \delta\left(\mathscr{E}[\rho] - E\right) \prod_{k=0}^{\infty} \delta\left(\mathscr{Z}_k[\rho] - Z_k\right) \times \prod_{ij} \delta\left(\overline{1}_{ij}\left[\rho_{ij}\right] - 1\right),\end{aligned} \tag{73}$$

where

$$\Omega(\rho) = \sum_{I_1=1}^{N_x} \cdots \sum_{I_n=1}^{N_x} \sum_{J_1=1}^{N_y} \cdots \sum_{J_n=1}^{N_y} \int \left[\prod_{n=1}^{NM} h_n^3 dh_n dq_n d\mu_n \right] \prod_{ij} \left[\hat{\delta}(p_{ij}[\chi_{\text{micro}}] - \rho_{ij}) \right] \tag{74}$$

is the volume of a macrostate ρ defined in Eq. (71) in the configuration space X_{micro} defined in Eq. (48), and where $\Omega\left(E, \{Z_k\}_{k\geq 0}\right)$ is the total volume in phase space defined in Eq. (66). The constraint $\delta\left(\overline{1}_{ij}\left[\rho_{ij}\right] - 1\right)$ is a normalization constraint for the $\left\{\rho_{ij}\right\}$, since $\overline{1}_{ij}\left[\rho_{ij}\right] = \int \mathrm{d}\sigma_h \mathrm{d}\sigma_q \mathrm{d}\sigma_\mu \ \rho_{ij}$. This normalization constraint also corresponds to the constraint that the fluid particles within a site must fit the available area, see Eq. (47). The term $\int \mathscr{D}\left[\rho_{ij}\right]$ means that the integral is performed over all the possible functions ρ_{ij}. The term $\hat{\delta}\left(p_{ij} - \rho_{ij}\right)$ is a Dirac delta distribution on the functional space of the empirical density field values $\rho_{ij}(\sigma_h, \sigma_q, \sigma_\mu)$, with $p_{ij}\left(\sigma_h, \sigma_q, \sigma_\mu\right)[\chi_{micro}]$ the empirical density field defined in Eq. (68).

3.3.4 Asymptotic Behavior of the Macrostates Volume and Derivation of Its Entropy

Let us compute the asymptotic form of $\Omega(\rho)$ defined in Eq. (74), by considering the limit $M \to \infty$, where M is the average number of particles per grid site (i, j). For a given set of macrostates ρ defined in Eq. (71), the number of fluid particles per grid site is

$$M_{ij} = M \int \mathrm{d}\sigma_h \mathrm{d}\sigma_q \mathrm{d}\sigma_\mu \ \sigma_h \rho_{ij}. \tag{75}$$

This is the only constraint on the particle positions in the grid for a microstate that belongs to the macrostates ρ. All the realizations of the particle positions that satisfies (75) count equally in the ensemble of macrostates ρ. Through combinatorial calculation, the number of realizations of $\{(I_n, J_n)\}$ that satisfy (75) is $(NM)!/\prod_{ij} M_{ij}!$. Using Eq. (52) to express M_{ij} in terms of $\overline{h}_{ij}$, we get

$$\Omega(\rho) = \frac{(NM)!}{\prod_{ij}\left(M\overline{h}_{ij}\right)!} \prod_{ij} \Omega_{ij}, \tag{76}$$

where

$$\begin{aligned} \Omega_{ij} \equiv & \int \left[\prod_{m=1}^{M\overline{h}_{ij}} h_m^3 \mathrm{d}h_m \mathrm{d}q_m \mathrm{d}\mu_m \right] \\ & \times \hat{\delta} \left(\frac{1}{M} \sum_{m=1}^{M\overline{h}_{ij}} \frac{1}{h_m} \delta\left(h_m - \sigma_h\right) \delta\left(q_m - \sigma_q\right) \delta\left(\mu_m - \sigma_\mu\right) - \rho_{ij} \right) \end{aligned} \tag{77}$$

is the number of possible configurations for a given set of $M_{ij} = M\overline{h}_{ij}$ fluid particles at site (i, j).

The asymptotic behavior of the pre-factor in Eq. (76) is computed through the Stirling formula:

$$\log\left(\frac{(NM)!}{\prod_{ij}\left(M\overline{h}_{ij}\right)!} \right) \underset{M\to\infty}{\sim} MN \left(-\frac{1}{N} \sum_{ij} \overline{h}_{ij} \log\left(\overline{h}_{ij}\right) + \log(N) \right). \tag{78}$$

The asymptotic behavior with M of Ω_{ij} defined in Eq. (77) can be computed by using Sanov's theorem.

Before applying this theorem to our problem, let us consider the simpler case of K independent and identically distributed variables $\{\chi_k\}_{1\leq k\leq K}$ with common probability density function $F(\chi)$. Those variable take values in a bounded interval of $\mathbb{R}$.[6] Sanov's theorem describes the large deviation of the empirical density distribution

$$f_K \equiv \frac{1}{K}\sum_{k=1}^{K}\delta(\chi_k - \chi), \tag{79}$$

which can be considered as an actual probability distribution for the variable χ. The probability distribution functional of this empirical density function is

$$\mathscr{P}[f] \equiv \int \prod_{k=1}^{K} F(\chi_k)\,\mathrm{d}\chi_k\ \hat{\delta}(f - f_K). \tag{80}$$

Sanov's theorem is a statement about the asymptotic behavior of the logarithm of $\mathscr{P}[f]$. For a given function $f(\chi)$, Sanov's theorem states

$$\log(\mathscr{P}[f]) \underset{K\to+\infty}{\sim} -K\int \mathrm{d}\chi\ f(\chi)\log\left(\frac{f(\chi)}{F(\chi)}\right) \tag{81}$$

if $\int \mathrm{d}\chi\ f(\chi) = 1$ and $\log(\mathscr{P}[f]) \sim -\infty$ otherwise. An heuristic discussion of Sanov's theorem is given in Ref [43].

Combining Eqs. (79), (80) and (81) and generalizing this result to K independent and identically distributed L-tuple of variables $\left\{\{\chi_{l,k}\}_{1\leq l\leq L}\right\}_{1\leq k\leq K}$ with common probability density function $F\left(\{\chi_l\}_{1\leq l\leq L}\right)$, Sanov's theorem is written in compact form as

$$\begin{aligned}&\log\left(\int \prod_{k=1}^{K} F\left(\{\chi_{l,k}\}_{1\leq l\leq L}\right)\prod_{l=1}^{L}\mathrm{d}\chi_{l,k}\ \hat{\delta}\left(f - \frac{1}{K}\sum_{k=1}^{K}\prod_{l=1}^{L}\delta\left(\chi_{l,k} - \chi_l\right)\right)\right)\\ &\underset{K\to\infty}{\sim} -K\int \prod_{l=1}^{L}\mathrm{d}\chi_l\ f\log\left(\frac{f}{F}\right)\end{aligned} \tag{82}$$

if $\int \prod_{l=1}^{L}\mathrm{d}\chi_l\ f\left(\{\chi_l\}_{1\leq l\leq L}\right) = 1$.

Let us come back to the asymptotic behavior of Ω_{ij} defined in Eq. (77), in the large M limit. Before applying Sanov's theorem, it is needed to recast this equation into a form similar to the argument of the logarithm in the lhs of Eq. (82). Because of the $1/h_m$ term appearing in the delta Dirac function of Eq. (77), one needs to perform first a change of variable from ρ_{ij} to

$$\pi_{ij} \equiv \frac{\sigma_h}{\overline{h}_{ij}}\rho_{ij} \tag{83}$$

The formal Jacobian $\mathscr{J}$ arising from this change of variable in the functional delta Dirac function depend only on $\overline{h}_{ij}$ which does not depend on M and will therefore not matter for the asymptotic behavior of $\log\left(\Omega_{ij}\right)$. In addition, the factor h_m^3 appearing in front of the Lebesgue measure in Eq. (77) must be divided by a normalization factor $Z = \int h_m^3 \mathrm{d}h_m \mathrm{d}q_m \mathrm{d}\mu_m$ so

[6] The fact that the variable χ_k have to be bounded is the reason why we set the cutoffs on the values of h_n, q_n and μ_n.

that $P(h_m, q_m, \mu_m) = h_m^3/Z$ can be interpreted as a probability distribution function.[7] Then Ω_{ij} writes:

$$\Omega_{ij} = \mathscr{J} Z^{M\overline{h}_{ij}} \int \prod_{m=1}^{M\overline{h}_{ij}} \left(\frac{h_m^3}{Z}\right) \mathrm{d}h_m \mathrm{d}q_m \mathrm{d}\mu_m \times \hat{\delta}\left(\pi_{ij} - \frac{1}{M\overline{h}_{ij}} \sum_{m=1}^{M\overline{h}_{ij}} \delta\left(h_m - \sigma_h\right) \delta\left(q_m - \sigma_q\right) \delta\left(\mu_m - \sigma_\mu\right)\right). \tag{84}$$

A direct application of Sanov's theorem to Eq. (84) then yields

$$\log\left(\Omega_{ij}\right) \underset{M\to\infty}{\sim} M\overline{h}_{ij}\left[-\int \mathrm{d}\sigma_h \mathrm{d}\sigma_q \mathrm{d}\sigma_\mu\, \pi_{ij} \log\left(\frac{\pi_{ij}}{\sigma_h^3}\right)\right]. \tag{85}$$

The normalization constraint on the distributions π_{ij} is already fulfilled by the definition of the coarse-grained height fields $\overline{h}_{ij} = \overline{h}_{ij} \int \mathrm{d}\sigma_h \mathrm{d}\sigma_q \mathrm{d}\sigma_\mu\, \pi_{ij}$ (see Eq. (70)). The inverse change of variable $\rho_{ij} = \overline{h}_{ij}\pi_{ij}/\sigma_h$ in Eq. (85) yields

$$\log\left(\Omega_{ij}\right) \underset{M\to\infty}{\sim} M\left[-\int \mathrm{d}\sigma_h \mathrm{d}\sigma_q \mathrm{d}\sigma_\mu\, \sigma_h \rho_{ij} \log\left(\frac{\rho_{ij}}{\sigma_h^2}\right) + \overline{h}_{ij} \log\left(\overline{h}_{ij}\right)\right]. \tag{86}$$

Combining Eq. (76) with Eqs. (78) and (86), we obtain the asymptotic behavior of $\Omega(\rho)$ with M:

$$\log\left(\Omega\left(\rho\right)\right) \underset{M\to\infty}{\sim} MN\, \mathscr{S}\left[\rho\right], \tag{87}$$

where

$$\mathscr{S}\left[\rho\right] = -\frac{1}{N} \sum_{ij} \int \mathrm{d}\sigma_h \mathrm{d}\sigma_q \mathrm{d}\sigma_\mu\, \sigma_h \rho_{ij} \log\left(\frac{\rho_{ij}}{\sigma_h^2}\right) \tag{88}$$

is the macrostate entropy.[8]

3.4 Continuous Limit

3.4.1 Expressions of the Macrostate Entropy, Energy and Potential Vorticity Moments

Considering now the limit of an infinite number of grid site ($N \to \infty$), the site coordinates (i, j) tend toward the continuous space coordinates $\mathbf{x}$ and the macrostate entropy $\mathscr{S}$ derived in Eq. (88) becomes

$$\mathscr{S}\left[\rho\right] = -\int \mathrm{d}\mathbf{x} \mathrm{d}\sigma_h \mathrm{d}\sigma_q \mathrm{d}\sigma_\mu\, \sigma_h \rho\left(\mathbf{x}, \sigma_h, \sigma_q, \sigma_\mu\right) \log\left(\frac{\rho\left(\mathbf{x}, \sigma_h, \sigma_q, \sigma_\mu\right)}{\sigma_h^2}\right). \tag{89}$$

The empirical density has become a probability density function (pdf). For any function $g : n \to g_n = g\left(h_n, q_n, \mu_n\right)$, its continuous coarse-grained field is now computed through

[7] Here, Z depends on the cutoffs introduced in Sect. 3.2. But we will see that it will vanish from the expression of the entropy in the end.

[8] Here we dropped the term $\log N$ coming from Eq. (78) as it is constant that can be discarded by redefining $\Omega_{E,\{Z_k\}_{k\geq 0}}$.

$$\overline{g}\left(\mathbf{x}\right) = \int \mathrm{d}\sigma_h \mathrm{d}\sigma_q \mathrm{d}\sigma_\mu \; \rho\left(\mathbf{x}, \sigma_h, \sigma_q, \sigma_\mu\right) g\left(\sigma_h, \sigma_q, \sigma_\mu\right), \tag{90}$$

The discrete mean flow defined in Eq. (55) becomes (by construction):

$$\mathbf{u}_{mf}\left[\overline{h}, \overline{hq}, \overline{h\mu}\right] = \nabla^\perp \Delta^{-1}\left(\overline{hq} - f\right) + \nabla \Delta^{-1/2}\left(\frac{\overline{h\mu}}{\overline{h}}\right), \tag{91}$$

where all the coarse-grained fields have been expressed in terms of an areal coarse-graining, using Eq. (54). Similarly, the potential vorticity moments defined in Eq. (56) for the discrete model become

$$\forall k \in \mathbb{N} \quad \mathscr{Z}_k\left[\rho\right] = \int \mathrm{d}\mathbf{x}\, \overline{hq^k}. \tag{92}$$

The total energy defined in Eq. (59) for the discrete model becomes

$$\mathscr{E}\left[\rho\right] = \frac{1}{2}\int \mathrm{d}\mathbf{x} \left[\overline{h}\mathbf{u}_{mf}^2 + \left(\overline{h\mu^2} - \frac{\overline{h\mu}^2}{\overline{h}}\right) + g\overline{(h + h_b - 1)^2}\right]. \tag{93}$$

We note that the total energy is a functional of $\overline{h}, \overline{h^2}, \overline{hq}, \overline{h\mu}, \overline{h\mu^2}$. Just as in the discrete case, this energy can be separated into a mean flow contribution (a large scale contribution including kinetic and potential energy), as well as a contribution from small scale kinetic energy due to local fluctuations of the divergent velocity field and a contribution from small scale potential energy due to local height fluctuations. The large scale (or mean flow) energy defined in Eq. (60) for the discrete model becomes

$$\mathscr{E}_{mf}\left[\overline{h}, \overline{hq}, \overline{h\mu}\right] = \frac{1}{2}\int \mathrm{d}\mathbf{x} \left[\overline{h}\mathbf{u}_{mf}^2 + g\left(\overline{h} + h_b - 1\right)^2\right]. \tag{94}$$

The small scale (or subgrid-scale) kinetic energy due to local fluctuations of the divergent part of the velocity field defined in Eq. (61) becomes

$$\mathscr{E}_{\delta\mu}\left[\overline{h}, \overline{\mu}, \overline{\mu^2}\right] = \frac{1}{2}\int \mathrm{d}\mathbf{x} \left(\overline{h\mu^2} - \frac{\overline{h\mu}^2}{\overline{h}}\right), \tag{95}$$

and the small scale (or sub-grid scale) potential energy due to local height fluctuations defined in Eq. (62) becomes

$$\mathscr{E}_{\delta h}\left[\overline{h}, \overline{h^2}\right] = \frac{g}{2}\int \mathrm{d}\mathbf{x} \left(\overline{h^2} - \overline{h}^2\right). \tag{96}$$

One can check that the total energy in Eq. (93) is the sum of the three contributions given in Eqs. (94)–(96):

$$\mathscr{E} = \mathscr{E}_{mf} + \mathscr{E}_{\delta\mu} + \mathscr{E}_{\delta h}. \tag{97}$$

3.4.2 Microcanonical Variational Problem for the Probability Density Field

Let us come back to the average of a macroscopic observable $\mathscr{A}$ defined in Eq. (73). Using the asymptotic estimate for $\Omega\left[\rho\right]$ given in Eq. (87), the average of an observable $\mathscr{A}$ defined in Eq. (73) becomes[9]

[9] Strictly speaking, the equal sign should be noted $\asymp$ which means that the logarithm of the terms on both sides are equivalent, see e.g. Ref. [43].

$$\langle \mathscr{A} \rangle_{d\mu^{M,N}_{q,h,\mu}} = \int \mathscr{D}[\rho]\ \mathscr{A}[\rho] \frac{\mathrm{e}^{NM\mathscr{S}[\rho]}}{\Omega(E,\{Z_k\})} \delta(\mathscr{E}[\rho] - E) \times \prod_{k=0}^{\infty} \delta(\mathscr{Z}_k[\rho] - Z_k) \prod_{\mathbf{x}} \delta\left(\overline{1}[\rho] - 1\right). \tag{98}$$

It comes to a Laplace-type integral where $NM \to \infty$. Thus, the value of $\langle \mathscr{A} \rangle_{d\mu^{M,N}_{q,h,\mu}}$ will be completely dominated by the contribution of the pdf ρ that maximizes the macrostate entropy defined in Eq. (89) while satisfying the normalization constraint

$$\overline{1}[\rho] = \int \mathrm{d}\sigma_h \mathrm{d}\sigma_q \mathrm{d}\sigma_\mu\ \rho\left(\mathbf{x}, \sigma_h, \sigma_q, \sigma_\mu\right) = 1, \tag{99}$$

and the microcanonical constraints $\mathscr{E}[\rho] = E$, $\{\mathscr{Z}_k[\rho] = Z_k\}_{k\geq 0}$, where the energy is defined in Eq. (93) and the potential vorticity moments are defined in Eq. (92). This variational problem can be written in compact form as:

$$\max_{\rho} \left\{ \mathscr{S}[\rho] \,\middle|\, \mathscr{E}[\rho] = E,\ \forall k \in \mathbb{N}\ \ \mathscr{Z}_k[\rho] = Z_k,\ \forall \mathbf{x} \in \mathscr{D}\ \ \overline{1}(\mathbf{x})[\rho] = 1 \right\}. \tag{100}$$

The probability measure ρ induced by the empirical density field has a concentration property. In other words, the average of an observable depending only on macrostates is dominated by the most probable macrostates, which are solutions of the variational problem (100).

An interesting limit case for the entropy in Eq. (89) is worth mentioning in order to relate the variational problem in Eq. (100) with previous studies on the shallow water system. Let us assume that there is neither height variation nor divergent fluctuations, which would be the case if considering a quasi-geostrophic model or 2D incompressible Euler equations. Then the only height level and the only divergence level are $\sigma_h = 1, \sigma_\mu = 0$, respectively. Defining $\rho_q\left(\mathbf{x}, \sigma_q\right) = \rho\left(\mathbf{x}, 1, \sigma_q, 0\right)$, Eq. (89) becomes up to an unimportant constant:

$$\mathscr{S}\left[\rho_q(\mathbf{x}, \sigma_q)\right] = -\int \mathrm{d}\mathbf{x}\mathrm{d}\sigma_q\ \rho_q \log \rho_q. \tag{101}$$

We recover in that case the macrostate entropy of the Miller–Robert–Sommeria theory [22, 34].

Let us now assume that the height varies with position but that there is no local height fluctuations. Then at point $\mathbf{x}$ the only height level is $\sigma_h = \overline{h}(\mathbf{x}) = h(\mathbf{x})$. Defining $\rho_{q\mu}\left(\mathbf{x}, \sigma_q, \sigma_\mu\right) = \rho\left(\mathbf{x}, h(\mathbf{x}), \sigma_q, \sigma_\mu\right)$, the macrostate entropy in Eq. (89) becomes up to an unimportant constant:

$$\mathscr{S}\left[\rho_{q\mu}\left(\mathbf{x}, \sigma_q, \sigma_\mu\right), h\left(\mathbf{x}\right)\right] = -\int \mathrm{d}\mathbf{x}\mathrm{d}\sigma_q\mathrm{d}\sigma_\mu\ h\rho_{q\mu} \log \rho_{q\mu}. \tag{102}$$

This form of the entropy was proposed by [7], without microscopic justification. Interestingly, [7] obtained Eq. (102) by assuming that the macrostate entropy can be written as

$$\mathscr{S} = \int \mathrm{d}\mathbf{x}\mathrm{d}\sigma_q\mathrm{d}\sigma_\mu h(\mathbf{x}) s\left(\rho_{q\mu}\left(\mathbf{x}, \sigma_q, \sigma_\mu\right)\right), \tag{103}$$

and by noting that $s(\rho) = -\rho \log \rho$ is the only function that leads to equilibrium states that are stationary.

4 General Properties of the Equilibria and Simplification of the Theory in Limiting Cases

General properties of equilibrium states, solutions of the variational problem in Eq. (100), are discussed in this section. Critical points of the variational problem are given in the first subsection ; they are computed in Appendix 3. This allows to obtain an equation for the large scale flow, and to show that equilibrium states of the shallow water model are positive temperature states. A weak height fluctuation limit is considered in a second subsection. It is found that the large scale flow and the small scale fluctuations are decoupled in this limit, and that there is equipartition between small scale potential energy and small scale kinetic energy. The quasi-geostrophic limit is investigated in a third subsection.

4.1 Equilibrium States are Stationary States with Positive Temperatures

4.1.1 Properties of the Critical Points

Critical points of the equilibrium variational problem defined in Eq. (100) are solutions of the equation

$$\forall \delta\rho, \quad \delta\mathscr{S}[\rho] - \beta\delta\mathscr{E}[\rho] - \sum_{k=0}^{+\infty}\alpha_k\delta\mathscr{Z}_k[\rho] - \int \mathrm{d}\mathbf{x}\,\xi(\mathbf{x})\int \mathrm{d}\sigma_h\mathrm{d}\sigma_q\mathrm{d}\sigma_\mu\,\delta\rho = 0 \quad (104)$$

where β, $\{\alpha_k\}_{k\geq 0}$ and $\xi(\mathbf{x})$ are the Lagrange multipliers associated with the conservation of the energy, the potential vorticity moments, and with the normalization constraint, respectively. The computation of the critical points is performed in Appendix 3.

A first key result of Appendix 3 is that solutions of Eq. (104) factorize as

$$\rho = \rho_h(\mathbf{x},\sigma_h)\,\rho_q(\mathbf{x},\sigma_q)\,\rho_\mu(\mathbf{x},\sigma_\mu). \quad (105)$$

A second result of Appendix 3 is that the pdf of the divergence field is a Gaussian

$$\rho_\mu(\mathbf{x},\sigma_\mu) = \sqrt{\frac{\beta}{2\pi}}\exp\left(-\frac{\beta}{2}(\sigma_\mu-\overline{\mu})^2\right). \quad (106)$$

Recalling that $\beta = \partial S/\partial E$ is the inverse temperature, we see that the variance of the pdf of the divergence field is given by the temperature of the flow:

$$\overline{\mu^2} - \overline{\mu}^2 = \beta^{-1}. \quad (107)$$

This equation has important physical consequences. First, fluctuations of the divergent field do not vary with space. Second, the temperature of the equilibrium state is necessary positive. This contrasts with equilibrium states of two-dimensional Euler flow, which can be characterized by negative temperature states [23,33]. This was realized first by Onsager for the point vortex model [28]. In the context of 2D Euler equations in doubly periodic domains, the equilibrium states are always characterized by negative temperature, just as in the case discussed by Onsager (this result is shown in [2]). However, the existence of large scale flow structures characterized by positive temperatures are possible at low energy in the presence of lateral boundaries and non-zero circulation, and/or in the presence of bottom topography in the framework of QG model. Such positive temperature states are known and documented in the literature (see e.g. the original papers by [18,23,34] or [4] and references therein).

In addition, it follows from Eqs. (95), (105) and (107) that the temperature is directly related to small scale kinetic energy due to the divergent velocity field:

$$\mathscr{E}_{\delta\mu} = \frac{1}{2\beta}. \tag{108}$$

A third result of Appendix 3 is the expression of the pdf of the height field:

$$\begin{aligned} \rho_h\left(\mathbf{x}, \sigma_h\right) &= \frac{1}{\mathbb{G}_h\left(\mathbf{x}\right)} \sigma_h^2 \exp\left(-\beta \frac{g}{2} \sigma_h - \frac{\xi_h\left(\mathbf{x}\right)}{\sigma_h}\right), \\ \mathbb{G}_h\left(\mathbf{x}\right) &= \int \mathrm{d}\sigma_h \, \sigma_h^2 \exp\left(-\beta \frac{g}{2} \sigma_h - \frac{\xi_h\left(\mathbf{x}\right)}{\sigma_h}\right), \end{aligned} \tag{109}$$

where $\xi_h\left(\mathbf{x}\right)$ a function related to $\bar{h}\left(\mathbf{x}\right)$ through $\bar{h} = \int \mathrm{d}\sigma_h \, \sigma_h \rho_h$.

A fourth result of Appendix 3 is the expression of the pdf of the potential vorticity field:

$$\begin{aligned} \rho_q\left(\mathbf{x}, \sigma_q\right) &= \frac{1}{\mathbb{G}_q\left(\beta \Psi_{mf}\right)} \exp\left(\beta \Psi_{mf} \sigma_q - \sum_{k=1}^{+\infty} \alpha_k \sigma_q^k\right), \\ \mathbb{G}_q\left(\beta \Psi_{mf}\right) &= \int \mathrm{d}\sigma_q \, \exp\left(\beta \Psi_{mf} \sigma_q - \sum_{k=1}^{+\infty} \alpha_k \sigma_q^k\right), \end{aligned} \tag{110}$$

where $\Psi_{mf}\left[\overline{h}, \overline{q}, \overline{\mu}\right]$ is the mass transport streamfunction of the mean flow defined through an Helmholtz decomposition of $\overline{h}\mathbf{u}_{mf}$:

$$\overline{h}\mathbf{u}_{mf} = \nabla^{\perp}\Psi_{mf} + \nabla\Phi_{mf}. \tag{111}$$

According to Eq. (110), the coarse-grained potential vorticity field is a function of the mass transport streamfunction:

$$\overline{q} = \frac{\mathbb{G}_q'(\beta\Psi_{mf})}{\mathbb{G}_q(\beta\Psi_{mf})}. \tag{112}$$

A fifth result of Appendix 3 is that the mass transport potential of the mean flow defined in Eq. (111) vanishes:

$$\Phi_{mf} = 0, \tag{113}$$

and the velocity field can now be written

$$\mathbf{u}_{mf} = \frac{1}{\overline{h}} \nabla^{\perp}\Psi_{mf}. \tag{114}$$

A sixth result of Appendix 3 concerns the Bernoulli function of the mean flow defined as

$$B_{mf} = \frac{1}{2}\mathbf{u}_{mf}^2 + g\left(\overline{h} + h_b - 1\right). \tag{115}$$

According to Eq. (218), combining Eq. (216) and Eq. (217) of Appendix 3 allows to express B_{mf} in terms of β, $\mathbb{G}_q$, $\mathbb{G}_h$ and a constant A_0 that can be computed in principle using the conservation of the total mass $\mathscr{Z}_0 = 1$:

$$B_{mf} = \beta^{-1} \log\left(\mathbb{G}_q \mathbb{G}_h\right) + g\overline{h} + A_0. \tag{116}$$

4.1.2 Equation for the Large Scale Flow

Let us now establish the equations allowing to compute the large scale flow. A first equation is obtained by injecting the expression for the mean flow $\mathbf{u}_{mf}$ given in Eq. (114) into the expression of the Bernoulli function defined in Eq. (115), and by combining Eq. (115) with Eq. (116):

$$\frac{1}{2}\frac{1}{\overline{h}^2}\left(\nabla\Psi_{mf}\right)^2 + gh_b = \frac{1}{\beta}\log\left(\mathbb{G}_q\mathbb{G}_h\right) + A_1, \tag{117}$$

with $A_1 = A_0 + g$. A second equation is obtained by taking first the curl of Eq. (91), which yields $\overline{hq} - f = \nabla^{\perp}\mathbf{u}_{mf}$. Then, replacing $\mathbf{u}_{mf}$ by its expression given in Eq. (114), remembering that the potential vorticity field and the height field of the critical points of the variational problem are decorrelated ($\overline{qh} = \overline{h}\,\overline{q}$), and replacing $\overline{q}$ by its expression given in Eq. (112) yields

$$\overline{h}\frac{\mathbb{G}_q'\left(\beta\Psi_{mf}\right)}{\mathbb{G}_q\left(\beta\Psi_{mf}\right)} - f = \nabla\left(\frac{\nabla\Psi_{mf}}{\overline{h}}\right). \tag{118}$$

The closed system of partial differential equations (117) and (118) must be solved for $\overline{h}$ and Ψ_{mf} for a given value of β, $\mathbb{G}_q$, $\mathbb{G}_h$, and A_1. The set of parameters β, $\{\alpha_k\}_{k\geq 1}$, A_1 must *in fine* be expressed in terms of the constraints of the problem given by the energy E, and the potential vorticity moments $\{Z_k\}_{k\geq 0}$. This may require a numerical resolution in the general case.

We have seen in Sect. 2.2 that a flow described by $(h, \mathbf{u})$ (or equivalently by (h, q, μ), or by (h, Φ, Ψ)) is a stationary state of the shallow water model if and only if $J(q, \Psi) = 0$ and $\Phi = 0$.

According to Eqs. (112) and (113), the large scale flow $\left(\overline{h}, \mathbf{u}_{mf}\right)$ is a stationary state of the shallow water model.

4.1.3 Comparison with Previous Results

The set of equations (117) and (118) describing the large scale flow is similar to the one obtained by Weichman and Petrich [56] (through a Kac-Hubbard-Stratonovich transformation) and by Chavanis and Sommeria [7] (through a phenomenological generalization of the Miller–Robert–Sommeria theory), excepted that the rhs of Eq. (117) contains an additional term $\frac{1}{\beta}\log\left(\mathbb{G}_h\right) + A_1$ which does not appear in these previous works. The reason for the presence of this additional term is that we have taken into account the presence of small scale fluctuations of height and velocity, which were neglected in Refs. [7,56]. We will see in Sect. 4.3 that this additional term becomes negligible with respect to the others in the quasi-geostrophic limit, in which case we recover exactly the set of equations for the large scale flow obtained in Refs. [7,56].

In addition, we have shown in Sect. 4.1.1 that only positive temperature states are allowed, which shows that only one subclass of the states described by Eqs. (117) and (118) are actual equilibrium states.

4.2 Equipartition and Decoupling in the Limit of Weak Local Height Fluctuations

We consider in this section the limit of weak local height fluctuations. This step makes possible computation of explicit solutions of the variational problem (100). Meanwhile, it

allows to explore the consequence of the presence of these small scale fluctuations on the structure of the large scale flow. By "limit of weak local height fluctuations", we mean

$$\forall \mathbf{x} \in \mathscr{D}, \quad \left(\overline{h^2} - \overline{h}^2\right)^{1/2} \ll \overline{h}. \tag{119}$$

As already argued in [56], this limit of weak local fluctuations is physically relevant, since the presence of shocks in the actual dynamics tends to dissipate small scale fluctuations of height or kinetic energy. This will be further discussed in Sect. 5.2.

4.2.1 The Height Distribution

Assuming in addition that height levels σ_h such that $\left|\sigma_h - \overline{h}\right| \gg \left(\overline{h^2} - \overline{h}^2\right)^{1/2}$ do not contribute significantly to the pdf ρ_h defined in Eq. (109), we perform an asymptotic development with $\left(\sigma_h/\overline{h} - 1\right) \ll 1$, and obtain at lowest order in this small parameter a Gaussian shape for the pdf:

$$\rho_h\left(\mathbf{x}, \sigma_h\right) = \sqrt{\frac{g\beta}{2\pi \overline{h}\left(\mathbf{x}\right)}} \exp\left(-\frac{g\beta}{2\overline{h}\left(\mathbf{x}\right)}\left(\sigma_h - \overline{h}\left(\mathbf{x}\right)\right)^2\right). \tag{120}$$

Similarly, the term $\mathbb{G}_h$ defined in Eq. (109) can be computed explicitly in this limit. One gets at lowest order

$$\mathbb{G}_h = \overline{h}^2\left(\mathbf{x}\right) \sqrt{\frac{2\pi \overline{h}\left(\mathbf{x}\right)}{g\beta}} \exp\left(-g\beta \overline{h}\left(\mathbf{x}\right)\right). \tag{121}$$

Using Eq. (120), the weak local height fluctuation limit given in Eq. (119) can be interpreted as a low temperature limit $g\overline{h} \gg 1/\beta$. Injecting Eq. (121) in the previously established relation in Eq. (116) yields

$$B_{mf} = \frac{1}{\beta} \log \mathbb{G}_q + \frac{5}{2\beta} \log \overline{h} + A_2, \tag{122}$$

where A_2 is a free parameter determined by the conservation of the total volume. In the rhs of Eq. (122), there remains an additional term $\frac{5}{2\beta} \log \overline{h}$ which is not present in the large scale flow equation obtained by [7,56], but considering the weak flow limit allowed to obtain an explicit expression for this additional term. We will see in Sect. 4.3 that this term becomes negligible with respect to $\frac{1}{\beta} \log \mathbb{G}_q$ in the quasi-geostrophic limit.

4.2.2 Equipartition and the Limit of Weak Small Scale Energy

Injecting Eq. (120) in the expression of the small scale potential energy defined in Eq. (96) yields

$$\mathscr{E}_{\delta h} = \frac{1}{2\beta}. \tag{123}$$

Comparing this result with Eq. (108) shows equipartition of the small scale energy between the potential energy and the kinetic energy. The total energy due to small scale fluctuations is

$$E_{fluct} \equiv \mathscr{E}_{\delta h} + \mathscr{E}_{\delta \mu} = \frac{1}{\beta}. \tag{124}$$

This equipartition result of the small scale energy was already obtained by Warn when computing equilibrium states of the Galerking truncated dynamics in a weak flow limit [53]. More precisely, Warn decomposed the dynamics into vortical modes and inertia-gravity modes (which are defined as the eigenmodes of the linearized dynamics), and concluded that the energy of the equilibrium state should be equipartitioned among inertia-gravity modes in the limit of infinite wavenumber cut-off. This equipartition of energy among inertia-gravity modes would lead to equipartition between potential and kinetic energy at small scales, just as in our case. Here we have recovered this result with a different approach and we have generalized it beyond the weak flow limit.

Finally, we remark that the equipartition result of Eq. (124) shows that the low temperature limit $g\overline{h} \gg 1/\beta$ corresponds to a limit of weak small scale energy due to local fluctuation of the height field and of the divergent field:

$$g\overline{h} \gg E_{fluct}. \tag{125}$$

4.2.3 Decoupling Between the Large Scale Flow and the Fluctuations

Still by considering the weak local height fluctuation limit, let us assume that E_{fluct} defined in Eq. (124) is given, which means that the temperature is given. According to Eq. (118) and Eq. (117), knowing the coarse-grained height field $\overline{h}$ and the pdf of potential vorticity levels $\rho_q(\mathbf{x}, \sigma_q)$ (which allows to compute $\mathbb{G}_q$) is sufficient to determine the mass transport streamfunction Ψ_{mf}, and hence the velocity $\mathbf{u}_{mf}$ by using Eq. (114). Then the mean-flow energy defined in Eq. (94) does not depend on ρ_μ:

$$\mathscr{E}_{mf}\left[\overline{h}, \rho_q\right] = \frac{1}{2}\int \mathrm{d}\mathbf{x}\left[\overline{h}\mathbf{u}_{mf}^2\left[\overline{h}, \overline{q}\right] + g\left(\overline{h} + h_b - 1\right)^2\right]. \tag{126}$$

The total energy defined in Eq. (97) is therefore the sum of the mean-field energy associated with a large scale flow that depends only on $\overline{h}$ and ρ_q, and of the energy of small scale fluctuations associated with height and divergence fluctuations:

$$\mathscr{E} = \mathscr{E}_{mf}\left[\overline{h}, \rho_q\right] + E_{fluct}. \tag{127}$$

In addition, injecting Eq. (105) in Eq. (92) gives the expression of the potential vorticity moments as a functional of $\overline{h}$ and ρ_q only:

$$\forall k \in \mathbb{N} \quad \mathscr{Z}_k\left[\overline{h}, \rho_q\right] = \int \mathrm{d}\mathbf{x}\mathrm{d}\sigma_q\ \overline{h}\rho_q\sigma_q^k. \tag{128}$$

Let us now consider the macrostate entropy functional defined in Eq. (89). Injecting Eqs. (106) and (120) in Eq. (105), and performing the asymptotic expansion of the integrand of the mean-field entropy with $\left(\sigma_h/\overline{h} - 1\right) \ll 1$ leads at lowest order to (up to a irrelevant constant)

$$\mathscr{S} = \mathscr{S}_{mf}\left[\overline{h}, \rho_q\right] + S_{fluct}\left(E_{fluc}\right), \tag{129}$$

$$\mathscr{S}_{mf}\left[\overline{h}, \rho_q\right] \equiv -\int \mathrm{d}\mathbf{x}\mathrm{d}\sigma_q\ \overline{h}\rho_q \log\frac{\rho_q}{\overline{h}^{5/2}}, \tag{130}$$

$$S_{fluct}\left(E_{fluct}\right) \equiv \log\left(E_{fluct}\right). \tag{131}$$

Since ρ_q and $\overline{h}$ are two fields allowing to compute the large scale flow of energy $\mathscr{E}_{mf}$, and since the fluctuations of the potential vorticity field do not contribute to the small scale energy

E_{fluct}, the entropy $\mathscr{S}_{mf}\left[\overline{h},\rho_q\right]$ will be referred to as the macrostate entropy of the large scale flow.

The second contribution to the total entropy in Eq. (129) depends only on the energy of the small scale fluctuations E_{fluct}. Since this energy is solely due to the local variance of the height field and of the divergent field, it will be referred to as the entropy of the small scale fluctuations. Note that in that case the height field is involved both in the large scale flow through its local mean value, and in the small scale fluctuations through its local variance.

The decoupling of the energy and the macrostate entropy functional into a part that depends only on ρ_q, $\overline{h}$ and another part that depends only on small scale height and divergent fluctuations with energy E_{fluct} has both a useful practical consequence and an interesting physical interpretation. The variational problem in Eq. (100) can now be recast into two simpler variational problems:

$$S\left(E,\{Z_k\}_{k\geq 0}\right)=\max_{E_{fluct}}\left\{S_{mf}\left(E-E_{fluct},\{Z_k\}_{k\geq 0}\right)+S_{fluct}\left(E_{fluct}\right)\right\}, \tag{132}$$

$$S_{mf}\left(E_{mf},\{Z_k\}_{k\geq 0}\right)=\max_{\rho_q,\int\rho_q=1,\overline{h}}\left\{\mathscr{S}_{mf}\left[\overline{h},\rho_q\right]\,\middle|\,\mathscr{E}_{mf}\left[\overline{h},\rho_q,\right]=E_{mf},\ \forall k\in\mathbb{N}\quad\mathscr{Z}_k\left[\rho_q,\overline{h}\right]=Z_k\right\}, \tag{133}$$

where $\mathscr{S}_{mf}$, $\mathscr{E}_{mf}$ and $\mathscr{Z}_k$ are the functional defined in Eqs. (130), (126), and (128), respectively. The variational problem in Eq. (132) describes two subsystems in thermal contact. In order to compute the equilibrium state, one can then compute independently the equilibrium state of each subsystem, and then equating their temperature in order to find the global equilibrium state. This classical argument follows directly from the maximization of (132). If the two subsystems can not have the same temperature (for instance when the temperature of both subsystem have a different sign), all the energy is stored in the subsystem with positive temperature in order to maximize the global entropy.

In the present case, a first subsystem is given by the large scale flow of energy E_{mf}, which involves the field $\overline{h}$ and the potential vorticity field described by the pdf of vorticity levels ρ_q. The equilibrium state of this subsystem is obtained by solving the variational problem in Eq. (133). This variational problem corresponds to the one introduced by [7] except that large scale flow energy is not the total energy but only the available energy when the energy of the fluctuations has been removed. The entropy of the large scale flow (130) in the variational problem (133) is closely related to the entropy introduced in [7] (up to a functional of $\overline{h}$). The potential vorticity moment constraints apply only to this subsystem. These additional constraints are essential since they allow for the possible existence of a large scale flow, see e.g. [4].

The second subsystem is given by the local small scale height fluctuations and the local small scale divergent fluctuations with total energy E_{fluct}, and with the entropy given in Eq. (131). The inverse temperature of this subsystem $\beta=\mathrm{d}S_{fluct}/\mathrm{d}E_{fluct}$, which, using Eq. (131), yields a temperature of $\beta^{-1}=E_{fluct}$.

In practice, it is easier to compute directly equilibrium states of the large scale flow subsystem in the canonical ensemble, where the energy constraint is relaxed. In that case the equilibrium states of this subsystem depend on the temperature E_{fluct} and on the dynamical invariants $\{Z_k\}_{k\geq 0}$. One just need to check a posteriori that this ensemble is equivalent to the microcanonical one by verifying that each admissible energy E_{mf} is reached when varying E_{fluct} form 0 to $+\infty$, for a given set of potential vorticity moments $\{Z_k\}_{k\geq 0}$. In order to find the actual equilibrium state associated with the total energy E, one then needs to solve the equation

$$E = E_{mf}\left(E_{fluct}, \{Z_k\}_{k\geq 0}\right) + E_{fluct}. \tag{134}$$

To conclude, it is now possible to study independently the large scale flow subsystem, to consider if necessary any approximation on this flow, such as the quasi-geostrophic limit or the Euler 2D limit, and finally to couple this subsystem with the small scale height and divergence fluctuations subsystem in order to select the actual equilibrium state. If one linearize the large scale flow entropy entropy (130) and the large scale flow energy (126), this picture of two subsystems in thermal contact gives a justification to the variational problem introduced by [45] and extended by [25]. [25,45] suggest that for a given frozen in space potential vorticity, the dynamics should relax through geostrophic adjustment to a state minimizing the total energy. This result is recovered from the coupled variational problem (132).

4.2.4 Either a Non-zero Circulation or a Non-zero Bottom Topography is Required to Sustain a Large Scale Flow at Equilibrium

It is shown in Appendix 4 that when circulation is zero (i.e. when $Z_1 = f$) and when topography is zero ($h_b = 0$), a state with a large scale flow at rest ($\mathbf{u}_{mf} = 0$) is a maximizer of the large scale flow macrostate entropy among all the possible energies:

$$S(0, \{Z_k\}_{k\geq 0}) = \max_{E_{mf}} \left\{S_{mf}\left(E_{mf}, \{Z_k\}_{k\geq 0}\right)\right\} \quad \text{when} \quad Z_1 = f \text{ and } h_b = 0. \tag{135}$$

According to Eq. (131), the fluctuation entropy S_{fluct} increases with the fluctuation energy E_{fluct}. The total macroscopic entropy $S_{mf}\left(E - E_{fluct}, \{Z_k\}_{k\geq 0}\right) + S_{fluct}\left(E_{fluct}\right)$ is therefore maximal when all the energy is transferred into fluctuations ($E_{fluct} = E$). This generalizes to a wider range of flow parameters and to a wider set of flow geometries a result previously obtained by Warn in a weak flow limit for a doubly periodic domain without bottom topography [53]. In addition, we will see in the next section that when there is a non-zero bottom topography and rotation, a large scale flow can be sustained at equilibrium.

4.3 The Quasi-geostrophic Limit

We show in this section that the variational problem of the Miller Robert Sommeria theory is recovered from Eq. (133) for the large scale flow subsystem when considering the quasi-geostrophic limit, which applies to strongly rotating and strongly stratified flows.

4.3.1 Geostrophic Balance

Let $E_{mf}^{1/2}$ be the typical velocity of the large-scale flow and let $L = \sqrt{|\mathscr{D}|}$ be the typical horizontal scale of the domain where the flow takes place. We introduce the Rossby number and the Rossby radius of deformation respectively defined as

$$Ro \equiv \frac{E_{mf}^{1/2}}{fL}, \quad R \equiv \frac{\sqrt{gH}}{f}. \tag{136}$$

Here f is the Coriolis parameter, $H = 1$ is the mean depth and g the gravity, see Sect. 2.1. If $f \neq 0$ we can always rescale time unit so that $f = 1$, and we make this choice in the following. It is also assumed that the aspect ratio of the domain where the flow takes place is of order one, so that $L = 1$ since we chose length unit so that $|\mathscr{D}| = 1$. The quasi-geostrophic

limit corresponds to small Rossby number, and to a Rossby radius of deformation that is not significantly larger than the domain length scale:

$$Ro \ll 1, \quad R^{-1} = \mathcal{O}(1). \tag{137}$$

By construction, the mean flow is of the order of the Rossby number: $|\mathbf{u}_{mf}| \sim Ro$. The coarse-grained interface height is given by

$$\overline{\eta} = \overline{h} - 1 + h_b. \tag{138}$$

Let us assume that the spatial variations in fluid depth are small compared to the total depth $H = 1$, with the scaling $\overline{\eta} \sim R^{-2} Ro$. At lowest order in Ro, the mean flow Bernoulli potential defined in Eq. (115) becomes $B_{mf} = R^2 \overline{\eta}$. Remembering that we consider in addition to the quasi-geostrophic limit a weak fluctuation limit given by Eq. (125), which can be expressed as $R^2 \gg \beta^{-1}$, Eq. (122) yields at lowest order

$$B_{mf} = R^2 \overline{\eta} = \beta^{-1} \log \mathbb{G}_q + cst. \tag{139}$$

This equation implies $\mathrm{d}B_{mf}/\mathrm{d}\Psi_{mf} = \overline{q}$, consistently with what we expected for a stationary flow in the absence of small scale fluctuations, see Sect. 2.2. Taking the curl of Eq. (139) and collecting the lowest order terms yields geostrophic balance[10]

$$R^2 \nabla^\perp \overline{\eta} = \mathbf{u}_{mf}. \tag{140}$$

Equation (140) also shows that the scaling hypothesis for $\overline{\eta}$ is self-consistent.

It is remarkable that equilibrium statistical mechanics predicts the emergence of geostrophic balance. We stress that those results, which have been obtained through the introduction of a semi-Lagrangian discrete model, are valid whatever the amplitude of bottom topography variations (i.e. beyond the usual approximation $h_b \sim Ro$ required to derive the quasi-geostrophic dynamics). By contrast, in the framework of a Eulerian discrete model, one would find that the large scale flow is not at geostrophic equilibrium unless $h_b \sim Ro$ or $h_b \ll Ro$, see Appendix 5.

4.3.2 Quasi-geostrophic Dynamics

The geostrophic balance is not a dynamical equation. When $h_b \sim Ro$, the dynamics if given by the quasi-geostrophic equations. At lowest order in Ro, we get $\overline{h}\mathbf{u}_{mf} = \mathbf{u}_{mf}$, and

$$\psi_{mf} = \Psi_{mf}, \quad \phi_{mf} = \Phi_{mf} = 0. \tag{141}$$

where Ψ_{mf} and ψ_{mf} are the transport streamfunction and the streamfunction obtained through the Helmholtz decomposition of $\overline{h}\mathbf{u}_{mf}$ and $\mathbf{u}_{mf}$, respectively. In that case, the relative vorticity is

$$\overline{\omega} = \Delta \psi_{mf}. \tag{142}$$

The geostrophic balance (140) is equivalent to $\overline{\eta} = R^{-2}\psi_{mf} + C$. The value of ψ_{mf} at the domain boundary can always be chosen such that the constant term vanishes, which yields

$$\overline{\eta} = \frac{\psi_{mf}}{R^2}. \tag{143}$$

[10] For the shallow water model, the fluid is at hydrostatic balance. Thus the pressure in the fluid is $P(x, y, z, t) = P_o + \rho g(H + \eta(x, y, t) - z)$. Then the pressure horizontal gradient is simply proportional to the interface height horizontal gradient. Hence, the geostrophic balance simply writes $R^2 \nabla^\perp \overline{\eta} = \mathbf{u}_{mf}$.

Mass conservation given in Eq. (2) leads then to the following constraint on the streamfunction:

$$\int \mathrm{d}\mathbf{x}\ \psi_{mf} = 0. \tag{144}$$

Given a potential vorticity level σ_q, a change of variable can be performed by introducing quasi-geostrophic potential vorticity levels[11]

$$\sigma_g \equiv \left(\sigma_q - 1\right). \tag{145}$$

The pdf of quasi-geostrophic levels is

$$\rho_g\left(\mathbf{x}, \sigma_g\right) = \rho_q\left(\mathbf{x}, 1 + \sigma_g\right). \tag{146}$$

The local quasi-geostrophic potential vorticity moments are defined as

$$\forall k \in \mathbb{N},\ \overline{q_g^k} \equiv \int \mathrm{d}\sigma_g\ \sigma_g^k \rho_g. \tag{147}$$

At lowest order in Ro, the coarse-grained quasi-geostrophic potential vorticity obtained by considering $k = 1$ in Eq. (147) becomes

$$\overline{q}_g = \overline{\omega} - \overline{\eta} + h_b. \tag{148}$$

which, using Eqs. (142) and (143), yields

$$\overline{q}_g = \Delta\psi_{mf} - \frac{\psi_{mf}}{R^2} + h_b\ . \tag{149}$$

In the quasi-geostrophic limit, the large scale flow is fully described by the streamfunction ψ_{mf}, which can be obtained by inverting the coarse-grained potential vorticity field defined in Eq. (149).

4.3.3 Quasi-geostrophic Constraints and Variational Problem

At lowest order in Ro, and after an integration by part, the expression of the mean-flow energy in Eq. (126) is equal to the quasi-geostrophic energy:

$$\mathscr{E}_{mf,g}\left[\overline{q}_g\right] \equiv \frac{1}{2}\int \mathrm{d}\mathbf{x}\ \left[\left(\nabla\psi_{mf}\right)^2 + \frac{\psi_{mf}^2}{R^2}\right], \tag{150}$$

where ψ_{mf} can be expressed in terms of $\overline{q}_g$ through Eq. (149). Similarly, the conservation of the potential vorticity moments defined in Eq. (128) implies the conservation of quasi-geostrophic potential vorticity moments

$$\forall k \in \mathbb{N},\quad \mathscr{Z}_{g,k} \equiv \int \mathrm{d}\mathbf{x}\ \overline{q_g^k}, \tag{151}$$

and the macrostate entropy of the large scale flow defined in Eq. (130) writes now

$$\mathscr{S}_{mf,g}\left[\rho_g\right] = -\int \mathrm{d}\mathbf{x}\mathrm{d}\sigma_q\ \rho_g \log \rho_g. \tag{152}$$

[11] This change of variable is a guess guided by the fact that the QG potential vorticity is usually obtained by expanding the SW potential vorticity in the limit of small height variations minus a constant and unimportant term. Here we start by removing the unimportant constant (1 in our unit system) from the potential vorticity levels, and then perform the small scale expansion in height.

Using Eq. (150)–(152), the variational problem in Eq. (133) is now recast into a simpler variational problem on the pdf ρ_g:

$$S_{mf,g}\left(E_{mf}, \{Z_k\}_{k\geq 1}\right) = \max_{\rho_g, \int \rho_g = 1} \left\{ \mathscr{S}_{mf,g}\left[\rho_g\right] \,\middle|\, \mathscr{E}_{mf,g}\left[\rho_g\right] = E_{mf},\ \forall k \in \mathbb{N} \quad \mathscr{Z}_{g,k}\left[\rho_g\right] = Z_k \right\}. \tag{153}$$

The entropy $\mathscr{S}_{mf,g}$, the energy $\mathscr{E}_{mf,g}$ and the potential vorticity moments $\left\{\mathscr{Z}_{g,k}\right\}_{k\geq 1}$ are defined in Eqs. (152), (150) and (151). The variational problem defined in Eq. (153) is the variational problem of the Miller–Robert–Sommeria statistical mechanics [22,33].

4.3.4 Maximum Energy States and Consistency of the Quasi-geostrophic Approximation

We have shown that in the weak height fluctuation limit and the quasi-geostrophic limit, computation of the large scale flow associated with the equilibrium state amounts to the computation of the solution of the variational problem in Eq. (153), with the restriction that the temperature is positive (due to the coupling with small scale fluctuations of height and divergence, as discussed in Sect. 4.1.1). Here we discuss the solutions of this variational problem, which are energy maxima for a given set of potential vorticity moments $\left\{\mathscr{Z}_{g,k}\right\}_{k\geq 1}$. Although the initial weak fluctuation or quasi-geostrophic limit may not be fulfilled for such states, they can always be computed, and it provides an upper bound for the energy of the large scale flow obtained in those limits.

It is known that for positive temperatures ($\beta^{-1} = E_{fluct} > 0$), the equilibrium entropy defined in Eq. (153) is concave [4], and the energy increases when β decreases. This means that the state with a maximum energy is reached when $\beta \to 0$, see e.g. [33].

Injecting $\beta = 0$ in the expression of ρ_q in Eq. (110) leads to a uniform mean potential vorticity field. According to Eq. (146) and (147), this implies that the quasi-geostrophic potential vorticity field is also uniform: $\overline{q}_g = Z_{g,1}$ where $Z_{g,1} = \int \mathrm{d}\mathbf{x}\, \overline{q}_g$ is the circulation. Since $\overline{q}_g$ is a constant, this state is referred to as the "mixed" state. We get

$$\Delta \psi_{mix} - \frac{\psi_{mix}}{R^2} = Z_{g,1} - h_b. \tag{154}$$

Let us call E_{mix} the energy of the mixed state:

$$E_{mix} \equiv \max_{\rho_g, \int \rho_g = 1} \left\{ \mathscr{E}_{mf} | \forall k \in \mathbb{N} \quad \mathscr{Z}_{g,k} = Z_{g,k} \right\}. \tag{155}$$

Using Eq. (150), it can formally be written

$$E_{mix} = -\frac{1}{2} \int \left(Z_{g,1} - h_b\right) \left(\Delta - \frac{1}{R^2}\right)^{-1} \left(Z_{g,1} - h_b\right). \tag{156}$$

For a given domain geometry, a given circulation $Z_{g,1}$ and a given bottom topography field h_b, a non trivial large scale flow can be observed whenever $E_{mix} > 0$. We see from Eq. (156) and (155) that the condition for a large scale flow to exist is that either the circulation $Z_{g,1}$ is non zero or the bottom topography h_b is non-zero. If both $Z_{g,1} = 0$ and $h_b = 0$, then the energy of the large scale flow vanishes ($E_{mf} = 0$), and all the energy is lost in small scale fluctuations ($E = E_{fluct}$), consistently with the results of Sect. 4.2.4. In this case, coupling thermally a large scale flow with fluctuations leads to a state with all the energy lost in fluctuations. Note that in the case $Z_{g,1} = 0$ $R \sim 1$, E_{mix} can also be interpreted as a norm of the topography field h_b.

Since $E_{mf} \leq E_{mix}$, and since E_{mix} depends only on the problem parameters (namely the circulation, the Rossby radius and the bottom topography), a sufficient condition to have $Ro \ll 1$ is

$$E_{mix}^{1/2} \ll 1. \tag{157}$$

If this condition is fulfilled, the quasi-geostrophic assumption is self-consistent (as well as for the scaling $h_b \sim Ro$ in the case $Z_{g,1} = 0$).

5 Explicit Computation of Phase Diagrams and Discussion

The aim of this section is to apply the results of the previous section to the actual computation of equilibria and their energy partition. In order to solve analytically the variational problem of the statistical mechanics theory, we focus on a subclass of equilibria referred to as the energy–enstrophy equilibrium states. This allows to build phase diagrams in a two parameter space, and to discuss the energy partition between a large scale flow and small scale fluctuations when these parameters are varied. We finally discuss the role of shocks that occur in the actual shallow water dynamics, and present a geophysical application to the Zapiola anticyclone.

5.1 Energy–enstrophy Equilibria for the Quasi-geostrophic Model

We consider the variational problem

$$\begin{aligned} &S_{g,mf}\left(E, Z_2\right) \\ &\quad = \max_{\rho_g, \int \rho_g = 1} \left\{ \mathscr{S}_{mf,g}\left[\rho_g\right] \mid \mathscr{E}_{mf,g}\left[\rho_g\right] = E_{mf},\ \mathscr{Z}_{g2}\left[\rho_g\right] = Z_2,\ \mathscr{Z}_{g1}\left[\rho_g\right] = 0 \right\}, \end{aligned} \tag{158}$$

where the functionals $\mathscr{S}_{mf,g}, \mathscr{E}_{mf,g}, \mathscr{Z}_{g1,2}$ are defined in Eqs. (152), (150), and (151), respectively.

The peculiarity of this variational problem is that only two potential vorticity moments (the circulation and the enstrophy) have been retained as a constraint, in addition to the energy. Such energy–enstrophy equilibria are a subclass of statistical equilibria solutions of the more general variational problem given in Eq. (153), see e.g. [1,26]. For a given global distribution of potential vorticity, several limit cases on the energy allow to simplify the computation of the solutions of the variational problem in Eq. (153) into the computation of the simpler variational problem in Eq. (158). For instance, assuming that bottom topography is non zero, and that the global potential distribution is such that the mixed state $\overline{q} = cst$ exists, the solutions of (158) are the solutions of the more general variational problem Eq. (153) when $E \to E_{mix}$.

The set of all potential vorticity fields $\overline{q}$ corresponding to solutions of the variational problem in Eq. (158) have been previously described by [6,26,49,51] in the case of a bounded geometry, and phase diagrams were obtained with energy E and circulation Z_1 as external parameters. The role of enstrophy Z_2 was not discussed. The main reason is that for a given large scale flow characterized by E_1 and Z_1, changing Z_2 would only imply changes in the small scale fluctuations of potential vorticity levels, see e.g. [26], and such small scale fluctuations do not contribute to the total energy. In the present case, Z_2 will play an important role in determining the energy partition between the large scale (vortical) flow and small scale fluctuations due to the height and divergent velocity field. For the sake of simplicity we consider vanishing circulations $Z_1 = 0$.

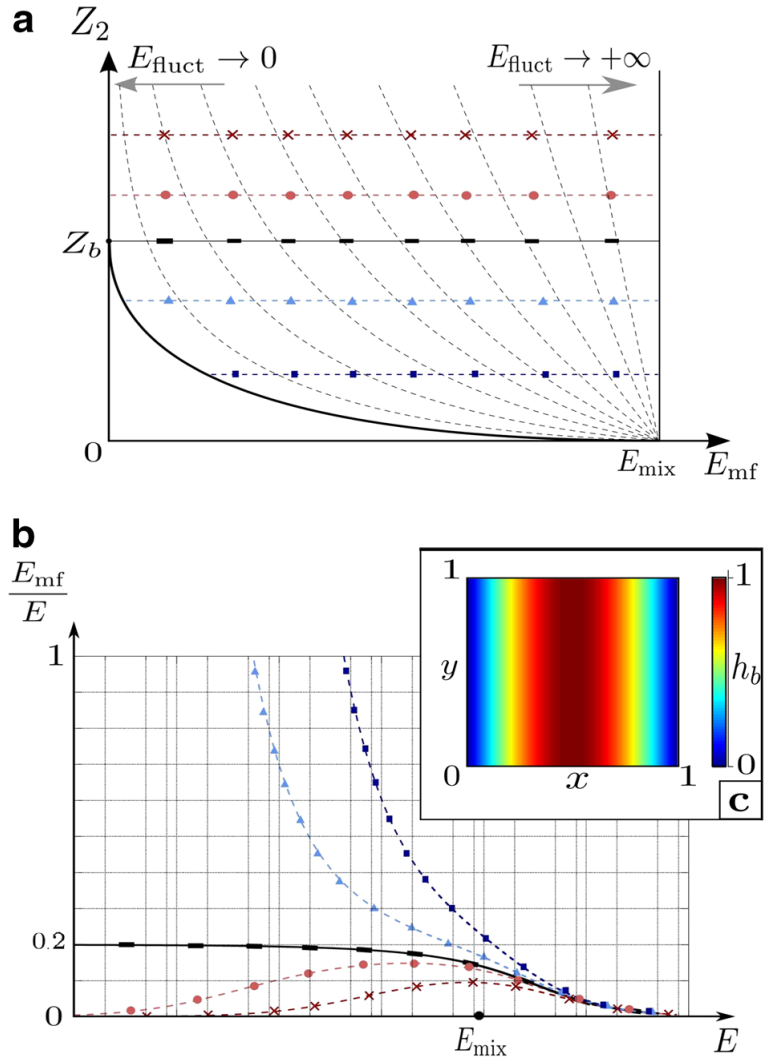

Fig. 2 **a** Phase diagram of the energy–enstrophy ensemble in the plane (Z_2, E_{mf}). Z_b is the maximum reachable value for the macroscopic enstrophy defined in Eq. (159). E_{mix} is the maximum reachable energy for the mean-flow defined in Eq. (155). The dashed lines corresponds to isotherms, on which the energy E_{fluct} of the small scale fluctuations is constant. The thick black line on the bottom left corner is a boundary below which no equilibria exist. **b** Ratio between the energy of the large scale flow E_{mf} over the total energy E_{mf}/E as a function of the total energy $E = E_{mf} + E_{fluct}$. The different curves correspond to different values of the initial microscopic enstrophy Z_2 represented by *horizontal marked lines* on **a**. The x-axis is on a logarithmic scale. c) Colormap plot of the bottom topography h_b used to compute the phase diagram in Fig. 2a, b and 3. Here, $h_b = \sin(\pi x)$ is a single mode of the Laplacian operator. Thus the stream function ψ and the potential vorticity field q_g are simply proportional to h_b for any values of the initial enstrophy Z_2 and the initial energy E

The problem (158) is solved in Appendix 6 for positive temperature states, and we present here the main results. A typical phase diagram is shown on Fig. 2. This figure is obtained by assuming that the bottom topography is proportional to the first Laplacian eigenmode (see Fig. 2-c) but it is explained in Appendix 6 that this phase diagram is generic to any bottom topography.[12]

[12] For such a bottom topography, the topography, the stream function and the potential vorticity field are all proportional to each other for any initial condition for the enstrophy Z_2 and the energy E. That is why we do not show plots of the flows for different point of the phase diagram in Fig. 2. We rather choose to consider the case of the Zapiola drift in Sect. 5.3 to see the effect of different value for the initial energy.

There are two important quantities related to the height field: the maximum allowed energy E_{mix} defined in Eq. (156), and the available potential enstrophy

$$Z_b \equiv \int \mathrm{d}\mathbf{x}\, h_b^2, \tag{159}$$

which is the maximum reachable value for the macroscopic enstrophy $\int \mathrm{d}\mathbf{x}\overline{q_g}^2$, see Appendix 6. Both Z_b and E_{mix} are a norm for the height field.

The phase diagram of the quasi-geostrophic energy–enstrophy ensemble restricted to positive temperature states is presented in Fig. 2a. As explained in Sect. 4.3, the energy of the large scale flow E_{mf} can not exceed the value E_{mix} defined in Eq. (155), due the restriction of positive temperature states. Depending on the sign of $Z_2 - Z_b$, where the potential enstrophy Z_b is defined in Eq. (159), the system behaves differently:

- When $Z_2 > Z_b$ the minimum admissible large scale flow energy is zero.
- When $Z_2 < Z_b$, there exists a minimum reachable large scale flow energy $E_{min}(Z_2)$ below which there is no equilibria. The curve E_{min} increases from 0 to E_{mix} when Z_2 decreases from Z_b to 0.

The thick black line in Fig. 2a delimits the domain of existence for the equilibria. The thin dashed black curves represent the isotherm, i.e. the points of the diagram with the same value of E_{fluct}. Note that there is no bifurcation in this phase diagram; to each point (E_{mf}, Z_2) corresponds a single equilibrium state, whose expression is given explicitly in Appendix 6. The structure of an equilibrium large scale flow above a topographic bump at low and high energy are presented in the last subsection.

The phase diagram in Fig. 2 allows to discuss the energy partition between small scale fluctuations and large scale flow when the quasi-geostrophic flow is coupled to small scale fluctuations of the height field and divergence field (through the shallow water dynamics). The motivation behind the works of [53] and [56] was the prediction of energy partition between large scale flow and small scale fluctuations. Here we provide for the first time an explicit expression for such energy partition.

We have seen that in the weak height fluctuation limit, the temperature of the large scale flow at equilibrium is given by the energy of the small scale fluctuations of height and divergence fields. The parameters are now the total energy E and enstrophy Z_2. The mean flow energy E_{mf} and the fluctuation energy E_{fluct} are found by solving

$$E = E_{mf}\left(E_{fluct}, Z_2\right) + E_{fluct}, \tag{160}$$

which is easily done graphically using the diagram of Fig. 2a, and performed numerically in practice, see Appendix 6 for more details. The ratio of the large scale energy E_{mf} over the total initial energy E as a function of the total initial energy E is shown on Fig. 2b for different values of initial enstrophy Z_2. According to computations performed in Appendix 6, four cases for the energy partition in the low energy limit are distinguished depending on the sign of $Z_2 - Z_b$ and the scaling of $Z_2 - Z_b$ with E:

- When $Z_2 < Z_b$, the ratio E_{mf}/E tends to 1 when E tends to the minimal admissible energy $E_{min}(Z_2)$.
- When $Z_2 > Z_b$, the ratio E_{mf}/E tends to 0 when E tends to zero.
- When $Z_2 > Z_b$ with $Z_2 - Z_b \sim E^{\alpha}$ with $\alpha > 1/2$, the ratio E_{mf}/E tends to $1/5$ when E tends to zero.
- When $Z_2 > Z_b$ with $Z_2 - Z_b \sim E^{1/2}$, the ratio E_{mf}/E tends to a finite value (depending on the proportionality coefficient between $Z_2 - Z_b$ and $E^{1/2}$ and the bottom topography).

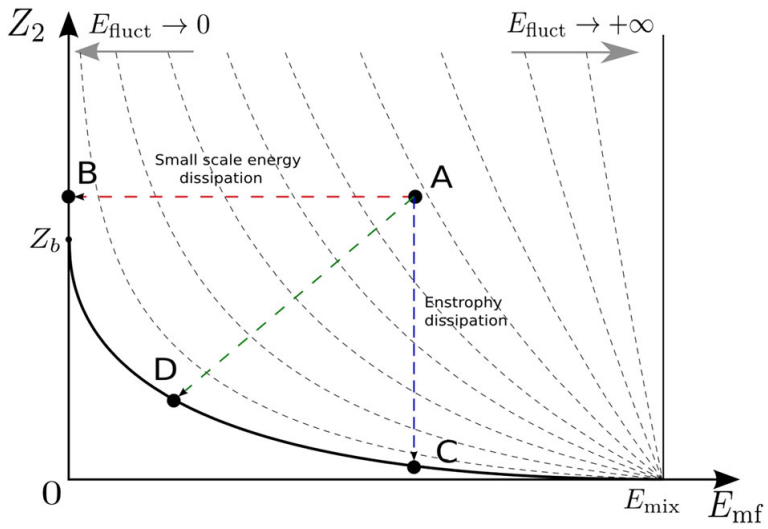

Fig. 3 Phase diagram of Fig. 2a with hypothetical trajectories of the shallow water system in the presence of dissipation. Trajectory A-B: the dynamics dissipates small scale fluctuations of height and divergence field only. Trajectory A-C: the dynamics dissipates small scale fluctuations of potential vorticity. Trajectory A-D: the dynamics dissipates small scale fluctuations of all the fields.

– When $Z_2 > Z_b$ with $Z_2 - Z_b \sim E^\alpha$ with $\alpha < 1/2$, the ratio E_{mf}/E tends to 0.

Whenever $Z_2 \geq Z_b$, we found $E_{fluct} \sim E$. We see on Fig. 2b that the ratio E_{mf}/E converges to one when $E \to E_{min}(Z_2 < Z_b)$, that it converges to zero for $Z_2 > Z_b$, and that it converges to $1/5$ for $Z_b = Z_2$. Note also that E_{mf} is bounded by E_{mix} such that E_{mf}/E tends to zero when E tends to infinity.

5.2 The Effect of Energy Dissipation and Enstrophy Dissipation

The actual shallow water dynamics is known to be characterized by shocks that prevent energy conservation. In addition, the presence of viscosity, no matter how small it is, may lead to enstrophy dissipation, and more generally would break the conservation of potential vorticity moments. The aim of this section is to discuss qualitatively the effect of these dissipative processes on the large scale flow, assuming that the system evolves through a sequence a equilibrium states, which is a natural hypothesis if there exists a separation of time scales.

For the sake of simplicity, let us focus on the phase diagram obtained in the energy–enstrophy ensemble and described in the previous subsection. Let us consider that the system has reached at some time an arbitrary equilibrium state denoted by A in Fig. 3.

Let us first consider a case where energy is conserved, but enstrophy is dissipated. Then the system will evolve form point A to point C of Fig. 3. In other words, the small scale enstrophy Z_2 will be dissipated so that the enstrophy of the system tends to the minimum admissible value of enstrophy $Z_{2\,min}(E_{mf})$. Note that the curve $Z_{2\,min}(E_{mf})$ is nothing but the curve of energy minima for a given $Z_2 < Z_b$. We saw previously that the mean-flow energy E_{mf} dominates the fluctuation energy E_{fluc} on this line. We conclude that enstrophy dissipation alone drives the system towards a large scale flow without small scale fluctuations. This large scale flow vanished when topography vanished (since E_{mix} and Z_b would also vanish).

Let us now consider that the enstrophy is not dissipated and look the effect of energy dissipation. Let us first explain why one may expect that even weak dissipation can lead to a significant decrease of the large scale flow energy E_{mf} when $E_{fluct} \neq 0$ (in the absence of small scale fluctuations, E_{mf} would not decrease significantly with weak dissipation). At

equilibrium, the energy of the small scale fluctuations E_{fluct} should be equipartitioned among all the modes of the height field and divergent field. Since there is an infinite number of such modes, this means a loss of energy through dissipative process, no matter how small they are. Since E_{mf} decreases with E_{fluct}, dissipating the energy E_{fluct} amounts to diminish the energy E_{mf}. For a given enstrophy $Z_2 > Z_b$, as in the case of point A Fig. (3), this dissipative process drives the system towards a zero energy state B. For a given enstrophy $Z_2 < Z_b$, this process would drive the system towards the line of minimal energy.

We expect to see both enstrophy and energy dissipation working together, so the trajectory of the system in phase diagram will be somewhere between the trajectory $A \to B$ and the trajectory $A \to C$, e.g. the trajectory e.g. $A \to D$. We conclude that in the presence of topography and small scale dissipation, we eventually reach a geostrophic regime at large time, provided that the initial enstrophy is sufficiently low (otherwise the final state contains no large scale flow). In addition, each time the system is perturbed by adding a little amount of energy without changing the enstrophy, it drives the system a bit more towards the mixed state $\left(E_{mf} = E_{mix}, Z_2 = 0\right)$.

5.3 Flow Structure of the Equilibrium States: Application to the Zapiola Anticyclone

So far we have discussed energy partition for shallow water equilibria in the quasi-geostrophic limit. Here we focus on the structure of the large scale flow associated with these equilibrium states. We consider for that purpose an oceanic application to the Zapiola anticyclone.

The Zapiola anticyclone is a strong anticyclonic recirculation taking place in the Argentine basin above a sedimentary bump known as the Zapiola drift [24,38,54]. The anticyclone is characterized by a mass transport as large as any other major oceanic current such as the Gulf Stream. It is a quasi-barotropic (depth independent) flow, with typical velocities of the order of $0.1\ m.s^{-1}$, and a lateral extension of the order of $800\ km$.

It is known from the earlier statistical mechanics studies that positive temperature states in the energy enstrophy ensemble of one layer models lead to anticyclonic circulations above topography anomalies, see e.g. [35] and references therein. A generalization of this result to the continuously stratified case with application to the Zapiola anticyclone is given in [48].

We have shown in this paper that quasi-geostrophic equilibria characterized by positive temperature states are also shallow water equilibria. The Zapiola anticyclone can therefore be interpreted as an equilibrium state of the shallow water model. Let us now show the qualitative difference between low energy states (when $Z_2 > Z_b$ and $E_{mf} \to 0$) and high energy states (when $E_{mf} \to E_{mix}$), which are shown on Fig. 4a and b, respectively.

In both cases the bottom topography is the same, and its isolines are visualized with thin black lines. Bottom topography has been obtained from data available online and described in [39]. We isolated the largest close contour defining the Zapiola drift (the sedimentary bump above which the recirculation takes place), and considered the actual bottom topography inside this contour, and a flat bottom outside this contour. It allows to focus on the interesting flow structure occurring above the Zapiola drift.

Energy–enstrophy equilibrium states are then computed using Eq. (234) in Appendix 6. We have seen that low energy limit corresponds to $\beta \to +\infty$ with $Z_2 > Z_b$. Taking this limit in Eq. (234) yields $\psi_{mf} = (Z_2 - Z_b)\, h_b/\beta$: the equilibrium state is a Fofonoff flow [12], meaning that streamlines are proportional to the isolines of topography, just as in Fig. 3a.

The maximum energy state corresponds to the case $\beta = 0$, which corresponds to the mixed state defined in Eq. (154). The streamfunction is $\psi_{mix} = \left(R^{-2} - \Delta\right)^{-1} h_b$. The operator

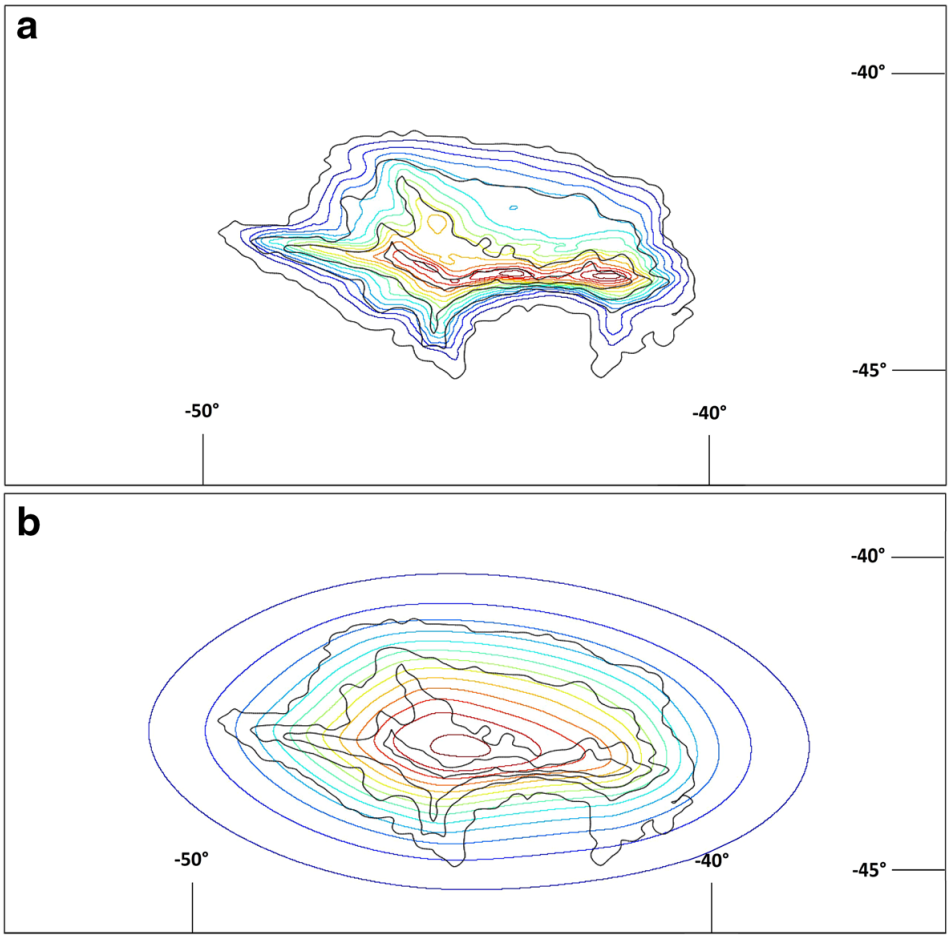

Fig. 4 Plots of the streamfunction isolines (*colored lines*) from higher values (*red*) to lower values (*blue*) over the Zapiola Drift topography iso-contours (*black lines*) for a small mean-flow energy (a)) and for a high mean-flow energy (b)) (Color figure online).

$\left(R^{-2} - \Delta\right)^{-1}$ with $R \sim 1$ is expected to smooth out the small scale topography features, just as in Fig. 4a.

6 Conclusion

We have presented in this paper analytical computations of equilibrium states for the shallow water system, giving thus predictions for the energy partition into small scale fluctuations and large scale flow. Our results rely on the definition of a discrete version of the shallow water model. Once our semi-Lagrangian discrete model was introduced, the whole machinery of equilibrium statistical mechanics could be applied.

We found that equilibrium states of the shallow water system are associated with the concomitant existence of a large scale flow which is a stationary state of the shallow water dynamics, superimposed with small scale fluctuations that may contain in some cases a substantial part of the total energy. The novelty of our work was to explicitly compute the contribution of these small scale fluctuations, and to decipher the physical consequences of the presence of these fluctuations.

In particular, we found that the presence of small scale fluctuations implies a positive temperature for the equilibrium state. This explains a previous result by Warn [53], who showed that equilibrium states in a weak flow limit admit no large scale flow when there

is no bottom topography and no lateral boundaries. We have generalized these results, by showing that a large scale vortical flow exists at equilibrium when there is both rotation and bottom topography, or when there is a non-zero circulation.

In the limit of weak height fluctuations, we found equipartition of the small scale kinetic and potential energy. We also obtained an interesting physical picture of the equilibrium state, which may be interpreted in that limit as two subsystems in thermal contact. One subsystem is the "large scale" potential vortical flow whose entropy is closely related to the one introduced heuristically by Chavanis and Sommeria (see [7]). Our work provides therefore a microscopic justification of their entropy with a complete statistical mechanics derivation and a generalization of this results by including the presence of small scales fluctuations of the height and divergence fields. We note however that it is wrong to interpret the "large scale" potential vortical flow entropy as the entropy of the system, it is only one part of it. The other subsystem contains the field of height fluctuations associated with small scale potential energy, and the field of velocity fluctuations, associated with small scale kinetic energy. These velocity fluctuations are due solely to the divergent part of the velocity field. Warn obtained a similar result in the weak flow limit, by projecting the non-linear dynamics into eigenmodes of the linearized dynamics [53]. He found an energy partition into a vortical flow on the one side, and on inertia-gravity waves on the other side, with a weak coupling between both subsystems. Hence we may interpret local height and divergent velocity fields fluctuations appearing in our model as inertia gravity waves.

We studied the quasi-geostrophic limit for the large scale flow, taking into account the presence of small scale fluctuations. We recovered in this limit the variational problem of the Miller–Robert–Sommeria theory, with the additional constraint that the temperature is positive. We obtained phase diagrams in the particular case of energy–enstrophy equilibria, with explicit prediction for the ratio of energy between small scale fluctuations and a large scale quasi-geostrophic flow. This allowed to discuss the qualitative effect of small scale dissipation and shocks on the temporal evolution of the system. The main result is that such dissipative processes drive the system towards a minimum energy state (depending on the enstrophy), which may be non-zero.

In view of those results, the semi-Lagrangian discrete model seems to be a good discretization of the shallow water system. It has the key desired properties to take into account of the conservation of fluid particle volume, while working in an Eulerian framework. This gives a clear framework, which allows for a rigorous derivation once the discretization is assumed. Moreover we stress that it leads to equilibrium states that are stationary states of the shallow water model, by contrast with other choices of discretization. What is not completely satisfactory however is that there is a degree of arbitrariness in the definition of the discrete model. We have tried to have the model consistent with the geometric constraints related to the Liouville theorem, even though the link between the model and the Liouville theorem is clearly not rigorous. There is clearly room for improvement, but we are afraid we are faced with extremely tricky mathematical problems. Nevertheless we guess that the invariant measure of the discrete model converge to the actual invariant measure of the shallow water system in the continuous limit, but proving this is beyond the scope of this paper.

The statistical mechanics prediction of a vanishing large scale flow in the absence of boundary and bottom topography seems to contradict some numerical results performed in such configurations, in which case long lived vortex were reported, see e.g. [11]. This issue is related to the estimation of a time scale for the convergence towards equilibrium. Indeed, if the coupling between the large scale flow (potential vortical modes) and the small scale fluctuations (inertia-gravity waves) is weak, and if one starts from an initially balanced and unstable large scale flow, then this large scale flow may self-organize spontaneously on a

short time scale into an equilibrium state of the quasi-geostrophic subsystem. This justifies the physical interest of the variational principle for the large scale flow introduced by [7] without small scale fluctuation. According to our statistical mechanics predictions, the energy of this large scale flow should leak into small scale fluctuations, but this process may be slow if coupling between both subsystems is weak. This difficult issue was already raised by Warn [53], and the interaction between geostrophic motion and inertia-gravity waves remains an active field of research [47]. In particular, very interesting models of interactions between near-inertial waves and geostrophic motion have been proposed [14,57,58]. In the context of statistical mechanics approaches, it has been proposed to compute equilibrium states with frozen degrees of freedom [36] or restricted partition functions in order to avoid the presence of inertia-gravity waves [16].

One of the main interests of the present study is the prediction of a concomitant large scale energy transfer associated with a large scale potential vortical flow and a small scale transfer of energy that is lost into small scale fluctuations interpreted as inertia-gravity waves. In that respect, the shallow water model lies between three dimensional and two-dimensional turbulence. There are other models for which the energy may be partitioned into a large scale flow and small scale fluctuations. There are, for instance, some strong analogies with the case of three-dimensional axisymmetric Euler equations, that is also intermediate between 2D and 3D flows. A statistical mechanics theory has been recently derived for this system by Thalabard et al. [41]. This statistical theory can also be understood as two subsystems in contact, one of them being the fluctuations, and thus leading to positive temperatures [41]. From this key observation, [41] concluded that the temperature of the system, that measures the variance of the fluctuations, is positive and uniform in space, as previously stressed in [27]. More generally, and beyond those simplified flow models that allow for analytical treatment, it is common to observe in bounded laboratory experiment the emergence of large scale structures at the domain scale superimposed with small scale energy fluctuations, see e.g. [42]. It is not clear whether equilibrium theory may be relevant to describe such problems, but we believe that it is at least a useful first step to address these questions.

Acknowledgments The authors warmly thank M. Potters and A. Licari for their preliminary work on this subject during a traineeship under the supervision of FB. The research leading to these results has received funding from the European Research Council under the European Union's Seventh Framework Programme (FP7/2007-2013 Grant Agreement no. 616811) (FB and AV). We warmly thank the three referees for their very positive evaluation of our work and for the numerous remark that helped us to improve our work. The level of commitment of the three referee in reading the detail of our computations has been extremely high, and we thank them for this important work.

Appendix 1: Invariant Measure and Formal Liouville Theorem

Formal Liouville Theorem for the Triplet of Fields (h, hu, hv)

The existence of a formal Liouville theorem for the shallow water dynamics is shown in this appendix. The shallow water system is fully described by the triplet of fields (h, hu, hv). We consider a measure written formally as

$$\mathrm{d}\mu = C\mathscr{D}[h]\,\mathscr{D}[hu]\,\mathscr{D}[hv]\,,$$

with uniform density in (h, hu, hv)-space (C is a constant). The average of any functional A over this measure is

$$\forall \mathscr{A}\,[h, uh, vh]\,,\ \langle \mathscr{A} \rangle_\mu = \int \mathrm{d}\mu\ \mathscr{A}. \tag{161}$$

The term $\int \mathscr{D}[h]\,\mathscr{D}[hu]\,\mathscr{D}[hv]$ means that the integral is formally performed over each possible triplet of fields $(h,\ hu,\ hv)$. The measure is said to be invariant if

$$\forall \mathscr{A},\quad \frac{\mathrm{d}}{\mathrm{d}t}\langle \mathscr{A} \rangle_\mu = 0 \tag{162}$$

This yields the condition

$$\forall \mathscr{A},\quad \int \mathscr{D}[h]\,\mathscr{D}[hu]\,\mathscr{D}[hv] \int d\mathbf{x}\ \frac{\delta \mathscr{A}}{\delta h}\partial_t h + \frac{\delta \mathscr{A}}{\delta (hu)}\partial_t (hu) + \frac{\delta \mathscr{A}}{\delta (hv)}\partial_t (hu) = 0. \tag{163}$$

An integration by parts yields

$$\forall \mathscr{A},\quad \int \mathscr{D}[h]\,\mathscr{D}[hu]\,\mathscr{D}[hv]\,\mathscr{A} \int d\mathbf{x}\ \left(\frac{\delta \partial_t h}{\delta h} + \frac{\delta \partial_t (hu)}{\delta (hu)} + \frac{\delta \partial_t (hv)}{\delta (hv)}\right) = 0. \tag{164}$$

We say that the equation follows a formal Liouville theorem if we formally have

$$\int d\mathbf{x}\ \left(\frac{\delta \partial_t h}{\delta h} + \frac{\delta \partial_t (hu)}{\delta (hu)} + \frac{\delta \partial_t (hv)}{\delta (hv)}\right) = 0, \tag{165}$$

which ensures that the measure $\mathrm{d}\mu$ is invariant.

The shallow water equations (5) and (6) can be written on the form

$$\partial_t (hu) = -\partial_x \left(hu^2 + \frac{1}{2}gh^2\right) - \partial_y (huv) + fhv, \tag{166}$$

$$\partial_t (hv) = -\partial_y \left(hv^2 + \frac{1}{2}gh^2\right) - \partial_x (huv) - fhu, \tag{167}$$

$$\partial_t h + \partial_x (hu) + \partial_y (hv) = 0. \tag{168}$$

We see that

$$\frac{\delta \partial_t h}{\delta h} + \frac{\delta \partial_t (hu)}{\delta (hu)} + \frac{\delta \partial_t (hv)}{\delta (hv)} = -\boldsymbol{\nabla} \cdot \left(\frac{\delta (h\mathbf{u})}{\delta h} + \frac{\delta (hu\mathbf{u})}{\delta (hu)} + \frac{\delta (hv\mathbf{u})}{\delta (hv)}\right). \tag{169}$$

As the divergence operator is a linear operator, it commutes with the functional derivatives. This allows to conclude that the measure μ is invariant. This shows formally the existence of a Liouville theorem for the fields (h, uh, vh).

Change of Variables from (h, hu, hv) to (h, q, μ)

The microcanonical measure can formally be written

$$\mathrm{d}\mu_{h,hu,hv} = \mathscr{D}[h]\,\mathscr{D}[hu]\,\mathscr{D}[hv]\,\delta(\mathscr{E} - E)\prod_{k=0}^{+\infty}\delta(\mathscr{Z}_k - Z_k)\,, \tag{170}$$

The constraints are more easily expressed in terms of the variables

$$h,\quad q = \frac{-\partial_y u + \partial_x v + f}{h},\quad \mu = \Delta^{-1/2}\left(\partial_x u + \partial_y v\right). \tag{171}$$

It will thus be more convenient to use these fields as independent variables. We call $J[(h, hu, hv)/(h, q, \mu)]$ the Jacobian of the transformation. We proceed step by step to

compute this Jacobian. The change of variables $(h, hu, hv) \rightarrow (h, u, v)$ involves a upper-diagonal Jacobian matrix at each point $\mathbf{r}$:

$$J\left[\frac{(h, hu, hv)}{(h, u, v)}\right] = \begin{pmatrix} 1 & u & v \\ 0 & h & 0 \\ 0 & 0 & h \end{pmatrix} \tag{172}$$

which implies $\det\left(J\left[(h, hu, hv)/(h, u, v)\right]\right) = h^2$ and

$$\mathscr{D}[h]\,\mathscr{D}[hu]\,\mathscr{D}[hv] = h^2\,\mathscr{D}[h]\,\mathscr{D}[u]\,\mathscr{D}[v]\,. \tag{173}$$

The change of variable $(h, u, v) \rightarrow (h, \omega, \mu)$ involves linear operators that do not depend on space coordinates, thus the determinant of the Jacobian of the transformation is an unimportant constant:

$$\mathscr{D}[h]\,\mathscr{D}[u]\,\mathscr{D}[v] = C\,\mathscr{D}[h]\,\mathscr{D}[\omega]\,\mathscr{D}[\mu]\,. \tag{174}$$

Using $\omega = qh - 1$, the change of variable $(h, \omega, \mu) \rightarrow (h, q, \mu)$ involves an upper diagonal Jacobian matrix at each point $\mathbf{r}$:

$$J\left[\frac{(h, \omega, \mu)}{(h, q, \mu)}\right] = \begin{pmatrix} 1 & q & 0 \\ 0 & h & 0 \\ 0 & 0 & 1 \end{pmatrix}, \tag{175}$$

with a determinant $\det\left(J\left[(h, \omega, \mu)/(q, h, \mu)\right]\right) = h$. Finally, the Jacobian of the transformation is $J\left[(hu, hv, h)/(q, h, \mu)\right] = h^3$ and the microcanonical measure can formally be written

$$\mathrm{d}\mu_{h,q,\mu} = Ch^3\,\mathscr{D}[h]\,\mathscr{D}[q]\,\mathscr{D}[\mu]\,\delta\left(\mathscr{E} - E\right)\prod_{k=0}^{+\infty}\delta\left(\mathscr{Z}_k - Z_k\right). \tag{176}$$

We note the presence of the pre-factor h^3 which gives the weight of each microscopic configuration in the (h, q, μ)-space.

Appendix 2: Relevance of the Constraints for the Discrete Model

In this appendix, we explain how the dynamical invariants of the shallow water model, given in Eqs. (32) and (34) respectively, are related to the constraints of the microcanonical ensemble for the discrete model, given in Eqs. (92) and (97), respectively.

Areal Coarse-Graining for Continuous Fields

Let us consider a field $g(\mathbf{x})$ on the domain $\mathscr{D}$ where the flow takes place, and let us consider the uniform grid introduced in Sect. 3.2.1. We define the local areal coarse-graining of the continuous field $g(\mathbf{x})$ over a site (i, j) as

$$\overline{g}_{ij} = N\int_{\text{site }(i,j)} \mathrm{d}\mathbf{x}\; g(\mathbf{x})\,, \tag{177}$$

where $1/N$ is the area of the site (i, j) and where $\int_{\text{site }(i,j)}$ means that we integrate over the site (i, j) only. With an abuse of notation, we use here the same notation $\overline{g}_{ij}$ as in Eq. (50),

since the coarse-graining operator defined in Eq. (177) generalizes to the continuous case the areal coarse-graining operator defined in Eq. (50) for the discrete microscopic model, taking into account the fact that for a fluid particle "n" of area $\mathrm{d}\mathbf{x}_n$ and height h_n, we get $N\mathrm{d}\mathbf{x}_n = 1/(Mh_n)$.

We denote $\overline{g}$ the continuous limit (large N) of $\overline{g}_{ij}$. Integrating a continuous field g amounts to perform the integration over its local average field $\overline{g}$:

$$\int \mathrm{d}\mathbf{x}\, g\,(\mathbf{x}) = \int \mathrm{d}\mathbf{x}\, \overline{g}\,(\mathbf{x})\,. \tag{178}$$

Potential Vorticity Moments

Using (178), the potential vorticity moments in Eq. (34) simply leads to

$$\mathscr{Z}_k = \int \mathrm{d}\mathbf{x}\, \overline{hq^k}. \tag{179}$$

Now that the potential vorticity moments are expressed in terms of the areal coarse-graining of moments of h and q, it can directly be expressed in terms of the probability density field $\rho\left(\sigma_h, \sigma_q, \sigma_\mu\right)$ through Eq. (90), and we recover the expression of the constraint given in Eq. (92), whose discrete representation is given in Eq. (56).

Energy

Using (178), recalling that we restrict ourself to bottom topographies such that $\overline{h}_b = h_b$, the total energy of the shallow water model defined in Eq. (32) can be decomposed into a mean flow kinetic energy defined in Eq. (94), a potential energy term due to local height fluctuations and defined in Eq. (96), a fluctuating kinetic energy term

$$\mathscr{E}_{c,fluct} \equiv \mathscr{E} - \mathscr{E}_{mf} - \mathscr{E}_{\delta h} \tag{180}$$

$$\mathscr{E}_{c,fluct} \equiv \frac{1}{2}\int \mathrm{d}\mathbf{x}\, \left(h\mathbf{u}^2 - \overline{h}\mathbf{u}_{mf}^2\right), \tag{181}$$

where the velocity fields $\mathbf{u}$ and $\mathbf{u}_{mf}$ are computed from the triplet (h, q, μ) and from the triplet $\left(\overline{h}, \overline{hq}, \overline{h\mu}\right)$, respectively through

$$\mathbf{u} = \nabla^\perp\psi + \nabla\phi, \quad (hq - f) = \Delta\psi, \quad \mu = \Delta^{1/2}\phi, \tag{182}$$

and through

$$\mathbf{u}_{mf} = \nabla^\perp\psi_{mf} + \nabla\phi_{mf}, \quad \left(\overline{hq} - f\right) = \Delta\psi_{mf}, \quad \frac{\overline{h\mu}}{\overline{h}} = \Delta^{1/2}\phi_{mf}. \tag{183}$$

We want to discuss the relation between decomposition of the energy for the discrete model, Eq. (97) and the decomposition for the actual total energy defined in Eq. (32). Our construction is relevant if these two decomposition coincide in the continuous limit, or equivalently if $\mathscr{E}_{c,fluct}$ is equal to $\mathscr{E}_{\delta\mu}$ (95) in the continuous limit. In the following we show that this is the case if some cross correlations are actually negligible. More precisely, we assume that

1. For any positive integers k, l, m, the coarse-grained fields $\overline{h^k q^l \mu^m}(\mathbf{x})$ defined through the coarse graining procedure in Eq. (178) exist. In the framework of our microscopic model introduced in Sect. 3.2, this hypothesis is automatically satisfied by assuming that the cut-off $\mu_{min}, \mu_{max}, q_{min}, q_{max}, h_{max}$ scales as N^α with $\alpha < 1$. Other fields may be

characterized by local extreme values such that the limit defined in Eq. (178) does not converge. For instance, we will see that the actual divergence $\zeta = \Delta\phi$ of the equilibrium state is not bounded, i.e. that $\overline{\zeta}$ would have no meaning.

2. The fields h, q, μ are decorrelated (in particular, $\overline{h^k q^l \mu^m} = \overline{h^k q^l}\,\overline{\mu^m}$). This point will be shown to be self-consistent when computing the equilibrium state.
3. The coarse-grained divergent velocity field is equal to the mean-flow velocity field $\overline{\nabla\phi} = \nabla\phi_{mf}$.
4. $\overline{\Delta\left[\left(\phi - \phi_{mf}\right)^2\right]} = 0$. While $\nabla(\phi - \phi_{mf})$ is a random vector field characterized by wild local fluctuation, this hypothesis amounts to assume that those fluctuations have no preferential direction.

We believe that these four assumptions would be satisfied by a typical triplet of fields (h, q, μ) picked at random among all the possible states satisfying the constraints of the dynamics. By typical, we mean that an overwhelming number of fields would share these properties.

We then prove that these four assumptions are sufficient to prove that $\mathscr{E}_{c,fluct}$ is equal to $\mathscr{E}_{\delta\mu}$ (95) in the continuous limit. According to the assumption 1, $\overline{\omega} = \overline{hq} - 1$ is well defined. Classical arguments show that the streamfunction of the coarse-grained vorticity field $\overline{\omega}$ is equal to the streamfunction of the vorticity field, i.e. that $\nabla\psi_{mf} = \nabla\psi$, see e.g. [21,33]. Qualitatively, this is due to the fact that inverting the Laplacian operator smooth out local fluctuations of the vorticity.[13] This yields

$$\mathbf{u} = \mathbf{u}_{mf} + \nabla\left(\phi - \phi_{mf}\right). \tag{184}$$

Injecting this expression in the kinetic energy density expression Eq. (181), using that h and μ are not correlated (assumption 2), and using $\overline{\nabla\phi} = \nabla\phi_{mf}$ (assumption 3) yields

$$\mathscr{E}_{c,fluct} = \frac{1}{2}\int \mathrm{d}\mathbf{x}\, \overline{h}\overline{\left(\nabla\left(\phi - \phi_{mf}\right)\right)^2}. \tag{185}$$

Let us now remember the definition of the coarse-graining operator in Eq. (178):

$$\overline{\left(\nabla\left(\phi - \phi_{mf}\right)\right)^2} = \lim_{N\to\infty} N\int_{S_{ij}} \mathrm{d}\mathbf{x}\left(\nabla\left(\phi - \phi_{mf}\right)\right)^2, \quad \text{for } \mathbf{x} \in S_{ij}, \tag{186}$$

where S_{ij} is the surface covered by a grid site (i, j). An integration by parts yields

$$\begin{aligned} N\int_{S_{ij}} \mathrm{d}\mathbf{x}\ \left(\nabla\left(\phi - \phi_{mf}\right)\right)^2 = -N\int_{S_{ij}} \mathrm{d}\mathbf{x}\ \left[\left(\Delta^{-1/2}\left(\mu - \overline{\mu}\right)\right)\left(\Delta^{1/2}\left(\mu - \overline{\mu}\right)\right)\right] \\ + N\oint_{\partial S_{ij}} \mathrm{d}l\ \mathbf{n}\cdot\left(\phi - \phi_{mf}\right)\nabla\left(\phi - \phi_{mf}\right) \end{aligned} \tag{187}$$

Projecting the first term of the rhs on Laplacian eigenmodes allows to simplify the expression of the first term of the rhs in Eq. (187):

$$-N\int_{S_{ij}} \mathrm{d}\mathbf{x}\ \left[\left(\Delta^{-1/2}\left(\mu - \overline{\mu}\right)\right)\left(\Delta^{1/2}\left(\mu - \overline{\mu}\right)\right)\right] = N\int_{S_{ij}} \mathrm{d}\mathbf{x}\ \left(\mu - \overline{\mu}\right)^2. \tag{188}$$

[13] The divergent part of the velocity field can not be treated in the same way. Indeed, the operator $\Delta^{-1/2}$ is less smooth than the operator Δ^{-1}, and one can not derive $\phi = \phi_{mf}$ by inverting $\mu = \Delta^{1/2}\phi$. One may want to use $\zeta = \Delta\phi$, but the result would be the same since ζ is not bounded (the field μ is characterized by fluctuations which are controlled by the kinetic energy, and hence by the total energy, but this is not the case for ζ).

The second term of the rhs in Eq. (187) can be written as

$$N \oint_{\partial S_{ij}} \mathrm{d}l\ \mathbf{n} \cdot \left(\phi - \phi_{mf}\right) \nabla \left(\phi - \phi_{mf}\right) = \frac{N}{2} \int_{S_{ij}} \Delta \left[\left(\phi - \phi_{mf}\right)^2\right] \tag{189}$$

which, according to assumption 4, vanishes in the large N limit. Finally, the kinetic energy density of the fluctuations is simply expressed as

$$\mathscr{E}_{c,fluct} = \frac{1}{2} \int \mathrm{d}\mathbf{x}\, \overline{h} \left(\overline{\mu^2} - \overline{\mu}^2\right). \tag{190}$$

Finally, we use again the assumption 2 to get

$$\mathscr{E}_{c,fluct} = \frac{1}{2} \int \mathrm{d}\mathbf{x} \left(\overline{h\mu^2} - \frac{\overline{h\mu}^2}{\overline{h}}\right) = \mathscr{E}_{\delta\mu}, \tag{191}$$

which is the expected result.

Appendix 3: Critical Points of the Mean-Flow Variational Problem

In this Appendix, we compute the critical points of the mean-flow variational problem (100) stated in Sect. 3. In a first step, we solve an intermediate variational problem in order to show the factorization of the probability density ρ with a Gaussian behavior for the divergence fluctuations. Knowing that, we solve in a second step the original variational problem.

Intermediate Variational Problem

As the energy and the potential vorticity moments depend only on the coarse-grained fields $\overline{h}$, $\overline{h^2}$, $\overline{h\mu}$, $\overline{h\mu^2}$ and the local potential vorticity moments $\left\{\overline{hq^k}\right\}$, we introduce an intermediate variational problem where these coarse-grained fields are given as constraint:

$$\max_{\rho, \int \rho = 1} \left\{ \mathscr{S}[\rho] \;\middle|\; \overline{h}, \overline{h^2}, \overline{h\mu}, \overline{h\mu^2}, \left\{\overline{hq^k}\right\}_{k\geq 1} \text{“fixed”} \right\}. \tag{192}$$

The idea of introducing the intermediate variational problem is to find a simpler ansatz for the probability density field ρ. This ansatz will be used afterward into the general variational problem (100).

In order to compute the critical points of the variational problem (192), we introduce the Lagrange multipliers $\alpha_h(\mathbf{x})$, $\alpha_{h2}(\mathbf{x})$, $\alpha_{h\mu}(\mathbf{x})$, $\alpha_{h\mu 2}(\mathbf{x})$, $\left\{\alpha_{hq,k}(\mathbf{x})\right\}_{k\geq 0}$ and $\xi(\mathbf{x})$ associated with the constraints $\overline{h}$, $\overline{h^2}$, $\overline{h\mu}$, $\overline{h\mu^2}$, $\left\{\overline{hq^k}\right\}_{k\geq 1}$ and the normalization constraint, respectively. Using Eq. (89) and the first variations

$$\forall \delta\rho,\ \delta S - \int \mathrm{d}\mathbf{x} \left[\alpha_h \delta\overline{h} + \alpha_{h2} \delta\overline{h^2} + \alpha_{h\mu} \delta\overline{h\mu} + \alpha_{h\mu 2} \delta\overline{h\mu^2} + \sum_{k=1}^{+\infty} \alpha_{hq,k} \delta\overline{hq^k} + \xi \int \delta\rho\right] = 0, \tag{193}$$

leads to

$$\sigma_h \log\left(\frac{\rho}{\sigma_h^2}\right) + \sigma_h + \xi + \alpha_h \sigma_h + \alpha_{h2}\sigma_h^2 + \alpha_{h\mu}\sigma_h\sigma_\mu + \alpha_{h\mu 2}\sigma_h\sigma_\mu^2 + \sum_{k=1}^{+\infty} \alpha_{hq,k}\sigma_h\sigma_q^k = 0 \tag{194}$$

We readily see from Eq. (194) that the probability density ρ factorizes into three decoupled probability densities ρ_q, ρ_h and ρ_μ corresponding respectively to the probability densities of the potential vorticity, the height and the divergence:

$$\rho = \rho_q\left(\mathbf{x}, \sigma_q\right)\rho_h\left(\mathbf{x}, \sigma_h\right)\rho_\mu\left(\mathbf{x}, \sigma_\mu\right). \tag{195}$$

Using the constraints $\overline{\mu} = \int \mathrm{d}\sigma_\mu\ \sigma_\mu \rho_\mu$, $\overline{\mu^2} = \int \mathrm{d}\sigma_\mu\ \sigma_\mu^2 \rho_\mu$, as well as the normalization constraints $\int \mathrm{d}\sigma_\mu\ \rho_\mu = \int \mathrm{d}\sigma_h\ \rho_h = \int \mathrm{d}\sigma_q\ \rho_q = 1$, we get

$$\left\{\begin{array}{rcl} \rho_q\left(\mathbf{x}, \sigma_q\right) & = & \dfrac{\exp\left(-\displaystyle\sum_{k=1}^{+\infty} \alpha_{hq,k}\left(\mathbf{x}\right)\sigma_q^k\right)}{\displaystyle\int \mathrm{d}\sigma_q^{'}\ \exp\left(-\sum_{k=1}^{+\infty} \alpha_{hq,k}\left(\mathbf{x}\right)\sigma_q^{'k}\right)} \\ \rho_h\left(\mathbf{x}, \sigma_h\right) & = & \dfrac{\sigma_h^2 \exp\left(-\alpha_{h2}\left(\mathbf{x}\right)\sigma_h - \dfrac{\xi\left(\mathbf{x}\right)}{\sigma_h}\right)}{\displaystyle\int \mathrm{d}\sigma_h^{'}\ \sigma_h^{'2} \exp\left(-\alpha_{h2}\left(\mathbf{x}\right)\sigma_h^{'} - \frac{\xi\left(\mathbf{x}\right)}{\sigma_h^{'}}\right)} \\ \rho_\mu\left(\mathbf{x}, \sigma_\mu\right) & = & \dfrac{\exp\left(-\dfrac{1}{2}\dfrac{\left(\sigma_\mu - \overline{\mu}\left(\mathbf{x}\right)\right)^2}{\overline{\mu^2}\left(\mathbf{x}\right) - \overline{\mu}^2\left(\mathbf{x}\right)}\right)}{\left(2\pi\right)^{1/2}\left(\overline{\mu^2}\left(\mathbf{x}\right) - \overline{\mu}^2\left(\mathbf{x}\right)\right)^{1/2}} \end{array}\right. . \tag{196}$$

We could now re-inject these expressions into the main variational problem (100), but only factorization and the Gaussian form of ρ_μ will be kept as an ansatz for ρ, which will simplify the computations. Thanks to this intermediate variational problem, we now know that the critical points of the original variational problem must be of the form:

$$\rho\left(\mathbf{x}, \sigma_h, \sigma_q, \sigma_\mu\right) = \rho_h\left(\sigma_h, \mathbf{x}\right)\rho_q\left(\sigma_q, \mathbf{x}\right)\frac{\exp\left(-\frac{1}{2}\frac{\left(\sigma_\mu - \overline{\mu}\right)^2}{\overline{\mu^2} - \overline{\mu}^2}\right)}{\left(2\pi\right)^{1/2}\left(\overline{\mu^2} - \overline{\mu}^2\right)^{1/2}}. \tag{197}$$

The entropy defined in Eq. (89) is therefore (up to a constant):

$$\begin{aligned} \mathscr{S}\left[\rho_h, \rho_q, \bar{\mu}, \bar{\mu^2} - \bar{\mu}^2\right] = & -\int \mathrm{d}\mathbf{x}\mathrm{d}\sigma_h\ \sigma_h\rho_h \log\left(\frac{\rho_h}{\sigma_h^2}\right) \\ & - \int \mathrm{d}\mathbf{x}\,\overline{h}\int \mathrm{d}\sigma_q \rho_q \log\left(\rho_q\right) + \int \mathrm{d}\mathbf{x}\,\frac{\overline{h}}{2}\log\left(\overline{\mu^2} - \overline{\mu}^2\right). \end{aligned} \tag{198}$$

As a consequence of Eq. (197), the height field, the potential vorticity field and the divergence field are decorrelated. This property allows to rewrite the energy defined in Eq. (93)

$$\mathscr{E}\left[\rho_h, \rho_q, \overline{\mu}, \overline{\mu^2} - \overline{\mu}^2\right] = \mathscr{E}_{mf}\left[\overline{h}, \overline{q}, \overline{\mu}\right] + \mathscr{E}_{\delta\mu}\left[\overline{h}, \overline{\mu^2} - \overline{\mu}^2\right] + \mathscr{E}_{\delta h}\left[\overline{h}, \overline{h^2}\right], \tag{199}$$

where

$$\begin{cases} \mathscr{E}_{mf}\left[\overline{h},\overline{q},\overline{\mu}\right] = \frac{1}{2}\int \mathrm{d}\mathbf{x}\,\left(\overline{h}\mathbf{u}_{mf}^2 + g\left(\overline{h}+h_b-1\right)^2\right) \\ \mathscr{E}_{\delta\mu}\left[\overline{h},\overline{\mu^2}-\overline{\mu}^2\right] = \frac{1}{2}\int \mathrm{d}\mathbf{x}\,\overline{h}\left(\overline{\mu^2}-\overline{\mu}^2\right) \\ \mathscr{E}_{\delta h}\left[\overline{h},\overline{h^2}\right] = \frac{g}{2}\int \mathrm{d}\mathbf{x}\,\left(\overline{h^2}-\overline{h}^2\right) \end{cases} \tag{200}$$

with $\mathbf{u}_{mf} = \nabla^{\perp}\Delta^{-1}\left(\overline{q}\overline{h}-f\right) + \nabla\Delta^{-1/2}\overline{\mu}$. Similarly the potential vorticity moments (96) can be rewritten

$$\forall k \quad \mathscr{Z}_k\left[\overline{h},\overline{q^k}\right] = \int \mathrm{d}\mathbf{x}\,\overline{h}\overline{q^k} \tag{201}$$

where the coarse-grained moments are now defined as

$$\overline{h^l} = \int \mathrm{d}\sigma_h\,\sigma_h^l\rho_h, \qquad \overline{q^m} = \int \mathrm{d}\sigma_q\,\sigma_q^m\rho_q. \tag{202}$$

Thus, the general variational problem of the equilibrium theory given in Eq. (100) can be recast into a new variational problem on the independent variables $\rho_h\left(\mathbf{x},\sigma_h\right)$, $\rho_q\left(\mathbf{x},\sigma_q\right)$, $\overline{\mu}\left(\mathbf{x}\right)$ and $\left[\overline{\mu^2}-\overline{\mu}^2\right](\mathbf{x})$:

$$S\left(E,D\right) = \max_{\substack{\rho_h,\rho_q,\overline{\mu},\overline{\mu^2}-\overline{\mu}^2 \\ \int\rho_h=1,\int\rho_q=1}} \left\{ \mathscr{S}\left[\rho_h,\rho_q,\overline{\mu},\overline{\mu^2}-\overline{\mu}^2\right] \Big| \right.$$
$$\left. \mathscr{E}\left[\rho_h,\rho_q,\overline{\mu},\overline{\mu^2}-\overline{\mu}^2\right] = E,\ \forall k \quad \mathscr{Z}_k\left[\rho_h,\rho_q\right] = Z_k \right\}. \tag{203}$$

Computation of the Critical Points

In this section, we compute the critical points of the variational problem defined in Eq. (203). We introduce the Lagrange multiplier β, $\{\alpha_k\}_{k\geq 0}$, $\xi_q\left(\mathbf{r}\right)$ and $\xi_h\left(\mathbf{r}\right)$ associated respectively with the energy, the potential vorticity moments and the normalization constraints. Critical points of the variational problem (203) are solutions of

$$\forall \delta\rho_q,\delta\rho_h,\delta\overline{\mu},\delta\left(\overline{\mu^2}-\overline{\mu}^2\right),$$
$$\delta\mathscr{S} - \beta\delta\mathscr{E} - \sum_{k=0}^{+\infty}\alpha_k\delta\mathscr{Z}_k - \int \mathbf{dx}\left(\xi_q\int\delta\rho_q + \xi_h\int\delta\rho_h\right) = 0. \tag{204}$$

The first variations of the macrostate entropy $\mathscr{S}$ (198) are

$$\begin{cases} \frac{\delta\mathscr{S}}{\delta\rho_h} = -\sigma_h\left(\log\left(\frac{\rho_h}{\sigma_h^2}\right)+1\right) - \sigma_h\int \mathrm{d}\sigma_q\,\rho_q\log\left(\rho_q\right) + \sigma_h\frac{1}{2}\log\left(\overline{\mu^2}-\overline{\mu}^2\right) \\ \frac{\delta\mathscr{S}}{\delta\rho_q} = -\overline{h}\left(\log\left(\rho_q\right)+1\right) \\ \frac{\delta\mathscr{S}}{\delta\overline{\mu}} = 0 \\ \frac{\delta\mathscr{S}}{\delta\left(\overline{\mu^2}-\overline{\mu}^2\right)} = \frac{\overline{h}}{2\left(\overline{\mu^2}-\overline{\mu}^2\right)} \end{cases}. \tag{205}$$

First variations of the energy given in Eqs. (199) and (200) contain three contributions: $\delta\mathscr{E} = \delta\mathscr{E}_{mf} + \delta\mathscr{E}_{\delta\mu} + \delta\mathscr{E}_{\delta h}$. The first contribution is

$$\delta\mathscr{E}_{mf} = \int \mathrm{d}\mathbf{x}\ \left[B_{mf}\delta\overline{h} + \left(\overline{h}\mathbf{u}_{mf}\right)\cdot\delta\mathbf{u}_{mf}\right], \tag{206}$$

where $B_{mf} = \mathbf{u}_{mf}^2/2 + g\left(\overline{h} + h_b - 1\right)$ is the mean-flow Bernoulli function defined in Eq. (115). Then, using the Helmholtz decompositions $\mathbf{u}_{mf} = \nabla^\perp\psi_{mf} + \nabla\phi_{mf}$ and recalling that $\overline{h}\mathbf{u}_{mf} = \nabla^\perp\Psi_{mf} + \nabla\Phi_{mf}$, two integrations by parts with the impermeability boundary condition yield

$$\delta\mathscr{E}_{mf} = \int \mathrm{d}\mathbf{x}\ \left[B_{mf}\delta\overline{h} - \Psi_{mf}\delta\Delta\psi_{mf} - \Phi_{mf}\delta\Delta\phi_{mf}\right]. \tag{207}$$

Using $\Delta\psi_{mf} = \overline{h}\overline{q} - f$ and $\Delta^{1/2}\phi_{mf} = \overline{\mu}$ and the definition of the operator $\Delta^{1/2}$ leads to the final expression

$$\delta\mathscr{E}_{mf} = \int \mathrm{d}\mathbf{x}\ \left[\left(B_{mf} - \overline{q}\Psi_{mf}\right)\delta\overline{h} - \overline{h}\Psi_{mf}\delta\overline{q} - \Delta^{1/2}\Phi_{mf}\delta\overline{\mu}\right]. \tag{208}$$

Finally, we get:

$$\begin{cases} \frac{\delta\mathscr{E}}{\delta\rho_h} = \sigma_h\left(B_{mf} - \overline{q}\Psi_{mf} + \frac{\overline{\mu^2}-\overline{\mu}^2}{2} + g\left(\frac{\sigma_h}{2} - \overline{h}\right)\right) \\ \frac{\delta\mathscr{E}}{\delta\rho_q} = -\sigma_q\Psi_{mf}\overline{h} \\ \frac{\delta\mathscr{E}}{\delta\overline{\mu}} = -\Delta^{1/2}\Phi_{mf} \\ \frac{\delta\mathscr{E}}{\delta\left(\overline{\mu^2}-\overline{\mu}^2\right)} = \frac{\overline{h}}{2} \end{cases}, \tag{209}$$

First variations of the potential vorticity moments are

$$\forall k \in \mathbb{N} \quad \begin{cases} \frac{\delta\mathscr{Z}_k}{\delta\rho_h} = \sigma_h\overline{q^k} \\ \frac{\delta\mathscr{Z}_k}{\delta\rho_q} = \bar{h}\sigma_q^k \\ \frac{\delta\mathscr{Z}_k}{\delta\overline{\mu}} = 0 \\ \frac{\delta\mathscr{Z}_k}{\delta\left(\overline{\mu^2}-\overline{\mu}^2\right)} = 0 \end{cases}, \tag{210}$$

Injecting Eqs. (205), (209), and (210) in Eq. (204), and collecting the term in factor of $\delta\left(\overline{\mu^2} - \overline{\mu}^2\right)$ leads to

$$\overline{\mu^2} - \overline{\mu}^2 = \frac{1}{\beta}. \tag{211}$$

Injecting Eq. (211) in the expression of ρ_μ given in Eq. (196) yields then

$$\rho_\mu\left(\mathbf{x}, \sigma_\mu\right) = \left(\frac{\beta}{2\pi}\right)^{1/2}\exp\left(-\frac{1}{2}\beta\left(\sigma_\mu - \overline{\mu}\left(\mathbf{x}\right)\right)^2\right). \tag{212}$$

Similarly, collecting the term in factor of $\delta\rho_q$ in Eq. (204) leads to

$$0 = \bar{h}\left(\log\left(p_q\right) + 1\right) - \beta\sigma_q\Psi_{mf}\bar{h} + \sum_{k=0}^{+\infty}\alpha_k\bar{h}\sigma_q^k + \xi_q, \tag{213}$$

which, using the normalization constraint, leads to

$$\rho_q\left(\mathbf{x},\sigma_q\right)=\frac{1}{\mathbb{G}_q}\exp\left(\beta\sigma_q\Psi_{mf}-\sum_{k=1}^{+\infty}\alpha_k\sigma_q^k\right),$$
$$\mathbb{G}_q=\int \mathrm{d}\sigma_q^{'}\ \exp\left(\beta\sigma_q^{'}\Psi_{mf}-\sum_{k=1}^{+\infty}\alpha_k\sigma_q^{'k}\right). \tag{214}$$

Note that the sum inside the exponential is performed from $k=1$ to $k=+\infty$. The Lagrange parameter ξ_q has been determined using the normalization condition for the pdf.

Collecting the term in factor of $\delta\rho_h$ in Eq. (204) yields

$$-\left(\log\left(\frac{\rho_h}{\sigma_h^2}\right)+1\right)-\int \mathrm{d}\sigma_q\rho_q\log\left(\rho_q\right)-\frac{1}{2}\log\left(\beta\right)-\beta\left(B_{mf}+\frac{\beta^{-1}}{2}+g\left(\frac{\sigma_h}{2}-\overline{h}\right)\right)$$
$$-\frac{\xi_h}{\sigma_h}+\beta\overline{q}\Psi_{mf}-\sum_{k\geq 0}\alpha_k\overline{q^k}=0, \tag{215}$$

which, using Eq. (214), leads to

$$-\left(\log\left(\frac{\rho_h}{\sigma_h^2}\right)+1\right)+\log\left(\mathbb{G}_q\right)-\frac{1}{2}\log\beta$$
$$-\beta\left(B_{mf}+\frac{\beta^{-1}}{2}+g\left(\frac{\sigma_h}{2}-\overline{h}\right)\right)-\frac{\xi_h}{\sigma_h}-\alpha_0=0. \tag{216}$$

Using the fact that $\mathbb{G}_q$ and B_{mf} are fields depending only on $\mathbf{x}$, and using the normalization constraint for the pdf $\rho_h(\mathbf{x},\sigma_h)$, Eq. (216) yields

$$\rho_h\left(\mathbf{x},\sigma_h\right)=\frac{\sigma_h^2}{\mathbb{G}_h}\exp\left(-\beta\frac{g}{2}\sigma_h-\frac{\xi_h}{\sigma_h}\right),\quad \mathbb{G}_h=\int \mathrm{d}\sigma_h^{'}\ \sigma_h^2\exp\left(-\beta\frac{g}{2}\sigma_h^{'}+\frac{\xi_h}{\sigma_h^{'}}\right). \tag{217}$$

Injecting Eq. (217) back into Eq. (216) yields

$$B_{mf}=\beta^{-1}\log\left(\mathbb{G}_q\mathbb{G}_h\right)+g\overline{h}+\beta^{-1}\left(-\alpha_0-\frac{3}{2}+\frac{1}{2}\log\beta\right). \tag{218}$$

One can notice that α_0 the Lagrange parameter related to the conservation of the total mass appears only here. Thus the last term $\beta^{-1}\left(\alpha_0-3/2+\log\left(\beta\right)/2\right)$ in Eq. (218) can be computed from the conservation of the total mass $\mathscr{Z}_0=Z_0$ and will be denoted A_0 in the following.

Collecting the terms in factor of $\delta\overline{\mu}$ in Eq. (204) leads to

$$\Phi_{mf}=0. \tag{219}$$

Appendix 4: Global Maximizers of the Entropy of the Large Scale Flow

We compute in this appendix an upper-bound for the macrostate entropy of the large scale flow defined in Eq. (130), for a given set of potential vorticity moment constraints defined in Eq. (92) (and arbitrary energy), and then show that when $Z_1=f$ and $h_b=0$, this upper bound for the macroscopic entropy is reached by the rest state.

This upper bound is the solution of the following variational problem:

$$S_{mf,max} = \max_{\substack{\overline{h},\rho_q \\ \int \rho_q = 1}} \left\{ \mathscr{S}_{mf}\left[\overline{h},\rho_q\right] \mid \forall k \quad \mathscr{Z}_k\left[\overline{h},\rho_q\right] = Z_k \right\}. \tag{220}$$

Introducing Lagrange parameters $\{\gamma_k\}_{k\geq 0}$ associated with the potential vorticity moment constraints and the Lagrange parameter $\xi(\mathbf{x})$ associated with the normalization constraint, the cancellation of first variations yields

$$\forall \delta\rho_q, \delta\overline{h}, \quad \delta\mathscr{S}_{mf} - \sum_{k=0}^{+\infty} \gamma_k \delta\mathscr{Z}_k + \int d\mathbf{x}\, \xi \delta\overline{1} = 0. \tag{221}$$

The solution of this equation is

$$\rho_q = \frac{\exp^{-\sum_{k=1}^{+\infty}\gamma_k\sigma^k}}{\int d\sigma\ \exp^{-\sum_{k=1}^{+\infty}\gamma_k\sigma^k}} \equiv \rho_{global}(\sigma) \tag{222}$$

where ρ_{global} depends only on the potential vorticity moments constraints $\{Z_k\}_{k\geq 1}$, and is independent from $\mathbf{x}$ and

$$\overline{h}(\mathbf{x}) = 1 \tag{223}$$

Note that the states characterized $\rho_q = \rho_{global}, \overline{h} = 1$ are solutions of the variational problem in Eq. (220), but this is only a subclass of the solutions of the variational problem of the equilibrium theory given in Eq. (153), which includes an additional energy constraint.

We have shown in Sect. 4.1 that for a given ρ_q, the large scale flow which is a solution (153) is obtained by solving Eqs. (117) and (118) for Ψ_{mf} and $\overline{h}$. Here we consider the particular case $\rho_q = \rho_{global}$ and $\overline{h} = 1$. One can compute $\overline{h}\overline{q}_{global} = \int d\mathbf{x}\, \sigma\rho_{global} = Z_1$. We conclude that the large scale flow of the equilibrium state is also a global entropy maximizer, i.e. a solution of (220) when

$$Z_1 - f = \Delta\Psi_{mf}\ , \tag{224}$$

$$\frac{1}{2}\left(\nabla\Psi_{mf}\right)^2 + gh_b = A_2. \tag{225}$$

where $A_2 = \beta \log \mathbb{G}_q - A_1$ is a constant. We see that in the case ($Z_1 = f$, $h_b = 0$), the solution of Eqs. (224) and (225) is the rest state $\Psi_{mf} = cst$ (with $A_2 = 0$). We conclude that the maximum of the macroscopic entropy of the large scale flow is reached by a flow at rest when there is no circulation ($Z_1 = f$) and no bottom topography ($h_b = 0$).

Appendix 5: Comparison with a Eulerian Discrete Model

The aim of this appendix is to discuss the construction of a possible invariant measure for the shallow water equations through an Eulerian discretization. We prove that the obtained equilibrium states differ from the one obtained through the semi-Lagrangian discretization used in the core of the paper. Moreover, we prove that the equilibrium states are not stationary states of the shallow water equations and that the statistical equilibria are not stable through coarse-graining.

We define a purely Eulerian discrete model by considering the same uniform $N \times N$ grid as for the semi-Lagrangian model, but assuming that each node is now divided into a finer

$n \times n$ uniform microscopic grid. A microscopic configuration is given by the values of the fields (h, q, μ) for all the nodes of the microscopic grid:

$$y_{\text{micro}} \equiv \{h_{IJ,ij}, q_{IJ,ij}, \mu_{IJ,ij}\}_{\substack{1\leq I,J\leq N,\\ 1\leq i,j\leq n}} \tag{226}$$

where (I, J) and (i, j) correspond respectively to the position on the macroscopic grid and the position on the microscopic grid within the macroscopic node.

Contrary to the semi-Lagrangian model, the Eulerian model has the desired property to possibly be compatible with the formal Liouville theorem derived in Appendix 1 for the continuous dynamics (although no mathematical result exist). However, the volume of fluid varies from one microscopic grid node to another in the Eulerian model, depending on the value of the height $h_{IJ,ij}$. By comparison, our semi-Lagrangian approach respects the Lagrangian conservation laws (the height h is defined through the particle mass conservation). Because of the need to go through a discretization to build the microcanonical measure, we see that both the Eulerian and the semi-Lagrangian approaches necessarily break part of the geometric conservation laws of the continuous model. Hopefully rigorous mathematical proof of the convergence of the measures of one of the discretized model to an invariant measure of the continuous equations will settle rigorously this issue in a near future, however nobody seem to know how to attack this problem mathematically. We are thus led to the conclusion that based on current knowledge, there is no clear mathematical or theoretical *a priori* argument to choose either the Eulerian or the semi-Lagrangian discretization in order to guess the microcanonical measures. For now, the use of one discrete model or another to guess the microcanonical measure of the continuous shallow water equations can therefore only be justified *a posteriori*.

Let us now define the empirical density field as

$$d_{IJ}(\sigma_h, \sigma_q, \sigma_\mu)[y_{\text{micro}}] = \frac{1}{n}\sum_{i,j=1}^{n} \delta(h_{IJ,ij} - \sigma_h)\delta(q_{IJ,ij} - \sigma_q)\delta(\mu_{IJ,ij} - \sigma_\mu). \tag{227}$$

One can now compute the entropy of the macrostates $\rho = \{y_{micro} \,|\, \forall I, J \;\; d_{IJ}\,[y_{micro}] = \rho_{IJ}\}$, which, after taking first the limit $n \to \infty$ and then the limit $N \to \infty$ leads to

$$\mathscr{S}_{\text{Eul}}[\rho] = -\int \mathrm{d}\mathbf{x}\mathrm{d}\sigma_h\mathrm{d}\sigma_q\mathrm{d}\sigma_\mu \quad \rho(\mathbf{x}, \sigma_h, \sigma_q, \sigma_\mu)\log\left(\frac{\rho(\mathbf{x}, \sigma_h, \sigma_q, \sigma_\mu)}{\sigma_h^3}\right). \tag{228}$$

This Eulerian macrostate entropy has to be compared with the macrostate entropy for the semi-Lagrangian discrete model given in Eq. (89). We can switch from expression to the other by changing ρ into $\sigma_h\rho$. We note that the two entropies become equivalent at lowest order in the limit of weak height fluctuations and weak height variations. However, in the general case, they are different, and therefore lead to different equilibrium states. In particular, is it straightforward to show that because of the absence of the factor σ_h in the expression of this Eulerian macrostate entropy (228), the critical points $\rho(\mathbf{x}, \sigma_h, \sigma_q, \sigma_\mu)$ of the microcanonical variational problem do not factorize. Consequently, small scale height and velocity fluctuations of the equilibrium state are correlated. One can then show that those correlations are associated with non-zero Reynolds stresses in the momentum equations. In particular, the equilibrium state of Eulerian model satisfies

$$J(\Psi, \overline{q}) = -\overline{J(\Psi', q')} - \overline{J(\Phi', q')}, \tag{229}$$

where the r.h.s. is non-zero. If one removes those small scale fluctuations, the large scale flow is not a stationary state of the dynamics since $J(\Psi, \overline{q}) \neq 0$. In other words, the equilibrium states of the Eulerian model are not stable by coarse-graining, contrary to the equilibria of the semi-Lagrangian model. Moreover, Eq. (229) and the properties of stationary states derived in Sect. 2.2 imply that neither the potential vorticy field $\overline{q}$ nor the Bernoulli potential $B_{\rm mf}$ can simply be expressed as a function of $\Psi_{\rm mf}$. As shown in Sect. 4.3.1, the fact that $B_{\rm mf}$ is a function of $\Psi_{\rm mf}$ is essential to prove that the equilibrium is characterized by geostrophic balance at lowest order in the Rossby number Ro, when $Ro \to 0$. Consequently, the proof of geostrophic balance derived in the framework of the semi-Lagrangian model does not hold in the framework of the Eulerian model, unless the bottom topography is sufficiently small ($h_b \sim Ro$).

Let us finally argue that the stability by coarse-graining is a desirable physical property for the equilibrium states.

The first argument is a body of empirical observations. In either experiments, geophysical flows or numerical simulations flows governed by the shallow water equations (or the Navier-Stokes equations or the primitive equations in a shallow water regime) in the inertial limit (when they are subjected to weak forcing and dissipation, with a clear time scale separation) do actually self-organize and form large scale coherent structures for which there is a gradual decoupling of the flow large scales and small scales. A prominent example is the velocity field of Jupiter's troposphere.

The second argument follows. Macrostates that evolve through an autonomous equation, must increase the Boltzmann entropy. This is a general result in statistical mechanics, which is a consequence of the definition of the macrostate entropy as a Boltzmann entropy. Indeed as the Boltzmann's entropy measure the number of microstates corresponding to a given macrostate, it must increase for most of initial conditions. When there is furthermore a concentration property (which is the case for the shallow water case, both the the Eulerian and sem–Lagrangian discretizations), the number of initial conditions for which the entropy can decrease decays exponentially with N (N is often the number of particles in statistical mechanics, here the number of degrees of freedom of our discretization). As a consequence, the set of equilibrium macrostates (entropy maxima) has to be stable through the dynamics for most initial conditions. In the shallow water case, in statistical equilibrium, obtained either using the semi-Lagrangian or Eulerian discretization discussed above, the stream function concentrates close to a single field (the stream function fluctuations vanish in the large N limit). As a consequence the macrostate stream function, which is a single field thanks to this concentration property, has to be stationary for the dynamics. Those two properties, that follow from the definition of the Boltzmann entropy, are actually verified for the equilibrium measure constructed from a semi-Lagrangian discretization, but not for the equilibrium measure constructed from a Eulerian discretization. For this reason, we conclude that the microcanonical measure constructed from the purely Eulerian discretization is inconsistent with the shallow water dynamics.

We note moreover that the stability of the equilibrium macrostates through coarse graining ensures that the equilibrium states of the inviscid system are not affected by perturbations such as a weak small scale dissipation in momentum equations. This property is not a-priori required for the invariant measure of the shallow-water equations. However It is extremely interesting as it is a hint that this invariant measure may be relevant for non perfect flow in the inertial limit.

Appendix 6: Energy–enstrophy Ensemble

Computation of the Critical Points

In this Appendix, we compute the solutions of the variational problem (158) and describe the corresponding phase diagram. Critical points of the variational problem (158) are computed through the variational principle:

$$\forall \delta\rho_g, \quad \delta\mathscr{S}_{mf,g} - \frac{1}{E_{fluct}}\delta\mathscr{E}_{mf,g} - \gamma_2\delta\mathscr{Z}_{g2} - \gamma_1\delta\mathscr{Z}_{g1} - \int \mathrm{d}\mathbf{x}\, \xi(\mathbf{x}) \int \mathrm{d}\sigma_q\, \delta\rho_g = 0, \tag{230}$$

where γ_2, γ_1 and $\xi($**x** are Lagrange multipliers associated with the enstrophy conservation, the circulation conservation, and the normalization respectively. Anticipating the coupling between the large scale quasi-geostrophic flow and the small scale fluctuations, the temperature is denoted E_{fluct} (the inverse temperature is the Lagrange parameter associated with energy conservation).This yields

$$\rho_g\left(\mathbf{x}, \sigma_q\right) = \sqrt{\frac{1}{2\pi\left(Z_2 - \overline{Z}_2\right)}} \exp\left[-\frac{1}{2\left(Z_2 - \overline{Z}_2\right)}\left(\sigma_q - \left(\frac{\psi_{mf}}{E_{fluct}} - \gamma_1\right)\left(Z_2 - \overline{Z}_2\right)\right)^2\right] \tag{231}$$

where we have introduced the enstrophy of the coarse-grained potential vorticity

$$\overline{Z}_2 \equiv \int \mathrm{d}\mathbf{x}\overline{q}_g^2. \tag{232}$$

Injecting (231) in Eq. (147), using the mass conservation constraint given in Eq. (144) and the zero circulation constraint $\mathscr{Z}_1\left[\overline{q}_g\right] = 0$ yields

$$\overline{q}_g = \widetilde{\beta}\psi_{mf} \quad \text{with } \widetilde{\beta} \equiv \frac{\left(Z_2 - \overline{Z}_2\right)}{E_{fluct}}. \tag{233}$$

Note that $\widetilde{\beta}$ is necessarily positive given that $Z_2 - \overline{Z}_2 \geq 0$. Injecting Eq. (233) in Eq. (149), the streamfunction can be computed explicitly by solving

$$\widetilde{\beta}\psi_{mf} = \Delta\psi_{mf} - \frac{1}{R^2}\psi_{mf} + h_b. \tag{234}$$

In order to solve this equation, it is convenient to introduce the Laplacian eigenmodes of the domain $\mathscr{D}$, with $k \in \mathbb{N}^+$:

$$\Delta e_k = -\lambda_k^2 e_k \quad \text{with } e_k = 0 \text{ on} \partial\mathscr{D}, \tag{235}$$

where the eigenvalues $-\lambda_k^2$ are arranged in decreasing order. We assume those eigenvalues are pairwise distinct. We also assume that the bottom topography is sufficiently smooth such that $\sum_k |h_{bk}|^2 \lambda_k^2 < +\infty$. Then, given that $\widetilde{\beta} > 0$, the projection of the mean flow streamfunction on the Laplacian eigenmode $e_k(\mathbf{x})$ is obtained directly from Eq. (234):

$$\psi_k = \frac{h_{bk}}{\widetilde{\beta} + \lambda_k^2 + R^{-2}}. \tag{236}$$

We see that there is a unique solution ψ_{mf} for each value of $\widetilde{\beta}$. This solution is therefore the equilibrium state. All the large scale flows associated with statistical equilibrium states of

the shallow water system restricted to the energy–enstrophy ensemble with zero circulation are obtained from Eq. (236) when varying $\widetilde{\beta}$ from 0 to $+\infty$.

Construction of the Phase Diagram

The problem is now to find which equilibrium state is associated with the constraints (E, Z_2). In the following, we explain how to find the equilibrium states associated with parameters (E_{mf}, Z_2), and how to compute the temperature E_{fluc} for each of those states. It is then straightforward to obtained the total energy $E = E_{mf} + E_{fluc}$.

Injecting Eq. (236) in the expression of the quasi-geostrophic mean-flow energy defined in Eq. (150) yields

$$E_{mf} = \frac{1}{2}\sum_{k=1}^{+\infty}\left(\lambda_k^2 + R^{-2}\right)\left(\frac{|h_{bk}|}{\widetilde{\beta} + \lambda_k^2 + R^{-2}}\right)^2. \tag{237}$$

The mixing energy E_{mix} defined in Eq. (155) is recovered for $\widetilde{\beta} = 0$, given that $Z_1 = 0$. In the range $\widetilde{\beta} > 0$, the energy E_{mf} is a decreasing function of $\widetilde{\beta}$, varying from $E_{mf} = E_{mix}$ to $E_{mf} = 0$, see Fig. 5b, d.

Injecting Eq. (236) in the expression of the macroscopic enstrophy given in Eq (232) yields

$$\overline{Z_2} = \sum_{k=1}^{+\infty}|h_{bk}|^2\left(1 - \frac{\lambda_k^2 + R^{-2}}{\widetilde{\beta} + \lambda_k^2 + R^{-2}}\right)^2. \tag{238}$$

The potential enstrophy Z_b defined in Eq. (159) is recovered for $\widetilde{\beta} = +\infty$. The macroscopic enstrophy $\overline{Z_2}$ is an increasing function of $\widetilde{\beta}$, varying from $\overline{Z_2} = 0$ (for $\widetilde{\beta} = 0$) to $\overline{Z_2} = Z_b$ for ($\widetilde{\beta} = +\infty$), see Fig. 5a, c.

Two expressions of the macroscopic enstrophy $\overline{Z_2}$ in terms of the parameters $\widetilde{\beta}$ have been obtained: one is given by Eq. (238), the other arises from the definition of $\widetilde{\beta}$ in Eq. (233), which yields

$$\overline{Z_2} = Z_2 - E_{fluct}\widetilde{\beta}. \tag{239}$$

For given values of E_{fluct} and Z_2, the values of $\widetilde{\beta}$ and $\overline{Z_2}$ are obtained by finding the intersection between the two curves defined in Eq. (238) and (239), respectively. Once $\widetilde{\beta}$ is obtained, Eq. (237) gives directly the value of the mean-flow energy E_{mf}. The phase diagram presented in Fig. 2 is obtained numerically by using this procedure. Graphical arguments presented in the following allow to understand the structure of this phase diagram.

Limit Cases for the Energy Partition

Let us first note through Fig. 5a, c that $\widetilde{\beta}$ is an decreasing function of E_{fluct}. Indeed, $\widetilde{\beta}$ is given by the intersection between the solid curve representing the expression of $\overline{Z_2}$ given Eq. (238) and the dashed line representing the affine expression of $\overline{Z_2}$ given Eq. (239) where $-E_{fluct}$ is the slope. Then we know that the total energy $E = E_{mf}(\widetilde{\beta}) + E_{fluct}$ is an increasing function of E_{fluct}. Let us now consider different limit cases.

The limit $E \to \infty$ with Z_2 fixed In this limit, we have also $E_{fluct} \to \infty$. and $\widetilde{\beta} \to 0$ Hence, one gets from Eq. (237) (see also Fig. 5b, d):

$$\lim_{E\to+\infty} E_{mf} = E_{mix}, \quad \lim_{E\to+\infty}\frac{E_{mf}}{E} = 0. \tag{240}$$

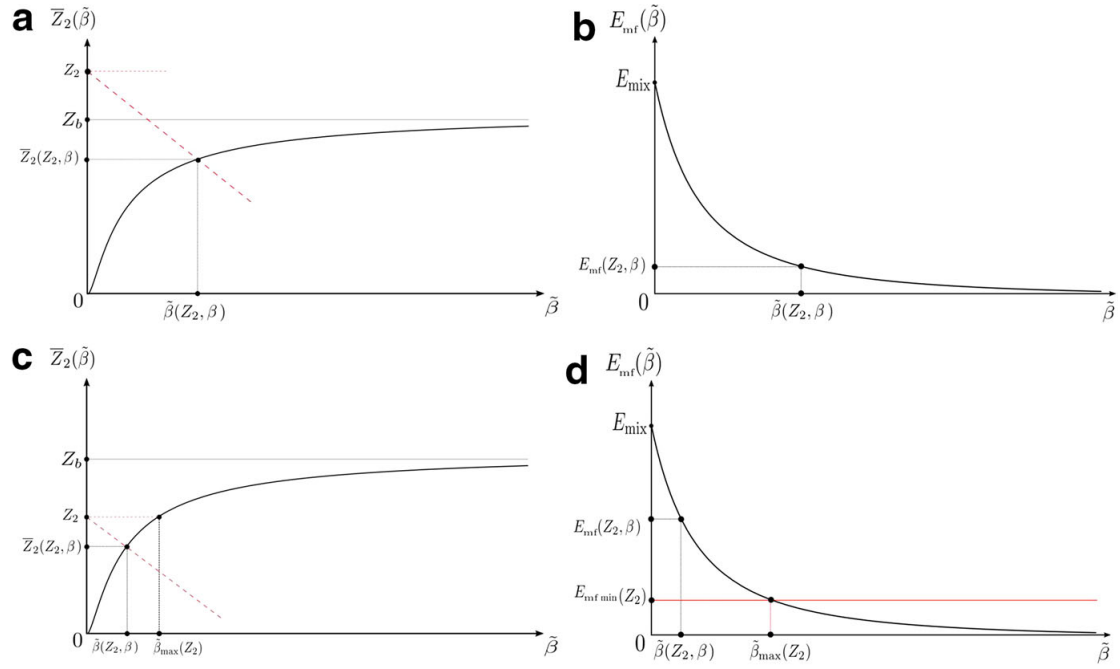

Fig. 5 **a** Variation of the macroscopic enstrophy Z_2 over $\widetilde{\beta}$, case $Z_2 > Z_b$. **b** Variation of the mean-flow energy E_{mf} with $\widetilde{\beta}$, case $Z_2 < Z_b$. c) Variation of the macroscopic enstrophy Z_2 with $\widetilde{\beta}$, case $Z_2 < Z_b$. d) Variation of the mean-flow energy E_{mf} with $\widetilde{\beta}$, case $Z_2 < Z_b$

The lowest E limit with $Z_2 < Z_b$ fixed In this limit, we have also $E_{fluct} \to 0$. One gets from Fig. 5-c that $\widetilde{\beta} \to \widetilde{\beta}_{max}(Z_2)$. Hence, E_{mf} reaches a minimum admissible energy $E_{min}(Z_2) = E_{mf}\left(\widetilde{\beta}_{max}(Z_2)\right)$. Then:

$$\lim_{E \to E_{min}(Z_2)} \frac{E_{mf}}{E} = 1. \tag{241}$$

The limit $E \to 0$ with $Z_2 > Z_b$ fixed In this limit, we have also $E_{fluct} \to 0$. One gets from Fig. 5a that $\widetilde{\beta} \to \infty$ and that $\overline{Z}_2 \to Z_b$. Hence, from Eqs. (237) and (239), we obtain:

$$\begin{cases} E_{mf} = C_b \widetilde{\beta}^{-2} + o\left(\widetilde{\beta}^{-2}\right) \\ \widetilde{\beta} \underset{E \to 0}{\sim} (Z_2 - Z_b)\, E_{fluct}^{-1} \end{cases}, \quad \text{with} \quad C_b = \frac{1}{2} \sum_{k=1}^{+\infty} |h_{bk}|^2 \left(\lambda_k^2 + R^{-2}\right). \tag{242}$$

Here, C_b is a constant depending on the topography only. Thus we have $E_{mf} \sim E_{fluct}^2 C_b / (Z_2 - Z_b)^2$, which leads to:

$$\lim_{E \to 0} \frac{E_{mf}}{E_{fluct}} = 0, \quad \lim_{E \to 0} \frac{E_{mf}}{E} = 0. \tag{243}$$

The limit $E \to 0$ with $Z_2 - Z_b \sim C_\alpha E^\alpha$ with $\alpha \geq 0$ In this limit, we have $E_{fluct} \to 0$. One gets from Fig. 5a that $\widetilde{\beta} \to \infty$. Hence, from Eqs. (237) and (238), we obtain:

$$\begin{cases} E_{mf} = C_b \widetilde{\beta}^{-2} + o\left(\widetilde{\beta}^{-2}\right) \\ Z_b - \overline{Z}_2 = 4 C_b \widetilde{\beta}^{-1} + o\left(\widetilde{\beta}^{-1}\right) \end{cases}, \tag{244}$$

where C_b is defined in Eq. (242). From those two equations along with Eq. (239) and using $Z_2 - Z_b \sim C_\alpha E^\alpha$, we can extract:

$$\widetilde{\beta} \underset{E \to 0}{\sim} \frac{C_\alpha E^\alpha + \sqrt{C_\alpha^2 E^{2\alpha} + 20 C_b E}}{2E}. \tag{245}$$

Now, we have to consider different cases for the value of α.

For $\alpha > 1/2$, we have from Eq. (245) that $\widetilde{\beta} \sim \sqrt{5C_b}E^{-1/2}$. Injecting this in Eq. (244), we gets:

$$\lim_{E\to 0} \frac{E_{mf}}{E} = \frac{1}{5} \tag{246}$$

For $\alpha < 1/2$, we have from Eq. (245) that $\widetilde{\beta} \sim C_\alpha E^{\alpha-1}$. Injecting this in Eq. (244), we gets:

$$\lim_{E\to 0} \frac{E_{mf}}{E} = 0 \tag{247}$$

For $\alpha = 1/2$, we have from Eq. (245) that $\widetilde{\beta} \sim C_{1/2}E^{-1/2}\left(1+\sqrt{1+20C_b/C_\alpha^2}\right)/2$. Injecting this in Eq. (244), we gets:

$$\lim_{E\to 0} \frac{E_{mf}}{E} = \frac{2C_b/C_\alpha^2}{\left(1+\sqrt{1+20C_b/C_\alpha^2}\right)^2}. \tag{248}$$

Contrary to the previous cases, here, the partition of the energy depends on the bottom topography.

References

1. Bouchet, F.: Simpler variational problems for statistical equilibria of the 2D Euler equation and other systems with long range interactions. Physica D **237**(14), 1976–1981 (2008)
2. Bouchet, F.: Statistical mechanics for geophysical flows. PhD Thesis, Université Joseph Fourier-Grenoble (December 2008)
3. Bouchet, F., Sommeria, J.: Emergence of intense jets and Jupiter's Great Red Spot as maximum-entropy structures. J. Fluid Mech. **464**, 165–207 (2002). doi:10.1017/S0022112002008789
4. Bouchet, F., Venaille, A.: Statistical mechanics of two-dimensional and geophysical flows. Phys. Rep. **515**, 227–295 (2012). doi:10.1016/j.physrep.2012.02.001
5. Bourgain, J.: Periodic nonlinear Schrödinger equation and invariant measures. Commun. Math. Phys. **166**(1), 1–26 (1994)
6. Chavanis, P.H., Sommeria, J.: Classification of self-organized vortices in two-dimensional turbulence: the case of a bounded domain. J. Fluid Mech. **314**, 267–297 (1996)
7. Chavanis, P.H., Sommeria, J.: Statistical mechanics of the shallow water system. Phys. Rev. E **65**(2), 026302 (2002)
8. Dubinkina, S., Frank, J.: Statistical relevance of vorticity conservation in the Hamiltonian particle-mesh method. J. Comput. Phys. **229**, 2634–2648 (2010). doi:10.1016/j.jcp.2009.12.012
9. Dubinkina, S., Frank, J.: Statistical relevance of vorticity conservation in the Hamiltonian particle-mesh method. J. Comput. Phys. **229**(7), 2634–2648 (2010)
10. Eyink, G.L., Sreenivasan, K.R.: Onsager and the theory of hydrodynamic turbulence. Rev. Mod. Phys. **78**, 87–135 (2006). doi:10.1103/RevModPhys.78.87
11. Farge, M., Sadourny, R.: Wave-vortex dynamics in rotating shallow water. J. Fluid Mech. **206**, 433–462 (1989)
12. Fofonoff, N.P.: Steady flow in a frictionless homogeneous ocean. J. Mar. Res. **13**, 254–262 (1954)
13. Frank, J., Gottwald, G., Reich, S.: A Hamiltonian particle-mesh method for the rotating shallow-water equations. In: Meshfree Methods for Partial Differential Equations, pp. 131–142. Springer, Berlin (2003)
14. Gertz, A., Straub, D.N.: Near-inertial oscillations and the damping of midlatitude gyres: a modeling study. J. Phys. Oceanogr. **39**(9), 2338–2350 (2009)
15. Herbert, C.: Additional invariants and statistical equilibria for the 2D Euler equations on a spherical domain. J. Stat. Phys. **152**(6), 1084–1114 (2013)
16. Herbert, C., Pouquet, A., Marino, R.: Restricted equilibrium and the energy cascade in rotating and stratified flows. J. Fluid Mech. **758**, 374–406 (2014)

17. Majda, A.J., Wang, X.: Nonlinear Dynamics and Statistical Theories for Basic Geophysical Flows. Cambridge University Press, Cambridge (2006)
18. Majda, A.J., Wang, X.: The emergence of large-scale coherent structure under small-scale random bombardments. Commun. Pure Appl. Math. **59**(4), 467–500 (2006)
19. Merryfield, W.J.: Effects of stratification on quasi-geostrophic inviscid equilibria. J. Fluid Mech. **354**, 345–356 (1998)
20. Merryfield, W.J., Cummins, P.F., Holloway, G.: Equilibrium statistical mechanics of barotropic flow over finite topography. J. Phys. Oceanogr. **31**, 1880–1890 (2001)
21. Michel, J., Robert, R.: Large deviations for young measures and statistical mechanics of infinite dimensional dynamical systems with conservation law. Commun. Math. Phys. **159**, 195–215 (1994)
22. Miller, J.: Statistical mechanics of euler equations in two dimensions. Phys. Rev. Lett. **65**(17), 2137–2140 (1990). doi:10.1103/PhysRevLett.65.2137
23. Miller, J., Weichman, P.B., Cross, M.C.: Statistical mechanics, Euler's equation, and Jupiter's Red Spot. Phys. Rev. A **45**, 2328–2359 (1992). doi:10.1103/PhysRevA.45.2328
24. Miranda, A., Barnier, B., Dewar, W.K.: On the dynamics of the Zapiola anticyclone. J. Geophys. Res. (1978–2012) **104**(C9), 21137–21149 (1999)
25. Nageswaran, V., Turkington, B.: Minmax variational principle for steady balanced solutions of the rotating shallow water equations. Commun. Math. Sci. **8**(2), 321–339 (2010)
26. Naso, A., Chavanis, P.H., Dubrulle, B.: Statistical mechanics of two-dimensional Euler flows and minimum enstrophy states. Eur. Phys. J. B **77**, 187–212 (2010)
27. Naso, A., Monchaux, R., Chavanis, P., Dubrulle, B.: Statistical mechanics of Beltrami flows in axisymmetric geometry: theory reexamined. Phys. Rev. E **81**, 066318 (2010)
28. Onsager, L.: Statistical hydrodynamics. Nuovo Cimento 6 **2**(Suppl.), 249–286 (1949)
29. Pedlosky, J.: Geophysical Fluid Dynamics. Springer, Berlin (1982)
30. Robert, R.: Etats d'équilibre statistique pour l'écoulement bidimensionnel d'un fluide parfait. C. R. Acad. Sci. **1**(311), 575–578 (1990)
31. Robert, R.: A maximum-entropy principle for two-dimensional perfect fluid dynamics. J. Stat. Phys. **65**, 531–553 (1991)
32. Robert, R.: On the statistical mechanics of 2D Euler equation. Commun. Math. Phys. **212**, 245–256 (2000)
33. Robert, R., Sommeria, J.: Statistical equilibrium states for two-dimensional flows. J. Fluid Mech. **229**, 291–310 (1991). doi:10.1017/S0022112091003038
34. Robert, R., Sommeria, J.: Relaxation towards a statistical equilibrium state in two-dimensional perfect fluid dynamics. Phys. Rev. Lett. **69**(19), 2776–2779 (1992). doi:10.1103/PhysRevLett.69.2776
35. Salmon, R.: Lectures on Geophysical Fluid Dynamics. Oxford University Press, Oxford (1998)
36. Salmon, R.: The shape of the main thermocline, revisited. J. Mar. Res. **68**(3–4), 541–568 (2010)
37. Sansón, L.Z., González-Villanueva, A., Flores, L.: Evolution and decay of a rotating flow over random topography. J. Fluid Mech. **642**, 159–180 (2010)
38. Saunders, P.M., King, B.A.: Bottom currents derived from a shipborne ADCP on WOCE cruise A11 in the South Atlantic. J. Phys. Oceanogr. **25**(3), 329–347 (1995)
39. Smith, W.H.F., Sandwell, D.T.: Global seafloor topography from satellite altimetry and ship depth soundings. Science **277**, 1957–1962 (1997)
40. Thalabard, S.: Contributions to the statistical mechanics of ideal two and a half dimensional flows. PhD Thesis, Université Paris Sud-Paris XI (2013)
41. Thalabard, S., Dubrulle, B., Bouchet, F.: Statistical mechanics of the 3D axisymmetric Euler equations in a Taylor–Couette geometry. J. Stat. Mech. (2014). doi:10.1088/1742-5468/2014/01/P01005
42. Thalabard, S., Saint-Michel, B., Herbert, É., Daviaud, F., Dubrulle, B.: Ferro-turbulence: a statistical mechanics framework for the large-scale structure of turbulent von Karman flows. New J. Phys. **17**(6), 063006 (2015)
43. Touchette, H.: The large deviation approach to statistical mechanics. Phys. Rep. **478**(1), 1–69 (2009)
44. Turkington, B., Majda, A., Haven, K., Dibattista, M.: Statistical equilibrium predictions of jets and spots on Jupiter. Proc. Natl Acad. Sci. U.S.A. **98**, 12346–12350 (2001)
45. Vallis, G.K.: Mechanisms and parameterizations of geostrophic adjustment and a variational approach to balanced flow. J. Atmos. Sci. **49**, 1144–1160 (1992)
46. Vallis, G.K.: Atmospheric and Oceanic Fluid Dynamics (2006). doi:10.2277/0521849691
47. Vanneste, J.: Balance and spontaneous wave generation in geophysical flows. Annu. Rev. Fluid Mech. **45**, 147–172 (2013)
48. Venaille, A.: Bottom-trapped currents as statistical equilibrium states above topographic anomalies. J. Fluid Mech. **699**, 500–510 (2012)
49. Venaille, A., Bouchet, F.: Statistical ensemble inequivalence and bicritical points for two-dimensional flows and geophysical flows. Phys. Rev. Lett. **102**(10), 104501 (2009)

50. Venaille, A., Bouchet, F.: Oceanic rings and jets as statistical equilibrium states. J. Phys. Oceanogr. **41**, 1860–1873 (2011). doi:10.1175/2011JPO4583.1
51. Venaille, A., Bouchet, F.: Solvable phase diagrams and ensemble inequivalence for two-dimensional and geophysical turbulent flows. J. Stat. Phys. **143**(2), 346–380 (2011)
52. Venaille, A., Vallis, G., Griffies, S.: The catalytic role of the beta effect in barotropization processes. J. Fluid Mech. **709**, 490–515 (2012)
53. Warn, T.: Statistical mechanical equilibria of the shallow water equations. Tellus A **38**, 1–11 (1986)
54. Weatherly, G.L.: On deep-current and hydrographic observations from a mudwave region and elsewhere in the Argentine basin. Deep Sea Res. Part II **40**(4), 939–961 (1993)
55. Weichman, P.B.: Equilibrium theory of coherent vortex and zonal jet formation in a system of nonlinear Rossby waves. Phys. Rev. E **73**(3), 036313 (2006)
56. Weichman, P.B., Petrich, D.M.: Statistical equilibrium solutions of the shallow water equations. Phys. Rev. Lett. **86**, 1761–1764 (2001)
57. Xie, J.H., Vanneste, J.: A generalised-lagrangian-mean model of the interactions between near-inertial waves and mean flow. arXiv preprint arXiv:1411.3748 (2014)
58. Young, W., Ben Jelloul, M.: Propagation of near-inertial oscillations through a geostrophic flow. J. Mar. Res. **55**(4), 735–766 (1997)

7. Conclusion

In this thesis, we tackled three problems involving the interaction between rapidly oscillating gravity waves and slowly evolving mean flows: i) We revisited idealised models for the equatorial reversals of zonal winds focusing on the nature of its variability taking a dynamical system point of view with an application to quasi-biennial oscillation on Earth. ii) With the use of a quasilinear approximation and multi-scale asymptotic expansion techniques, we addressed the generation of mean flows within the viscous boundary layers of internal waves. iii) Using the tools of equilibrium statistical mechanics, we studied the partition between gravity waves and mean flow in the shallow-water system. These different works participate in the broader study of the multi-scale dynamics of macroscopic geophysical structures or patterns through the development and analysis of reduced models.

After two introductory chapters - the first acquainted us with internal gravity waves streaming, the second derived a simplified coupled wave-mean flow model based on a quasilinear approximation and multi-scale expansions - , the last three chapters detailed the main contributions of this thesis with respect to the three problems considered. We now provide a summary of the key results and their associated perspectives, chapter by chapter, followed by a list of the published and submitted scientific publications.

7.1 Bifurcations in model quasi-biennial oscillation

Key results

In Chapter 4, we investigated the recently observed periodicity disruption of the quasi-biennial oscillation (QBO) on Earth and attempted to assess whether its variability is of extrinsic or intrinsic nature. We revisited idealised models of the QBO and highlighted a possible intrinsic origin of its variability. This study led essentially to four results:

- Considering the canonical 1D model of the QBO, we revisited the bifurcation from a stable rest state towards the periodic limit cycle building on previous work by Yoden & Holton [171]. While Yoden & Holton considered a no-slip bottom condition for the mean flow, we considered the free-slip case, allowing us to analytically derive a prediction for the critical parameter at which the bifurcation take places. We also showed that the bifurcation is different from the Hopf bifurcation of the no-slip case. This study is provided in appendix B. To our knowledge, such analytical prediction

had never been derived in the literature regarding the standard 1D model of the QBO.
– When the wave forcing is further increased in the 1D model, we exhibited the existence of additional intrinsic bifurcations towards regimes with disrupted periodicity. The first glimpse into these altered periodicity has already been provided by Kim & McGregor [81] within a similar model applied to the solar tachocline. However, their pioneering observations were sparse, and they did not build any bifurcation diagram. Here, we have filled this gap: introducing an additional parameter, we analysed in details the bifurcation diagrams and unveiled a rich and complex road-map to chaos with frequency-locked states embedded in quasiperiodic or chaotic states. This result is discussed in section 4.3.
– We conducted fully nonlinear numerical simulations of a forced-dissipated stratified flow using the MIT general circulation model [96, 2]. We reported the existence of a bifurcation from periodic states towards quasiperiodic and frequency locked regimes. This showed that transitions observed in the quasilinear 1D models are robust to wave-wave interactions and should be observable in numerical models of higher complexity. This result is discussed in section 4.3.
– Within the periodic regime, we computed the relaxation time when the system is nudged out of its attractor. We exhibited a power-law divergence of this recovery time as the system approaches the secondary bifurcation from periodic to quasiperiodic states; a phenomenon often referred to as "critical slowing down". We are not aware of previous studies describing a critical slowing down for a transition from a limit cycle to a quasiperiodic oscillation. This observation, made in both the idealised 1D model and the fully nonlinear simulations, suggests that parts of the QBO variability may arise from its intrinsic dynamics. This contrasts with previous work linking its variability to the synchronisation with the annual cycle [126] or to extra-tropical influences [29, 48]. This result is discussed in section 4.3.

Perspectives

These works suggest us several extended studies. The bifurcation from the rest state towards periodic solutions needs to be better characterised. It will be useful for that purpose to derive normal forms. Then, such reduced model could be a starting point to study similar quasi-periodic route to chaos in a simpler setting. To address the relevance of this route to chaos for the actual QBO, it will be necessary to consider more comprehensive atmospheric numerical models, including rotation, 3D effects, and realistic forcing. To do this, we could build upon the configuration of the MIT general circulation model that we have already used for this work. We could also build upon the recent 3D simulations of gas giants conducted by Showman and al. [1] who observed low-frequency reversals of equatorial zonal winds. The rotation could deserve a particular attention as the mechanism by which it controls the meridional extent of the QBO is still poorly understood.

It would also be interesting to see how the synchronisations on the seasonal cycle [126] coexist with the quasiperiodic route to chaos. Another important point to address is whether reproducing this route to chaos is attainable in laboratory (using, for instance, the experimental set up of [147]). The strong mixing induced by the large-amplitude waves may well by crippling, unless the stratification is controlled by temperature.

7.2 Boundary streaming by internal waves

Key results

In Chapter 5, we exploited the analogy between internal gravity wave streaming and acoustic streaming to address the generation of mean flows within the viscous boundary layers of internal gravity waves; a phenomenon known as boundary streaming. While boundary streaming had thoroughly been studied in the context of acoustic wave streaming, it had never been addressed in association with internal gravity waves. We investigated boundary streaming using the zonally symmetric framework introduced in Chapter 3 along with multi-scale asymptotic expansions. This led to five main results:

- Just as in the case of acoustic waves, we reported the generation of a boundary flow within internal gravity wave viscous boundary layers that depend strongly on the considered boundary conditions. We considered both no-slip and free-slip conditions using a quasilinear approximation. In both cases, we showed that, at early-time, the boundary flow dominates over the bulk flow generated by the viscous damping of the wave beam. However, at a later time, the bulk streaming takes over the boundary streaming.
- For the free-slip case, we compared the quasilinear predictions to fully nonlinear simulations of the Boussinesq model (using the MIT general circulation model) with good agreements.
- In the no-slip scenario, we showed that the Reynolds stress divergence integrated over the domain vanishes. Consequently, the boundary streaming is opposite to the bulk and is much stronger than in the free-slip scenario. This leads to the rapid establishment of a strong boundary flow going in the opposite direction to the bulk flow.
- Following the approach of Muraschko and collaborators [111], we derived a novel WKB expansion for the propagation of viscous internal wave within a background shear flow, frozen in time.
- To address the interplay between boundary streaming, waves and mean-flows, we treated the case of a standing wave forcing. We used an *ad hoc* quasilinear truncation of the dynamics similar to the one used to describe the QBO in Chapter 4 but contains additional forcing terms representing the effect of boundary layers. We reported that boundary streaming significantly alters the mean flow reversals by either inhibiting them, decreasing their period or modifying their periodic structures.

Perspectives

A direct extension to this work would be to look at the boundary streaming associated with the reflection of an internal wave on a plane wall. Another important future task is to investigate the effect of higher nonlinearities. In particular, we should verify if the prediction that the integral of Reynolds stress divergence vanishes still holds when the boundary layer is nonlinear. In that case, the bulk streaming would necessarily be compensated by a strong and opposite streaming force at the bottom, driven by the nonlinear boundary layer. To do so, a Lagrangian-mean approach would become useful as it allows treating waves with finite amplitude. Finally, our quasilinear predictions for the no-slip scenario must be tested with additional fully nonlinear simulations allowing for the motion of immersed boundaries or, ideally, against laboratory experiments.

7.3 Statistical wave-mean flow equilibrium

Key results

In Chapter 6, we addressed a coupled wave-mean flow problem following an approach contrasting with quasilinear approximations and asymptotic expansions. Using the tools of statistical mechanics, we investigated stationary energy partition between gravity waves and the mean flow considering the free evolution of a fully nonlinear inviscid flow model. The simplest model accounting for the concomitant existence of gravity waves and vortical flows is the shallow-water model. While the application of equilibrium statistical mechanics to simple 2D fluid models, such as 2D-Euler or quasi-geostrophic models, had predicted a concentration of energy at large scales, the energy partition in the presence of surface waves has remained an open question. In our approach, the mean flow is defined through a coarse-graining procedure which amounts to a local spatial averaging. The fluctuations are interpreted as gravity wave motions. With the help of an intermediate finite dimensional model, we computed the statistical equilibria of the shallow-water system. This led to several results:

- We showed that equilibrium states of the shallow-water system are associated with the coexistence of a mean flow which is a stationary state of the shallow-water dynamics, superimposed with gravity waves that may contain in some cases a substantial part of the initial energy. In particular, we showed that a large-scale mean flow can emerge at equilibrium starting from an initial state with only waves. This effect could be called inviscid streaming to contrast with the streaming spawned by dissipation, studied in the previous chapters.
- We found that the presence of gravity waves implies a positive temperature for the equilibrium state which contrasts with the existence of negative temperature states for the previously studied 2D Euler or quasi-geostrophic models.
- We showed that the existence of non-zero equilibrium mean flow requires both rotation and bottom topography, or a non-zero initial circulation.
- In a weak energy limit, consistently with previous work by Warn [167], we found equipartition of the wave's kinetic and potential energy. We also obtained an interesting physical picture of the equilibrium state, which may be interpreted in that limit as two subsystems in thermal contact. A first subsystem is the mean flow and the second one corresponds to gravity waves. Considering the quasi-geostrophic limit for the mean flow, the associated subsystem becomes in every way equivalent to the quasi-geostrophic system. In our case, the thermal contact with the gravity waves subsystem selects a subclass of the quasi-geostrophic equilibria with positive temperature.

Perspectives

In the future, the dynamics of the relaxation towards equilibrium should be addressed along with out-of-equilibrium problems with both forcing and dissipation.

7.4 Scientific publications

- Published:
  A. Renaud, A. Venaille and F. Bouchet, "Equilibrium Statistical Mechanics and Energy Partition for the Shallow Water Model", *Journal of Statistical Physics*, 2016
  DOI: 10.1007/s10955-016-1496-x

- Under review:
  A. Renaud and A. Venaille, "Boundary Streaming by Internal Waves", *Journal of Fluid Mechanics*, 2018
  ARXIV:`https://arxiv.org/abs/1708.00068`
- Submitted:
  A. Renaud, L.P. Nadeau and A. Venaille, "Periodicity Disruption of a Model Quasi-Biennial Oscillation"

Additional contributions

- In preparation:
  F. Bouchet, E. Woillez, V. Lecomte and A. Renaud, "Lecture notes on large deviation theory and application to physics (provisional title)", chapter 4: *Large deviation principle for the empirical measure*

Appendices

A Numerical resolution of the 1D QBO-model

In this appendix, we present the numerical methods used to solve the Plumb's model summarised in frame 4.2.1.

For clarity, we reproduce here the integrodifferential equation

$$\partial_T \overline{u} - \frac{1}{\widetilde{F}} \partial_Z^2 \overline{u} = -\partial_Z \left(e^{-\int_0^Z \frac{\mathrm{d}Z'}{(1-\overline{u})^2}} - e^{-\int_0^Z \frac{\mathrm{d}Z'}{(1+\overline{u})^2}} \right), \tag{1}$$

along with the no-slip bottom condition

$$\overline{u}|_{Z=0} = 0. \tag{2}$$

Numerically, a finite sized domain must be considered such that an additional boundary condition must be considered at a height $Z_{\max}$. Here, we consider a free-slip boundary condition such that

$$\partial_Z \overline{u}|_{Z=Z_{\max}} = 0. \tag{3}$$

In subsection A1, we present our spatial discretisation scheme while the time discretisation scheme is discussed in subsection A2. The approach is largely inspired from a python script written by J.K. Vallis[1].

A1 Spatial discretisation: a second-order finite-difference scheme

We discretise the vertical axis in N_z+2 evenly spaced point between $Z=0$ and $Z=Z_{\max}$ labeled by $0 \leq n \leq N_z+1$ with vertical grid-step $\delta Z = Z_{max}/(N_z+1)$ (see Fig. 1). The mean flow $\overline{u}$ is spatially discretised on this grid with $\overline{u}_n = \overline{u}|_{Z=n\delta Z}$. The finite dimensional representation boundary conditions (2) and (3) imposes $\overline{u}_0 = 0$[2] and $\overline{u}_{N_z+1} = \overline{u}_{N_z}$. Finally, the undetermined part of the discretised flow is the N-dimensional vector $\{\overline{u}_n\}_{1\leq n\leq N_z}$.

[1] This code can be found on his web page:
`http://empslocal.ex.ac.uk/people/staff/gv219/codes/qbo.html`

[2] For a free-slip condition, simply consider $\overline{u}_0 = \overline{u}_1$ instead.

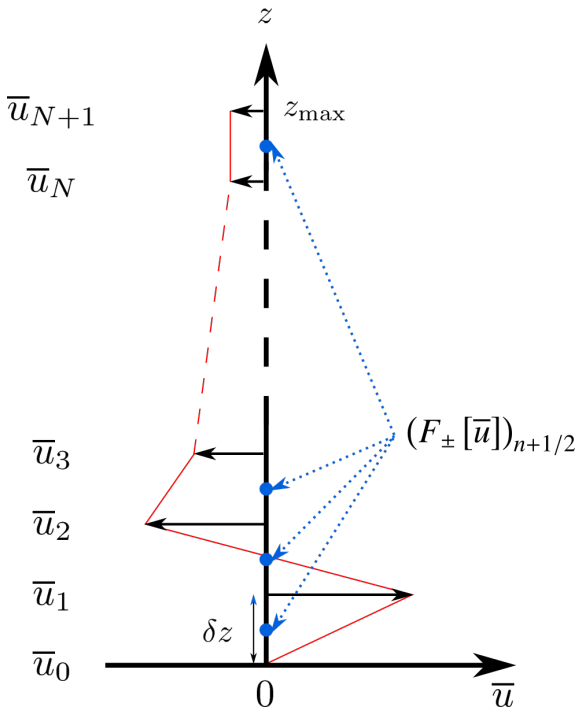

Figure 1: **Sketch of the vertical discretisation scheme.**

The Laplacian operator ∂_Z^2 is discretised using a centred finite difference scheme with

$$\left(\partial_Z^2 \overline{u}\right)_n \equiv \frac{\overline{u}_{n+1} - 2\overline{u}_n + \overline{u}_{n-1}}{\delta Z^2} \quad \forall 1 \leq n \leq N_z + 1. \tag{4}$$

Let us introduce the operator

$$F_\pm[\overline{u}] \equiv e^{-\int_0^Z \frac{\mathrm{d}Z'}{(1\mp\overline{u})^2}}. \tag{5}$$

We discretise this operator on a grid shifted by $\delta Z/2$

$$\left(F_\pm[\overline{u}]\right)_{n+1/2} \equiv e^{-\delta Z\left(\frac{1}{2(1-\overline{u}_0)^2} + \sum_{m=1}^{n} \frac{1}{(1\mp\overline{u}_m)^2}\right)} \quad \forall 0 \leq n \leq N_z, \tag{6}$$

where we used a direct trapezoidal quadrature. The index $n+1/2$ is used to keep track of the shifted grid (see Fig. 1). Finally, we the vertical derivative using the centered finite difference scheme with

$$\left(\partial_Z F_\pm[\overline{u}]\right)_n \equiv \frac{\left(F_\pm[\overline{u}]\right)_{n+1/2} - \left(F_\pm[\overline{u}]\right)_{n-1/2}}{\delta Z} \quad \forall 1 \leq n \leq N_z. \tag{7}$$

The streaming force on the right-hand side of Eq. (1) is thus discretised on the same grid as the mean flow.

Particularity in the presence of critical layers

If the mean flow exceeds the critical value 1 somewhere, we compute

$$n_c = \min\left\{1 \leq n \leq N_z \,|\, \overline{u}_n \geq 1\right\} \tag{8}$$

and set

$$(F_+[\overline{u}])_{n+1/2} = 0 \quad \forall n \geq n_c.. \tag{9}$$

This simple parametrisation amounts to assume that the wave necessarily breaks right-below the critical layer. Identical parametrisation is implemented for the opposite critical value -1.

A2 Time discretisation: three step Adams-Bashforth scheme

Equation (1) is order one in time. Forgetting about the spatial discretisation for a moment, this equation can formally be rewritten in the form

$$\partial_T \overline{u}(T) = f(T) \tag{10}$$

where $f(T)$ is a functional of the mean flow at time T. We discretise the time uniformly with timestep δT and label by i the field evaluated at $T = i\delta T$. We use a three steps Adams-Bashforth scheme to integrate (10) in time [140]. Starting from the initial condition $\overline{u}_0$, it gives

$$\begin{cases} \overline{u}_1 &= \overline{u}_0 + f_1 \delta T \\ \overline{u}_2 &= \overline{u}_1 + (3f_1 - f_0)\,\frac{\delta T}{2} \\ \overline{u}_i &= \overline{u}_{i-1} + (23f_{i-1} - 16f_{i-2} + 5f_{i-3})\,\frac{\delta T}{12} \quad \forall i \geq 3. \end{cases} \tag{11}$$

B QBO bifurcation with free-slip boundary condition

In this appendix, we compute analytically the critical parameter $\widetilde{F}_c$ of the 1D model (4.8) considering a bottom free-slip condition for the mean flow. To our knowledge, such analytical prediction has never been proposed in the literature.

For clarity let us rewrite the model's equation

$$\partial_T \overline{u} - \frac{1}{\widetilde{F}} \partial_Z^2 \overline{u} = -\partial_Z \left(e^{-\int_0^Z \frac{\mathrm{d}Z'}{(1-\overline{u})^2}} - e^{-\int_0^Z \frac{\mathrm{d}Z'}{(1+\overline{u})^2}} \right). \tag{12}$$

We consider a free-slip bottom boundary condition for the mean flow

$$\partial_Z \overline{u}|_{Z=0} = 0. \tag{13}$$

We further assume that the mean flow vanishes at infinity with $\overline{u}|_{Z\to\infty} = 0$.

B1 Linear-stability analysis

To investigate the linear stability of the rest state, let us linearise Eq. (12):

$$\partial_T \overline{u} - \frac{1}{\widetilde{F}} \partial_Z^2 \overline{u} = 4\partial_Z \left(e^{-Z} \int_0^Z \overline{u} \right). \tag{14}$$

To simplify this equation, let us introducing $U = \int_0^Z \overline{u}$. The free-slip condition (13) now writes $\partial_Z^2 U|_{Z=0} = 0$ and the additional bottom boundary condition $U|_{Z=0} = 0$ must be

fulfilled. At infinity, we have $\partial_Z U_{Z\to\infty} = 0$. Integrating the linearised equation (14) from 0 to Z gives

$$\partial_T U - \frac{1}{\widetilde{F}}\partial_Z^2 U = 4e^{-Z}U. \tag{15}$$

Performing the change of variable $Z \to X = 4e^{-Z/2}\sqrt{\widetilde{F}}$, Eq. (15) can be rewritten in the form

$$\partial_T U = \frac{4}{\widetilde{F}}\left(X^2\partial_X^2 + X\partial_X + X^2\right)U. \tag{16}$$

In terms of X, the boundary conditions $U|_{Z=0} = 0$ and $\partial_Z U|_{Z\to\infty}$ write

$$\begin{cases} U\left(4\sqrt{\widetilde{F}}\right) & = 0 \quad (17a) \\ (X\partial_X U)|_{X\to 0} & = 0. \quad (17b) \end{cases}$$

The rest state is stable if the operator on the right-hand side of Eq. (16) admits eigenvalues with a negative real part only. The operator $X^2\partial_X^2 + X\partial_X + X^2$ associated with the boundary conditions (17) is Hermitian in $]0, 4\sqrt{\widetilde{F}}]$. As a consequence, its eigenvalues are real and so is the largest one. The QBO bifurcation occurs when the largest eigenvalue passes from negative to positive.

The critical eigenvalue problem takes the form of the zeroth order Bessel differential equation

$$X^2\partial_X^2 U + X\partial_X U + X^2 U = 0, \tag{18}$$

whose solutions are written in terms of zeroth order Bessel functions

$$U(X) = C_1 J_0(X) + C_2 Y_0(X), \tag{19}$$

where J_0 and Y_0 are the Bessel function of the first and second kind respectively and C_1 and C_2 are two integration constant. We have $(X\partial_X J_0)|_{X\to 0} = 0$ and $(X\partial_X Y_0)|_{X\to 0} = 2/\pi$ such that the boundary condition in (17b) yields $C_2 = 0$. Looking for non-zero solution, the boundary condition (17a) leaves us with the condition

$$J_0\left(4\sqrt{\widetilde{F}_c}\right) = 0. \tag{20}$$

At the critical value $\widetilde{F}_c$, the largest eigenvalue of the operator on the right-hand side of (16) must be zero. Then, $4\sqrt{\widetilde{F}_c}$ is necessarily the first non-zero root of the J_0, denoted $j_{0,1}$. Indeed, any higher order root of J_0 is also a root of a higher order Bessel function J_α with $\alpha > 0$. Then, α^2 is the largest eigenvalue and greater than zero.

The critical value thus writes

$$\widetilde{F}_c = \frac{j_{0,1}^2}{16} \approx 0.36. \tag{21}$$

Discussion

The free-slip case allows for an analytical prediction of the critical parameter $\widetilde{F}_c$ for the bifurcation from the rest state to the periodic limit cycle. Figure 4.8c (page 73) shows peak-to-peak amplitude of the stationary state obtained by solving directly the fully nonlinear 1D model starting from a random initial condition. The prediction of the critical value $\widetilde{F}_c$ obtained in Eq. (21) is in very good agreement with the one obtained by the direct numerical resolution of the model.

An additional interesting observation given by the linear stability analysis is that above the threshold $\widetilde{F}_c$, the growth rates obtained with the eigenvalue problem are real and positive without imaginary parts. Oscillation arises necessarily due to the presence of nonlinearity. The period of the limit cycles computed with the direct resolution of the model is diverging when approaching the threshold (see Fig. 4.8d). This behavior is strikingly different from the no-slip problem (see fig 4.8b). In addition, there is more than an order of magnitude difference for the critical value $\widetilde{F}_c$ between the two cases.

Let us remark that the free-slip condition is considered for the mean flow only. The momentum flux associated with the two contra-propagating waves are assumed to be symmetric. This is true only if the mean flow vanishes at the bottom with $\overline{u}|_{z=0} = 0$; then, the momentum flux expressions obtained in Eq. (4.3) are indeed symmetric at the bottom.

There is another possibility to recover a symmetric momentum flux bottom value without requiring the mean flow to vanish at the bottom. Let us assume that the amplitude of the wave at the bottom depends on the bottom mean flow amplitude such that the boundary condition (3.79) is modified in the following way

$$\tilde{\psi}(0) = -\varepsilon\sqrt{1-\overline{u}|_{z=0}}. \tag{22}$$

Then, the momentum flux (4.3) becomes symmetric at the bottom.

Finer study of the effect of the choice of the boundary condition should be made.

C Poincaré sections and bifurcation diagram of the QBO regimes

This appendix summerise the method used to compute the bifurcation diagrams shown in section 4.3.

In order to build a bifurcation diagram, we compute a Poincaré section of the mean flow $\overline{u}(Z,T)$. In a first step, we project the phase space trajectories on a 2D space defined by the mean flow taken at two different heights: $u_1 = \overline{u}(Z = Z_1, T)$ and $u_2 = \overline{u}(Z = Z_2, 0)$ with $Z_1 < Z_2$. Then, we store the values the upper mean flow $u_2(T)$ takes when the reversals occur at the bottom with $\overline{u}_2$. For each value of $\widetilde{F}$, we have an ensemble of mean flow values

$$\mathbb{O}_{\widetilde{F}} = \{\overline{u}(Z = Z_2, T) \,|\, \overline{u}(Z = Z_1, T) = 0\}. \tag{23}$$

Now, the bifurcation diagram can be generated by plotting in a $\overline{u}_2 \times \widetilde{F}$ panel the scatter graph of the following ensemble

$$\bigcup_{\widetilde{F}} \left\{ \bigcup_{\overline{u}_2 \in \mathbb{O}_{\widetilde{F}}} \left\{ \left(\overline{u}_2, \widetilde{F} \right) \right\} \right\}. \tag{24}$$

An other way is to compute a histogram of the ensembles $\mathbb{O}_{\widetilde{F}}$ and plot them as a function of $\widetilde{F}$ with a binary colourmap darking out the populated bins while keeping white the empty ones. Figure 4.11 summarises this method (with $(Z_1, Z_2) = (0.1, 0.3)$.

Bibliography

[1] X. Zhang A.P. Showman X. Tan. "Atmospheric Circulation of Brown Dwarfs and Jupiter and Saturn-like Planets: Zonal Jets, Long-term Variability, and QBO-type Oscillations". In: *arXiv* (2018). DOI: arXiv:1807.08433.

[2] A. Adcroft et al. *MIT-gcm's user manual*. https://mitgcm.readthedocs.io/en/latest/. 2018.

[3] F. Ait-Chaalal et al. "Cumulant expansions for atmospheric flows". In: *New Journal of Physics* (2016). DOI: 10.1088/1367-2630/18/2/025019.

[4] M.K. Aktas and B. Farouk. "Numerical simulation of acoustic streaming generated by finite-amplitude resonant oscillations in an enclosure". In: *The Journal of the Acoustical Society of America* (2004). DOI: 10.1121/1.1795332.

[5] D. G. Andrews and M. E. McIntyre. "Planetary Waves in Horizontal and Vertical Shear: The Generalized Eliassen-Palm Relation and the Mean Zonal Acceleration". In: *Journal of the Atmospheric Sciences* (1976). DOI: 10.1175/1520-0469(1976)033<2031:PWIHAV>2.0.CO;2.

[6] P.G. Baines. "Internal Tides, Internal Waves and Near-Inertial Motions". In: *Baroclinic Processes on Continental Shelves*. 2013. Chap. 2. DOI: 10.1029/CO003p0019.

[7] M.P. Baldwin et al. "The quasi-biennial oscillation". In: *Reviews of Geophysics* (2001). DOI: 10.1029/1999RG000073.

[8] F. Beckebanze, K. Raja, and L.R. M. Maas. "Mean flow generation by three-dimensional non-linear internal wave beams". In: *Journal of Fluid Mechanics* (2018).

[9] T. H. Bell. "Topographically generated internal waves in the open ocean". In: *Journal of Geophysical Research* (1975). DOI: 10.1029/JC080i003p00320.

[10] M. Berhanu et al. "Magnetic field reversals in an experimental turbulent dynamo". In: *Europhysics Letters* (2007). DOI: 10.1209/0295-5075/77/59001.

[11] A. Berson. *Bericht über die aerologische Expedition des königlichen aeronautischen Observatoriums nach Ostafrika im Jahre 1908 (Report on the aeronautical expedition of the Royal Aeronautical Observatory to East Africa in 1908)*. F. Vieweg, 1910.

[12] S. Boluriaan and P.J. Morris. "Acoustic Streaming: From Rayleigh to Today". In: *International Journal of Aeroacoustics* (2003). DOI: 10.1260/147547203322986142.

[13] J.R. Booker and F.P. Bretherton. "The critical layer for internal gravity waves in a shear flow". In: *Journal of Fluid Mechanics* (1967). DOI: 10.1017/S0022112067000515.

[14] G. Bordes et al. "Experimental observation of a strong mean flow induced by internal gravity waves". In: *Physics of Fluids* (2012). DOI: 10.1063/1.4745880.

[15] V. Botton et al. *Convection and instabilities in presence of ultrasound waves*. 2014. URL: http://lmfa.ec-lyon.fr/spip.php?article565&lang=en.

[16] F. Bouchet, C. Nardini, and T. Tangarife. "Stochastic averaging, large deviations and random transitions for the dynamics of 2D and geostrophic turbulent vortices". In: *Fluid Dynamics Research* (2014).

[17] F. Bouchet and J. Sommeria. "Emergence of intense jets and Jupiter's Great Red Spot as maximum-entropy structures". In: *Journal of Fluid Mechanics* (2002). DOI: 10.1017/S0022112002008789.

[18] F. Bouchet and A. Venaille. "Statistical mechanics of two-dimensional and geophysical flows". In: *Physics Reports* (2012). DOI: 10.1016/j.physrep.2012.02.001.

[19] F.P. Bretherton. "Momentum transport by gravity waves". In: *Quarterly Journal of the Royal Meteorological Society* (1969). DOI: 10.1002/qj.49709540402.

[20] 0. Bühler and C.J. Muller. "Instability and focusing of internal tides in the deep ocean". In: *Journal of Fluid Mechanics* (2007). DOI: 10.1017/S0022112007007410.

[21] O. Bühler. *Waves and mean flows*. Cambridge University Press, 2014.

[22] S. Cabanes et al. "A laboratory model for deep-seated jets on the gas giants". In: *Nature Physics* (2017). DOI: 10.1038/nphys4001.

[23] J.L. Cairns and G.O. Williams. "Internal wave observations from a midwater float, 2". In: *Journal of Geophysical Research* (1976). DOI: 10.1029/JC081i012p01943.

[24] J. G. Charney and P. G. Drazin. "Propagation of planetary-scale disturbances from the lower into the upper atmosphere". In: *Journal of Geophysical Research* (1961). DOI: 10.1029/JZ066i001p00083.

[25] P.H. Chavanis and J. Sommeria. "Statistical mechanics of the shallow water system". In: *Physiscal Review E* (2002). DOI: 10.1103/PhysRevE.65.026302.

[26] M. Cortini and C.C. Barton. "Chaos in geomagnetic reversal records: A comparison between Earth's magnetic field data and model disk dynamo data". In: *Journal of Geophysical Research: Solid Earth* (1994). DOI: 10.1029/94JB01237.

[27] R. G. Cosentino et al. “New Observations and Modeling of Jupiter’s Quasi-Quadrennial Oscillation”. In: *Journal of Geophysical Research: Planets* (2017). DOI: 10.1002/2017JE005342.

[28] L.A. Couston et al. “Order Out of Chaos: Slowly Reversing Mean Flows Emerge from Turbulently Generated Internal Waves”. In: *Physical Review Letters* (2018). DOI: 10.1103/PhysRevLett.120.244505.

[29] L. Coy et al. “Dynamics of the Disrupted 2015/16 Quasi-Biennial Oscillation”. In: *Journal of Climate* (2017). DOI: 10.1175/JCLI-D-16-0663.1.

[30] T. Dauxois et al. “Instabilities of Internal Gravity Wave Beams”. In: *Annual Review of Fluid Mechanics* (2018). DOI: 10.1146/annurev-fluid-122316-044539.

[31] P. Delplace, J.B. Marston, and A. Venaille. “Topological origin of equatorial waves”. In: *Science* (2017). DOI: 10.1126/science.aan8819.

[32] H.A. Dijkstra. *Nonlinear physical oceanography: a dynamical systems approach to the large scale ocean circulation and El Nino*. Springer Science & Business Media, 2005.

[33] H.A. Dijkstra. *Les houches summer school on fundamental aspects of turbulent flows in climate dynamics: Dynamical Systems Analysis of Climate Variability*. Lecture notes, École de physique des Houches. 2018. URL: https://climate-houches.sciencesconf.org/resource/page/id/2.

[34] T.E. Dowling. “Planetary science: Music of the stratospheres”. In: *Nature* (2008). DOI: 10.1038/453163a.

[35] T.J. Dunkerton. “Inertia–Gravity Waves in the Stratosphere”. In: *Journal of the Atmospheric Sciences* (1984). DOI: 10.1175/1520-0469(1984)041<3396:IWITS>2.0.CO;2.

[36] T.J. Dunkerton. “The role of gravity waves in the quasi-biennial oscillation”. In: *Journal of Geophysical Research: Atmospheres* (1997). DOI: 10.1029/96JD02999.

[37] T.J. Dunkerton. “The quasi-biennial oscillation of 2015–2016: Hiccup or death spiral?” In: *Geophysical Research Letters* (2016).

[38] M.I. Dykman et al. “Stochastic resonance in perspective”. In: *Il Nuovo Cimento D* (1995). DOI: 10.1007/BF02451825.

[39] R.A. Ebdon. “The Tropical Stratospheric Wind Fluctuation”. In: *Weather* (1963). DOI: 10.1002/j.1477-8696.1963.tb05133.x.

[40] P. Echeverri et al. “Tidally generated internal-wave attractors between double ridges”. In: *Journal of Fluid Mechanics* (2011). DOI: 10.1017/S0022112010005069.

[41] C. Eckart. “Vortices and Streams Caused by Sound Waves”. In: *Physical Review* (1948). DOI: 10.1103/PhysRev.73.68.

[42] A. Eliassen and E. Palm. “On the transfer of energy in stationary montain waves”. In: *Geofysiske Publikasjoner* (1961). DOI: 10.1029/JZ066i001p00083.

[43] C.C. Eriksen. “Implications of Ocean Bottom Reflection for Internal Wave Spectra and Mixing”. In: *Journal of Physical Oceanography* (1985). DOI: 10.1175/1520-0485(1985)015<1145:IOOBRF>2.0.CO;2.

[44] M. Ern and P. Preusse. “Wave fluxes of equatorial Kelvin waves and QBO zonal wind forcing derived from SABER and ECMWF temperature space-time spectra”. In: *Atmospheric Chemistry and Physics* (2009). DOI: 10.5194/acp-9-3957-2009.

[45] M. Falorni. “The discovery of the Great Red Spot of Jupiter”. In: *Journal of the Britannic Astronomical Association* (1987).

[46] M. Farge and R. Sadourny. “Wave-vortex dynamics in rotating shallow water”. In: *Journal of Fluid Mechanics* (1989). DOI: 10.1017/S0022112089002351.

[47] S. Fauve. *Summer study program in geophysical fluid dynamics: patterns in fluid flow*. Technical report, Woods Hole Oceanographic Institution. 1991. URL: https://darchive.mblwhoilibrary.org/handle/1912/802?show=full.

[48] L.N. Fletcher et al. “Disruption of Saturn’s quasi-periodic equatorial oscillation by the great northern storm”. In: *Nature Astronomy* (2017).

[49] T. Fouchet et al. “An equatorial oscillation in Saturn’s middle atmosphere”. In: *Nature* (2008). DOI: 10.1038/nature06912.

[50] C.D. Fritts and H.-G. Chou. “An Investigation of the Vertical Wavenumber and Frequency Spectra of Gravity Wave Motions in the Lower Stratosphere”. In: *Journal of the Atmospheric Sciences* (1987). DOI: 10.1175/1520-0469(1987)044<3610:AIOTVW>2.0.CO;2.

[51] B. Gallet et al. “Reversals of a large-scale field generated over a turbulent background”. In: *Geophysical & Astrophysical Fluid Dynamics* (2012). DOI: 10.1080/03091929.2011.648629.

[52] B. Galperin et al. “Cassini observations reveal a regime of zonostrophic macroturbulence on Jupiter”. In: *Icarus* (2014). DOI: 10.1016/j.icarus.2013.08.030.

[53] C.S. Gardner, C. A. Hostetler, and S.J. Franke. “Gravity wave models for the horizontal wave number spectra of atmospheric velocity and density fluctuations”. In: *Journal of Geophysical Research: Atmospheres* (1993). DOI: 10.1029/92JD02051.

[54] A.E. Gargett and G. Holloway. “Dissipation and diffusion by internal wave breaking”. In: *Journal of Marine Research* (1984). DOI: doi:10.1357/002224084788506158.

[55] P.R. Gent. “The Gent–McWilliams parameterization: 20/20 hindsight”. In: *Ocean Modelling* (2011). Modelling and Understanding the Ocean Mesoscale and Submesoscale. DOI: 10.1016/j.ocemod.2010.08.002.

[56] P.R. Gent and J.C. Mcwilliams. “Isopycnal Mixing in Ocean Circulation Models”. In: *Journal of Physical Oceanography* (1990). DOI: 10.1175/1520-0485(1990)020<0150:IMIOCM>2.0.CO;2.

[57] M. Giglio, S. Musazzi, and U. Perini. “Period Doubling Bifurcation Route to Chaos”. In: *Nonlinear Phenomena at Phase Transitions and Instabilities*. Springer, 1982. DOI: 10.1007/978-1-4684-4127-7_16.

[58] J.P. Gollub and S.V. Benson. “Many routes to turbulent convection”. In: *Journal of Fluid Mechanics* (1980). DOI: 10.1017/S0022112080001243.

[59] L. Gostiaux. *Étude expérimentale des ondes de gravité internes en présence de topographie. Émission, propagation, réflexion*. 2006.

[60] L. Gostiaux et al. “A novel internal waves generator”. In: *Experiments in Fluids* (2006). DOI: 10.1007/s00348-006-0225-7.

[61] L. Gostiaux et al. “Quantitative laboratory observations of internal wave reflection on ascending slopes”. In: *Physics of Fluids* (2006). DOI: 10.1063/1.2197528.

[62] L. Gostiaux et al. “Quantitative laboratory observations of internal wave reflection on ascending slopes”. In: *Physics of Fluids* (2006). DOI: 10.1063/1.2197528.

[63] N. Grisouard et al. “Large Scale Energy Transfer from an Internal Gravity Wave Reflecting on a Simple Slope”. In: *Procedia IUTAM* (2013). DOI: https://doi.org/10.1016/j.piutam.2013.04.016.

[64] S. Guerlet et al. “Equatorial Oscillation and Planetary Wave Activity in Saturn’s Stratosphere Through the Cassini Epoch”. In: *Journal of Geophysical Research: Planets* (2018). DOI: 10.1002/2017JE005419.

[65] A.M. Guzmán and C.H. Amon. “Transition to chaos in converging–diverging channel flows: Ruelle–Takens–Newhouse scenario”. In: *Physics of Fluids* (1994). DOI: 10.1063/1.868206.

[66] R.A. Hall, J.M. Huthnance, and R.G. Williams. “Internal Wave Reflection on Shelf Slopes with Depth-Varying Stratification”. In: *Journal of Physical Oceanography* (2013). DOI: 10.1175/JPO-D-11-0192.1.

[67] P. Haynes. “Stratospheric Dynamics”. In: *Annual Review of Fluid Mechanics* (2005). DOI: 10.1146/annurev.fluid.37.061903.175710.

[68] P. Haynes and E. Shuckburgh. “Effective diffusivity as a diagnostic of atmospheric transport: 1. Stratosphere”. In: *Journal of Geophysical Research: Atmospheres* (2000). DOI: 10.1029/2000JD900093.

[69] P. Haynes and E. Shuckburgh. “Effective diffusivity as a diagnostic of atmospheric transport: 2. Troposphere and lower stratosphere”. In: *Journal of Geophysical Research: Atmospheres* (2000). DOI: 10.1029/2000JD900092.

[70] I. Held. *Isaac Held’s blog: Odd recent evolution of the QBO*. https://www.gfdl.noaa.gov/blog_held/72-odd-recent-evolution-of-the-qbo/. 2016.

[71] I.M. Held. *Equatorial superrotation in Earth-like Atmospheric Models*. Bernhard Haurwitz Memorial Lecture. 1999. URL: https://www.gfdl.noaa.gov/wp-content/uploads/files/user_files/ih/lectures/super.pdf.

[72] I.M. Held. “The Gap between Simulation and Understanding in Climate Modeling”. In: *Bulletin of the American Meteorological Society* (2005). DOI: 10.1175/BAMS-86-11-1609.

[73] M. Hénon. “A two-dimensional mapping with a strange attractor”. In: *The Theory of Chaotic Attractors*. Springer, 1976, pp. 94–102.

[74] J.R. Holton. “The Influence of Gravity Wave Breaking on the General Circulation of the Middle Atmosphere”. In: *Journal of the Atmospheric Sciences* (1983). DOI: 10.1175/1520-0469(1983)040<2497:TIOGWB>2.0.CO;2.

[75] J.R. Holton and R.S. Lindzen. “An Updated Theory for the Quasi-Biennial Cycle of the Tropical Stratosphere”. In: *Journal of the Atmospheric Sciences* (1972). DOI: 10.1175/1520-0469(1972)029<1076:AUTFTQ>2.0.CO;2.

[76] D.W. Hughes, R. Rosner, and N.O. Weiss. *The Solar Tachocline*. Cambridge University Press, 2007. DOI: 10.1017/CBO9780511536243.

[77] G.N. Ivey, K.B. Winters, and J.R. Koseff. “Density Stratification, Turbulence, but How Much Mixing?” In: *Annual Review of Fluid Mechanics* (2008). DOI: 10.1146/annurev.fluid.39.050905.110314.

[78] F.-F. Jin, J.D. Neelin, and M. Ghil. “El Niño on the Devil’s Staircase: Annual Subharmonic Steps to Chaos”. In: *Science* 264 (1994). DOI: 10.1126/science.264.5155.70.

[79] T. Kataoka and T.R. Akylas. “On three-dimensional internal gravity wave beams and induced large-scale mean flows”. In: *Journal of Fluid Mechanics* (2015). DOI: 10.1017/jfm.2015.143.

[80] G.N. Kiladis et al. “Convectively coupled equatorial waves”. In: *Reviews of Geophysics* (2009). DOI: 10.1029/2008RG000266.

[81] E.-J. Kim and K.B. MacGregor. “Gravity wave-driven flows in the solar tachocline”. In: *The Astrophysical Journal Letters* (2001).

[82] J.M. Klymak, S. Legg, and R. Pinkel. “A Simple Parameterization of Turbulent Tidal Mixing near Supercritical Topography”. In: *Journal of Physical Oceanography* (2010). DOI: 10.1175/2010JPO4396.1.

[83] E. Kunze. “Internal-Wave-Driven Mixing: Global Geography and Budgets”. In: *Journal of Physical Oceanography* (2017). DOI: 10.1175/JPO-D-16-0141.1.

[84] G. Launay et al. “Transition to chaos in an acoustically-driven cavity flow”. In: *arXiv* (2018). DOI: arXiv:1806.09214.

[85] P. Leard, P. Le Gal, and M. Le Bars. personal communication. 2018.

[86] S. Legg. “Scattering of Low-Mode Internal Waves at Finite Isolated Topography”. In: *Journal of Physical Oceanography* (2014). DOI: 10.1175/JPO-D-12-0241.1.

[87] B. Legras, B. Joseph, and F. Lefèvre. “Vertical diffusivity in the lower stratosphere from Lagrangian back-trajectory reconstructions of ozone profiles”. In: *Journal of Geophysical Research: Atmospheres* (). DOI: 10.1029/2002JD003045.

[88] T.M. Lenton. “Early warning of climate tipping points”. In: *Nature Climate Change* (2011).

[89] C.B. Leovy, A.J. Friedson, and S.G. Orton. “The quasiquadrennial oscillation of Jupiter’s equatorial stratosphere”. In: *Nature* (1991). DOI: 10.1038/354380a0.

[90] J. Lighthill. “Acoustic streaming”. In: *Journal of Sound and Vibration* (1978). DOI: 10.1016/0022-460X(78)90388-7.

[91] D. K. Lilly, D. E. Waco, and S. I. Adelfang. “Stratospheric Mixing Estimated from High-Altitude Turbulence Measurements”. In: *Journal of Applied Meteorology* (1974). DOI: 10.1175/1520-0450(1974)013<0488:SMEFHA>2.0.CO;2.

[92] R.S. Lindzen and J.R. Holton. “A Theory of the Quasi-Biennial Oscillation”. In: *Journal of the Atmospheric Sciences* (1968). DOI: 10.1175/1520-0469(1968)025<1095:ATOTQB>2.0.CO;2.

[93] J.R. Lister and B.A. Buffett. “Stratification of the outer core at the core-mantle boundary”. In: *Physics of the Earth and Planetary Interiors* 105 (1998). DOI: 10.1016/S0031-9201(97)00082-4.

[94] E.N. Lorenz. “Deterministic Nonperiodic Flow”. In: *Journal of the Atmospheric Sciences* (1963). DOI: 10.1175/1520-0469(1963)020<0130:DNF>2.0.CO;2.

[95] F. Lott, L. Guez, and P. Maury. “A stochastic parameterization of non-orographic gravity waves: Formalism and impact on the equatorial stratosphere”. In: *Geophysical Research Letters* (2012). DOI: 10.1029/2012GL051001.

[96] J. Marshall et al. “A finite-volume, incompressible Navier Stokes model for studies of the ocean on parallel computers”. In: *Journal of Geophysiscal Research* (1997). DOI: 10.1029/96JC02775.

[97] A. Mashayek, C.P. Caulfield, and W.R. Peltier. “Role of overturns in optimal mixing in stratified mixing layers”. In: *Journal of Fluid Mechanics* (2017). DOI: 10.1017/jfm.2017.374.

[98] A. Mashayek et al. “Efficiency of turbulent mixing in the abyssal ocean circulation”. In: *Geophysical Research Letters* (2017). DOI: 10.1002/2016GL072452.

[99] L.R.M. Mass et al. “Observation of an internal wave attractor in a confined, stably stratified fluid”. In: *Nature* 388 (1997). DOI: 10.1038/41509.

[100] T. Matsuno. “Quasi-Geostrophic Motions in the Equatorial Area”. In: *Journal of the Meteorological Society of Japan* (1966). DOI: 10.2151/jmsj1965.44.1_25.

[101] F.T. Mayer and 0.B. Fringer. “An unambiguous definition of the Froude number for lee waves in the deep ocean”. In: *Journal of Fluid Mechanics* (2017). DOI: 10.1017/jfm.2017.701.

[102] P.L. McFadden et al. “Reversals of the Earth’s magnetic field and temporal variations of the dynamo families”. In: *Journal of Geophysical Research: Solid Earth* (1991). DOI: 10.1029/90JB02275.

[103] M.E. McIntyre. “An introduction to the generalized Lagrangian-mean description of wave, mean-flow interaction”. In: *Pure and Applied Geophysics* (1980). DOI: 10.1007/BF01586449.

[104] M.E. McIntyre. “The Quasi-Biennial Oscillation (QBO): Some Points about the Terrestrial QBO and the Possibility of Related Phenomena in the Solar Interior”. In: *The Solar Engine and Its Influence on Terrestrial Atmosphere and Climate* (1994). DOI: 10.1007/978-3-642-79257-1_18.

[105] O. Meincke and C. Egbers. “Routes into chaos in small and wide gap Taylor-Couette flow”. In: *Physics and Chemistry of the Earth, Part B: Hydrology, Oceans and Atmosphere* (1999). DOI: 10.1016/S1464-1909(99)00030-1.

[106] G. L. Mellor and T. Yamada. “Development of a turbulence closure model for geophysical fluid problems”. In: *Reviews of Geophysics* (1982). DOI: 10.1029/RG020i004p00851.

[107] M.J. Mercier et al. “Large-scale, realistic laboratory modeling of M2 internal tide generation at the Luzon Strait”. In: *Geophysical Research Letters* (2013). DOI: 10.1002/2013GL058064.

[108] J. Michel and R. Robert. “Statistical mechanical theory of the great red spot of jupiter”. In: *Journal of Statistical Physics* (1994). DOI: 10.1007/BF02179454.

[109] J. Miller, P. Weichman, and M.C. Cross. “Statistical mechanics, Euler’s equation, and Jupiter’s Red Spot”. In: *Physical Review A* (1992). DOI: 10.1103/PhysRevA.45.2328.

[110] P.D. Mininni, D.O. Gómez, and G.B. Mindlin. “Biorthogonal Decomposition Techniques Unveil the Nature of the Irregularities Observed in the Solar Cycle”. In: *Physical Review Letters* (2002). DOI: 10.1103/PhysRevLett.89.061101.

[111] J. Muraschko et al. “On the application of Wentzel-Kramer-Brillouin theory for the simulation of the weakly nonlinear dynamics of gravity waves”. In: *Quarterly Journal of the Royal Meteorological Society* (2015). DOI: 10.1002/qj.2381.

[112] B. Naujokat. “An Update of the Observed Quasi-Biennial Oscillation of the Stratospheric Winds over the Tropics”. In: *Journal of the Atmospheric Sciences* (1986). DOI: 10.1175/1520-0469(1986)043<1873:AUOTOQ>2.0.CO;2. URL: http://www.geo.fu-berlin.de/en/met/ag/strat/produkte/qbo/.

[113] S. Newhouse, D. Ruelle, and F. Takens. “Occurrence of strange Axiom A attractors near quasiperiodic flows on $T^m, m \geq 3$”. In: *Communications in Mathematical Physics* (1978).

[114] P.A. Newman et al. “The anomalous change in the QBO in 2015–2016”. In: *Geophysical Research Letters* (2016).

[115] M. Nikurashin and R. Ferrari. “Overturning circulation driven by breaking internal waves in the deep ocean”. In: *Geophysical Research Letters* (2013). DOI: 10.1002/grl.50542.

[116] A. Nowicki et al. “Estimation of acoustical streaming: theoretical model, Doppler measurements and optical visualisation”. In: *European Journal of Ultrasound* (1998). DOI: 10.1016/S0929-8266(98)00020-2.

[117] W.L. Nyborg. “Acoustic Streaming near a Boundary”. In: *The Journal of the Acoustical Society of America* (1958). DOI: 10.1121/1.1909587.

[118] S. M. Osprey et al. “An unexpected disruption of the atmospheric quasi-biennial oscillation”. In: *Science* 353.6306 (2016), pp. 1424–1427.

[119] N. Otobe et al. “Visualization and WKB analysis of the internal gravity wave in the QBO experiment”. In: *Japan Society of Fluid Mechanics* (1998).

[120] W.R. Peltier and C.P. Caulfield. “Mixing Efficiency in Stratified Shear Flows”. In: *Annual Review of Fluid Mechanics* (2003). DOI: 10.1146/annurev.fluid.35.101101.161144.

[121] F. Pétrélis and S. Fauve. “Mechanisms for magnetic field reversals”. In: *Philosophical Transactions of the Royal Society of London A: Mathematical, Physical and Engineering Sciences* (2010). DOI: 10.1098/rsta.2009.0250.

[122] R.A. Plumb. “The Interaction of Two Internal Waves with the Mean Flow: Implications for the Theory of the Quasi-Biennial Oscillation”. In: *Journal of the Atmospheric Sciences* (1977). DOI: 10.1175/1520-0469(1977)034<1847:TIOTIW>2.0.CO;2.

[123] R.A. Plumb and A.D. McEwan. “The Instability of a Forced Standing Wave in a Viscous Stratified Fluid: A Laboratory Analogue of .the Quasi-Biennial Oscillation”. In: *Journal of the Atmospheric Sciences* (1978). DOI: 10.1175/1520-0469(1978)035<1827:TIOAFS>2.0.CO;2.

[124] K. L. Polzin et al. “Spatial Variability of Turbulent Mixing in the Abyssal Ocean”. In: *Science* (1997). DOI: 10.1126/science.276.5309.93.

[125] V.D. Pope et al. “The impact of new physical parametrizations in the Hadley Centre climate model: HadAM3”. In: *Climate Dynamics* (2000). DOI: 10.1007/s003820050009.

[126] K. Rajendran et al. “Synchronisation of the equatorial QBO by the annual cycle in tropical upwelling in a warming climate”. In: *Quarterly Journal of the Royal Meteorological Society* (2015). DOI: 10.1002/qj.2714.

[127] L. Rayleigh. “On the circulation of air observed in Kundt’s tubes, and on some allied acoustical problems”. In: *Philosophical Transactions of the Royal Society of London* (1884).

[128] P.L. Read. “A Chorus of the Winds—On Saturn!” In: *Journal of Geophysical Research: Planets* (2018). DOI: 10.1029/2018JE005625.

[129] P.L. Read and A.A. Castrejón-Pita. “Phase synchronization between stratospheric and tropospheric quasi-biennial and semi-annual oscillations”. In: *Quarterly Journal of the Royal Meteorological Society* (2012). DOI: 10.1002/qj.1872.

[130] R.J. Reed et al. “Evidence of a downward-propagating, annual wind reversal in the equatorial stratosphere”. In: *Journal of Geophysical Research* (1961). DOI: 10.1029/JZ066i003p00813.

[131] O. Reynolds. “An Experimental Investigation of the Circumstances Which Determine Whether the Motion of Water Shall Be Direct or Sinuous, and of the Law of Resistance in Parallel Channels”. In: *Philosophical Transactions of the Royal Society of London* (1883).

[132] N. Riley. “Acoustic Streaming”. In: *Theoretical and Computational Fluid Dynamics* (1998). DOI: 10.1007/s001620050068.

[133] R. Robert and J. Sommeria. “Statistical equilibrium states for two-dimensional flows”. In: *Journal of Fluid Mechanics* (1991). DOI: 10.1017/S0022112091003038.

[134] C. Rodda et al. “Baroclinic, Kelvin and inertia-gravity waves in the barostrat instability experiment”. In: *Geophysical & Astrophysical Fluid Dynamics* (2018). DOI: 10.1080/03091929.2018.1461858.

[135] T.M. Rogers. “Numerical Simulations of Gravity Wave Driven Shear Flows in the Solar Tachocline”. In: *AIP Conference Proceedings* (2007). DOI: 10.1063/1.2819013.

[136] T. Rossby et al. “On the long-term stability of Gulf Stream transport based on 20 years of direct measurements”. In: *Geophysical Research Letters* (2013). DOI: 10.1002/2013GL058636.

[137] W.B. Rossow, A.D. Del Genio, and T. Eichler. “Cloud-tracked winds from Pioneer Venus OCPP images”. In: *Journal of Atmospheric Science* (1990). DOI: 10.1175/1520-0469(1990)047<2053:CTWFVO>2.0.CO;2.

[138] M.A. Rutgers. “Forced 2D Turbulence: Experimental Evidence of Simultaneous Inverse Energy and Forward Enstrophy Cascades”. In: *Physical Review Letters* (1998). DOI: 10.1103/PhysRevLett.81.2244.

[139] S. S. Sadhal. “Acoustofluidics 13: Analysis of acoustic streaming by perturbation methods”. In: *Lab Chip* (2012). DOI: 10.1039/C2LC40202E.

[140] L.F. Sampine and M.K. Gordon. *Computer Solution of Ordinary Differential Equations: the Initial Value Problem*. Freeman, 1975.

[141] M. Scheffer et al. “Early-warning signals for critical transitions”. In: *Nature* (2009).

[142] H. Schlichting. “Berechnung ebener periodischer Grenzschichtströmmungen calcul of plane periodic boundary layer streaming)”. In: *Physik Zeitung* (1932).

[143] R.W. Schmitt. “Double Diffusion in Oceanography”. In: *Annual Review of Fluid Mechanics* (1994). DOI: 10.1146/annurev.fl.26.010194.001351.

[144] U. Schumann. “Subgrid scale model for finite difference simulations of turbulent flows in plane channels and annuli”. In: *Journal of Computational Physics* (1975). DOI: 10.1016/0021-9991(75)90093-5.

[145] R.S. Scorer. “Theory of waves in the lee of mountains”. In: *Quarterly Journal of the Royal Meteorological Society* (1949). DOI: 10.1002/qj.49707532308.

[146] B. Sémin and S. Fauve. personal communication. 2018.

[147] B. Sémin et al. “Generation of a mean flow by an internal wave”. In: *Physics of Fluids* (2016). DOI: 10.1063/1.4962937.

[148] J. Smagorinsky. “General circulation experiments with the primitive equations”. In: *Monthly Weather Review* (1963). DOI: 10.1175/1520-0493(1963)091<0099:GCEWTP>2.3.CO;2.

[149] J. Sommeria et al. “Laboratory modelling of momentum transport by internal gravity waves and eddies in the Antarctic circumpolar current”. In: *International Symposium on Stratified Flows Proceedings* (2016).

[150] I.-S. Song, H.-Y. Chun, and T.P. Lane. “Generation Mechanisms of Convectively Forced Internal Gravity Waves and Their Propagation to the Stratosphere”. In: *Journal of the Atmospheric Sciences* 60 (2003). DOI: 10.1175/1520-0469(2003)060<1960:GMOCFI>2.0.CO;2.

[151] D.A. Stainforth et al. “Uncertainty in predictions of the climate response to rising levels of greenhouse gases”. In: *Nature* (2005). DOI: 10.1038/nature03301.

[152] C. Staquet and J. Sommeria. “Internal Gravity Waves: From Instabilities to Turbulence”. In: *Annual Review of Fluid Mechanics* (2002). DOI: 10.1146/annurev.fluid.34.090601.130953.

[153] M.J. Suarez and D.G. Duffy. “Terrestrial Superrotation: A Bifurcation of the General Circulation”. In: *Journal of the Atmospheric Sciences* 49 (1992). DOI: 10.1175/1520-0469(1992)049<1541:TSABOT>2.0.CO;2.

[154] B.R. Sutherland. “Internal wave instability: Wave-wave versus wave-induced mean flow interactions”. In: *Physics of Fluids* (2006). DOI: 10.1063/1.2219102.

[155] B.R. Sutherland. *Internal gravity waves*. Cambridge University Press, 2010.

[156] H.L. Swinney. “Observations of order and chaos in nonlinear systems”. In: *Physica D: Nonlinear Phenomena* (1983). DOI: 10.1016/0167-2789(83)90111-2.

[157] R.O. Thompson. “A prograde jet driven by Rossby waves”. In: *Journal of the Atmospheric Sciences* (1980).

[158] S.A. Thorpe. “An experimental study of critical layers”. In: *Journal of Fluid Mechanics* (1981). DOI: 10.1017/S0022112081001365.

[159] S.M. Tobias and J.B. Marston. “Direct Statistical Simulation of Out-of-Equilibrium Jets”. In: *Physical Review Letters* (2013). DOI: 10.1103/PhysRevLett.110.104502.

[160] G.K. Vallis. “Mechanisms and Parameterizations of Geostrophic Adjustment and a Variational Approach to Balanced Flow”. In: *Journal of the Atmospheric Sciences* (1992). DOI: 10.1175/1520-0469(1992)049<1144:MAPOGA>2.0.CO;2.

[161] G.K. Vallis. *Atmospheric and Oceanic Fluid Dynamics: Fundamentals and Large-Scale Circulation*. 2nd ed. Cambridge University Press, 2017. DOI: 10.1017/9781107588417.

[162] W. Van Bemmelen. *Der intertropische Teil der allgemeinen Zirkulation nach Beobachtungen in Batavia (The intertropical part of the general circulation after observations in Batavia)*. 1924.

[163] A. Venaille. “Bottom-trapped currents as statistical equilibrium states above topographic anomalies”. In: *Journal of Fluid Mechanics* (2012). DOI: 10.1017/jfm.2012.146.

[164] A.C. Verdiere. “Keeping the Freedom to Build Idealized Climate Models”. In: *Eos, Transactions American Geophysical Union* (2009). DOI: 10.1029/2009EO260005.

[165] J.M. Wallace and V.E. Kousky. “Observational Evidence of Kelvin Waves in the Tropical Stratosphere”. In: *Journal of the Atmospheric Sciences* (1968). DOI: 10.1175/1520-0469(1968)025<0900:OEOKWI>2.0.CO;2.

[166] C. Wang and P. C. Fiedler. “ENSO variability and the eastern tropical Pacific: A review”. In: *Progress in Oceanography* (2006). A Review of Eastern Tropical Pacific Oceanography. DOI: 10.1016/j.pocean.2006.03.004.

[167] T. Warn. “Statistical mechanical equilibria of the shallow water equations”. In: *Tellus A* (1986). DOI: 10.1111/j.1600-0870.1986.tb00448.x.

[168] N.P. Wedi and P.K. Smolarkiewicz. “Direct numerical simulation of the Plumb–McEwan laboratory analog of the QBO”. In: *Journal of the atmospheric sciences* (2006).

[169] P.B. Weichman. “Competing turbulent cascades and eddy-wave interactions in shallow water equilibria”. In: *Physical Revivew Fluids* (2017). DOI: 10.1103/PhysRevFluids.2.034701.

[170] P.B. Weichman and D.M. Petrich. “Statistical Equilibrium Solutions of the Shallow Water Equations”. In: *Physiscal Review Letters* (2001). DOI: 10.1103/PhysRevLett.86.1761.

[171] S. Yoden and J.R. Holton. “A new look at equatorial quasi-biennial oscillation models”. In: *Journal of the atmospheric sciences* (1988).

[172] L. K. Zarembo. “High–Intensity Ultrasonic Fields”. In: New York: Plenum, 1971. Chap. -Acoustic streaming-.

Résumé

La dynamique des écoulements géophysiques planétaires est fortement influencée par des processus physiques souvent non résolus par les modèles numériques de circulation générale. Il est essentiel de comprendre les mécanismes physiques sous-jacents pour paramétrer l'effet des petites échelles sur les grandes. Dans cette thèse, nous étudions un problème emblématique d'interactions entre ondes et écoulements moyens : la dynamique des écoulements zonaux forcés par des ondes internes de gravité. Une manifestation remarquable de ces interactions est l'oscillation quasi-biennale (QBO) des vents équatoriaux dans l'atmosphère terrestre. Dans un premier temps, nous décrivons une transition vers le chaos dans un modèle quasi-linéaire classique du QBO. Nous montrons que ces bifurcations persistent dans des simulations numériques directes. À l'aune de ces résultats, nous proposons une interprétation de l'observation d'une rupture inattendue de la périodicité du QBO en 2016. Le mécanisme de génération d'écoulements moyens par les ondes dans les fluides stratifiés nécessite la prise en compte d'effets dissipatifs. Il s'agit d'un phénomène analogue au "streaming" acoustique. Dans un second temps nous exploitons cette analogie en étudiant la génération d'écoulements moyens par les ondes internes proche d'une paroi, à l'aide d'approches asymptotiques multiéchelles. Finalement, nous proposons une approche inertielle pour décrire l'émergence spontanée d'écoulements vorticaux en présence d'ondes : nous appliquons les outils de mécanique statistique pour calculer la partition d'énergie entre petites et grandes échelles dans le modèle d'eau peu profonde.

Abstract

The dynamics of planetary-scale geophysical flows is strongly influenced by physical processes, mostly unresolved by general circulation numerical models. To parametrise the coupling between small and large scales, it is essential to understand the underlying physical mechanisms. In this thesis, we study an emblematic problem of interactions between waves and mean flows: the dynamics of zonal flows forced by internal gravity waves. A striking manifestation of these interactions is the quasi-biennial oscillation (QBO) of equatorial winds in the Earth's atmosphere. First, we describe a transition to chaos in a classical quasilinear model of the QBO and show that these bifurcations persist in direct numerical simulations. Based on these results, we suggest an interpretation for the observation of the unexpected periodicity disruption of the QBO in 2016. The mechanism by which mean flows are generated by waves in stratified fluids requires the consideration of dissipative effects. This phenomenon is analogous to acoustic "streaming". In a second time, we exploit this analogy to study the generation of mean flows by internal gravity waves close to a wall, using multi-scale asymptotic approaches. Finally, we propose an inertial approach to describe the spontaneous emergence of vortical flows in the presence of waves: we apply the tools of statistical mechanics to calculate the partition of energy between small and large scales in the shallow-water model.